REPORT DOCUMENTATION PAGE

AFRL-SR-BL-TR-98- 0404

1. AGENCY USE ONLY (Leave Blank)	2. REPORT DATE	3. REPORT TYPE AND DATES COVERED
	March 1993	Final

4. TITLE AND SUBTITLE
Control of Dynamic Systems Using Semi-Active Friction Damping

5. FUNDING NUMBERS

6. AUTHORS
Jeffrey S. Lane

7. PERFORMING ORGANIZATION NAME(S) AND ADDRESS(ES)
Georgia Institute of Technology

8. PERFORMING ORGANIZATION REPORT NUMBER

9. SPONSORING/MONITORING AGENCY NAME(S) AND ADDRESS(ES)
AFOSR/NI
110 Duncan Avenue, Room B-115
Bolling Air Force Base, DC 20332-8080

10. SPONSORING/MONITORING AGENCY REPORT NUMBER

11. SUPPLEMENTARY NOTES

12a. DISTRIBUTION AVAILABILITY STATEMENT
Approved for Public Release

12b. DISTRIBUTION CODE

13. ABSTRACT *(Maximum 200 words)*
None

14. SUBJECT TERMS

15. NUMBER OF PAGES

16. PRICE CODE

17. SECURITY CLASSIFICATION OF REPORT	18. SECURITY CLASSIFICATION OF THIS PAGE	19. SECURITY CLASSIFICATION OF ABSTRACT	20. LIMITATION OF ABSTRACT
Unclassified	Unclassified	Unclassified	UL

CONTROL OF DYNAMIC SYSTEMS USING SEMI-ACTIVE FRICTION DAMPING

A THESIS

Presented to
The Academic Faculty

by

Jeffrey S. Lane

In Partial Fulfillment
of the Requirement for the Degree
Doctor of Philosophy
in the School of Mechanical Engineering

Georgia Institute of Technology
March 1993

CONTROL OF DYNAMIC SYSTEMS USING SEMI-ACTIVE FRICTION DAMPING

A THESIS

Presented to
The Academic Faculty

by

Jeffrey S. Lane

In Partial Fulfillment
of the Requirement for the Degree
Doctor of Philosophy
in the School of Mechanical Engineering

Georgia Institute of Technology
March 1993

CONTROL OF DYNAMIC SYSTEMS USING SEMI-ACTIVE FRICTION DAMPING

Approved:

Aldo A. Ferri

Dr. Aldo A. Ferri, Chairman

Wayne J. Book

Dr. Wayne J. Book

Dr. Stephen L. Dickerson

Bonnie S. Heck

Dr. Bonnie S. Heck

J. V. R. Prasad

Dr. J. V. R. Prasad

Nader Sadegh

Dr. Nader Sadegh

2/18/93

Date Approved by Chairman

Dedicated To

Darlene, Kevin, and Keith

ACKNOWLEDGEMENTS

It would be difficult (if not impossible) to acknowledge each person who in some way has helped me to complete this research and the other requirements of the Ph.D. degree. Help and guidance have been received in a variety of areas and from a variety of sources.

I remember seeking the guidance of Dr. Tom Leland prior to entering the Ph.D. program. He cautioned me to expect the unexpected, both good and bad. His predictions certainly proved accurate. I am indebted to the many who have given me encouragement and the benefit of their wisdom. My advisor, Dr. Al Ferri, has had a large impact on my research work. I could always count on him to come through when I needed him. Charles Ingram and Alan Bindemann provided many valuable ideas for the design of the quarter car experimental assembly. Heartfelt thanks also go to Donald Long whose expert craftsmanship turned these ideas into tangible reality. Encouragement was received from many people. One who stands out in my memory is Homer Brown. Unknown to him, his encouraging words came at a time when I most needed them. Perhaps the most useful and enduring help came from Dr. Mike Brissett. And the list goes on.

Returning to school on a full-time basis would not have been possible if not for the financial assistance received from the Department of Defense, the School of

Mechanical Engineering, and Delco Chassis NDH Division of General Motors Corporation. I gratefully acknowledge this assistance. Others, such as Mr. and Mrs. Charles Ingram, Peggy Lane, and Jimmy Lane, have lovingly given when we were in need.

When it comes to acknowledging my family, I'm not sure what to say. Not sure whether the Ph.D. has been the best or the worst thing to enter our lives. Few know the true cost of this endeavor. Whatever the case, I'm grateful for the loving support of my family. Never have I known such love, patience, and forgiveness as has been received the last few years. To you, Darlene, Kevin, and Keith, I offer my sincerest thanks.

Surely I'm living in the care of the Almighty.

TABLE OF CONTENTS

LIST OF TABLES

LIST OF FIGURES

SUMMARY

The control of vibrational motion in mechanical systems has long been a problem of interest. This research investigates using friction damping for flexible structure control and for automotive suspension control. The hallmark feature of this approach is that the normal force at the frictional interface is actively controlled. This eliminates the undesirable stick-slip motion found in systems damped by friction in which the normal force is constant. Since the normal force is physically constrained to be positive (compressive) or zero only dissipative work can be done by the controller. Actively controlling the normal force therefore classifies this as a semi-active controller.

Friction damping is used to dissipate vibrational energy in a pinned-pinned two beam system in which a single semi-active joint connects the beams. The results of the research indicate that significant damping (modal damping ratios up to 0.20) can be added to the structure by the semi-active joint. A controller designed using linear quadratic regulator theory with an energy related cost functional is shown to be particularly effective at dissipating the flexural motion. The semi-active nature of the controller is enforced by clipping the control input to ensure that only dissipative work is done by the joint. However, this ad-hoc method of control clipping is shown to be very close to the true optimal solution in which the semi-active nature of the joint is an explicit control constraint. Issues which arise when the joint controller is incorporated into a structure

with an attitude control system are also investigated. It is shown that the design of the joint controller should not be independent of the attitude controller design process if optimal performance is desired. A variable gain system is also designed in which the joint controller emulates viscous damping with a time varying viscous coefficient. This system has improved performance over all the constant gain designs of this type. Finally, the semi-active joint is incorporated in a free floating two beam system. Since some vibratory modes produced little (or in some cases zero) joint motion for this configuration, the semi-active joint is relatively ineffective.

Semi-active friction damping for automotive suspension control is also investigated. A scale model, quarter car experimental assembly was designed, fabricated, and utilized in this study. The semi-active friction damping is achieved using an electromagnetic friction clutch under active computer control. One particular attribute of the suspension controller which is demonstrated is the ability to provide shock isolation via software control. This requires setting a limit on the resistive force of the friction damper. Since the resistive force is decoupled from the suspension velocity (a property not seen in hydraulic dampers) the shock isolation control is even achievable using a low bandwidth controller. Suspension control is also demonstrated using a low bandwidth controller. This is the first experimental demonstration of semi-active friction damping as well as the first experimental demonstration of a low bandwidth semi-active suspension control system. The results indicate that this is a viable candidate for automotive suspension control systems.

CHAPTER I

INTRODUCTION

The control of vibrational motion in mechanical systems has long been a problem of interest. Many innovative techniques have been used to eliminate or minimize vibratory motion. Vibration control was traditionally achieved by passive devices such as shock absorbers or by intentionally designing the system to be stiff or rigid. Developments of the past few decades in space transportation and the introduction of inexpensive digital computers have generated new challenges for vibration control in which the earlier techniques are no longer feasible.

Two areas of significant interest are the control of unwanted flexural motion in large space structures (LSS) and the control of car body motion in automotive systems. The former is a result of the desire to fabricate large space structures using as little mass as necessary. Large, lightweight structures will unfortunately be flexible which will compromise many mission objectives. Since adding mass to stiffen the structure is undesirable due to the transportation costs, vibration control systems which can remove the flexural energy are being investigated. The interest in automotive systems stems from the introduction of inexpensive digital computers. Significant improvements can be made

in vehicle handling qualities by replacing passive suspension elements with active or semi-active elements. However, due to the highly competitive nature of the automotive market, intelligent control system design is required to achieve large performance improvements at as low a cost as possible.

This thesis investigates using semi-active friction damping for flexible structure control and for automotive suspension control. The research on flexible structure control is theoretical in nature. Analytical tools and concepts are used to design the control systems while performance studies are carried out using a digital simulation. Conversely, the research on automotive suspension control systems is experimental in nature.

The following chapter formally introduces the concept of applying semi-active friction damping to large space structures. Relevant background material and related work are discussed. Chapters 3-8 discuss modeling and control system design issues for the large space structure application. Chapters 9 and 10 discuss the automotive suspension control system design and associated experimental results. Chapter 11 contains concluding remarks and recommendations for future work.

CHAPTER II

LSS VIBRATION CONTROL CONCEPTS

2.1 Introduction

The anticipated deployment of large space structures (LSS) has focused attention on the need for new advances in the area of flexible structure control. Large flexible solar arrays, antennas, and precision optical systems are a few of the currently conceived structures to be deployed in space [1], [2]. In order to accomplish design objectives, these systems have stringent requirements for attitude and shape control. These systems are typically constructed using large built-up truss structures. The truss structures being considered for LSSs exhibit very low modal damping (0.1% - 0.5% [3], [4]). The large size (10s to 100s of meters), configuration, and relatively low weight will result in very low, closely spaced natural frequencies. Proposed control systems will have bandwidths that contain several major structural resonant frequencies. Thus interaction between the attitude and shape controllers and the flexural modes of the structure are inevitable. For good performance of the attitude and shape controllers to be achieved, some form of structural vibration control is necessary.

2.2 Active Vibration Control

Designing a flexible structure control system for a LSS is a very challenging task. Initial research in this area focused primarily on active vibration control (sometimes referred to as modal control). These control systems can be generally segregated into two categories depending on the type of actuation system used. In discrete actuation systems the actuator exerts a force or moment at a specific location. In distributed actuation systems the actuator exerts a control force on a non-localized (or continuous) domain.

Modal control using discrete actuation systems was the dominant area of research for many years. There are numerous publications for designs of this type; see, for example, references [3]-[13]. The plant (or LSS) is a distributed parameter system with infinitely many modes. Discrete control systems are limited to controlling and observing only a few of the low frequency modes due to computational limitations. A variety of control system design techniques have been examined to date. One of the most popular is linear optimal control. In this case, the plant is reduced in order, usually through modal truncation, and linearized if necessary. The resulting system equation takes the form,

$$\dot{\underline{x}} = [A]\underline{x} + [B]\underline{u} \, . \tag{2.1}$$

The control is defined to be $\underline{u} = -[k]\underline{x}$, where [k] is chosen to minimize a desired performance index. For the case of quadratic cost criteria, the cost functional has the

form

$$J = \int_0^\infty \left(\underline{x}^T [Q] \underline{x} + \underline{u}^T [R] \underline{u} \right) dt \, . \tag{2.2}$$

The feedback gain matrix which minimizes J is known to be

$$[k] = [R]^{-1} [B]^T [P] \tag{2.3}$$

where [P] satisfies the algebraic Riccati equation

$$[A]^T [P] + [P][A] - [P][B][R]^{-1} [B]^T [P] + [Q] = [0] \, . \tag{2.4}$$

Since the state $\underline{x}$ is rarely available for feedback, linear observers or estimators have also been investigated for use in LSS. However, as discussed below, the stability of estimated state-feedback systems is difficult to ensure.

A major obstacle which must be overcome in designs of this type is spillover. As mentioned above, the controller only controls and observes several of the low frequency modes. This leads to an effect known as spillover. Control spillover occurs when some of the energy intended for the controlled modes is pumped into the uncontrolled modes. This results in a degradation in performance. Observer spillover occurs when some of the energy in the uncontrolled modes is attributed to the observed modes by the observer. In [5], Balas shows that when observer spillover is present, even small uncertainties in the original eigenvalues can cause instabilities in the closed loop system. This fact was verified experimentally by Cannon and Rosenthal in [14]. Systems most sensitive to

spillover induced instabilities are those which use noncolocated actuators and sensors. If colocated sensors and actuators are used, one can guarantee stability for all modes with relatively simple control laws [15], [16]. The very low inherent damping of LSS aggravates the spillover problem and necessitates the requirement for better (often more complex) controller designs or adherence to the requirement of collocation of sensors and actuators.

A relatively new approach to flexible structure control involves the use of distributed actuation systems [17]-[21]. Distributed control is achieved by bonding a layer of piezoelectric material to the surface of the flexible structure and creating surface strains on the structure by imposing a voltage differential on the piezoelectric material. The attractiveness of this approach is that by using a distributed actuator, modal truncation is not necessary. Theoretically, all the modes of vibration can be controlled at once, provided that the structure is controllable through the actuator [18]. In [19], Connally and Hubbard used this approach to increase the damping ratios of the first two modes of a cantilever beam from 0.21 and 0.14 to 0.66 and 0.58 respectively. A major disadvantage of this approach is that it requires the application of piezoelectric material along substantial portions of the structure surface.

2.3 Passive Vibration Control

An alternative approach to active vibration control is passive control. In active control the undesirable motion is counteracted by an externally powered actuator. In passive control the system is required to do nonconservative (i.e. dissipative) work when the undesired motion occurs. From an external viewpoint, passive control techniques increase the system's inherent damping. There are several approaches to designing passive control systems. One approach investigated by Lane in [22] and Alberts in [23] for flexible beam vibration control is to apply a viscoelastic material and a constraining layer to the exterior of the beam. This approach may be difficult to use in LSS control due to the effect of the environmental conditions of space on the viscoelastic material [24]. Impact damping has also been used as a means of increasing the passive damping levels of lightly damped systems [25], [26]. In large truss structures another source of passive vibration control is joint damping [27]-[30]. Hertz and Crawley in [28] and Ferri in [29] develop models of sleeve joints. Energy dissipation occurs as a result of beam-sleeve impacts and from friction forces present at the sliding interfaces. In [30] Bowden and Dugundji discuss truss structures which have linear viscous dampers at the joints. Energy dissipation at the joints could possibly be the dominant source of inherent damping in LSS due to the very low levels of material damping. As an example, in [7], where an experimental flexible beam was constructed for testing, Schaechter and Eldred identified the primary sources of damping as joint damping and atmospheric drag. Given

that there will be no atmospheric damping in space, the only significant source of damping would come from the joints.

2.4 Combination of Active and Passive Vibration Control

Passive control techniques can be used as stand-alone vibration control systems; however, their greatest utility appears to occur when used in conjunction with an active controller. This technique was applied to the control of a flexible manipulator arm by Alberts et al in [23] and [31]. Bicos et al in [4] applied passive damping treatments to elements of an LSS truss structure (the Neutral Particle Beam Integrated Space Experiment truss structure) to aid the active flexural vibration controller. Chen, Garba, and Wada in [11] used passive damping via constrained viscoelastic layer treatments in conjunction with active struts to control the truss structure for the Precision Segmented Reflector. Adding passive damping to the system decreases the difficulty of active controller design. With higher inherent damping, the active controller is less sensitive to plant variations, spillover effects, noise, and other error sources.

2.5 Semi-Active Joint Damping

Joints in LSS have already been identified as a major source of passive damping. However, this damping is in large part inadvertent. The joints are designed to meet structural and assembly requirements with little or no concern for the structural damping

they will provide. This is certainly a viable design approach for earth based structures which can be structurally stiffened to prevent flexural motion. However in LSS design, this approach could ignore a potentially significant source of damping. LSS are expected to have such low levels of inherent damping that any contributor to system stability should be investigated. This research investigates the concept of increasing the damping of the structure via actively controlled, energy dissipating joints. The energy dissipation mechanism in the joints will be Coulomb friction. An actively controlled pin joint design is shown in Figure 2.1. The two beams have a well defined frictional interface and an actuation system capable of exerting a variable normal force. This joint could then become a subsystem of an overall attitude/shape control system.

Since the control at the joint is the normal force, the active joint is only capable of removing energy from the structure. It thus acts only to enhance the damping. Actively controlling a passive damping source to enhance its effectiveness classifies this as a semi-active controller. Semi-active control systems have several notable advantages over their active counterparts. In particular, they usually have higher bandwidths [76] and have lower power requirements [39] than fully-active controllers. Furthermore, the closed loop system is guaranteed to be dissipative, thus stability is ensured (even in the absence of the active control).

Many systems use dry (unlubricated) friction for damping and vibration control. Friction damping has been used in turbine blade disk assemblies [32], earthquake tolerant structures [33], washing machines [34], and others. In the area of LSS, friction damping

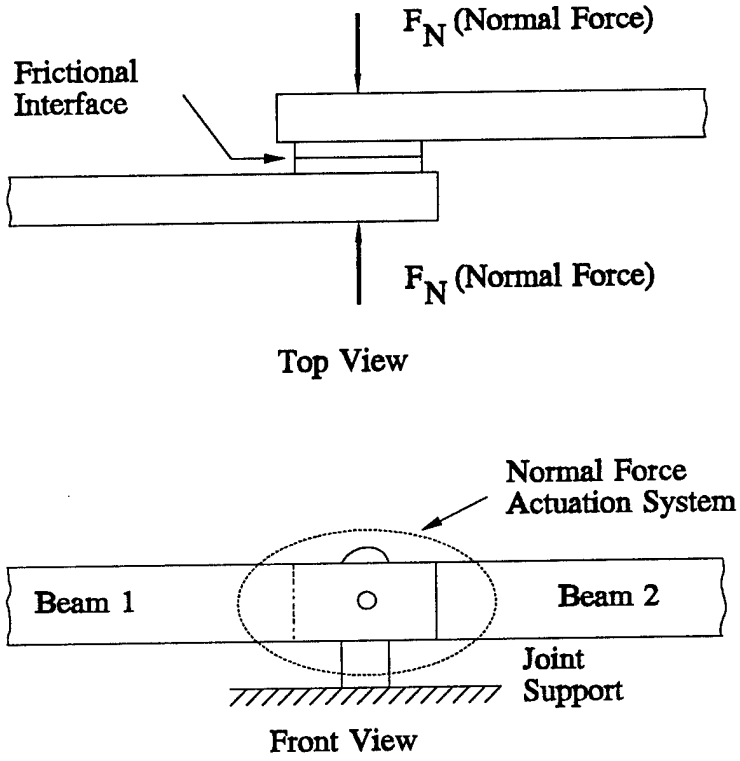

Figure 2.1 Semi-Active Joint

in joints has been analyzed by several researchers ([27]-[29], [35], [36]), but joints have not yet been designed with friction damping in mind. The joint is designed to meet structural or assembly requirements and the frictional damping is a property of the joint which must be accounted for in order to get an accurate system model. Designing a joint to specifically address its energy dissipation properties was investigated by Prucz et al ([37], [38]). The energy dissipation at the joints was accomplished using a constrained viscoelastic layer bonded to the structural members. Relative motion between the structural members caused shear flow in the viscoelastic material which dissipated the vibrational energy. In many cases the benefit which resulted from increased energy dissipation was offset by a reduction in joint stiffness.

Active and passive joints designed primarily for their energy dissipating capabilities were proposed in [39]. A two beam structure with pinned joints was subjected to transverse vibrations. The study focused on how to define the normal force at the center joint to increase the damping. In the passive joint design, the normal force was defined as

$$F_N = k_0 + k_1 |\theta| \tag{2.5}$$

where k_0 and k_1 are design parameters and θ is the joint angle. This form for F_N defines the passive joint design because it can be realized without an external actuation system (for example with an elliptical joint pin). In the semi-active joint design an actuation system is used to generate the joint normal force. A feedback control law of the form

$$F_N = k_0 + k_1 |\theta| + k_2 |\dot{\theta}| \tag{2.6}$$

was investigated where k_0, k_1, and k_2 are design parameters (assumed to be positive) and θ and $\dot{\theta}$ are the joint angular displacement and rate. The study indicated that significant increases in joint damping were achievable when the normal force was not constrained to be constant. The research in this thesis further investigates the semi-active joint design idea. Note that because the normal force is controlled and not the torque, no energy can be added to the system. This is fundamentally different than the case of flexible robotic manipulators [40] or the case of an active hinge explored by Cudney et al [41]. For the active hinge a torque motor, gear box, tachometer, and strain gauge are located at the joint. Control inputs are not restricted to merely opposing motion. Experimental results by Cudney on a jointed cantilever beam system with an active hinge showed little improvement in first mode damping, 130% increase in the second mode damping ratio, and 180% increase in the third mode damping ratio. The small improvement in first mode damping was due to the actuator being placed at a node of the first mode.

Chapters 3-8 investigate the semi-active joint control concept in detail. Chapter 3 develops a model for the two beam system with the semi-active joint. Simulations are used to identify the number and type of flexural modes needed to accurately model the system. Chapter 4 looks at several constant coefficient, linear feedback control designs for the joint controller. Chapter 5 investigates the optimal performance of the semi-active joint controller. Chapter 6 looks at issues which arise when the joint controller is

implemented in a two beam system which includes additional attitude and shape controllers. Chapter 7 describes the design of an adaptive or gain scheduled joint controller. The performance of the semi-active joint in a free-free beam architecture is then discussed in Chapter 8.

CHAPTER III

TWO BEAM SYSTEM MODEL

3.1 Introduction

Before any control system analysis and design can be performed, a mathematical model of the system is required. In this chapter, the equations of motion for the pinned-pinned beam system are derived using the assumed modes method. Trade off studies are also performed in order to define the number of modes and the mode shape functions necessary for accurate control system design and system simulation studies.

3.2 Equations of Motion

The two beam system is shown in Figure 3.1. It consists of two beams and three pin joints, the center joint being semi-active. Figure 2.1 shows the semi-active joint in more detail, the main features being a controllable normal force and a frictional interface.

Using the assumed modes method, the transverse displacement of beam i (i=1 or 2) is given by

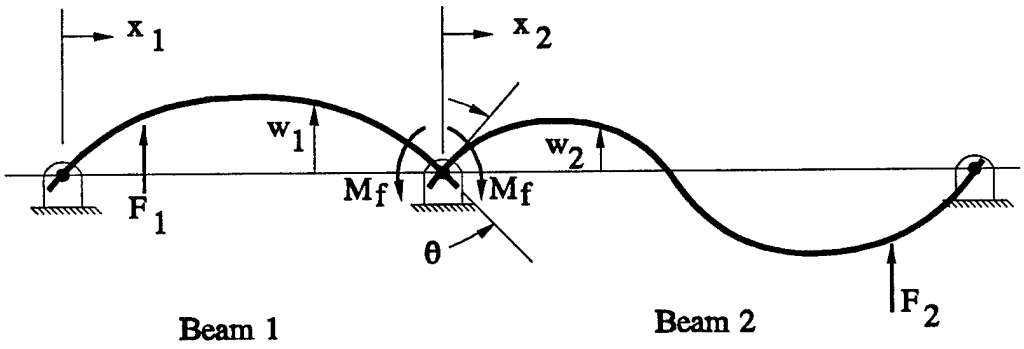

Figure 3.1 Pinned-Pinned Beam System

$$w_i(x_i,t) = \sum_{j=1}^{N_i} \phi_{ij}(x_i)\,\eta_{ij}(t) \ , \tag{3.1}$$

where $\phi_{ij}(x_i)$ is the j^{th} mode shape function, $\eta_{ij}(t)$ is the j^{th} modal amplitude, and N_i is the number of modes used to model the i^{th} beam. Since the beams are connected by a frictional interface, two cases of motion must be considered. In the first case, sliding (or slipping) occurs at the frictional interface. If the normal force is sufficiently large the joint will lock up and no relative motion occurs. This is termed sticking and is the second case to be considered.

The equations of motion for the two beam system (for sliding or sticking motion) are,

$$\eta_{1j}) \sum_{k=1}^{N_1} \left[\rho_1 A_1 \int_0^{L_1} \phi_{1j}\,\phi_{1k}\,dx_1\right]\ddot{\eta}_{1k} + \sum_{k=1}^{N_1} \left[E_1 I_1 \int_0^{L_1} \phi''_{1j}\,\phi''_{1k}\,dx_1\right]\eta_{1k} \tag{3.2}$$

$$= \left[\phi_{1j}(x_{F1})\right]F_1 + \left[\phi'_{1j}(L_1)\right]M_f \quad j = 1, \ldots, N_1$$

$$\eta_{2j}) \sum_{k=1}^{N_2} \left[\rho_2 A_2 \int_0^{L_2} \phi_{2j}\,\phi_{2k}\,dx_2\right]\ddot{\eta}_{2k} + \sum_{k=1}^{N_2} \left[E_2 I_2 \int_0^{L_2} \phi''_{2j}\,\phi''_{2k}\,dx_2\right]\eta_{2k} \tag{3.3}$$

$$= \left[\phi_{2j}(x_{F2})\right]F_2 + \left[-\phi'_{2j}(0)\right]M_f \quad j = 1, \ldots, N_2 \ .$$

These equations can be written in matrix form as,

$$[M]\ddot{\underline{\eta}} + [K]\underline{\eta} = [B_1]\underline{F} + \underline{B}_2 M_f \,, \tag{3.4}$$

where [M] is the mass matrix, [K] is the stiffness matrix, $\underline{F}$ is the disturbance input vector, M_f is the frictional moment imparted to each beam, and $[B_1]$ and $\underline{B}_2$ are appropriate coefficient matrices. $\underline{\eta}$ is the modal amplitude vector defined as

$$\underline{\eta} = \left[\eta_{11}\ \eta_{12}\ \cdots\ \eta_{1N_1}\ \eta_{21}\ \eta_{22}\ \cdots\ \eta_{2N_2}\right]^T \,, \tag{3.5}$$

and $\underline{F}$ is the disturbance vector defined as

$$\underline{F} = \begin{bmatrix} F_1 \\ F_2 \end{bmatrix}. \tag{3.6}$$

As seen from equation (3.4), no material damping has been modeled, thus any energy dissipated within the two beam system can be attributed to the external control system. The mass matrix is composed of two submatrices as follows,

$$[M] = \left[\begin{array}{c|c} [M_1] & [0] \\ \hline [0] & [M_2] \end{array}\right]. \tag{3.7}$$

The elements of the mass submatrices are given by

$$\left[M_i\right]_{jk} = \rho_i A_i \int_0^{L_i} \phi_{ij}(x_i)\, \phi_{ik}(x_i)\, dx_i \,, \tag{3.8}$$

where ρ_i is the density, A_i is the cross sectional area, and L_i is the length of the i^{th} beam.

Similarly, the stiffness matrix is given by

$$[K] = \begin{bmatrix} [K_1] & | & [0] \\ \text{-----} & | & \text{-----} \\ [0] & | & [K_2] \end{bmatrix} \tag{3.9}$$

where

$$\left[K_i\right]_{jk} = E_i I_i \int_0^{L_i} \phi''_{ij}(x_i)\, \phi''_{ik}(x_i)\, dx_i \ . \tag{3.10}$$

In (3.10), E_i and I_i are the elastic modulus and area moment of inertia of beam i respectively. The coefficient matrices for $\underline{F}$ and M_f are given by

$$\left[B_1\right] = \begin{bmatrix} \phi_{11}(x_{F1}) & \cdots & \phi_{1N_1}(x_{F1}) & 0 & \cdots & 0 \\ 0 & \cdots & 0 & \phi_{21}(x_{F2}) & \cdots & \phi_{2N_2}(x_{F2}) \end{bmatrix}^T \tag{3.11}$$

$$\underline{B}_2 = \left[\phi'_{11}(L_1) \ \cdots \ \phi'_{1N_1}(L_1) \ -\phi'_{21}(0) \ \cdots \ -\phi'_{2N_2}(0)\right]^T , \tag{3.12}$$

where x_{F1} and x_{F2} are the points of application of F_1 and F_2, respectively. In order to write (3.4) in terms of first order differential equations, define $\underline{x}$ as

$$\underline{x} = \begin{bmatrix} \dot{\underline{\eta}} \\ \underline{\eta} \end{bmatrix}, \tag{3.13}$$

which results in the following equations of motion,

$$\dot{\underline{x}} = \left[A_{SL}\right]\underline{x} + \left[B_{\underline{F}}\right]\underline{F} + \underline{B}_M M_f \,, \tag{3.14}$$

where

$$\left[A_{SL}\right] = \left[\begin{array}{c|c} [0] & -[M]^{-1}[K] \\ \hline [I] & [0] \end{array}\right] \tag{3.15}$$

$$\left[B_{\underline{F}}\right] = \left[\begin{array}{c} [M]^{-1}\left[B_1\right] \\ \hline [0] \end{array}\right] \tag{3.16}$$

$$\underline{B}_M = \left[\begin{array}{c} [M]^{-1}\,\underline{B}_2 \\ \hline \underline{0} \end{array}\right]. \tag{3.17}$$

When slipping is occurring at the frictional interface, the moment imparted to each beam as a result of the joint normal force and the frictional interface is

$$M_f = k_G\,\mu_D\,F_N\,\mathrm{sgn}(\dot{\theta}) \tag{3.18}$$

where k_G is an appropriate geometric factor, μ_D is the kinetic coefficient of friction, F_N is the joint normal force, and $\dot{\theta}$ is the relative joint angular rate. The joint normal force, F_N, is constrained to be positive, which from equation (3.18) implies

$$F_N \geq 0 \quad \Rightarrow \quad M_f \dot{\theta} \geq 0 \ . \tag{3.19}$$

The equations of motion can also be expressed in terms of the joint normal force in which case

$$\dot{\underline{x}} = \left[A_{SL} \right] \underline{x} + \left[\underline{B_F} \right] \underline{F} + \underline{B}_F \, \mathrm{sgn}(\dot{\theta}) \, F_N \ , \tag{3.20}$$

where

$$\underline{B}_F = k_G \, \mu_D \, \underline{B}_M \ . \tag{3.21}$$

The joint angular rate can be expressed in terms of the state vector by

$$\dot{\theta} = \left[C_{\dot{\theta}} \right] \underline{x} \tag{3.22}$$

where

$$\left[C_{\dot{\theta}} \right] = \left[-\phi'_{11}(L_1) \ \ldots \ -\phi'_{1N_1}(L_1) \ \phi'_{21}(0) \ \ldots \ \phi'_{2N_2}(0) \ 0 \ \ldots \ 0 \right] . \tag{3.23}$$

Since the beams are coupled by a frictional interface, joint lock up (or sticking) can occur if $\dot{\theta}=0$ and the normal force is large enough to overcome the beam moments at the joint. The maximum frictional moment which can be developed when $\dot{\theta}=0$ is given by

$$M_f^{max} = k_G \, \mu_s \, F_N \ , \tag{3.24}$$

where μ_S is the static coefficient of friction. Defining the frictional moment using equations (3.18) and (3.24) corresponds to the Coulomb friction model with stiction. The moment necessary to cause sticking is given by

$$M_f^{stick} = -\frac{1}{\left[C_{\dot\theta}\right]\underline{B}_M}\left[C_{\dot\theta}\right]\left[A_{SL}\right]\underline{x} - \frac{1}{\left[C_{\dot\theta}\right]\underline{B}_M}\left[C_{\dot\theta}\right]\left[B_{\underline{F}}\right]\underline{F} \qquad (3.25)$$

which was found by calculating the moment necessary for $\ddot\theta=0$ ($\dot\theta=0$ is already assumed) using equation (3.14) and the fact that

$$\ddot\theta = \left[C_{\dot\theta}\right]\dot{\underline{x}} \; . \qquad (3.26)$$

If the frictional moment is not large enough to prohibit sliding and $\dot\theta=0$, M_f will take its maximum value (specified by (3.24)) in the direction which opposes motion. Thus when $\dot\theta=0$,

$$M_f = \begin{cases} M_f^{stick} & M_f^{Max} \geq abs\left(M_f^{stick}\right) \quad \text{(sticking)} \\ M_f^{max}\, sgn\left(M_f^{stick}\right) & \text{otherwise} \qquad\qquad \text{(sliding)} \; . \end{cases} \qquad (3.27)$$

The calculation of M_f is shown in block diagram form in Figure 3.2. Note that the $\dot\theta=0$ requirement is replaced with $abs(\dot\theta)\leq\varepsilon$, where ε is a small number representing approximately zero joint motion. This is necessary for the digital simulation. Aside from the modification to M_f, the equations of motion for the $\dot\theta=0$ and the $\dot\theta\neq0$ cases are identical.

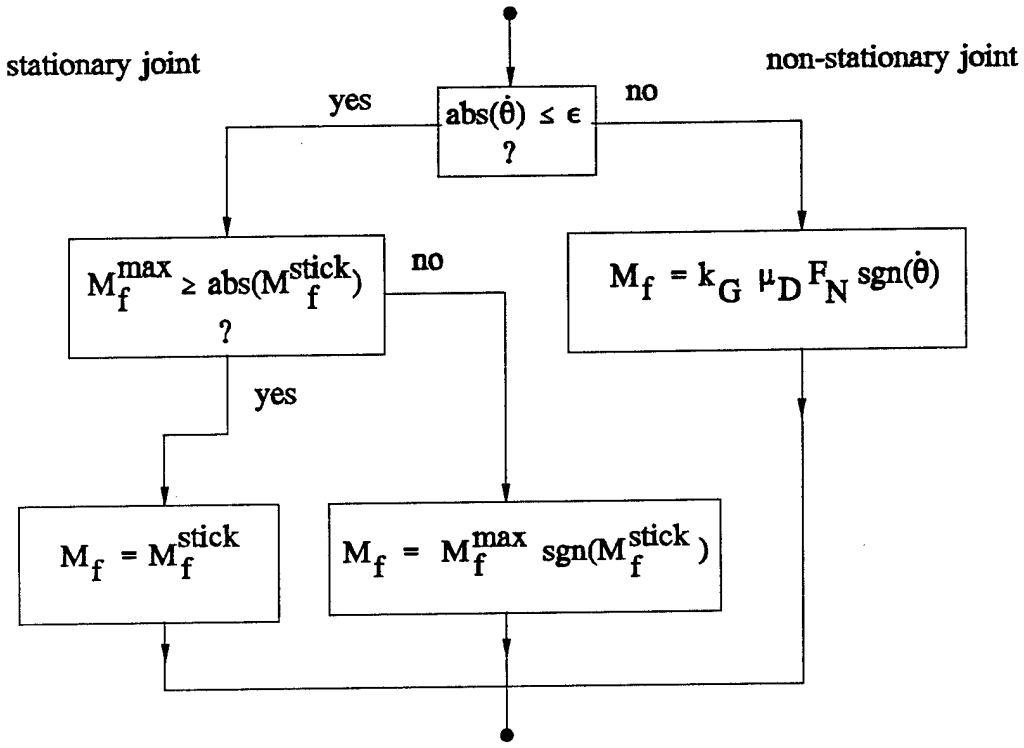

Figure 3.2 Coulombic Friction Law Implementation

3.3 Trade Studies

Specifying the assumed modes method for modeling the two beam system does not fully define the system model. Additional studies are needed to define the mode shape functions and how many modes are needed to accurately represent the physical system. Mode shape functions and the number of modes required for an accurate model are related quantities. A poor choice of shape functions may result in an undesirably high number of modes being required.

To evaluate and compare different models against each other, three types of evaluation criteria will be used. The baseline model used in the evaluation criteria (and throughout the thesis) is the two beam system with the physical parameters shown in Table 3.1. For the modeling studies, the joint normal force is defined as

Table 3.1 Two Beam System Parameters

$$\rho_1 A_1 = \rho_2 A_2 = 0.4 \text{ kg/m}$$
$$E_1 I_1 = E_2 I_2 = 20 \text{ N-m}^2$$
$$L_1 = 1.0 \text{ m} \quad L_2 = 1.8 \text{ m}$$
$$\mu_S = \mu_D = 0.5$$
$$k_G = 0.025 \text{ m}$$
$$x_{F1} = 0.25 \text{ m} \quad x_{F2} = 1.35 \text{ m}$$

$$F_N = 150\,\mathrm{abs}(\dot{\theta}) \,, \tag{3.28}$$

which is a design that first appeared in [39]. This control (as will be shown later) linearizes the system. The first measure of model accuracy are the eigenvalues of the closed loop system. The eigenvalues, as with the other evaluation criteria, should converge as the number of modes is increased. Frequency response data from the beam 1 disturbance input (F_1) to various system outputs will be the second measure of performance. The final performance measure is the system response to a pulse disturbance on beam 1 in the time domain.

3.3.1 Sine Modes

The most natural choice for mode shapes of the two beam system are sine modes of the form

$$\phi_{ij}(x_i) = \sqrt{2}\,\sin\left(\frac{j\,\pi\,x_i}{L_i}\right). \tag{3.29}$$

These modes are the exact solution for the mode shapes of a single pinned-pinned beam. As suggested by Ferri in [42], the modes have been normalized such that

$$\int_0^{L_i} \phi_{ij}\,\phi_{ik}\,dx_i = L_i\,\delta_{jk} \,. \tag{3.30}$$

Normal modes result in diagonal [M] and [K] matrices, a fact that makes it possible to

incorporate modal damping in an easy, straight forward method. As required, these mode shapes satisfy the geometric boundary conditions,

$$\begin{aligned} &\text{i) } w_i(0,t) = 0. \\ &\text{ii) } w_i(L_i,t) = 0. \end{aligned} \tag{3.31}$$

for each beam in the two beam system. Natural boundary conditions, however, require that a moment exist at the center pin on each beam due to the semi-active joint. This is not satisfied by the sine modes which have zero moments at both ends of each beam. Since this is a natural boundary condition the modes are nonetheless appropriate. It should be noted that as increasingly more modes are added, moments can be carried by the beam closer and closer to the ends. Thus by increasing the modes, the moment carrying capacity near the pin joints is increased.

Eigenvalue data for various numbers of sine modes per beam is shown in Table 3.2. Note the convergence as the number of modes is increased. In Table 3.2, a pair of numbers in the form [ζ,ω] represents a complex conjugate eigenvalue pair with damping ζ and natural frequency ω in rad/sec. A single number in the form (ω) represents a real eigenvalue. Frequency response data is shown in Figures 3.3 - 3.7. In Figures 3.3 and 3.4, the frequency response from F_1 to θ is shown for the cases of $N_1 = N_2 = 1, 2, 3$, and 4. Note that as more modes are added, agreement between the curves occurs out to higher and higher frequencies. Figures 3.5 - 3.7 show frequency response data for the cases of i) N_1=4, N_2=6, ii) N_1=6, N_2=8, iii) N_1=8, N_2=8. ε_1 and ε_2 are beam strains at

Table 3.2 Closed Loop Eigenvalues for Sine Modes

N_1, N_2	Closed Loop Eigenvalues					
1		[.314/27.4]	[.830/54.9]			
2	(20.9)	[.182/27.2]	[.010/79.8]	[.238/176]		
3	(17.4)	[.152/26.9]	[.011/79.3]	[.132/130]	[.030/222]	
4	(16.1)	[.138/26.7]	[.011/79.1]	[.116/122]	[.023/216]	[.010/320]
6	(14.9)	[.126/26.5]	[.011/78.9]	[.100/116]	[.018/212]	[.010/315]
8	(14.3)	[.120/26.3]	[.011/78.7]	[.092/114]	[.016/211]	[.010/313]
10	(14.0)	[.117/26.3]	[.011/78.6]	[.087/113]	[.015/210]	[.010/312]
20	(13.4)	[.110/26.2]	[.011/78.5]	[.078/110]	[.013/209]	[.010/309]

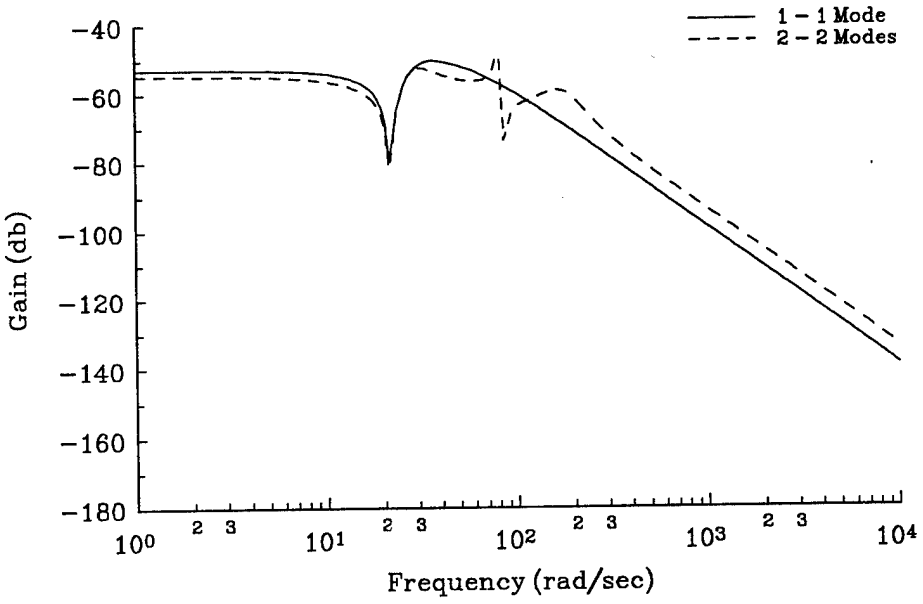

Figure 3.3 $\theta(s)/F_1(s)$ Comparison of 1-1 and 2-2 Sine Mode Models

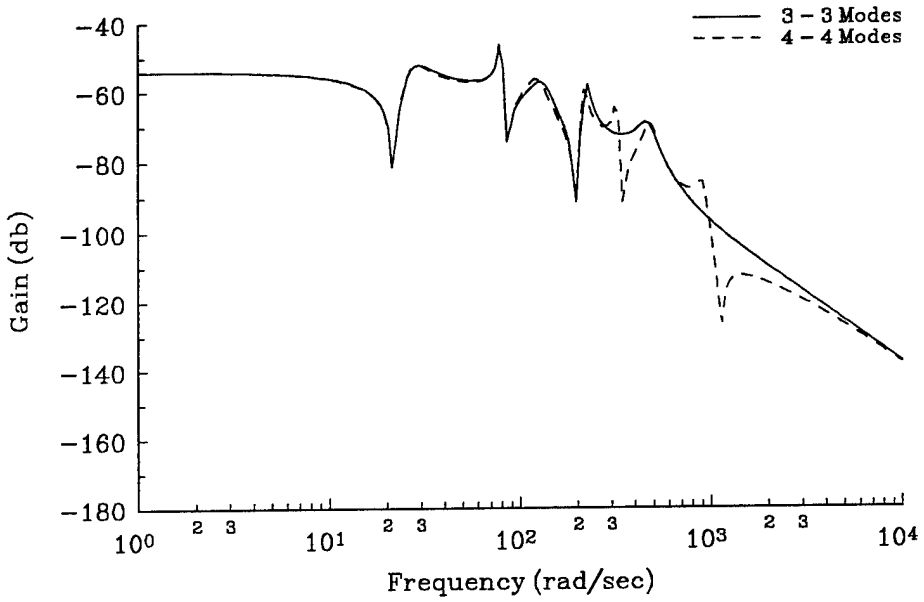

Figure 3.4 $\theta(s)/F_1(s)$ Comparison of 3-3 and 4-4 Sine Mode Models

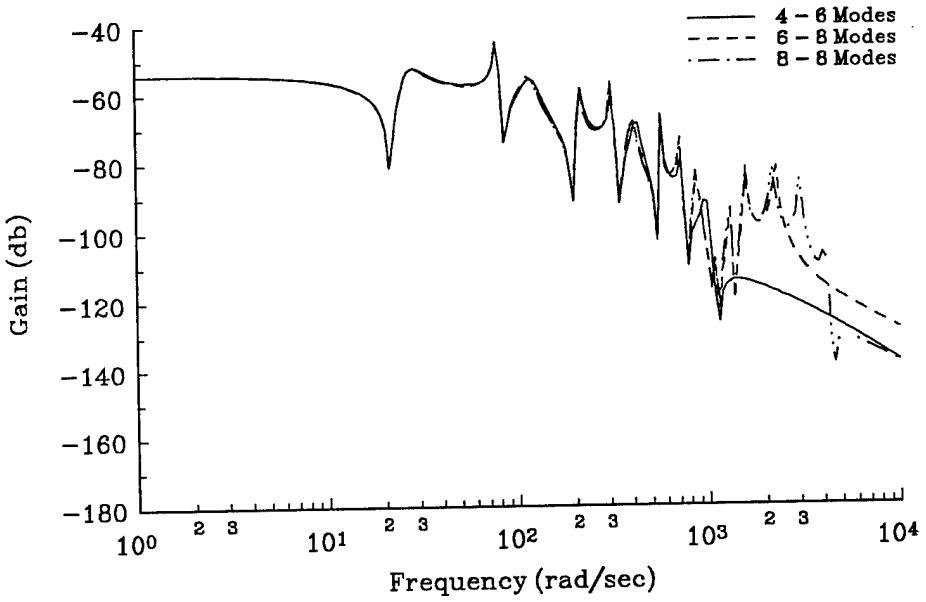

Figure 3.5 $\theta(s)/F_1(s)$ Comparison of 4-6, 6-8, and 8-8 Sine Mode Models

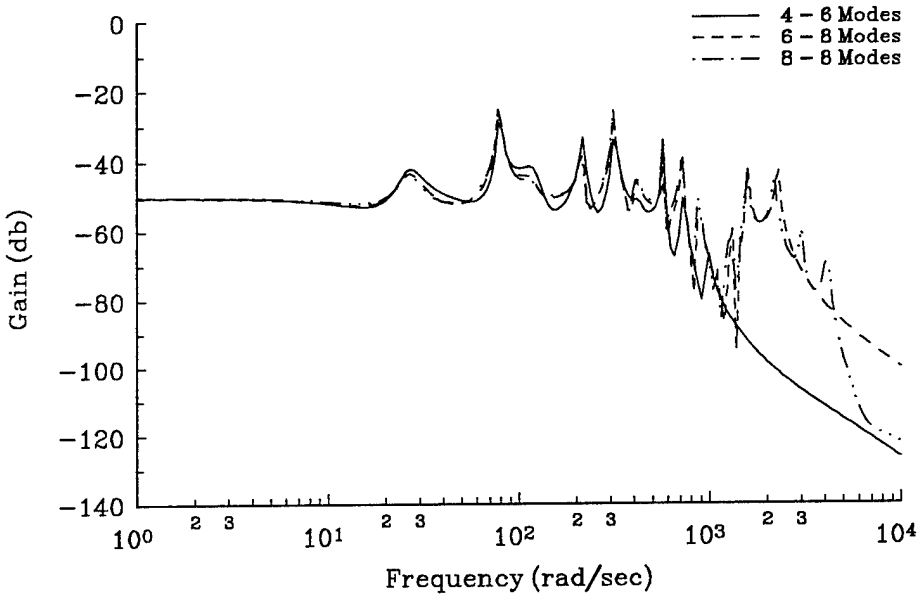

Figure 3.6 $\varepsilon_1(s)/F_1(s)$ Comparison of 4-6, 6-8, and 8-8 Sine Mode Models

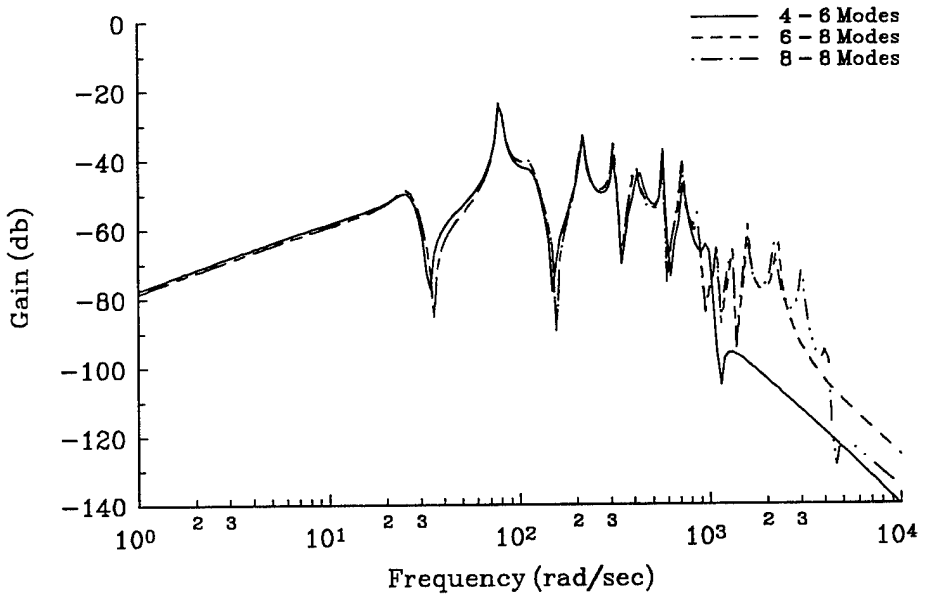

Figure 3.7 $\varepsilon_2(s)/F_1(s)$ Comparison of 4-6, 6-8, and 8-8 Sine Mode Models

$0.75L_1$ and $0.25L_2$, respectively. Figures 3.8 - 3.12 show system responses in the time domain to a pulse disturbance on beam 1. The pulse disturbance is given by

$$F_1 = \begin{cases} 25.\ \text{N} & 0 \le t \le 0.01 \\ 0. & t > 0.01\ . \end{cases} \tag{3.32}$$

Convergence is evident in all curves.

3.3.2 Polynomial Modes

Mode shapes which better satisfy the natural boundary conditions usually exhibit improved convergence properties. In order to investigate shape functions which can carry a moment at the center pin, the following polynomial mode shapes were investigated,

$$\begin{aligned} \phi_{11}(x_1) &= \left(\frac{x_1}{L_1}\right) - \left(\frac{x_1}{L_1}\right)^3 \\ \phi_{1j}(x_1) &= \left(\frac{x_1}{L_1}\right)^{j+1} - \left(\frac{x_1}{L_1}\right)^{j+2} \quad j \ge 2 \end{aligned} \tag{3.33}$$

$$\begin{aligned} \phi_{21}(x_2) &= \left(\frac{L_2 - x_2}{L_2}\right) - \left(\frac{L_2 - x_2}{L_2}\right)^3 \\ \phi_{2j}(x_2) &= \left(\frac{L_2 - x_2}{L_2}\right)^{j+1} - \left(\frac{L_2 - x_2}{L_2}\right)^{j+2} \quad j \ge 2\ . \end{aligned} \tag{3.34}$$

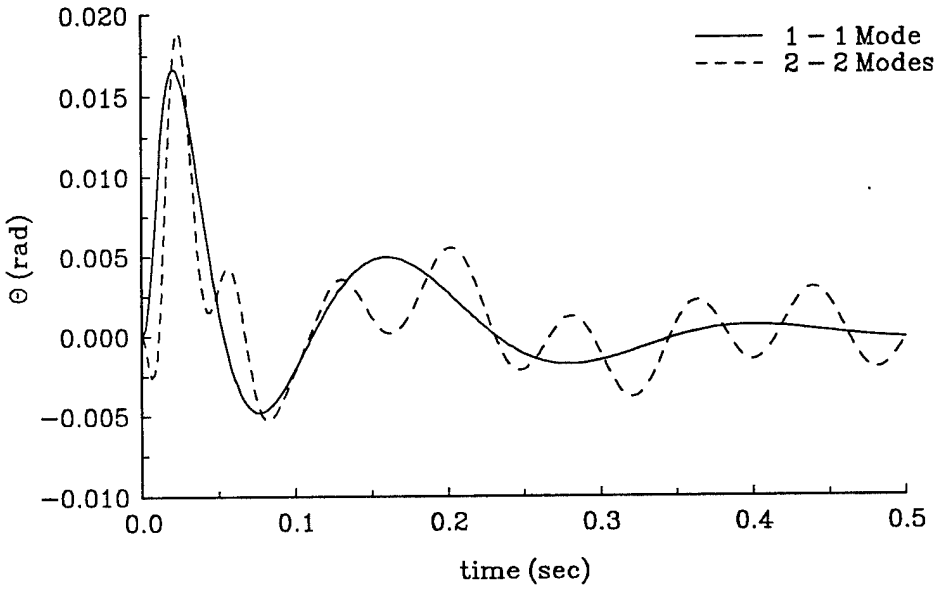

Figure 3.8 θ vs t Comparison of 1-1 and 2-2 Sine Mode Models

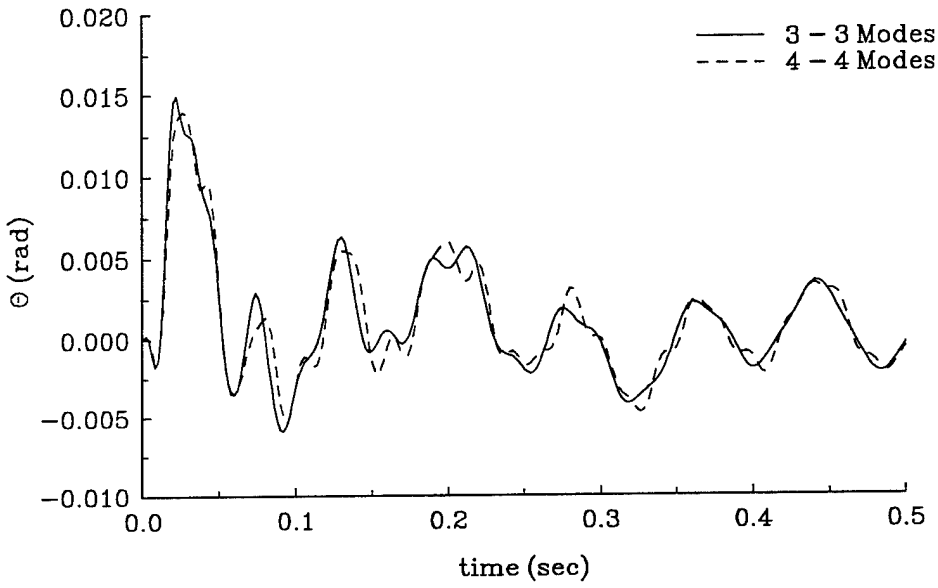

Figure 3.9 θ vs t Comparison of 3-3 and 4-4 Sine Mode Models

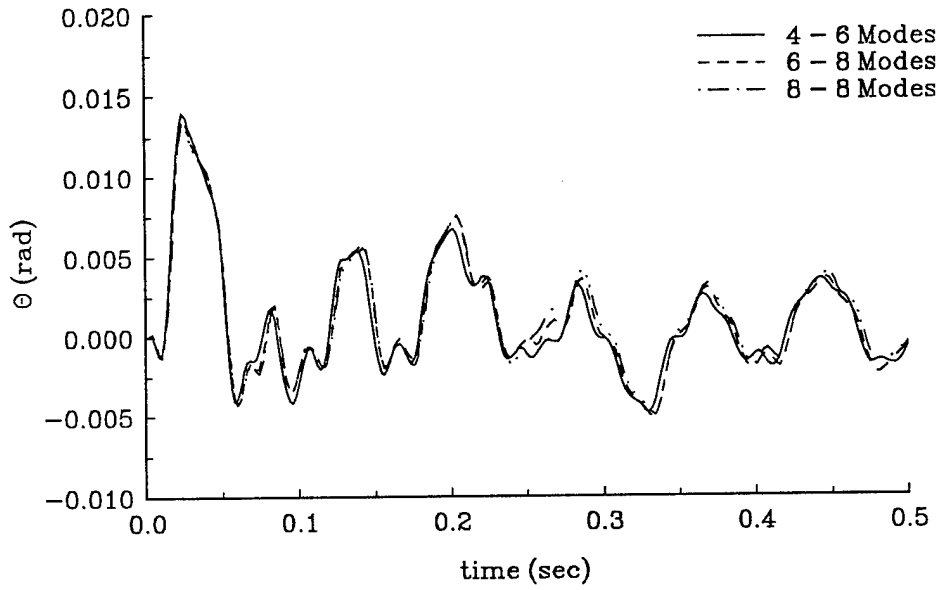

Figure 3.10 θ vs t Comparison of 4-6, 6-8, and 8-8 Sine Mode Models

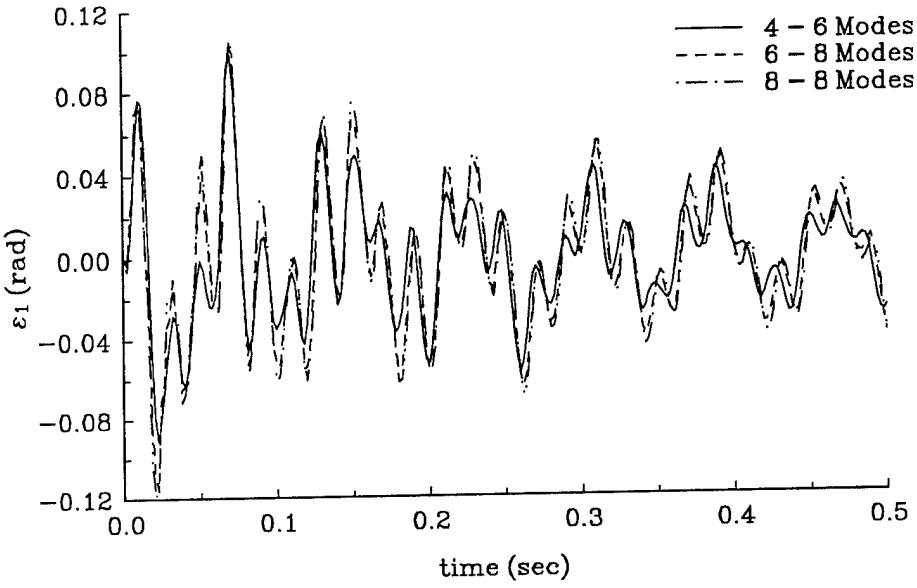

Figure 3.11 ε_1 vs t Comparison of 4-6, 6-8, and 8-8 Sine Mode Models

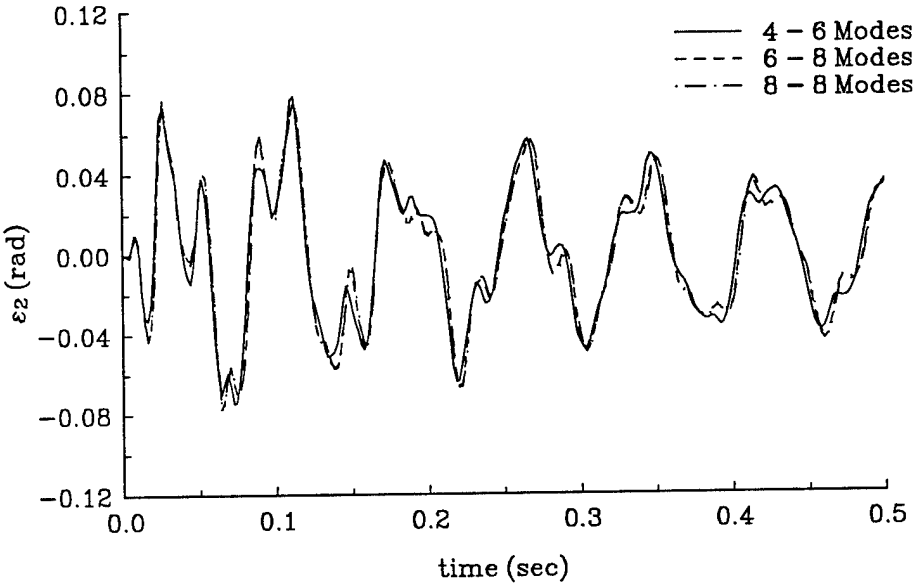

Figure 3.12 ε_2 vs t Comparison of 4-6, 6-8, and 8-8 Sine Mode Models

These mode shapes have several interesting features. First, as mentioned above, a moment can be carried at the center pin while retaining zero moments at the outer pin joints. Also, the first mode is the static deflection profile for a pinned-pinned beam with a moment at one pin. Figure 3.13 shows several of the polynomial mode shapes for beam 1. These modes, however, are nonorthogonal and thus result in fully populated $[M_i]$ and $[K_i]$ matrices. This would prohibit the easy inclusion of modal damping if desired.

Eigenvalue data for $N_1 = N_2 = 1, ..., 10$ is shown in Table 3.3. Frequency response data for $N_1 = N_2 = 1, 2, 3,$ and 4 is shown in Figures 3.14 and 3.15. Pulse response plots for the same cases are shown in Figures 3.16 and 3.17.

3.4 Discussion of Results

Eigenvalue data, frequency response data, and pulse response data all indicate that both mode shape functions are converging. The eigenvalue data shows a more rapid convergence for the polynomial modes but the frequency domain and time domain measures do not indicate a particular advantage of one series over another. The deciding factor in choosing mode shape functions was ease of simulation, since other factors are approximately equal. The sine modes were much easier to simulate than the polynomial modes. The polynomial shape functions resulted in numerically stiffer systems which required significantly more CPU time to integrate. A simulation using 2 modes per beam took 50% longer for the polynomial modes than the sine modes. This ratio went up

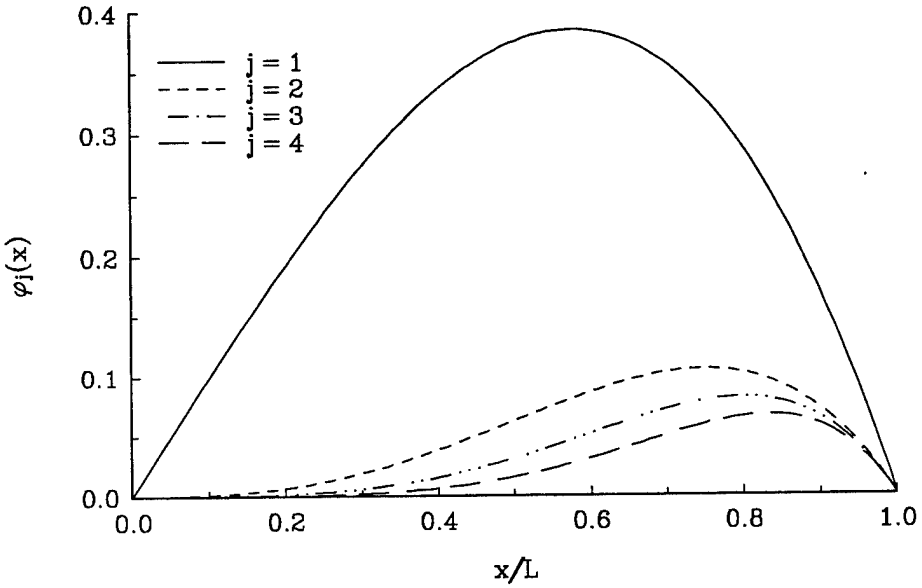

Figure 3.13 Polynomial Mode Shape Functions

Table 3.3 Closed Loop Eigenvalues for Polynomial Modes

N_1, N_2	Closed Loop Eigenvalues					
1	(13.1)	[.151/41.4]				
2	(12.9)	[.104/26.1]	[.031/82.3]	[.080/209]		
3	(12.9)	[.104/26.1]	[.011/78.5]	[.072/109]	[.002/293]	
4	(12.9)	[.104/26.1]	[.011/78.4]	[.070/108]	[.011/213]	[.020/320]
6	(12.9)	[.104/26.1]	[.011/78.3]	[.070/108]	[.011/208]	[.011/309]
8	(12.9)	[.104/26.1]	[.011/78.3]	[.070/108]	[.011/208]	[.009/307]
10	(12.9)	[.103/26.1]	[.011/78.1]	[.071/108]	[.011/203]	[.011/316]

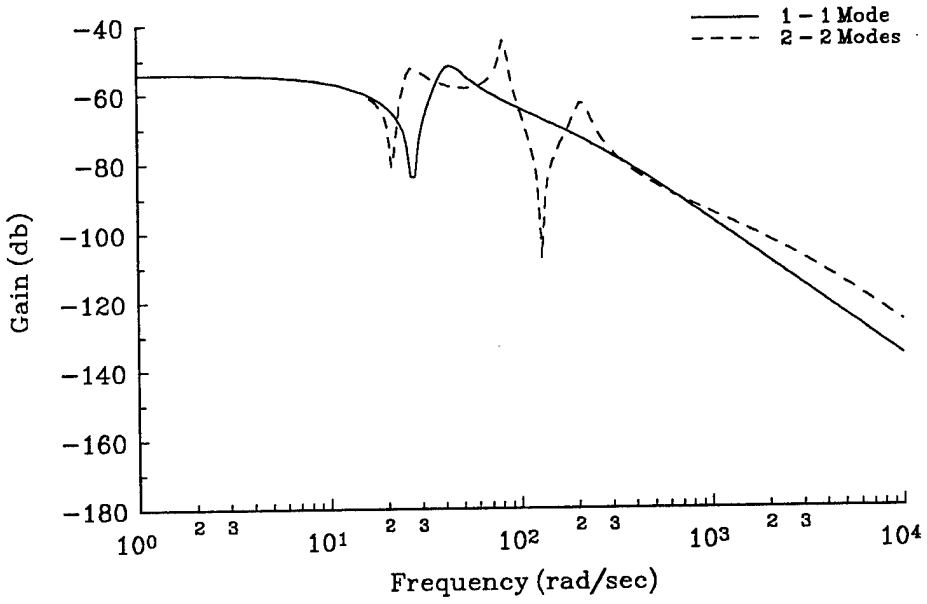

Figure 3.14 $\theta(s)/F_1(s)$ Comparison of 1-1 and 2-2 Polynomial Mode Models

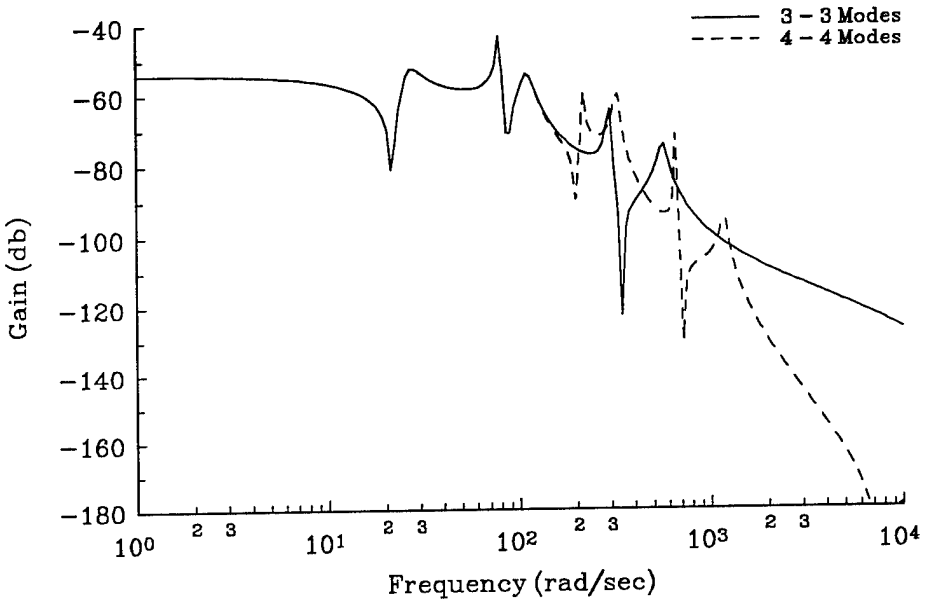

Figure 3.15 $\theta(s)/F_1(s)$ Comparison of 3-3 and 4-4 Polynomial Mode Models

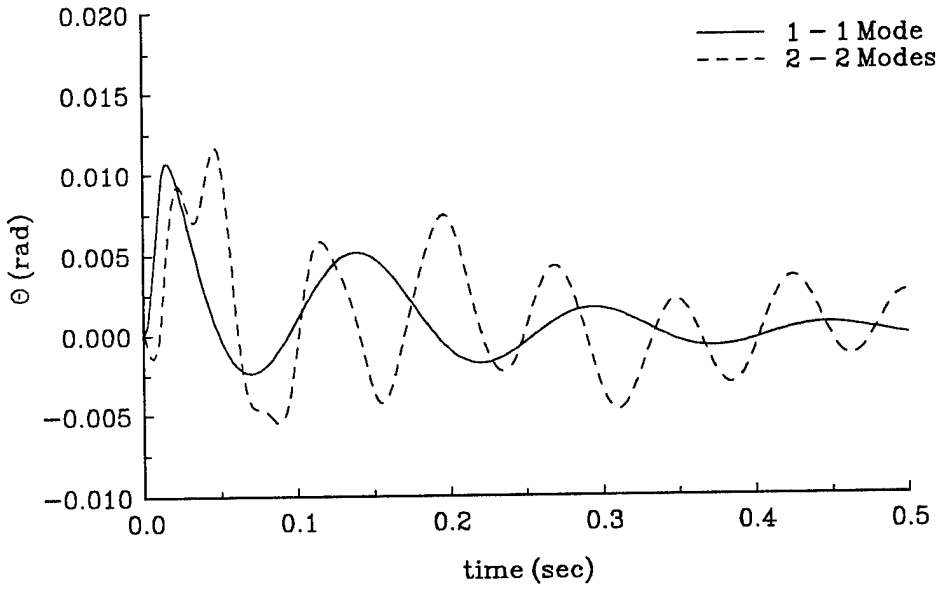

Figure 3.16 θ vs t Comparison of 1-1 and 2-2 Polynomial Mode Models

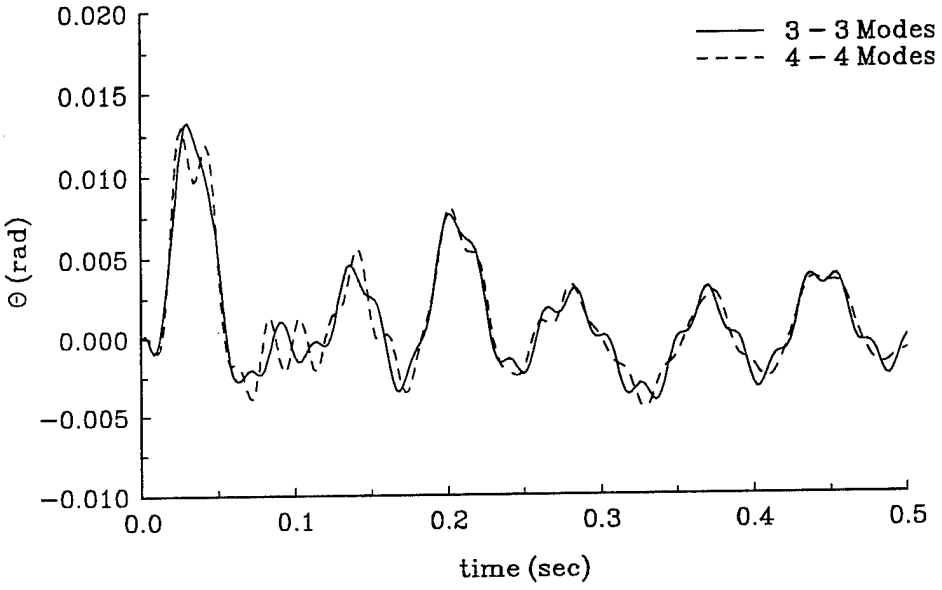

Figure 3.17 θ vs t Comparison of 3-3 and 4-4 Polynomial Mode Models

dramatically as the number of modes was increased.

The sine mode evaluation data led to the establishment of two models. The first is a model used for control system design. For this case, a 3-mode-per-beam model is sufficient. This model captures all of the necessary dynamics for designing a control system. In order to evaluate observer spillover effects, a second, more accurate model is also required. For this purpose a model consisting of 4 modes for beam 1 and 6 modes for beam 2 is sufficient. Convergence data for θ, ε_1, and ε_2 were shown in the preceding figures since these will be used as observer inputs in later work.

In addition to the above mode shapes, one additional approach to choosing the ϕ's was investigated. This was prompted by studies by Meirovitch and Kwak [43] in which convergence was improved by choosing admissible functions which although individually do not satisfy the natural boundary conditions, linear combinations of the ϕ's do. As an added advantage, the set of assumed modes is able to support a moment at the center pin, but should eliminate the numerical stiffness problem. The chosen set was:

$$\phi_{11}(x_1) = \left(\frac{x_1}{L_1}\right) - \left(\frac{x_1}{L_1}\right)^3$$
$$\phi_{1j}(x_1) = \sqrt{2}\,\sin\left(\frac{j\pi x_1}{L_1}\right) \quad j \geq 2\ , \tag{3.35}$$

and similarly reflected mode shapes for beam 2. This choice did show convergence, but at a slower rate than either the sine or polynomial modes.

CHAPTER IV

LINEAR JOINT CONTROLLER DESIGNS

4.1 Introduction

Joints have already been identified as a major source of damping in large space structures. The semi-active joint is intended to maximize the damping at the joints by controlling the normal force, F_N, at the frictional interface. The feedback control law governing F_N can be designed in a variety of ways. Perhaps the simplest class of controller designs involve linear, constant coefficient feedback gain matrices. These designs can be based on output or state feedback. In this chapter, several linear, constant gain joint controller designs will be investigated. The goal is to control the vibrational energy to the largest extent possible using only the semi-active joint. Two approaches are investigated. The first approach involves output feedback of $\dot{\theta}$ and the second approach uses full state feedback with feedback gains defined using linear quadratic regulator theory.

4.2 Viscous Joint Design

In reference [39], Ferri and Heck proposed two types of joint controllers. The first defined the normal force as

$$F_N = k_0 + k_1 |\theta| \ . \tag{4.1}$$

This is described as a passive joint because it is possible to implement this functional form or structure for F_N without an externally powered actuation system. The semi-active joint design defined F_N as

$$F_N = k_0 + k_1 |\theta| + k_2 |\dot{\theta}| \ . \tag{4.2}$$

This structure for F_N would require an external actuation system due to the $\dot{\theta}$ feedback. Of particular interest is the more restrictive case of

$$F_N = k_{VJ} |\dot{\theta}| \ . \tag{4.3}$$

Substituting (4.3) into (3.20), and setting $\underline{F}=\underline{0}$ gives

$$\begin{aligned} \dot{\underline{x}} &= \left[A_{SL}\right]\underline{x} + \underline{B}_F k_{VJ} |\dot{\theta}| \operatorname{sgn}(\dot{\theta}) \\ &= \left[A_{SL}\right]\underline{x} + \underline{B}_F k_{VJ} \dot{\theta} \ . \end{aligned} \tag{4.4}$$

Substituting (3.22) into (4.4) and simplifying,

$$\dot{\underline{x}} = \left[\left[A_{SL}\right] + k_{VJ}\underline{B}_F\left[C_{\dot{\theta}}\right]\right]\underline{x} \; . \tag{4.5}$$

Since equation (4.5) is linear and the gain k_{VJ} is scalar, the appropriate selection of k_{VJ} can be accomplished using root locus techniques. This design is termed the *viscous joint* design because the resulting frictional moment is equivalent to that generated by a rotary, viscous damper at the joint. In addition to its ease of design, the viscous joint design is also desirable in that joint sticking will not occur since $|F_N| \rightarrow 0$ as $|\dot{\theta}| \rightarrow 0$.

Root locus plots for a 3 sine mode per beam model are shown in Figures 4.1 and 4.2. Due to the different rates of travel of each pole, no single value of k_{VJ} offers optimal damping for all the modes. Ferri and Heck in [39] chose k_{VJ}=150 based on a 1 sine mode per beam model. This proved to be a good value for the 3 mode per beam model as well. The closed loop eigenvalues for this case are shown in Table 4.1.

Table 4.1 Closed Loop Eigenvalues for Viscous Joint

ζ	ω
----	----
1.0	17.4
.152	26.9
.011	79.3
.132	130
.030	222
.098	464
1.0	1351

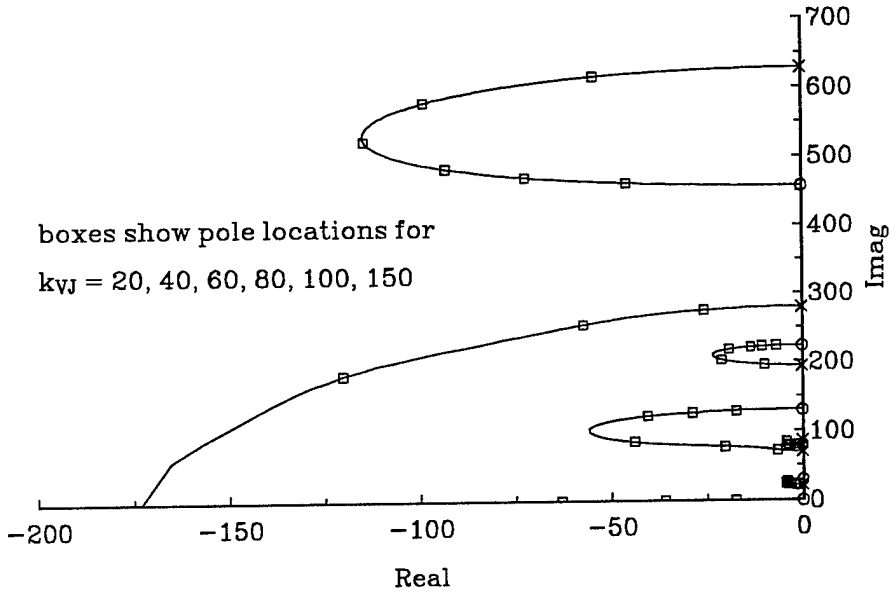

Figure 4.1 Root Locus for 2 Beam System with Viscous Joint

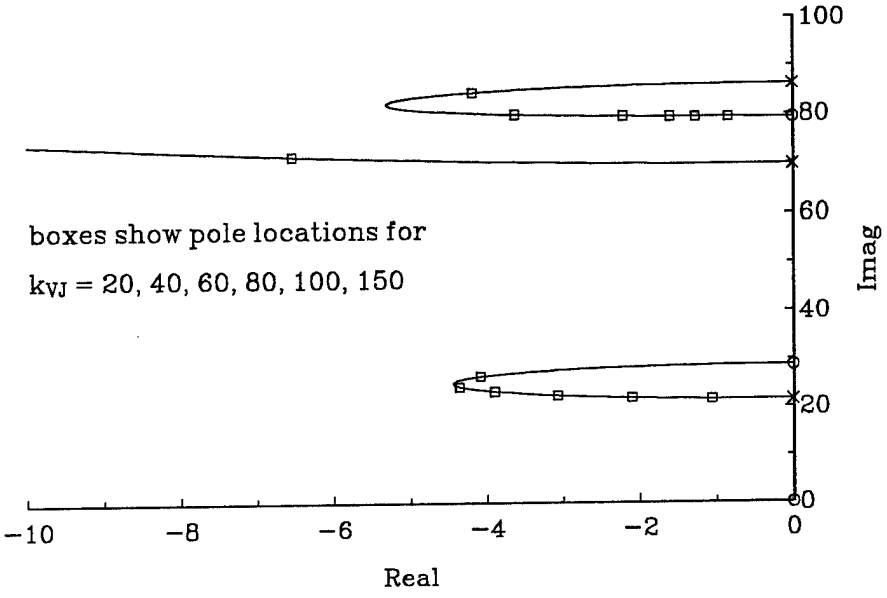

Figure 4.2 Root Locus for 2 Beam System with Viscous Joint

Simulation data is shown in Figures 4.3 - 4.5 for a pulse disturbance on beam 1. Figure 4.3 shows the normal force time history, Figure 4.4 the joint angular rate, and Figure 4.5 shows the total energy in the two beam system.

4.3 LQR Designs

An alternative design approach utilizes linear quadratic regulator (LQR) theory. A linear model of the two beam system is given in equation (3.14) with the control taken to be the frictional moment, M_f, rather than the normal force, F_N. The performance index is chosen to be

$$J = \frac{1}{2}\int_0^{t_f} \underline{x}^T [Q]\,\underline{x} + r\,M_f^2\,dt\ . \tag{4.6}$$

The M_f which extremizes J and satisfies the state equations is given by

$$M_f = -\underline{B}_M{}^T [S(t)]\,\underline{x}/r\ . \tag{4.7}$$

[S(t)] in equation (4.7) is the solution to the following matrix Riccati equation,

$$\begin{aligned} -[\dot{S}(t)] = [A_{SL}]^T[S(t)] + [S(t)][A_{SL}] \\ - [S(t)]\underline{B}_M\underline{B}_M{}^T[S(t)]/r + [Q]\ . \end{aligned} \tag{4.8}$$

Letting $t_f \rightarrow \infty$ and using the steady state value of [S(t)] gives the suboptimal control

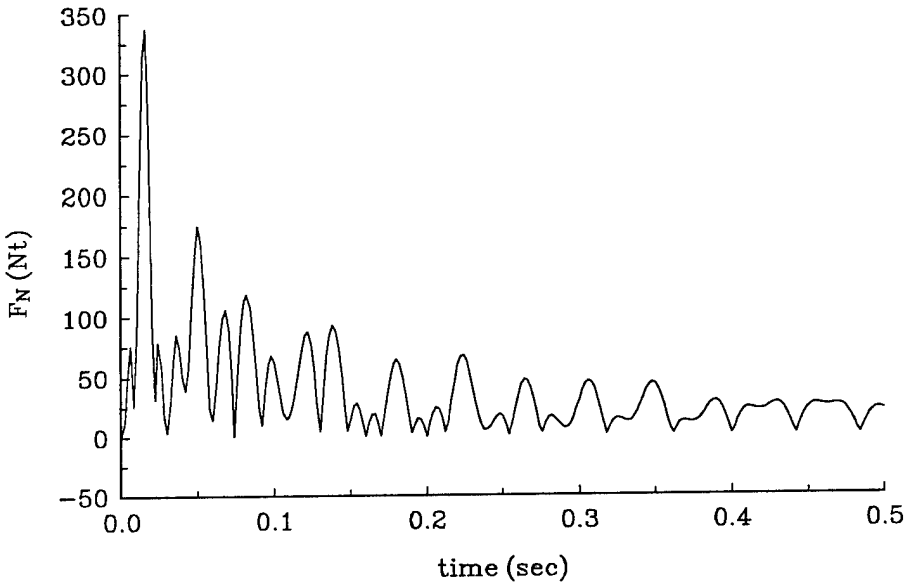

Figure 4.3 F_N vs t, Viscous Joint

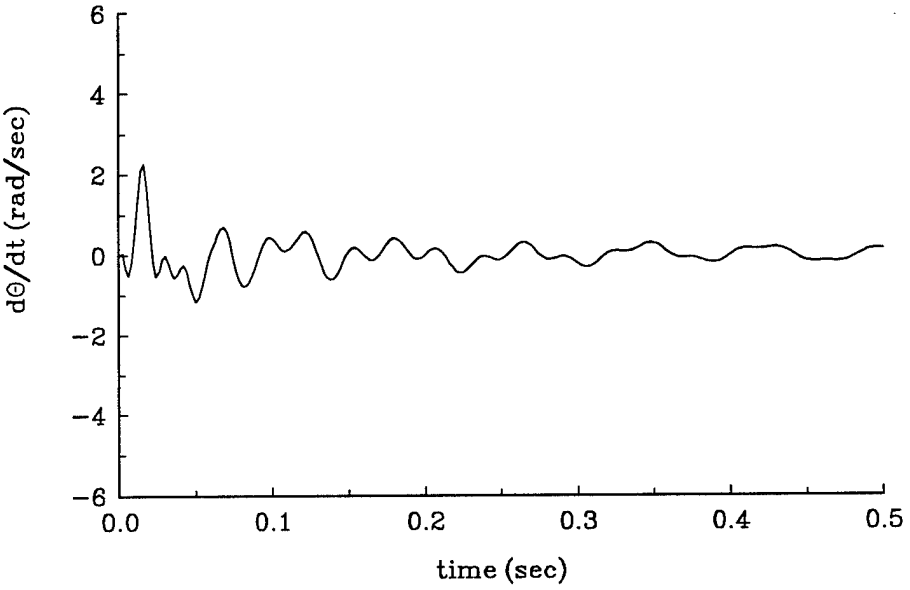

Figure 4.4 $\dot{\theta}$ vs t, Viscous Joint

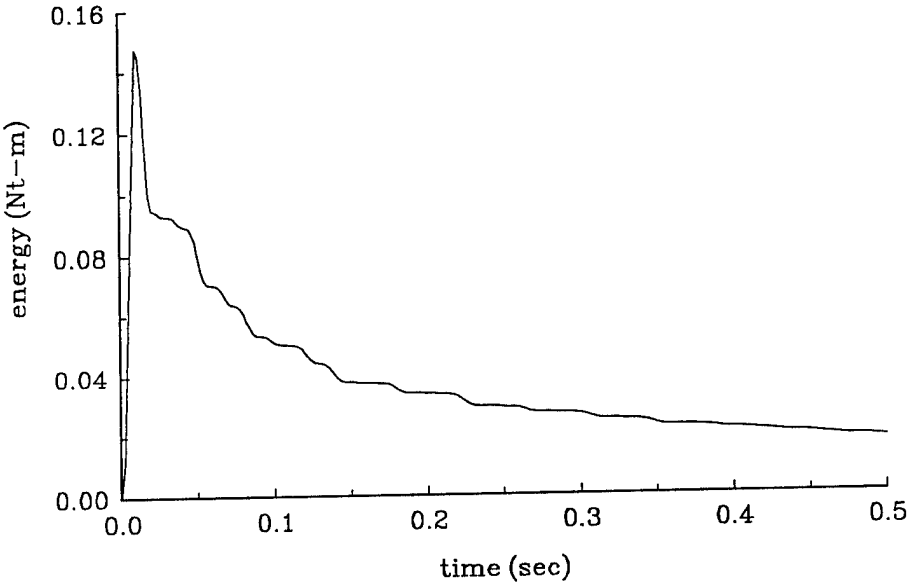

Figure 4.5 Energy vs t, Viscous Joint

$$M_f = -\underline{B}_M{}^T [S(\infty)]\,\underline{x}/r$$
$$= -\left[k_\infty\right]\underline{x} \qquad (4.9)$$

where $[k_\infty]$ is the steady state gain matrix. Defining M_f as the control variable is advantageous because the resulting state equations are linear, however, in the physical system F_N is the control variable. Substituting equation (4.9) into (3.18) and solving for F_N gives

$$F_N = -\frac{1}{\mu_D k_G}\left[k_\infty\right]\underline{x}\,\mathrm{sgn}(\dot{\theta}) \qquad (4.10)$$
$$\text{if } F_N < 0 \text{ then } F_N = 0\ .$$

The limiting of F_N to values greater than or equal to zero is necessary since the first equation in (4.10) does not guarantee that $F_N \geq 0$. This type of control will be referred to as *clipped LQR* control. Obviously clipping F_N is undesirable because it causes the control (and state) to deviate from the desired optimal trajectories. The degree to which clipping occurs will depend on the selection of [Q] and r in (4.6). Also there is no guarantee that sticking will not occur when this design approach is used, a factor which is also influenced by the selection of [Q] and r.

The difficulty in designing LQR controllers is usually in defining a suitable cost functional and in obtaining measurements or estimates of the state vector. In this section the state vector is assumed available and attention will be given to the selection of J.

Since the goal of the control system is to dissipate energy, a suitable performance index is

$$J = \int_0^\infty (T + V) + \rho M_f^2 \, dt \, , \tag{4.11}$$

where T and V represent the total kinetic and total potential energies for the two-beam system, respectively. The task is then to choose an appropriate value for ρ. Since the linear system is controllable, any desired level of performance can be achieved by allowing $\rho \rightarrow 0$. Very small values of ρ, however, will result in very large feedback gains. The value of ρ=0.1 was chosen after some iterative studies. The closed loop eigenvalues for this design are shown in Table 4.2. Pulse response data for this design is shown in Figures 4.6 - 4.8. In Figure 4.6, clipping of F_N is most evident in the period

Table 4.2 Closed Loop Eigenvalues for Energy Based LQR Design

ζ	ω
.196	22.0
.143	71.5
.092	85.5
.068	194
.078	280
.053	629

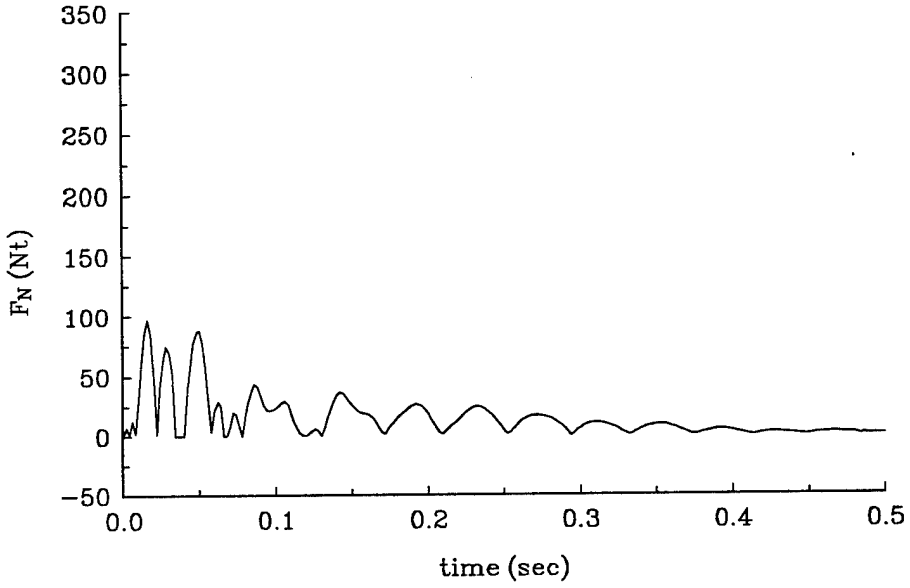

Figure 4.6 F_N vs t, Energy Based LQR Joint

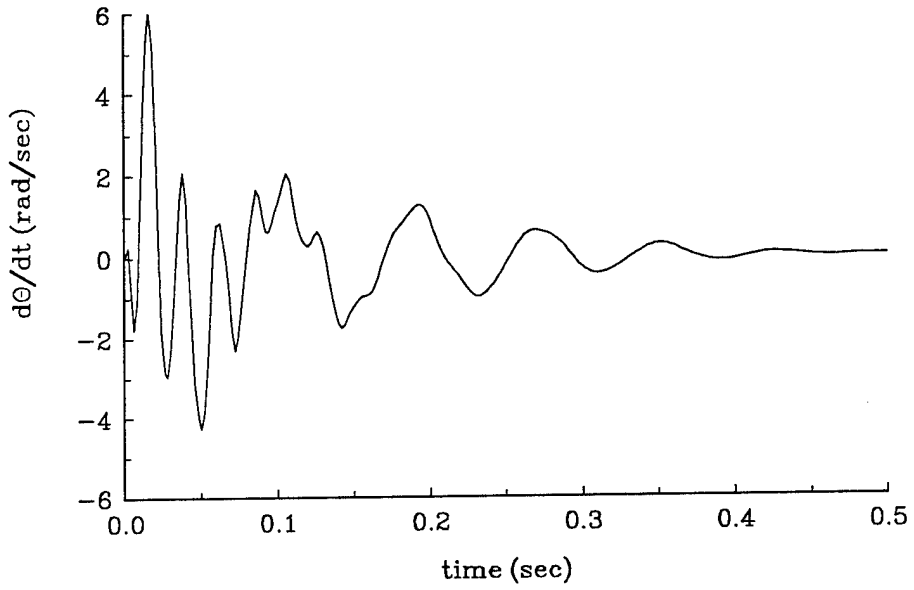

Figure 4.7 $\dot{\theta}$ vs t, Energy Based LQR Joint

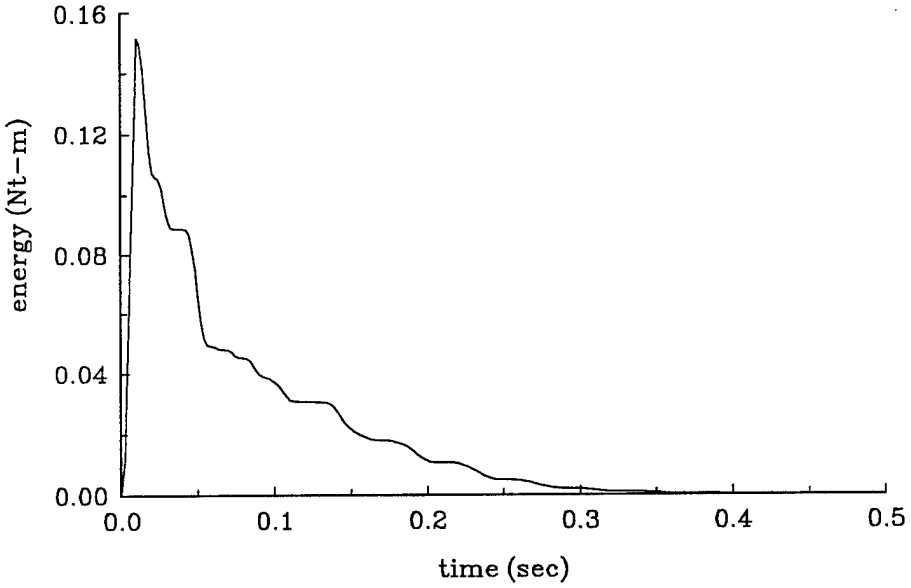

Figure 4.8 Energy vs t, Energy Based LQR Joint

from 0.034 sec to 0.041 sec.

Using energy in the performance index has intuitive appeal. Equally appealing is using the energy dissipation rate, i.e. minimize

$$J = \int_0^{\infty} \frac{d}{dt}(T + V) + \rho M_f^2 \, dt \, . \tag{4.12}$$

Note that energy *dissipation* corresponds to $d(T+V)/dt < 0$. Unfortunately this performance index results in a state weighting matrix, [Q], that violates the requirement that [Q] be positive semi-definite (see Appendix A for details).

A third approach for defining J is to use the implicit model following (IMF) technique [44]. This technique makes the linear system described by

$$\dot{\underline{x}} = \left[A_{SL}\right]\underline{x} + \underline{B}_M M_f \tag{4.13}$$

$$\underline{y} = \left[C\right]\underline{x} \tag{4.14}$$

have the desired output dynamics specified by

$$\dot{\underline{y}} = \left[A_Y\right]\underline{y} \, . \tag{4.15}$$

This is accomplished by defining the performance index as

$$J = \int_0^{\infty} \left(\dot{\underline{y}} - \left[A_Y\right]\underline{y}\right)^T \left[Q\right]\left(\dot{\underline{y}} - \left[A_Y\right]\underline{y}\right) + r M_f^2 \, dt \, . \tag{4.16}$$

The above problem is easily transformed into the standard LQR format by substituting

$$\dot{\underline{y}} = [C]\left(\left[A_{SL}\right]\underline{x} + \underline{B}_M M_f\right) \tag{4.17}$$

and (4.14) into (4.16) and simplifying. For the two beam system, the desired output dynamics were defined as follows,

$$\underline{y} = \begin{bmatrix} w_1(L_1/2, t) \\ \dot{w}_1(L_1/2, t) \\ w_1(L_1/4, t) \\ \dot{w}_1(L_1/4, t) \\ w_2(L_2/2, t) \\ \dot{w}_2(L_2/2, t) \\ w_2(L_2/4, t) \\ \dot{w}_2(L_2/4, t) \end{bmatrix} \tag{4.18}$$

$$\left[A_Y\right] = \begin{bmatrix} 0 & 1 & & & & & & \\ -\omega_1^2 & -2\zeta_1\omega_1 & & & & & & \\ & & 0 & 1 & & & & \\ & & -\omega_2^2 & -2\zeta_2\omega_2 & & & & \\ & & & & 0 & 1 & & \\ & & & & -\omega_3^2 & -2\zeta_3\omega_3 & & \\ & & & & & & 0 & 1 \\ & & & & & & -\omega_4^2 & -2\zeta_4\omega_4 \end{bmatrix} \tag{4.19}$$

.

The midspan and quarterspan displacements are included in $\underline{y}$ to ensure damping of all modes. For example, if only midspan deflections are used, the IMF controller will move the energy from the first mode to the second mode since the second mode has a node at the beam midspan. Letting

$$\begin{aligned} \zeta_1 = \zeta_2 = \zeta_3 = \zeta_4 &= 0.4 \\ \omega_1 = \omega_2 &= 80 \\ \omega_3 = \omega_4 &= 30 \end{aligned} \tag{4.20}$$

defines the output dynamics as a two beam system in which the midspan and quarterspan displacements of beam 1 have the dynamics of a second order system with damping ζ=0.4 and frequency ω=80 rad/sec. Similarly, the midspan and quarterspan displacements of beam 2 have the dynamics of a second order system with damping ζ=0.4 and frequency ω=30 rad/sec. The desired dynamics were chosen to be close in frequency to each beam's fundamental mode. Closed loop eigenvalues for this design with [Q]=[I] and r=1 are shown in Table 4.3. Pulse response data is shown in Figures 4.9 - 4.11. Figure 4.9 shows a higher frequency content for F_N (note the well damped high frequency modes in Table 4.3). Several regions of joint lock-up ($\dot{\theta}$=0) are noticeable in Figure 4.10.

4.4 Comparison of Linear, Constant Gain Joint Controllers

From a performance perspective, the energy based LQR design is clearly superior to the other constant gain controllers considered. This design dissipates more energy

Table 4.3 Closed Loop Eigenvalues for IMF Based LQR Design

ζ	ω
.157	22.4
.443	77.7
.076	82.6
.299	186
.283	239
.672	542

using less control effort than either the viscous controller or the IMF based LQR controller. It was also easy to design this controller since the entire design is paramaterized as a function of the scalar ρ. The drawback of this design is the dependence on full state feedback, a topic which will be addressed in later chapters. The IMF based LQR controller performed slightly poorer than the energy based design (compare Figures 4.8 and 4.11). In addition to dissipating less energy, this controller used more control effort (see Figures 4.6 and 4.9). The higher frequency content of F_N in Figure 4.9 can be traced to the fact that this controller is trying to force the system to behave as a low frequency, second order system, thus much control effort is expended in

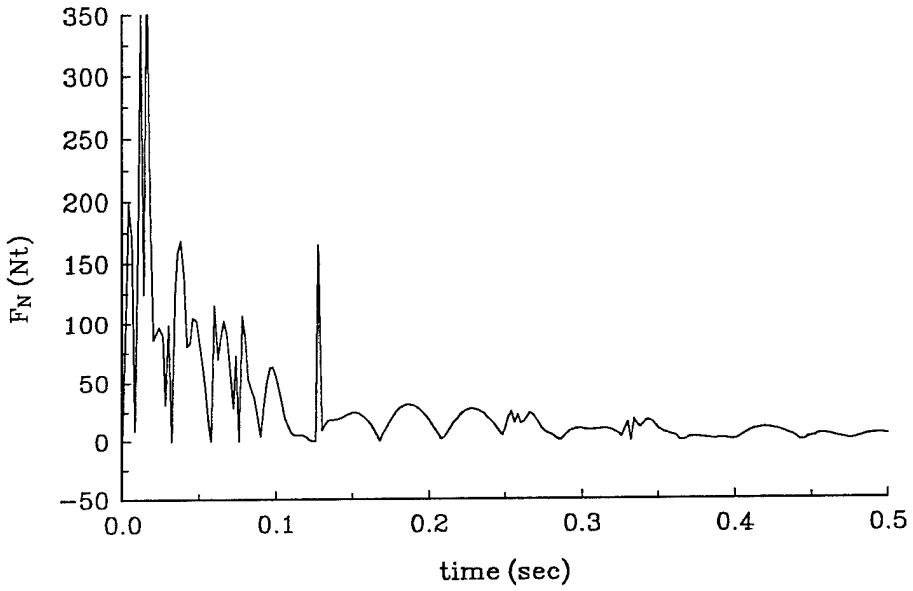

Figure 4.9 F_N vs t, IMF Based LQR Joint

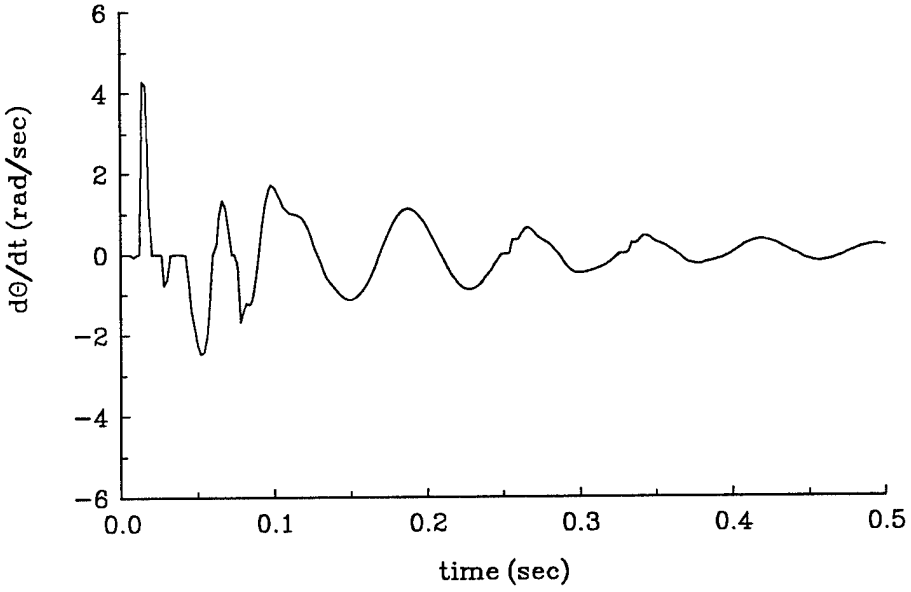

Figure 4.10 $\dot{\theta}$ vs t, IMF Based LQR Joint

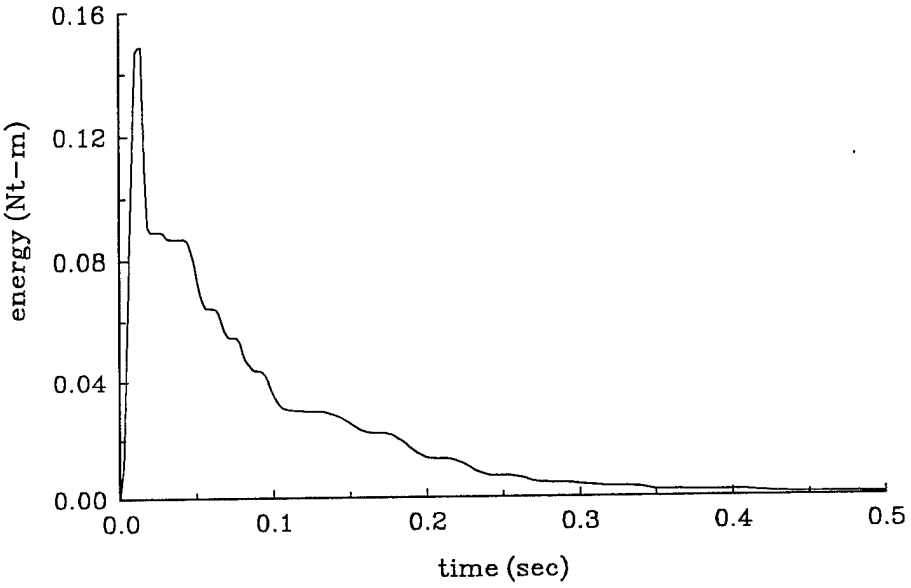

Figure 4.11 Energy vs t, IMF Based LQR Joint

controlling the high frequency modes. In a fully active system, performance could be improved for the IMF based controller by increasing the magnitude of the elements in [Q] thus forcing the actual system to perform more like the desired system. For the semi-active system, however, increasing [Q] resulted in pronounced clipping of F_N and periods of joint lock-up which significantly degraded performance. Other choices of the output dynamics matrix $[A_Y]$ were not investigated but may result in improved performance. The viscous joint controller dissipated the least amount of energy, clearly implying that if only joint damping is present, viscous damping is not optimal. It is possible that slightly better energy dissipation could have been obtained with the viscous joint controller using the optimal output feedback approach. This technique was not applied to the two beam system and is suggested as possible future work.

CHAPTER V

OPTIMAL JOINT CONTROLLER DESIGN

5.1 Introduction

The design of the clipped LQR controller deviated from the true optimal solution because only steady-state Kalman gains were used and the $F_N \geq 0$ constraint was incorporated in an ad hoc manner. An alternative approach is to use time varying Kalman gains and to incorporate the appropriate constraints and nonlinearities into the optimization problem. This joint controller would be open loop in nature, but it would represent the true optimal controller. Although not a candidate for implementation in the actual system, the true optimal controller represents a worthwhile benchmark to which other designs can be compared.

The joint controller design problem is similar in structure to the semi-active suspension problem. In reference [45], Hrovat et al present a comprehensive treatment of the optimal semi-active suspension problem. As discussed in [45], there are two approaches to formulating the optimal control problem using semi-active control. In the first approach (termed the linear formulation), the model equations are linear and a state-control inequality constraint is required to enforce the semi-active nature of the controller.

In the second approach (termed the bilinear formulation), the model equations are nonlinear and a simple control inequality constraint enforces the semi-active requirement. Both approaches are discussed below.

In both problem formulations, only the sliding joint dynamics have been included. Omission of the sticking dynamics from the problem formulation is based on physical reasoning. Since the semi-active joint is intended to be an energy dissipating device it is likely that the performance indices (J) of interest will be energy related. If the joint sticks, no energy is dissipated, causing an increase in J. Conversely, it seems plausible that under certain circumstances, locking the joint at strategic times could allow for more energy dissipation. An analytical proof as to the existence or exclusion of sticking intervals in the optimal response has thus far proved elusive.

5.2 Linear Formulation

The general form of the performance index is

$$J = \phi(\underline{x}, t)\,|_{t=t_f} + \int_0^{t_f} L(\underline{x}, M_f, t)\,dt\ , \tag{5.1}$$

where $\phi(\cdot)$is a terminal state penalty function and $L(\cdot)$ is a path dependent penalty function. For the problems considered in the joint controller formulation, $\underline{x}(0)$ and t_f are specified quantities. In the linear formulation, the performance index in (5.1) is to be

extremized subject to the following path constraints,

$$\dot{\underline{x}} = \left[A_{SL}\right]\underline{x} + \underline{B}_M M_f \tag{5.2}$$

$$-M_f \dot{\theta} \leq 0. \tag{5.3}$$

As seen in (5.2), the equations of motion are linear. Equation (5.3) is a 0^{th} order state-control constraint (zero derivatives are required to make the constraint an explicit function of the control). The state-control constraint limits the trajectory of M_f to the unshaded regions shown in Figure 5.1. Using the variational approach described in Section 3.10 of Bryson and Ho [46], the state equations and the inequality constraint are adjoined to the path dependent penalty function using Lagrange multipliers to form the Hamiltonian,

$$H = L\left(\underline{x}, M_f, t\right) + \underline{\lambda}^T\left[\left[A_{SL}\right]\underline{x} + \underline{B}_M M_f\right] + \mu\left(-M_f \dot{\theta}\right). \tag{5.4}$$

The Lagrange multiplier associated with the state-control constraint is only active when the control is on a boundary surface, i.e.,

$$\mu \begin{cases} > 0, & -M_f \dot{\theta} = 0 \\ = 0, & -M_f \dot{\theta} < 0 \end{cases}. \tag{5.5}$$

When the control is not on a boundary surface, the problem reverts to the unconstrained optimal control problem. The Euler-Lagrange equations are

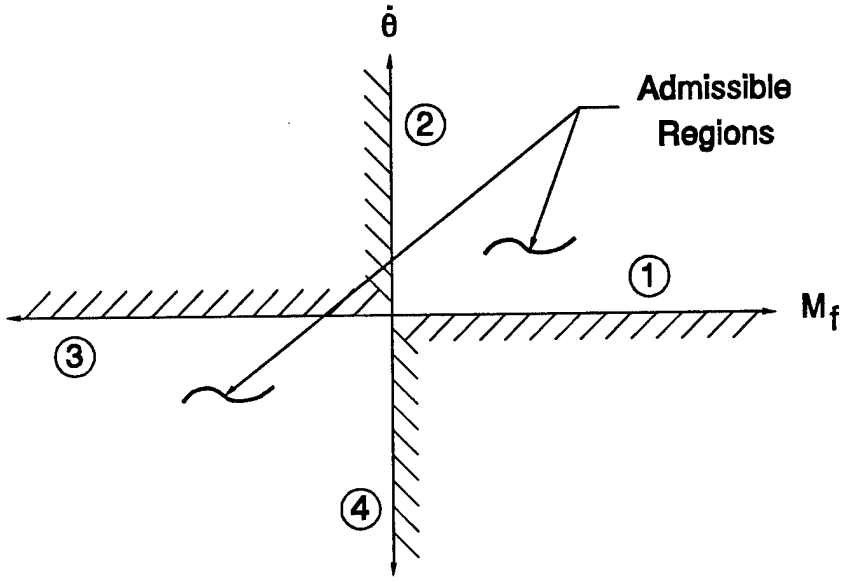

Figure 5.1 $\dot{\theta}$ - M_f Constraint Space

$$\underline{\dot{\lambda}}^T = -\frac{\partial H}{\partial \underline{x}} = \begin{cases} -\frac{\partial L}{\partial \underline{x}} - \underline{\lambda}^T\left[A_{SL}\right] + \mu M_f\left[C_{\dot{\theta}}\right] & -M_f\dot{\theta} = 0 \\ -\frac{\partial L}{\partial \underline{x}} - \underline{\lambda}^T\left[A_{SL}\right] & -M_f\dot{\theta} < 0 \end{cases} \tag{5.6}$$

and the optimality condition is

$$\frac{\partial H}{\partial M_f} = 0 = \begin{cases} \frac{\partial L}{\partial M_f} + \underline{\lambda}^T \underline{B}_M - \mu\dot{\theta} & -M_f\dot{\theta} = 0 \\ \frac{\partial L}{\partial M_f} + \underline{\lambda}^T \underline{B}_M & -M_f\dot{\theta} < 0 \end{cases} \tag{5.7}$$

The problem becomes indeterminate, however when the control trajectory lies on two of the four constraint surfaces. Consider the case of the control trajectory being on either surface 1 or 3 in Figure 5.1. On these surfaces, $\dot{\theta}=0$ and the state-control constraint is satisfied regardless of the value of M_f. Since $\dot{\theta}=0$ on these constraint surfaces, μ drops out of the optimality equation and the M_f calculated using (5.7) will violate the $\dot{\theta}=0$ requirement. This ambiguity can be resolved by examining the development of the necessary conditions for an extremal solution in problems of this type in reference [47]. A clear (implicit) assumption in the derivation is

$$\frac{\partial}{\partial M_f}\left(-M_f\dot{\theta}\right) = -\dot{\theta} \neq 0. \tag{5.8}$$

Since $\dot{\theta}$ will almost certainly cross zero repeatedly, the linear formulation is seen to be inappropriate for this problem.

5.3 Bilinear Formulation

To circumvent the problems which arise when using the linear formulation, the bilinear formulation is used for the semi-active joint controller. In this formulation, the performance index is given by (5.1) but the state equations and semi-active control constraint are given by

$$\dot{\underline{x}} = \left[A_{SL}\right]\underline{x} + \underline{B}_F \operatorname{sgn}(\dot{\theta}) F_N \tag{5.9}$$

$$F_N \geq 0 \ , \tag{5.10}$$

respectively. Note that the reduction in complexity of the state-control constraint in the linear case to a simple control constraint in the bilinear case is accompanied by an increase in the complexity of the state equations (from linear to nonlinear).

Since energy-related performance indices are to be used, quadratic terms will be assumed in J. The final time (t_f) and initial state ($\underline{x}(0)$) are assumed given. The optimal control problem is thus to extremize

$$J = \frac{1}{2}\underline{x}^T\left[S_f\right]\underline{x}\Big|_{t=t_f} + \frac{1}{2}\int_0^{t_f}\underline{x}^T\left[Q\right]\underline{x} + r F_N^2\, dt \qquad (5.11)$$

subject to the following constraints,

$$\begin{aligned} &\text{i) } \dot{\underline{x}} = \left[A_{SL}\right]\underline{x} + \underline{B}_F \operatorname{sgn}(\dot{\theta}) F_N \\ &\text{ii) } F_N \geq 0 \\ &\text{iii) } \underline{x}(0),\ t_f \text{ specified} \\ &\text{iv) } \underline{x}(t_f) \text{ free .} \end{aligned} \qquad (5.12)$$

To facilitate implementation of the optimization problem in a numerical optimization program (to be described below), convert the above "Bolza" type problem to an equivalent "Mayer" problem. This is accomplished by adjoining the Lagrangian to the state vector. Let

$$\dot{z} = \frac{1}{2}\underline{x}^T\left[Q\right]\underline{x} + \frac{1}{2} r F_N^2 , \qquad (5.13)$$

and the augmented state vector, $\underline{x}_A$, be defined as

$$\underline{x}_A = \begin{bmatrix} \underline{x} \\ -- \\ z \end{bmatrix}. \qquad (5.14)$$

The optimization problem is now to extremize

$$J = \frac{1}{2}\underline{x}^T\left[S_f\right]\underline{x}\Big|_{t=t_f} + z\left(t_f\right) \tag{5.15}$$

subject to

$$\text{i)} \begin{bmatrix} \dot{\underline{x}} \\ -- \\ \dot{z} \end{bmatrix} = \begin{bmatrix} \left[A_{SL}\right]\underline{x} + \underline{B}_F \operatorname{sgn}\left(\dot{\theta}\right) F_N \\ \text{----------} \\ \frac{1}{2}\underline{x}^T\left[Q\right]\underline{x} + \frac{1}{2} r F_N^2 \end{bmatrix} \tag{5.16}$$

ii) $F_N \geq 0$

iii) $\underline{x}(0)$, t_f specified
$z(0) = 0$

iv) $\underline{x}(t_f)$, $z(t_f)$ free

The Hamiltonian is

$$H = \underline{\lambda}^T\left(\left[A_{SL}\right]\underline{x} + \underline{B}_F \operatorname{sgn}\left(\dot{\theta}\right) F_N\right) + \lambda_Z\left(\frac{1}{2}\underline{x}^T\left[Q\right]\underline{x} + \frac{1}{2} r F_N^2\right) \tag{5.17}$$

where the influence coefficient terms $\underline{\lambda}$ and λ_Z can be thought of as partitioned subvectors of an overall coefficient vector:

$$\underline{\lambda}_A = \begin{bmatrix} \underline{\lambda} \\ -- \\ \lambda_Z \end{bmatrix} \begin{matrix} \text{corresponds to } \underline{x} \\ \\ \text{corresponds to } z \end{matrix} . \tag{5.18}$$

The state equations are piecewise linear. Figure 5.2 illustrates the two possibilities for $\dot{\theta}$ changing sign. The only difference in the state equations between regions 1 and 2 is a sign change on the control term occurring at $t=t_i$. This discontinuity in the state equations is treated as an interior point constraint as discussed in Section 3.6 of Bryson and Ho [46]. Let

$$\underline{B}_F^1 = \underline{B}_F \, \mathrm{sgn}(\dot{\theta}) \, |_{t<t_i} . \tag{5.19}$$

The state equations on each side of t_i are then

$$\dot{\underline{x}} = \begin{cases} \left[A_{SL} \right] \underline{x} + \underline{B}_F^1 F_N & t < t_i \\ \left[A_{SL} \right] \underline{x} - \underline{B}_F^1 F_N & t > t_i \end{cases} . \tag{5.20}$$

The Hamiltonian is

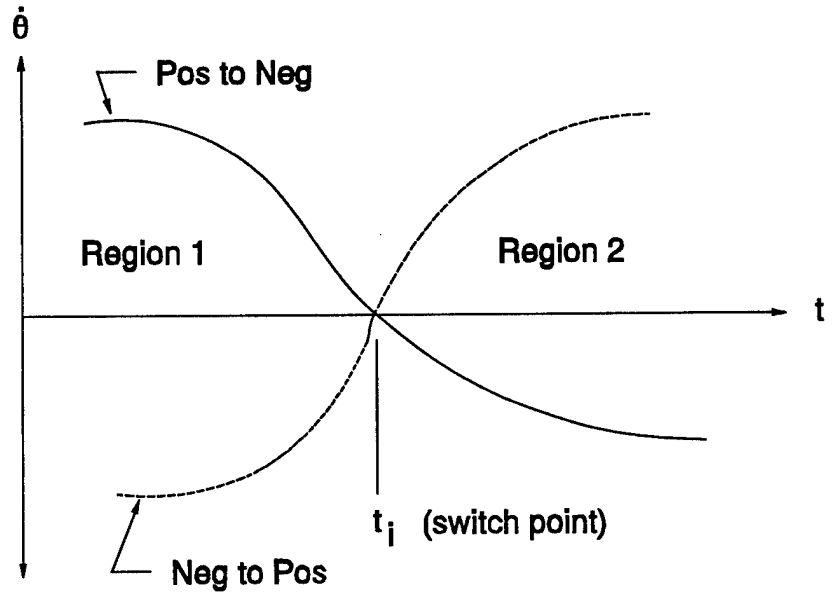

Figure 5.2 $\dot{\theta}$ Switching Curve

$$H = \begin{cases} \underline{\lambda}^T\left(\left[A_{SL}\right]\underline{x} + \underline{B}_F^1 F_N\right) + \lambda_Z\left(\frac{1}{2}\underline{x}^T\left[Q\right]\underline{x} + \frac{1}{2} r F_N^2\right) & t < t_i \\ \underline{\lambda}^T\left(\left[A_{SL}\right]\underline{x} - \underline{B}_F^1 F_N\right) + \lambda_Z\left(\frac{1}{2}\underline{x}^T\left[Q\right]\underline{x} + \frac{1}{2} r F_N^2\right) & t > t_i \end{cases} \quad (5.21)$$

The costate dynamics are

$$-\dot{\underline{\lambda}}^T = \frac{\partial H}{\partial \underline{x}} = \underline{\lambda}^T\left[A_{SL}\right] + \lambda_Z \underline{x}^T\left[Q\right], \quad \forall\ t \quad (5.22)$$

$$-\dot{\lambda}_Z = \frac{\partial H}{\partial z} = 0\ , \quad \forall\ t\ . \quad (5.23)$$

The costate jumps at $t=t_i$ (t_i specified by $\dot{\theta}=[C_{\dot{\theta}}]\underline{x}=0$) are given by

$$\begin{aligned} \underline{\lambda}^T(t_i^-) &= \underline{\lambda}^T(t_i^+) + \sigma \frac{\partial \dot{\theta}}{\partial \underline{x}}\Big|_{t=t_i} \\ &= \underline{\lambda}^T(t_i^+) + \sigma\left[C_{\dot{\theta}}\right] \end{aligned} \quad (5.24)$$

$$\begin{aligned} \lambda_Z(t_i^-) &= \lambda_Z(t_i^+) + \sigma_Z \frac{\partial \dot{\theta}}{\partial z} \\ &= \lambda_Z(t_i^+)\ , \end{aligned} \quad (5.25)$$

where σ is a Lagrange multiplier determined so that the $\dot{\theta}=0$ constraint is met. The

optimality condition defines the optimal control as,

$$F_N = \begin{cases} \dfrac{-\underline{\lambda}^T \underline{B}_F^1}{\lambda_Z r} & t < t_i \\ \\ \dfrac{\underline{\lambda}^T \underline{B}_F^1}{\lambda_Z r} & t > t_i \end{cases} . \tag{5.26}$$

Using (5.24), (5.25), and (5.26), it can be shown that

$$F_N(t_i^+) = -F_N(t_i^-) - \frac{\sigma\left[C_{\dot{\theta}}\right]\underline{B}_F^1}{\lambda_Z r} . \tag{5.27}$$

The Hamiltonian is related at t_i^- and t_i^+ as follows

$$H(t_i^-) = H(t_i^+) - \sigma \frac{\partial \dot{\theta}}{\partial t} . \tag{5.28}$$

In Appendix B the unconstrained linear model formulation is used to prove that $\sigma=0$. Therefore,

- H is continuous at switch points; $H(t_i^-) = H(t_i^+)$
- $\underline{\lambda}$, λ_Z are continuous at switch points
- $F_N(t_i^+) = -F_N(t_i^-)$.

The sign change on F_N at the switch points in conjunction with the $F_N \geq 0$ requirement results in the following conclusions,

- if $F_N(t_i^-)$ is unconstrained (i.e. positive), then $F_N(t_i^+)$ will be constrained

  (i.e. $F_N(t_i^+) = 0$)

- if $F_N(t_i^-)$ is constrained, then $F_N(t_i^+)$ will be unconstrained.

Boundary conditions on the state and costate vectors are

$$\begin{array}{ll} \underline{x}(0) \text{ specified} & \underline{x}(t_f) \text{ free} \\ z(0) = 0 & z(t_f) \text{ free} \\ \underline{\lambda}(0) \text{ free} & \underline{\lambda}(t_f) = \left[S_f \right] \underline{x}(t_f) \\ \lambda_Z(0) \text{ free} & \lambda_Z(t_f) = 1. \end{array} \tag{5.29}$$

The boundary conditions on $\underline{\lambda}(t_f)$ and $\lambda_Z(t_f)$ are found from the transversality condition. Equations (5.23) and (5.25) along with the boundary conditions on λ_Z result in λ_Z=1. The optimal control solution involves solving a two point boundary value problem in which the normal force is defined by regions of constrained and unconstrained arcs. Switching between the unconstrained and constrained arcs occurs at $\dot{\theta}$=0 crossings. Due to the difficulty in solving the nonlinear, discontinuous optimization problem analytically, a numerical optimization procedure was used. The optimization routine, BNDSCO [48], uses the multiple shooting method [49] to find the optimal switching points, state and costate trajectories, and control.

5.4 Numerical Optimization Results

Determining optimal control solutions via numerical methods is often a very difficult task. The semi-active joint controller problem proved to be no exception. Defining the structure of the optimal control solution and writing the optimization software to interface with the BNDSCO optimization routines are *significant* efforts in themselves. Obtaining numerical results proved to be an even *greater challenge.* Convergence was achieved for several cases which will be described below. Even when the numerical solution did converge, some questions still remained.

BNDSCO requires initial estimates of the state, costate, and control time histories. The initial estimates were generated using the following procedure:

(1) Solve the unconstrained optimization problem using the model given in (5.2) and the desired performance index. The optimal M_f is given by equation (4.7). Simulating the system using the control given by (4.7) generates the *unconstrained LQ* solution.

(2) Use the time varying Kalman gains found in the first step to calculate the optimal normal force, then limit the normal force to be positive. Simulating the system using this strategy generates the *clipped LQ* solution.

(3) Using the time history of $[\underline{x}]$ found in step 2, integrate equation (5.22) from t_f to 0 to get an estimate of the costate. The initial condition for the

reverse integration of (5.22) is

$$\underline{\lambda}(t_f) = [S_f]\,\underline{x}(t_f) \ . \tag{5.30}$$

The initial estimate for the time history of $\underline{x}$ and the control are found in step 2 and the estimate of the costate is found in step 3. Due to the difficulty of solving the nonlinear optimization problem, only one sine mode per beam was used to generate the system model.

The first case considered is one for which t_f=0.06 sec, and the performance index is

$$J = (T + V)|_{t=.06} + \int_0^{.06} (T + V) + .1\,M_f^2 \ dt \ . \tag{5.31}$$

The initial state vector is

$$\underline{x} = [\ -0.02251 \quad 0. \quad 0.007071 \quad 0.\ ]^T \ , \tag{5.32}$$

which represents an initial midspan deflection of beam 1 of 10 mm and an initial beam 1 velocity such that $\dot{\theta}$=-.1 rad/sec. Figures 5.3 and 5.4 show the F_N and $\dot{\theta}$ time histories for the 3 types of control (unconstrained LQ, clipped LQ, numerically optimized) discussed above. Note the negative normal force in the unconstrained LQ solution. The performance index for each case is shown below,

J = 0.010449 unconstrained LQ

J = 0.011202 clipped LQ

J = 0.011237 constrained numerical solution.

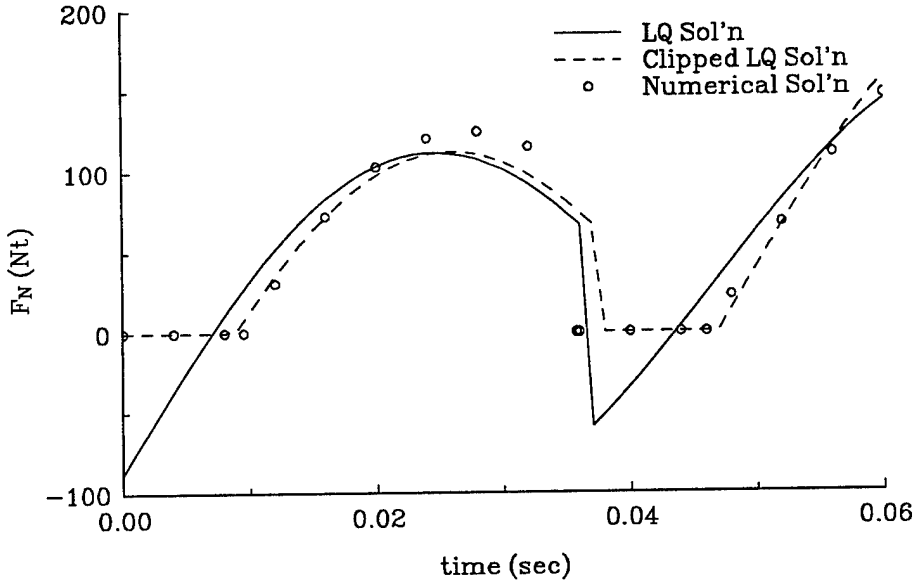

Figure 5.3 F_N vs t for Numerical Optimization Case 1

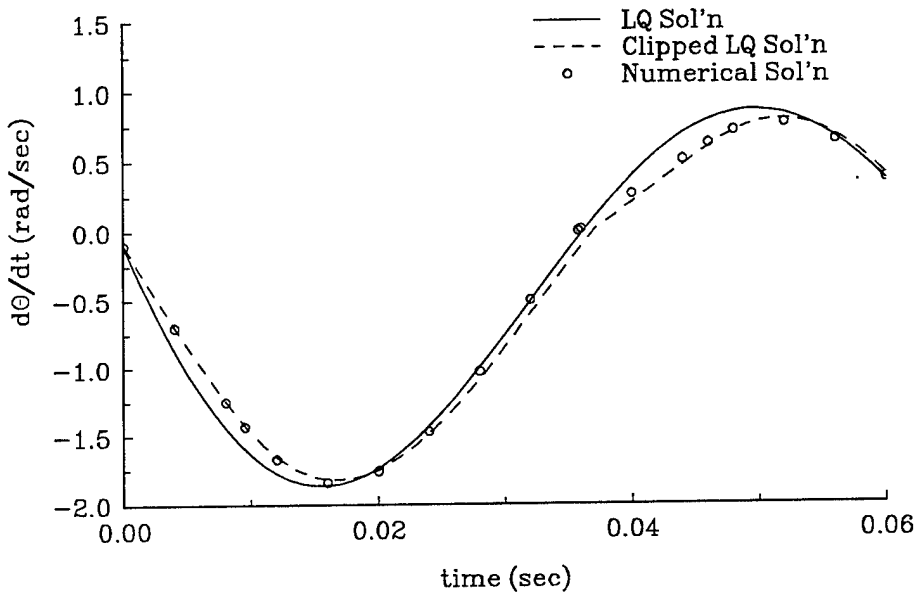

Figure 5.4 $\dot{\theta}$ vs t for Numerical Optimization Case 1

The performance index for the second case is

$$J = (T + V)|_{t=.2} + \int_0^{.2} (T + V) + .1\, M_f^2 \, dt \,, \tag{5.33}$$

where t_f=0.2 sec. The initial state vector is the same as in case 1. The longer final time results in 9 switches as opposed to 3 switches in case 1. Figures 5.5 and 5.6 show the F_N and $\dot{\theta}$ time histories for this case. The performance indicies are,

J = 0.004883 unconstrained LQ

J = 0.004908 clipped LQ

J = 0.004911 constrained numerical solution.

Finally, the performance index for the third case is

$$J = (T + V)|_{t=.03} + \int_0^{.03} (T + V) + .1\, M_f^2 \, dt \,, \tag{5.34}$$

where t_f=0.03 sec. The initial state vector is

$$\underline{x} = [\, 0. \quad 0.04051 \quad 0. \quad 0.007071 \,]^T \,, \tag{5.35}$$

which represents an initial midspan deflection of beam 2 of 10 mm and an initial beam 2 velocity such that $\dot{\theta}$=.1 rad/sec. Figures 5.7 and 5.8 show the F_N and $\dot{\theta}$ time histories for the 3 types of control. The performance index for each case is shown below,

J = 0.009082 unconstrained LQ

J = 0.009085 clipped LQ

J = 0.009085 constrained numerical solution.

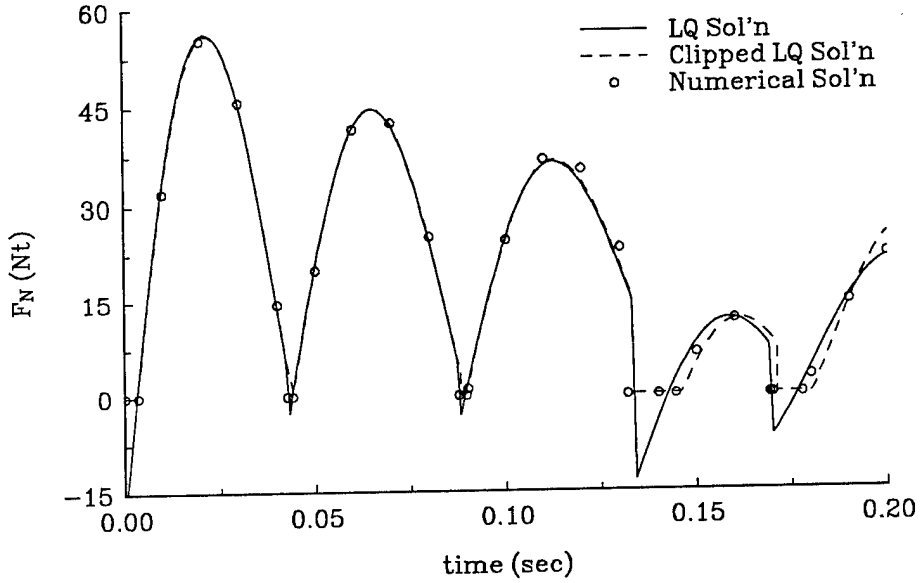

Figure 5.5 F_N vs t for Numerical Optimization Case 2

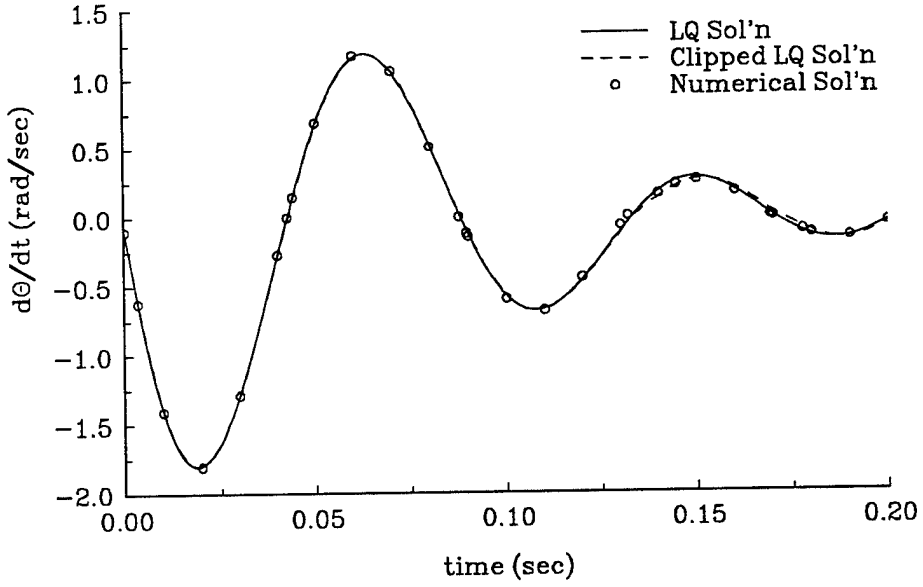

Figure 5.6 $\dot{\theta}$ vs t for Numerical Optimization Case 2

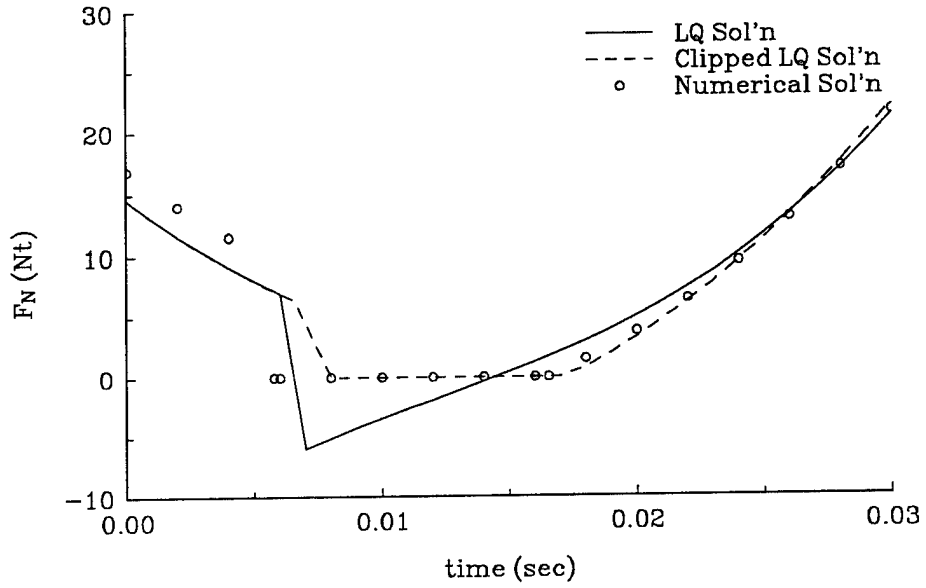

Figure 5.7 F_N vs t for Numerical Optimization Case 3

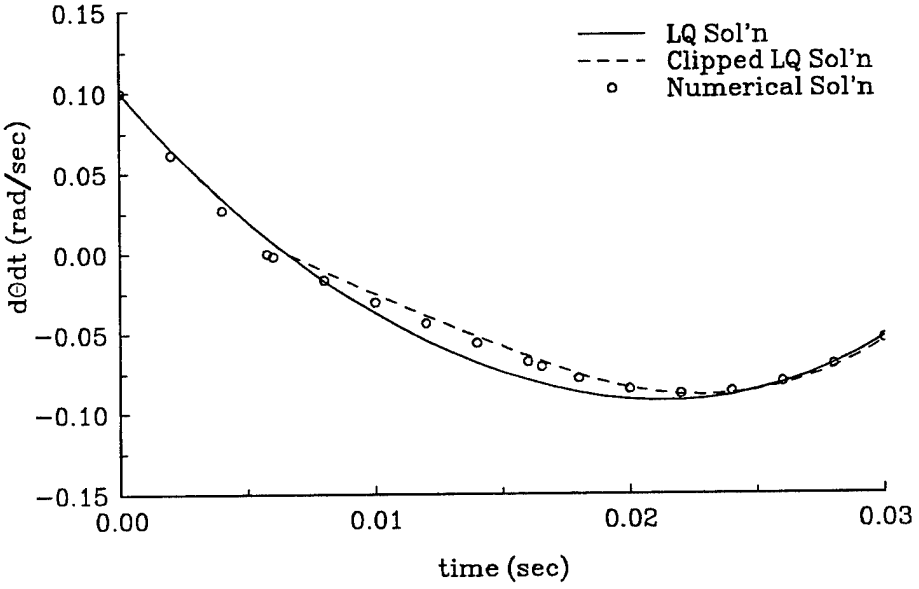

Figure 5.8 $\dot{\theta}$ vs t for Numerical Optimization Case 3

As expected, the unconstrained solution had the lowest value of J for all three cases. However, the constrained numerical solution should have a lower J than the clipped LQ solution. The reason for the discrepancy is not clear. Several diagonistic checks were made on all of the programs used and the results were unchanged. One viable hypothesis is that the clipped LQ solution is very close to the optimal solution and the constrained numerical solution is within the accuracy of BNDSCO. In [50], Butsuen and Hedrick prove that the clipped LQR solution is the optimal semi-active solution for the regulator problem; i.e., for the case where $t_f=\infty$. Clearly the clipped LQ solution is not optimal in the current case but will approach optimality as the final time becomes "sufficiently" large and the sensitivity to $[S_f]$ vanishes. Hrovat, et al in [45] obtained similar trends in their studies of optimal semi-active suspensions. Their approach to finding the optimal solution however, was to use penalty functions to force $F_N \geq 0$ rather than to solve the nonlinear optimal control problem directly.

Despite the anomalies between the clipped LQ solution and the constrained numerical solution, it is encouraging that only small penalties in the performance index were realized by forcing the joint to be semi-active. In the first case, the constrained numerical solution is only 7.5% larger than the unconstrained LQ solution. The difference drops to 0.57% for case 2 and to 0.03% for case 3. This is due to an effective choice for the performance index, which resulted in minimal enforcement of the semi-active nature of the joint. Thus for judicious choices of the performance index, the clipped control is approximately optimal.

CHAPTER VI

CONTROL SYSTEM DESIGN AND ANALYSIS

6.1 Introduction

Earlier chapters have investigated the design of various joint controller designs for dissipating vibrational energy. In this chapter, the design issues which arise when the semi-active joint is used in conjunction with an attitude or shape control system are investigated. These issues include choosing the control system structure, observer design, and performance assessment measures.

6. 2 Control System Structure

Consider the two beam system shown in Figure 6.1. The center joint is a semi-active friction joint. The two forces F_1 and F_2 shown in Figure 6.1 are control inputs for an attitude or shape controller (F_1 and F_2 were used as disturbance inputs in the joint controller design studies) and the joint normal force F_N is the control input for the joint controller. The four disturbance inputs are denoted as D_i, i=1...4. The three measurement variables include $\dot{\theta}$ (joint angular rate) and ε_1 and ε_2 (beam 1 and beam 2 strain

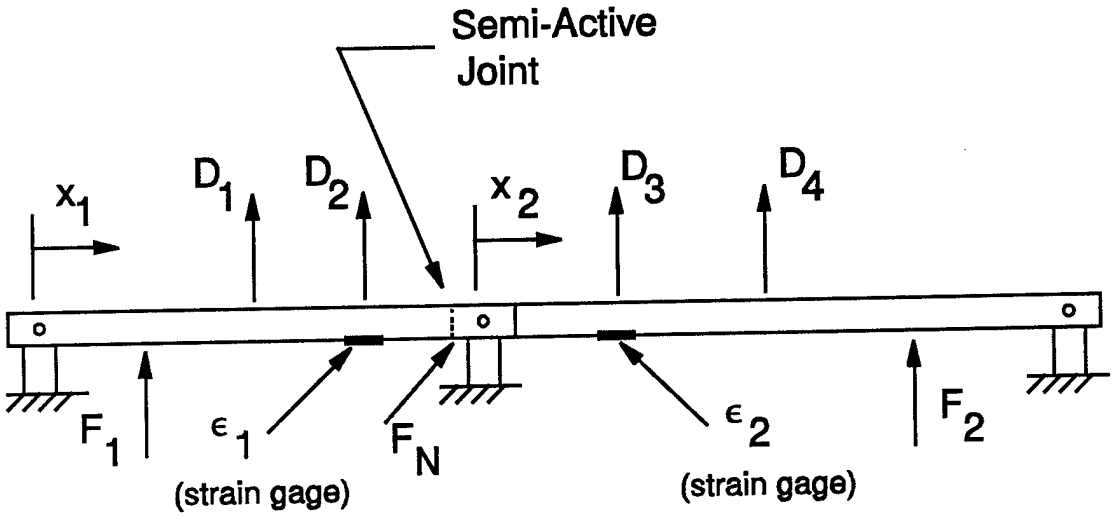

Figure 6.1 Two Beam System

measurements). For example, if the two beam structure were part of an LSS, the force inputs F_1 and F_2 could be used for attitude control of the structure. Superimposed on the attitude control commands would be vibration suppression commands. Assuming that the two tasks can be separated during the controller design allows the vibration control problem to be considered as a separate design problem. Thus we are interested in defining F_1, F_2, and F_N to provide the maximum vibration suppression possible.

The design of control systems is not a rigorously defined procedure. Consideration must be given to the structure of a control system in addition to the methodology which will be used to design a particular compensator. Two control structures will be investigated herein. The first control structure is shown in Figure 6.2 where $\underline{N}$ denotes additive noise that contaminates sensory measurements $\underline{y}$. The motivation for this design is to segregate the control system into two smaller subsystems, a joint controller and a shape controller. The joint controller will define the normal force at the frictional interface (F_N) and the shape controller will define the attitude/shape controller forces (F_1, F_2). This design approach is similar to the inner-to-outer loop design process prevalent in single input single output (SISO) control system design. The joint controller is designed first, without any explicit regard to the fact that an additional controller will be designed around it. "Without any explicit regard" denotes the fact that there are no mathematical or formal restrictions imposed on the design of the joint controller by the subsequent addition of the shape controller. In reality however, the joint controller must be designed to augment the function of the shape controller.

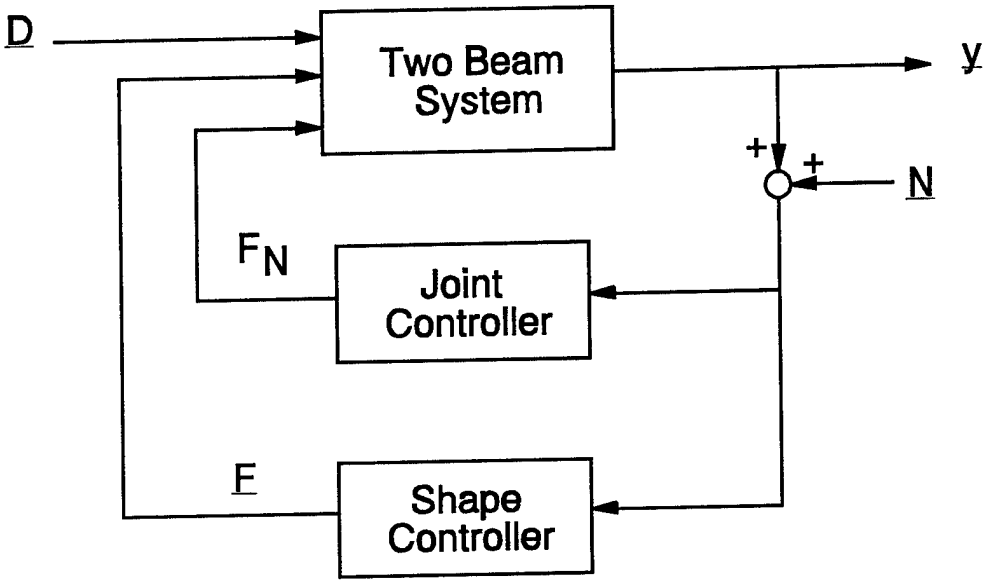

Figure 6.2 Segregated Control System

Due to its simplicity, ease of design, and output feedback structure, the viscous joint controller is an appealing choice for the joint controller in the segregated design approach. The normal force is defined as

$$F_N = k_{VJ} |\dot{\theta}| , \tag{6.1}$$

which gives the following equations of motion once the joint controller is implemented,

$$\dot{\underline{x}} = \left[A_{VJ}\right]\underline{x} + \left[B_{\underline{F}}\right]\underline{F} + \left[B_D\right]\underline{D} , \tag{6.2}$$

where

$$\left[A_{VJ}\right] = \left[A_{SL}\right] + k_G \mu_D k_{VJ} \underline{B}_M \left[C_{\dot{\theta}}\right] . \tag{6.3}$$

The function of the shape controller is to define $\underline{F}$ given the two beam system and viscous joint controller. Since the semi-active plant is linear, LQR design techniques are appropriate for designing the shape controller. Based on the desire to dissipate vibrational energy, the following performance index is chosen:

$$J = \int_0^\infty \rho_E (T + V) + \underline{F}^T \underline{F} \, dt \tag{6.4}$$

where T and V are the total kinetic and potential energies in the two beam system and ρ_E is a weighting term. $\underline{F}$ is determined such that J is minimized subject to (6.2) (with $\underline{D} = \underline{0}$) and

$$\underline{F} = -[k]\underline{x} \; . \tag{6.5}$$

The above design procedure has two "degrees of freedom". The viscous joint controller is defined by the viscous gain k_{VJ} and the shape controller by the energy weighting parameter ρ_E. This design is termed the VJEW (viscous joint - energy weighting) design.

Before discussing the second control structure a few comments about the about the VJEW design are in order. Typically the separation principle is invoked to allow separate design of the feedback controller and the state estimator (or observer). Strictly speaking, this is not appropriate here since the plant is infinite order and the controller/observer will be a low order approximation. Optimal projection theory [51] can effectively handle this type of constrained optimization problem. However, designing the controller and observer in two separate (unrelated) steps is appropriate as long as the reduced order controller/observer pair is evaluated using a high order system model. This will ensure that spillover effects will not be lost. The motivation for investigating the VJEW structure relates to controller portability and expected system robustness. In an LSS it would be desirable if the joint controller could be designed without specific knowledge of its placement within the structure. If this were the case, the joint controller would be considered portable. Since the joint controller uses $\dot{\theta}$ feedback, no observer is necessary (assuming that the joint angular velocity is a measured quantity). The joint controller consists of a viscous gain (k_{VJ}) which causes the friction device to emulate a rotary viscous damper. The plant to be controlled by the shape controller consists of the

beam system with the semi-active joint. Whereas the joint controller was designed to control a system with zero damping, the shape controller controls a plant with damping (added by the joint controller). The two beam system is fully controllable from $\underline{F}$ so performance is not a direct issue regardless of the inclusion of the joint controller. However, the shape controller needs an observer to supply it with estimates of the state. The observer must now model a system with damping, which should improve system robustness.

The second control structure to be investigated is shown in Figure 6.3. This controller integrates the joint and shape controllers into one control system. Using LQR design techniques, the performance index is defined as

$$J = \int_0^\infty (T + V) + \rho_F \underline{F}^T \underline{F} + \rho_M M_f^2 \, dt \, , \tag{6.6}$$

where ρ_F and ρ_M are control effort weighting parameters. The control variables, $\underline{F}$ and M_f are determined such that J is minimized subject to

$$\dot{\underline{x}} = \left[A_{SL}\right]\underline{x} + \left[B_{\underline{F}}\right]\underline{F} + \underline{B}_M M_f \, , \tag{6.7}$$

(with $\underline{D} = \underline{0}$) and

$$\begin{bmatrix} \underline{F} \\ M_f \end{bmatrix} = -\left[k\right]\underline{x} \, . \tag{6.8}$$

As in the VJEW design, there are two parameters (ρ_F, ρ_M) which determine the controller

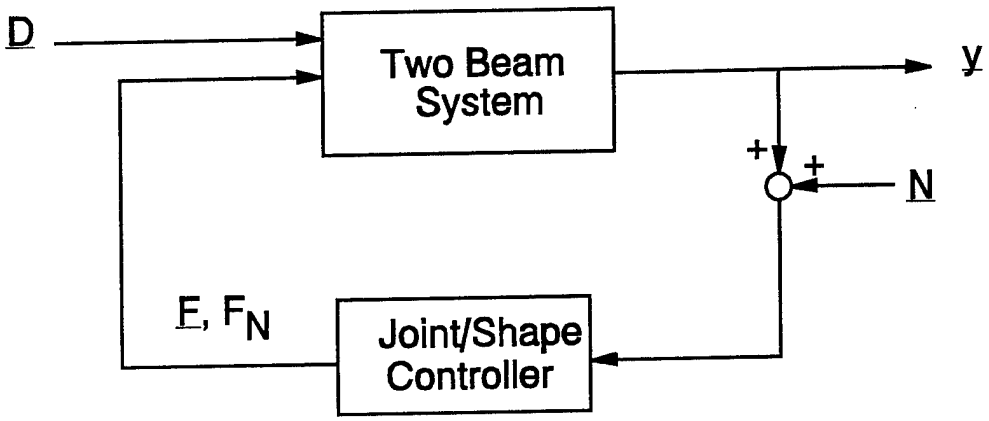

Figure 6.3 Integrated Control Structure

design. This design will be referred to as the EW design. There are several reasons why this design approach is attractive. If the true performance goal of the controller can be accurately described using a quadratic performance index, then the integrated design using the LQR technique will yield the best constant gain controller. The main drawback of this approach is portability. This design couples M_f to $\underline{F}$ to the extent necessary in minimizing the performance index. This precludes the concept of an intelligent joint (a stand-alone, semi-active joint which can be placed at will in an LSS). Also, since M_f is defined from the state vector $\underline{x}$, there is no guarantee that the desired M_f will be of the same sign as $\dot{\theta}$. M_f and $\dot{\theta}$ being opposite in polarity implies $F_N<0$ which is physically impossible. Control clipping may therefore be necessary and actual performance will be degraded.

6.3 Observer Design

Design techniques based on LQR theory assume the state vector is available from either direct measurements or from an observer. In most physical systems, all the state variables are not available for measurement, thus observers are required. The use of observers is unavoidable when designing reduced order, state feedback compensators as in the present case. As mentioned previously, using finite order observers in control systems for infinite order plants can result in instabilities caused by observer spillover [5]. Observer spillover occurs when some of the energy in the uncontrolled/unobserved modes

is attributed to the observed modes by the observer.

The first task in observer design is to identify a set of measurement variables. The system should be observable from these measurements. It can be shown that the system is observable from the following measurement set,

$$\underline{y} = \left[\dot{\theta}\, \varepsilon_1\, \varepsilon_2\right]^T , \tag{6.9}$$

where ε_1 is the strain on beam 1 at $x_1 = 0.75L_1$ and ε_2 is the strain on beam 2 at $x_2 = 0.25L_2$ (see Figure 6.1). The observer equations are given by

$$\dot{\underline{x}}^o = \left[A^o\right]\underline{x}^o + \left[B^o\right]\underline{u} + \left[L^o\right]\left(\underline{y} - \underline{y}^o\right) , \tag{6.10}$$

where the "o" superscript refers to observer parameters. The control $\underline{u}$ is given by

$$\underline{u} = -\left[k\right]\underline{x}^o , \tag{6.11}$$

where [k] is the feedback gain matrix. The observer based output vector is

$$\underline{y}^o = \left[C^o\right]\underline{x}^o , \tag{6.12}$$

where $[C^o]$ is the observer output matrix. Substituting (6.11) and (6.12) into (6.10) and simplifying gives

$$\dot{\underline{x}}^o = \left[\left[A^o\right] - \left[B^o\right]\left[k\right] - \left[L^o\right]\left[C^o\right]\right]\underline{x}^o + \left[L^o\right]\underline{y} . \tag{6.13}$$

The feedback gain matrix, [k], is defined during the controller design. The plant, input,

and output matrices, $[A^0]$, $[B^0]$, $[C^0]$, are defined by choosing the number of modes to model per beam and by choosing appropriate mode shapes. The observer gain matrix, $[L^0]$, is the final observer parameter to define. A common approach for choosing $[L^0]$ which has intuitive appeal is to use a pole placement technique and define $[L^0]$ so that the observer eigenvalues are "sufficiently" faster than the plant eigenvalues [52]. This approach however, was shown to have unsatisfactory system robustness properties [53,54]. Loop transfer recovery (LTR) techniques have been developed to define $[L^0]$ such that some (or all) of the robustness properties of a system with LQR based full state feedback can be recovered. In [53], Doyle and Stein describe a recovery procedure in which $[L^0]$ is determined by designing a Kalman Bucy Filter (KBF) for the system (A^0,B^0,C^0) with input and measurement covariances given respectively by

$$[Q] = q^2[B^0][B^0]^T \tag{6.14}$$

$$[R] = [I]. \tag{6.15}$$

As $q \rightarrow \infty$, the system with the observer based feedback recovers all of the robustness properties of the system with full state feedback. An important caveat to the LTR procedure is that this technique is only valid in the limit ($q=\infty$) for minimum phase plants because some of the observer error dynamics eigenvalues migrate to the transmission zeros of the plant as $q \rightarrow \infty$. Stein and Athans [55] discuss some of the implications of using this LTR procedure on nonminimum phase plants. In this case, loop transfer

recover can only be improved over a given frequency range with a corresponding degradation elsewhere. Even if full recovery is not achievable, as in the case for nonminimum phase plants, the technique is valid for partial loop recovery. Indeed because LTR often results in poor measurement noise rejection, partial LTR which aims at making a compromise with measurement noise attenuation is usually desirable [56]. In [57], Turan and Goodwin relax the requirement that the observer be unbiased and develop LTR techniques for biased observers. (An observer is unbiased if in the absence of modeling errors and noise, and for any input signal, the expected value of the state estimate converges to the expected value of the true state.) These techniques include asymptotic LQG methods as discussed above and frequency domain methods which involve minimizing an H_∞ norm.

Regardless of the technique used for achieving LTR, there is a caveat which must not be ignored when designing an observer for use in a flexible structure control system. The controller and observer must necessarily be of lower order than the actual plant. The natural inclination is to assess LTR using the low order approximation and then check for stability when implementing the low order control system with the high order plant (for example, see [58]). However, as will be shown later, good LTR in the reduced order system does not always indicate the same in the high order system. Contrary to the case in which the observer is full order, better robustness for reduced order observers may be achieved by decreasing the input covariance factor q.

6.4 SVD Analysis

The primary objective of the two-beam control system is to provide flexural vibration control. There are many control system designs that can provide this. However, the primary objective of vibration control is augmented by secondary considerations such as noise rejection and robustness. Systems which perform equally well under nominal conditions often show large differences under non-ideal conditions. To help assess these secondary design issues, additional performance criteria are needed. For multi-input-multi-output (MIMO) control systems, frequency domain techniques utilizing singular values are particularly appealing. There are many references for singular value analysis, one of the most notable being [59]. The analysis in this paper will follow that developed by Safanov et al in [60]. Four control system properties will be investigated using singular values; disturbance rejection, sensor noise rejection, disturbance rejection sensitivity to plant variations, and MIMO gain and phase margins.

Consider the system shown in Figure 6.4. Let the output $\underline{y}$ be composed of two components, one due to $\underline{D}$ and one due to $\underline{N}$,

$$\underline{y} = \underline{y}_D + \underline{y}_N \cdot \tag{6.16}$$

Since $\underline{y}$ is given by

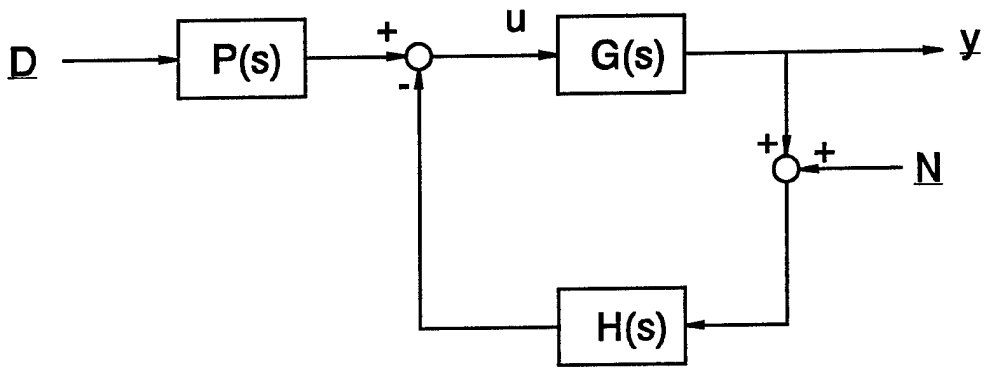

Figure 6.4 General Control System Structure

$$\underline{y} = [I + GH]^{-1}[GP]\underline{D} - [I + GH]^{-1}[GH]\underline{N}\,, \tag{6.17}$$

the disturbance and noise components are

$$\underline{y}_D = [I + GH]^{-1}[GP]\underline{D} \tag{6.18}$$

$$\underline{y}_N = -[I + GH]^{-1}[GH]\underline{N}\,. \tag{6.19}$$

The output sensitivity and complimentary sensitivity matrices (derived from the return difference matrix with the loop broken at the plant output) are

$$[So] = [I + GH]^{-1} \tag{6.20}$$

$$\begin{aligned}[To] &= [I] - [So] \\ &= [I + GH]^{-1}[GH]\,.\end{aligned} \tag{6.21}$$

In terms of [So] and [To], the disturbance and noise components are

$$\underline{y}_D = [SoGP]\underline{D} \tag{6.22}$$

$$\underline{y}_N = -[To]\underline{N}\,. \tag{6.23}$$

The sensitivity of a feedback control system has to do with the effects that variations in the plant have on other system variables. Of special interest is the effect of plant

variations on the disturbance rejection properties. From Theorem 1 in [60] we have the following result:

If the actual plant is given by

$$[G] = [I + \Delta G]^{-1}[G_0], \tag{6.24}$$

where $[G_0]$ represents the nominal system and $[I + \Delta G]^{-1}$ is a multiplicative uncertainty element, then $\underline{y}_D$ is

$$\underline{y}_D = [I + So_0 \Delta G]^{-1} \underline{y}_{Do} . \tag{6.25}$$

In (6.25) $[So_0]$ and $\underline{y}_{Do}$ are nominal values given by

$$[So_0] = [I + G_0 H]^{-1} \tag{6.26}$$

$$\underline{y}_{Do} = [I + G_0 H]^{-1}[G_0 P]\underline{D} . \tag{6.27}$$

The representation of uncertainty in (6.24) is the inverse output multiplicative form. The types of uncertainty represented by this form are discussed by Postlethwaite and Foo in [61]. All types of uncertainties which occur at the plant output are described by this representation, but uncertainties which occur at other points in the loop may not be able to be reflected to the plant output. (The number of plant outputs must be greater than or equal to the number of plant inputs for this property to be true.)

From (6.22), (6.23), and (6.25), the following qualitative assessments can be made,

i) as [SoGP] becomes smaller, disturbance rejection properties improve

ii) as [To] becomes smaller, noise rejection properties improve

iii) as [So] becomes smaller, disturbance rejection properties become less sensitive to plant variations.

The appropriate measure of smallness for MIMO systems is the maximum singular value of the respective system matrix.

In SISO systems, common measures of control system robustness are gain and phase margins. MIMO generalizations of these measures are derived in [62] and shown graphically in [63]. The gain and phase margins are found by inserting an uncertainty element [U] into the loop at the input to the plant. Elements of [U] are given by

$$[U] = \mathrm{diag}\left[k_n e^{j\phi_n}\right]. \tag{6.28}$$

Margins are defined by finding the k_n and ϕ_n (gain and phase errors) which cause instability in the closed loop system. They are

$$GM = 20 \log_{10} \frac{1}{1 \pm \alpha} \text{ db} \tag{6.29}$$

$$PM = \pm\cos^{-1}\left(1 - \frac{\alpha^2}{2}\right), \tag{6.30}$$

where

$$\alpha = \min_{\omega}\left[\sigma_{MIN}[I + HG]\right]. \tag{6.31}$$

The interpretation of the gain margins is that simultaneously in each loop of the feedback system there is a guaranteed gain margin specified by (6.29). Also, simultaneously in each loop there is a phase margin given by (6.30). This does not mean (just as in the SISO case) that gains *and* phases may vary simultaneously.

To assess the disturbance rejection, noise rejection, and robustness measures derived above, the VJEW and the EW controller designs must be represented as shown in Figure 6.4. Figures 6.5 and 6.6 show the two control systems. From Figure 6.5, the parameters for the VJEW system are

$$[G] = [C][sI - A]^{-1}[B] \tag{6.32}$$

$$[H] = \left[-k_G \mu_D k_{VJ}\begin{bmatrix}0\\ \frac{6}{1}\end{bmatrix}[1\ 0\ 0]\right] + \left[\begin{bmatrix}[0]_{4x2}\\ [I]_{2x2}\\ [0]_{1x2}\end{bmatrix}[k]\left[sI - A^{o}_{VJ}\right]\left[L^{o}\right]\right] \tag{6.33}$$

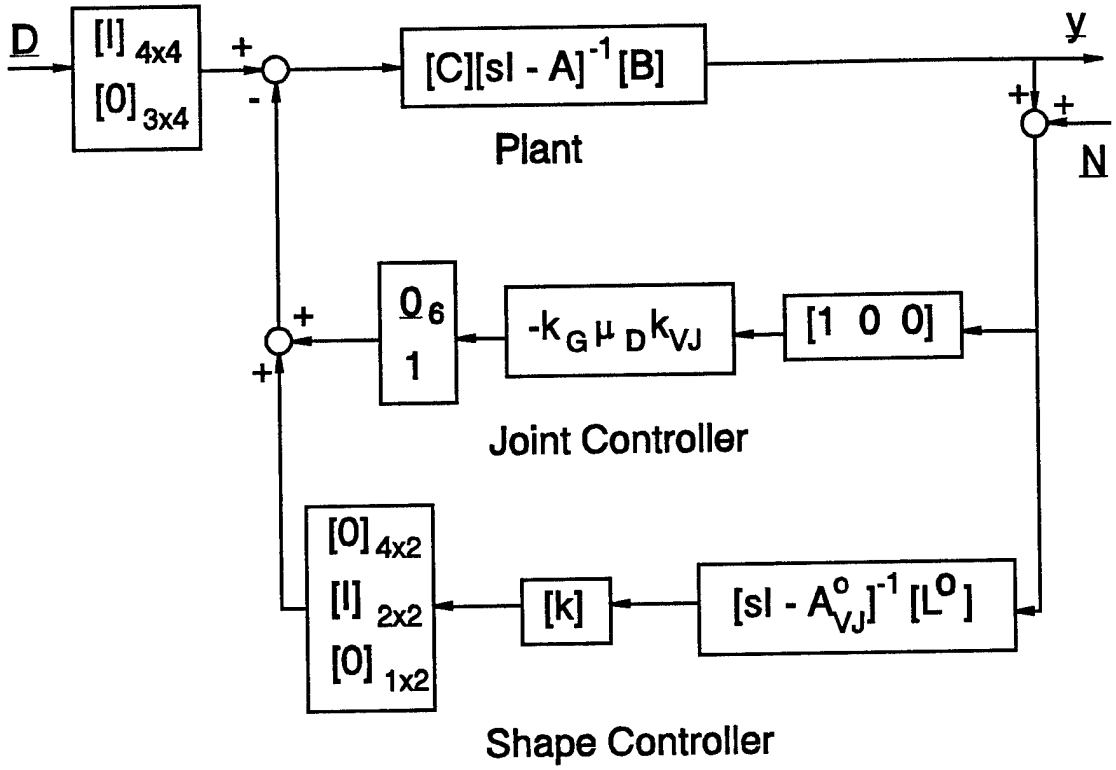

Figure 6.5 VJEW Control System

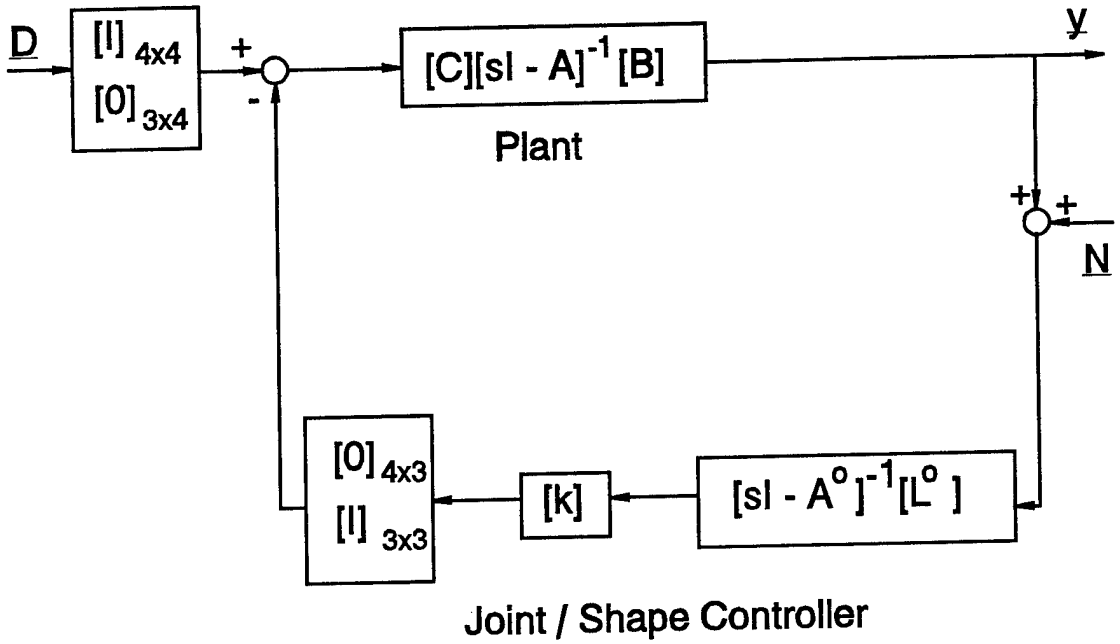

Figure 6.6 EW Control System

$$[P] = \begin{bmatrix} [I]_{4x4} \\ [0]_{3x4} \end{bmatrix}, \tag{6.34}$$

where

$$[B] = \left[[B_F] | \underline{B}_M | [B_D] \right] \tag{6.35}$$

and [C] is the output matrix for the outputs given in (6.9).

For the EW system,

$$[H] = \begin{bmatrix} [0]_{4x3} \\ [I]_{3x3} \end{bmatrix} [k] [sI - A^{o}]^{-1} [L^{o}], \tag{6.36}$$

with [G] and [P] given by (6.32) and (6.34), respectively.

6.5 Analysis Results

Controller design studies were completed to find values for k_{VJ} and ρ_E (VJEW design) and ρ_F and ρ_M (EW design). In order to assess which design is "best"; realistic, physical performance measures were identified. It is desirable to remove as much energy as possible from the two beam system using as little control effort (energy) as possible. Additionally, the bandwidth of the shape controllers should be as low as possible. A pulse disturbance force of 25 Newtons was applied to beam 1 or beam 2 for 0.01 seconds. The flexural energy in the two beam system at 0.1 seconds was used as a measure of the

energy dissipation capability of each design. The measure of control effort is

$$E_F = \int_0^{0.1} (F_1 \dot{w}_1)^2 + (F_2 \dot{w}_2)^2 \, dt \, , \tag{6.37}$$

where $\dot{w}_1$ and $\dot{w}_2$ are the beam velocities at the actuator locations. Minimizing E_F will minimize control effort and controller bandwidth. Figures 6.7 and 6.8 show VJEW design results for various values of k_{VJ} and ρ_E for a pulse disturbance on beam 1 and beam 2, respectively. Each curve is generated by choosing a value of k_{VJ} and then varying ρ_E. As expected, as ρ_E increases more vibrational energy is dissipated but at the expense of control effort. If the pulse is on beam 1, $k_{VJ} = 40$, $\rho_E = 80$ appears best, while $k_{VJ} = 80$, $\rho_E = 40$ is best if the pulse is on beam 2. The best design is the one which comes closest to the origin. (This assumes minimizing flexural energy and control energy are of equal value.) An interesting observation is that the optimal value of k_{VJ} depends on which beam is disturbed. Beam 1 is the shorter beam and has higher natural frequencies. If the disturbance is on beam 1 it is desirable to retain more of the energy in beam 1 since it can be dissipated more quickly than in beam 2. Conversely if beam 2 is disturbed, it is desirable to transfer more of the energy to beam 1 (i.e., use higher k_{VJ}). This argument doesn't hold for limiting values of k_{VJ} ($k_{VJ} = 0$ or $k_{VJ} = \infty$) since for either case the joint dissipates no energy and energy dissipated by the joint is "free" (neither F_N or M_f appear in the control energy measure). A root locus of the two beam system for varying k_{VJ} did not indicate any special significance to the values of 40 or 80, thus the simulation studies appear to be the only way to determine the optimal values. The flexural energy versus

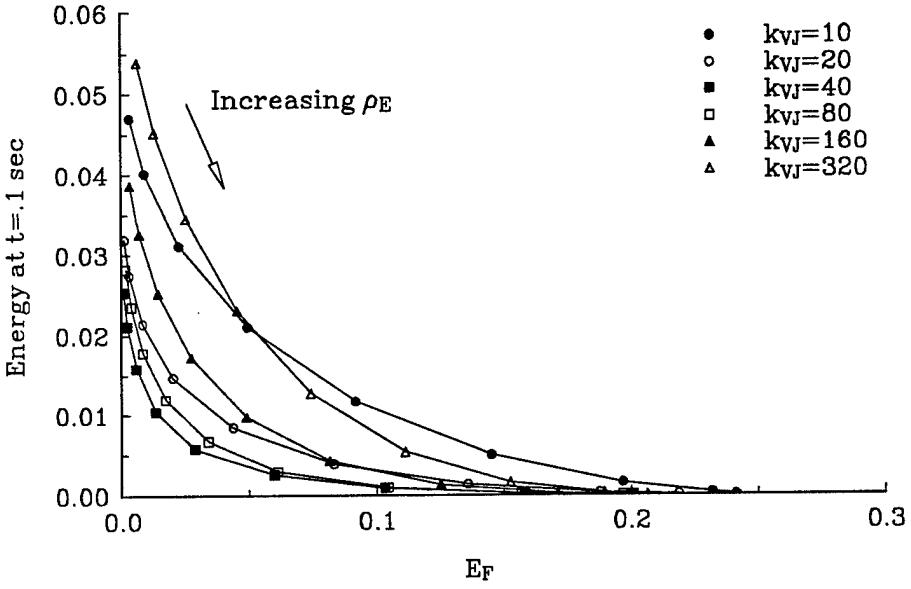

Figure 6.7 VJEW Design, Pulse Disturbance on Beam 1

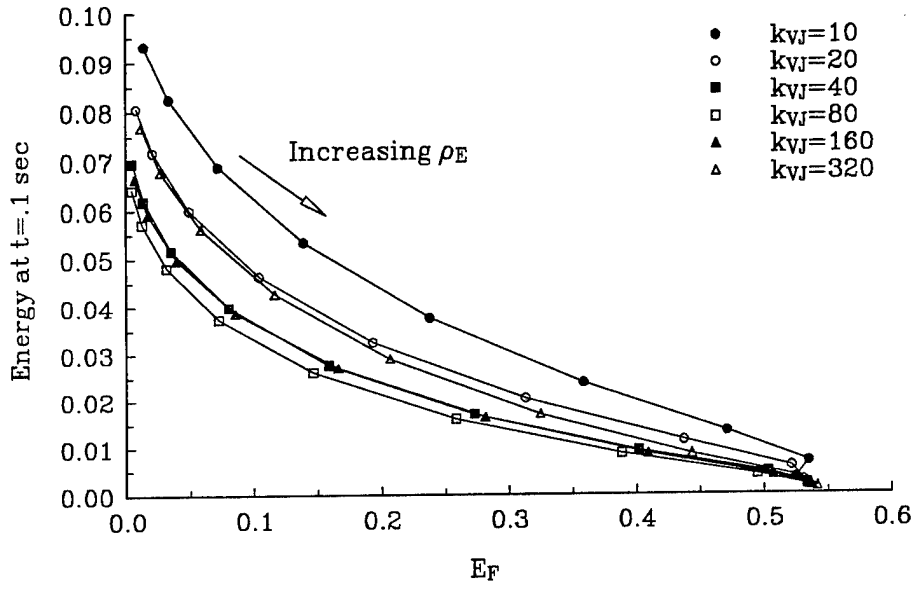

Figure 6.8 VJEW Design, Pulse Disturbance on Beam 2

E_F plot for the EW design with the pulse disturbance on beam 1 is shown in Figure 6.9. (It should be noted that Figure 6.9 is obtained using the simulated performance of the closed-loop system. Since the EW design is based on the "linear plant" with M_f as an input, control clipping was enforced when necessary.) For this case the curves tend to asymptotically approach the origin as ρ_M decreases. For decreasing values of ρ_F, more energy is dissipated but at the expense of control effort. A good choice for ρ_M and ρ_F is 1/32 and 1/80, respectively. When the pulse was applied to beam 2, similar trends were observed indicating that the EW design is not sensitive to the location of the disturbance as is the VJEW design.

The controller design studies identified three candidate designs,

VJEW Design 1: $k_{VJ} = 40$, $\rho_E = 80$

VJEW Design 2: $k_{VJ} = 80$, $\rho_E = 40$

EW Design: $\rho_M = 1/32$, $\rho_F = 1/80$.

All three designs require an observer since full state feedback is not available. To ensure that spillover effects are not neglected, low-order observer/controller pairs will be evaluated using a higher order plant. The controller and observer are based on a 2 mode per beam model while the plant is based on a 4 mode model for beam 1 and a 6 mode model for beam 2. Thus the controller is $8^{\underline{th}}$ order and the plant is $20^{\underline{th}}$ order. The LTR method of Doyle and Stein parameterizes the observer gain matrix in terms of the parameter q (see equation (6.14)). Once q is defined, $[L^o]$ can be determined. Regardless of the fact that an observer is present, the primary goal of the control system is still to

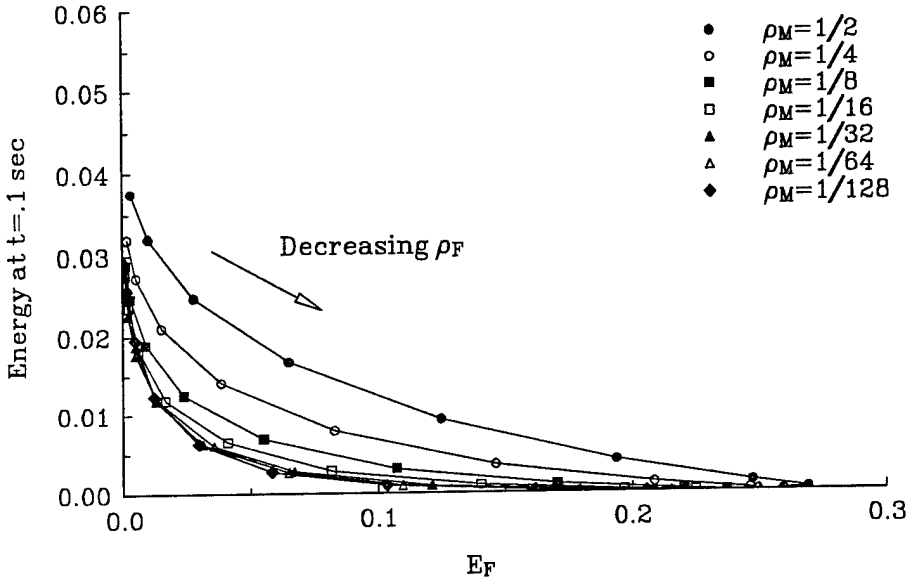

Figure 6.9 EW Design, Pulse Disturbance on Beam 1

remove as much flexural energy as possible while expending as little control effort as possible, thus the energy versus E_F plots are still appropriate. Figures 6.10 and 6.11 show the performance of each design for various values of q. The value of q = 1000 gives the best performance in all cases. In all three designs, the closed loop system is unstable for q=10000. This is clearly a result of observer spillover.

The singular value plots for disturbance rejection, noise rejection, and disturbance rejection sensitivity to plant uncertainty are shown in Figures 6.12, 6.13, and 6.14, for each design with q = 1000. These plots do not indicate that one design has any distinct advantage over another. The gain and phase margin data is given in Table 6.1. This table shows a surprising and somewhat counter-intuitive result. The EW design has higher gain and phase margins than the VJEW designs for q = 1000. This contradicts the belief that the VJEW design would be more robust due to the viscous joint. The error

Table 6.1 Gain and Phase Margin Data

	VJEW Design 1		VJEW Design 2		EW Design	
q	GM	PM	GM	PM	GM	PM
1	-5.2,15.	±49.	-4.8,12.	±43.	-2.5,3.6	±20.
10	-3.2,5.2	±26.	-3.5,6.0	±29.	-3.2,5.2	±26.
100	-2.5,3.6	±20.	-3.5,5.8	±28.	-4.0,7.5	±34.
1000	-0.8,0.9	±5.7	-1.8,2.3	±13.	-2.9,4.4	±23.
10,000	unstable		unstable		unstable	

GM = Gain Margin (db) PM = Phase Margin (deg)

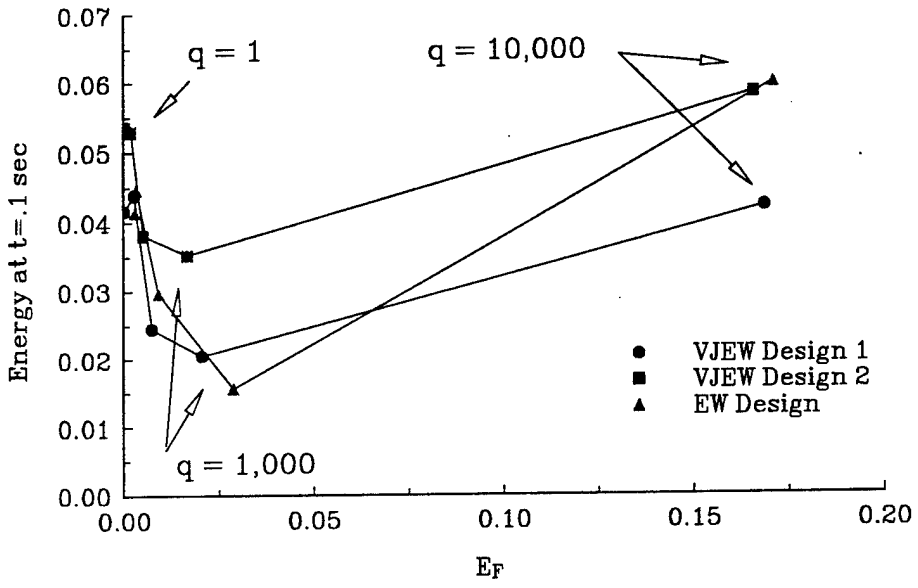

Figure 6.10 Control System Performance, Pulse Disturbance on Beam 1

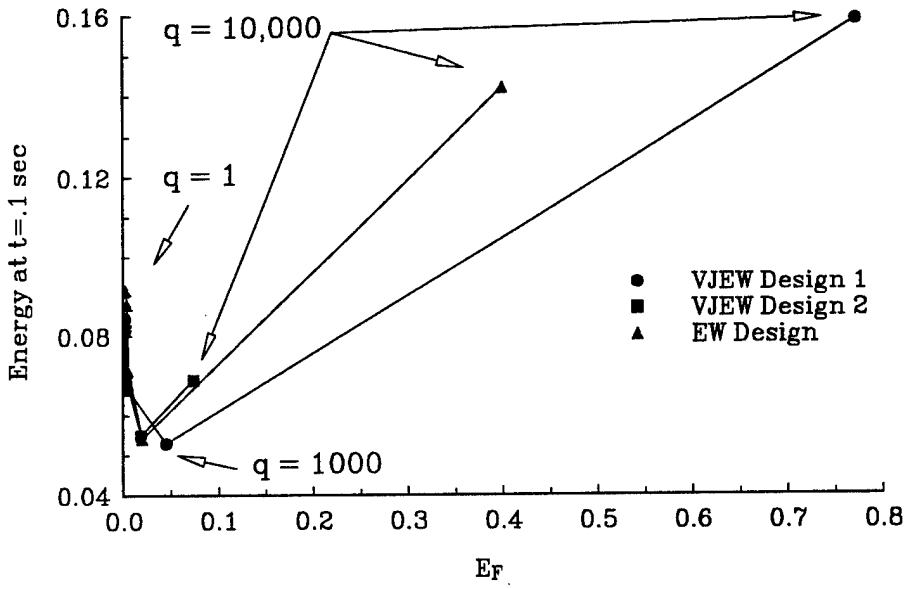

Figure 6.11 Control System Performance, Pulse Disturbance on Beam 2

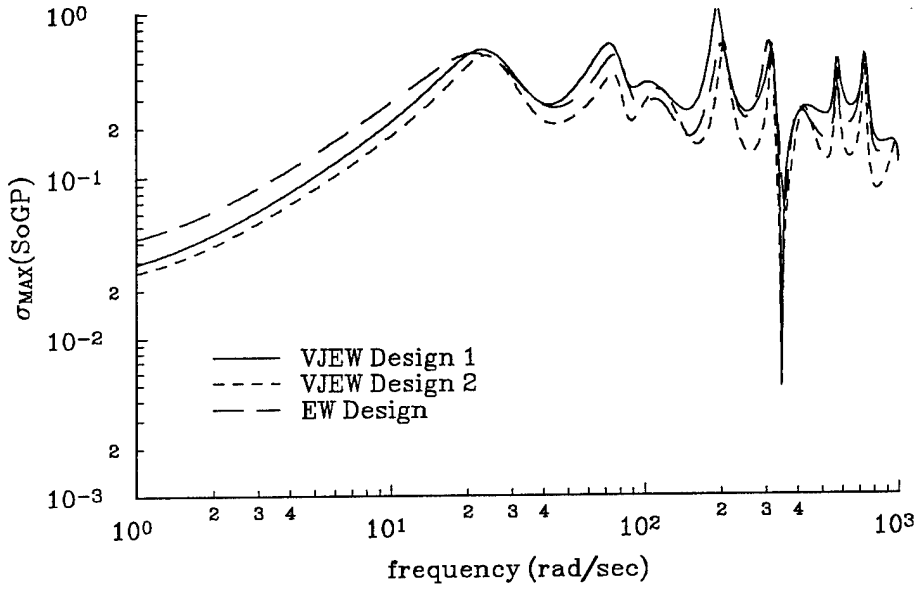

Figure 6.12 Sensitivity Function of $\underline{Y}$ to $\underline{D}$

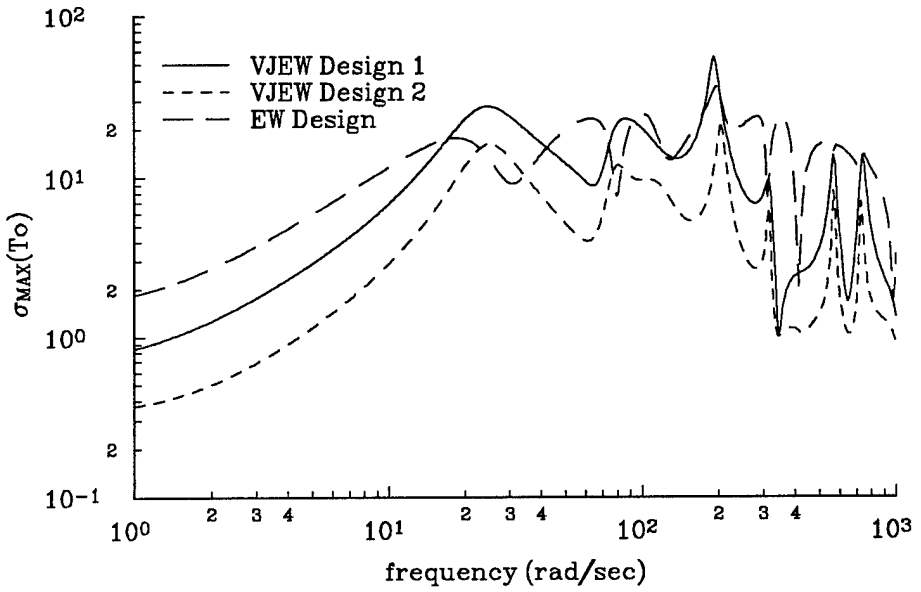

Figure 6.13 Sensitivity Function of $\underline{Y}$ to $\underline{N}$

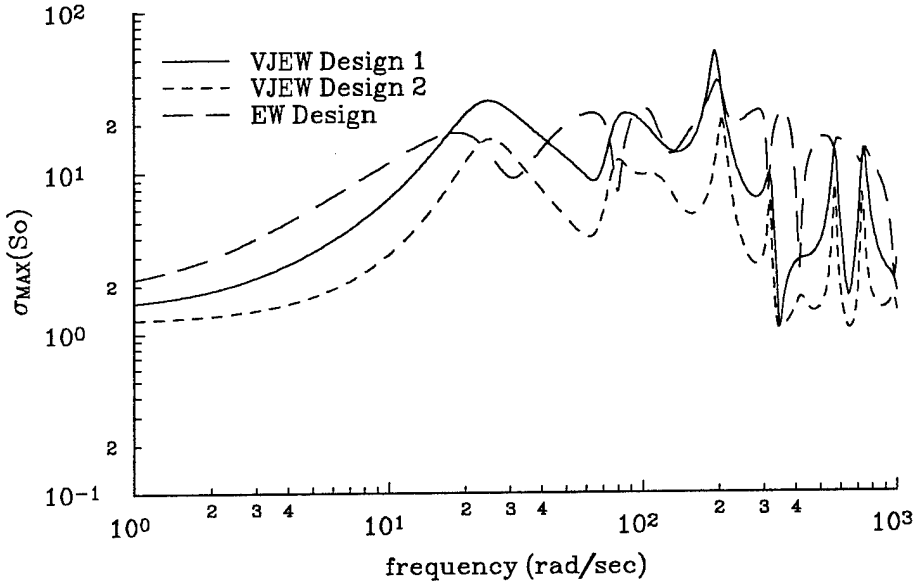

Figure 6.14 Sensitivity of Y_D to Variations in [G]

in the assumption that the viscous joint would improve robustness by adding structural damping is due to the oversight that gain and phase errors are possible in the joint controller loop. If purely passive means were used to add damping then gain and phase errors would only be present in the shape controller loop and robustness would be improved. Also evident in the gain and phase margin data is the fact that higher values of q do not improve robustness when using reduced order controllers.

The motivating ideas for investigating the VJEW designs were to allow the joint controller to be portable and to improve system robustness. These expected advantages did not materialize. The choice of k_{VJ} could not be made prior to implementing the shape controller because no physical significance could be attributed to the optimal values. Furthermore, the optimal value depended on which beam was disturbed. Robustness of the VJEW design also proved to be less than expected. The initial expectations of improved robustness failed to consider the effect of uncertainty in the joint controller loop and its effect on total system performance. Based on this study, the EW design appears to be the best control design strategy from the perspective of stability robustness. A careful inspection of Figures 6.12 - 6.14 suggests that the VJEW design #2 has slightly better performance than either the VJEW design #1 or the EW design from the perspective of disturbance rejection, insensitivity to noise, and insensitivity to plant uncertanties.

CHAPTER VII

ADAPTIVE VJEW CONTROL SYSTEM DESIGN

7.1 Introduction

Earlier VJEW controller design studies indicate that the desired value of the viscous joint parameter, k_{VJ}, is influenced by the location of the disturbance input. Two VJEW designs were designed and analyzed since one design was not deemed superior to the other. In this chapter the choice of k_{VJ} will once again be addressed. However, the motivation is to determine a physical understanding of the role of k_{VJ} and based on this understanding to develop a single VJEW controller which has desirable performance properties. Using the physical insights, a design procedure will also be recommended.

7.2 Physical Interpretation of VJEW Performance Data

The performance index used in evaluating the various control systems was the energy in the two beam system at t=0.1 seconds. Figure 7.1 shows the final energy as a function of k_{VJ} for the VJEW design with ρ_E=80. (The same trends are evident for other values of ρ_E as well.) For each value of k_{VJ}, an energy based cost functional was

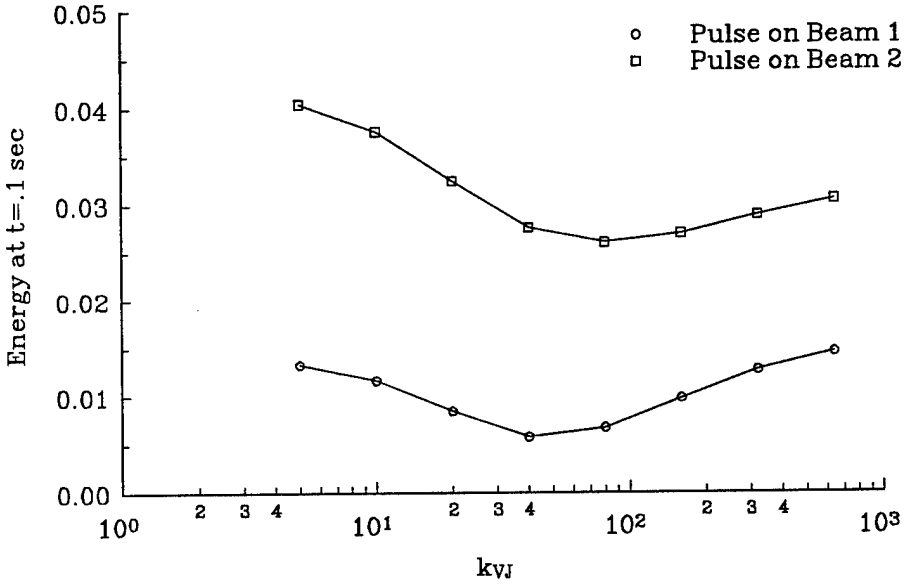

Figure 7.1 Final Energy vs k_{VJ}

minimized to define the feedback gain matrix [k]. From the curves in Figure 7.1 the energy reaches a minimum at k_{VJ}=40 for a beam 1 disturbance and at k_{VJ}=80 for a beam 2 disturbance. (This data was generated using a 3 sine mode per beam model with full state feedback.) What is the significance of k_{VJ}=40 and k_{VJ}=80? Will the minimums vary as the nature of the disturbance changes? To answer these questions more information is needed.

Figures 4.1 and 4.2 in chapter 4 show the root locus of the two-beam system with the viscous joint alone. The input for the SISO system is M_f and the output is $\dot{\theta}$. The values of 40 and 80 do not appear to have any physical significance in this case. This implies that the value of k_{VJ} must be selected in conjunction with the shape controller. Table 7.1 contains eigenvalue data for the two beam system with the joint and shape controller active. The eigenvalues shown are classified according to whether they emanate (at k_{VJ}=0) from the fundamental mode of beam 1 or 2. (For reference, the open loop eigenvalues of the two beam system are given in Table 7.2.) The parameter η in Table 7.1 represents the magnitude of the decay envelope curve at t=.1 seconds for the associated eigenvalue. The physical significance of k_{VJ}=40 and 80 is now evident. Choosing k_{VJ}=40 corresponds to maximum damping of the fundamental mode of beam 1. Additionally, the decay parameter is minimum at this point for beam 1. Since the pulse disturbance will transmit most of its energy into the first mode, maximizing first mode damping provides best performance. Similarly, k_{VJ}=80 represents peak damping for the first mode of beam 2. However, the decay parameter is slightly lower at k_{VJ}=160

Table 7.1 Eigenvalue Data for VJEW Design

k_{VJ}	Beam 1 Fundamental Mode $[\zeta/\omega]$	Beam 1 Fundamental Mode $\eta=e^{-.1\zeta\omega}$	Beam 2 Fundamental Mode $[\zeta/\omega]$	Beam 2 Fundamental Mode $\eta=e^{-.1\zeta\omega}$
5	[.144 / 70.6]	.362	[.318 / 22.7]	.486
10	[.151 / 70.8]	.343	[.320 / 22.7]	.484
20	[.177 / 71.7]	.281	[.324 / 22.8]	.478
40	[.272 / 79.5]	.115	[.342 / 23.2]	.452
80	[.141 / 80.1]	.323	[.386 / 24.9]	.382
160	[.134 / 80.0]	.342	[.346 / 28.7]	.370
320	[.132 / 80.0]	.348	[.294 / 29.7]	.418
640	[.132 / 80.0]	.348	[.278 / 29.9]	.436

Table 7.2 Beam Natural Frequencies

Mode	Beam 1 ω (r/s)	Beam 2 ω (r/s)
1	69.79	21.54
2	279.2	86.16
3	628.1	193.9
4	1117.	344.6
5	1745.	538.5
6	2512.	775.4
7	3420.	1055.
8	4467.	1379.

(the lower damping was offset by a higher frequency). It should be noted that other types of disturbances may require maximizing damping in other modes. If the disturbance transfers most of its energy into a given mode, then damping for that mode should be maximized. If the disturbance transfers energy into several modes then all of those modes should be considered. However, for most conventional structures, the lowest mode for each subsystem should be the most important one.

7.3 Nonlinear VJEW Design

The problem facing the control system designer at this point is a common one. Valid design approaches are:

1. Choose k_{VJ}=40 or k_{VJ}=80 to maximize performance for the most likely case and accept the performance degradation in the less likely case.
2. Choose k_{VJ}=60 to achieve middle of the road performance.
3. Design an adaptive control system to vary k_{VJ} to achieve optimum performance.

Depending on the particular circumstances, any of the approaches may be appropriate. The third approach, if feasible, may not require advanced knowledge of the location of the disturbance to achieve the desired performance. To be feasible, a suitable means of varying k_{VJ} must be defined. No "rigorous" mathematical tools for doing this,

for example, fuzzy logic, were explored in this research. Adaptive designs of this type usually rely on the designer's experience and physical understanding of the problem. One approach for choosing k_{VJ} is discussed below.

In the VJEW design process, a feedback gain matrix [k] is determined via LQR techniques after k_{VJ} is defined. In a real time controller, it is not desirable to solve the algebraic Riccati equation in real time as k_{VJ} is varied. Since the expected values of k_{VJ} are between 40 and 80, [k] will be defined using k_{VJ}=60 (and ρ_E=80) and subsequently held constant. Table 7.3 shows the eigenvalues of the fundamental mode for each beam as k_{VJ} is varied, holding [k] fixed. Figure 7.2 shows final energy data versus k_{VJ}. The same trends are evident as before, the value of k_{VJ} which maximizes damping in the disturbed beam's fundamental mode also minimizes final energy. An additional case in which a pulse disturbance is simultaneously imparted to both beams is shown in the figure. The minimum for this case expectedly occurs at k_{VJ}=60. Table 7.4 contains numerical values of the energy for several values of k_{VJ}.

Designing an adaptive system to achieve optimum performance hinges on identifying the means by which k_{VJ} should vary. The data in Table 7.3 and Figure 7.2 suggests that k_{VJ} should be based upon the location of the disturbance, more specifically, the value of k_{VJ} should be based on where the bulk of the system energy is initially located. If the disturbance is on beam 1, then most of the system energy is in beam 1, thus choose k_{VJ} to give best energy dissipation for beam 1. Similarly for beam 2. Figure 7.3 shows a variation of k_{VJ} based upon the percentage of total energy in beam 1. When

Table 7.3 Eigenvalue Data for VJEW Design with Fixed [k]

k_{VJ}	Beam 1 Fundamental Mode $[\zeta/\omega]$	Beam 1 Fundamental Mode $\eta=e^{-.1\zeta\omega}$	Beam 2 Fundamental Mode $[\zeta/\omega]$	Beam 2 Fundamental Mode $\eta=e^{-.1\zeta\omega}$
5	[.104 / 70.9]	.478	[.251 / 22.9]	.563
10	[.126 / 70.8]	.410	[.262 / 22.9]	.549
20	[.170 / 71.5]	.297	[.283 / 22.9]	.523
40	[.273 / 78.9]	.116	[.325 / 23.2]	.470
80	[.140 / 80.0]	.326	[.396 / 24.9]	.373
160	[.129 / 79.8]	.357	[.354 / 28.8]	.361
320	[.124 / 79.7]	.372	[.280 / 29.5]	.438
640	[.122 / 79.7]	.378	[.244 / 29.5]	.487

Table 7.4 Final Energy Data for Constant k_{VJ} Design

k_{VJ}	Disturbance on Beam(s)	$(T+V)\|_{t=.1}$
20	1	.009016
20	2	.03609
20	1 & 2	.05750
40	1	.005544*
40	2	.02827
40	1 & 2	.04452
60	1	.005879
60	2	.02630
60	1 & 2	.04212*
80	1	.006994
80	2	.02592*
80	1 & 2	.04303
160	1	.01245
160	2	.02817
160	1 & 2	.05159

"*" denotes minimum value

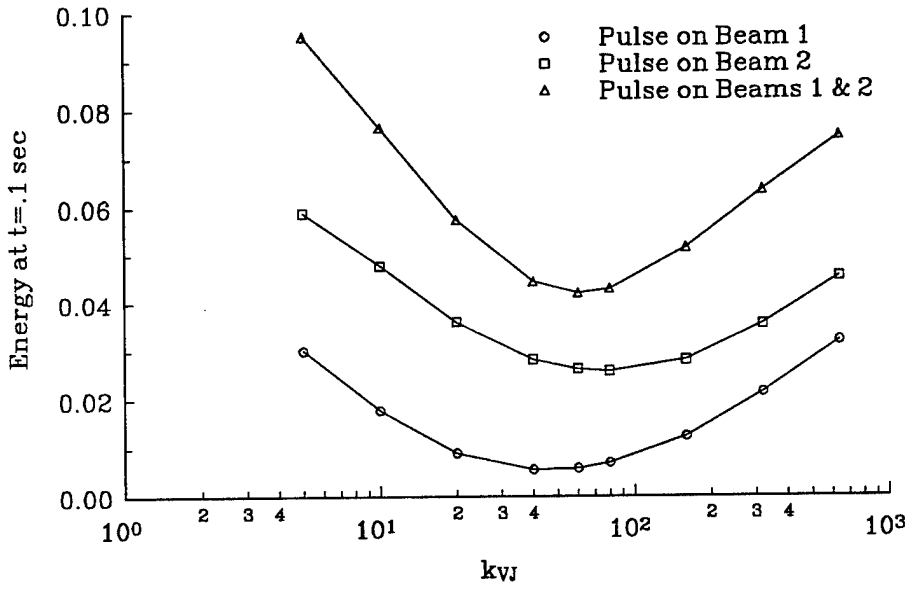

Figure 7.2 Final Energy vs k_{VJ} for Fixed [k]

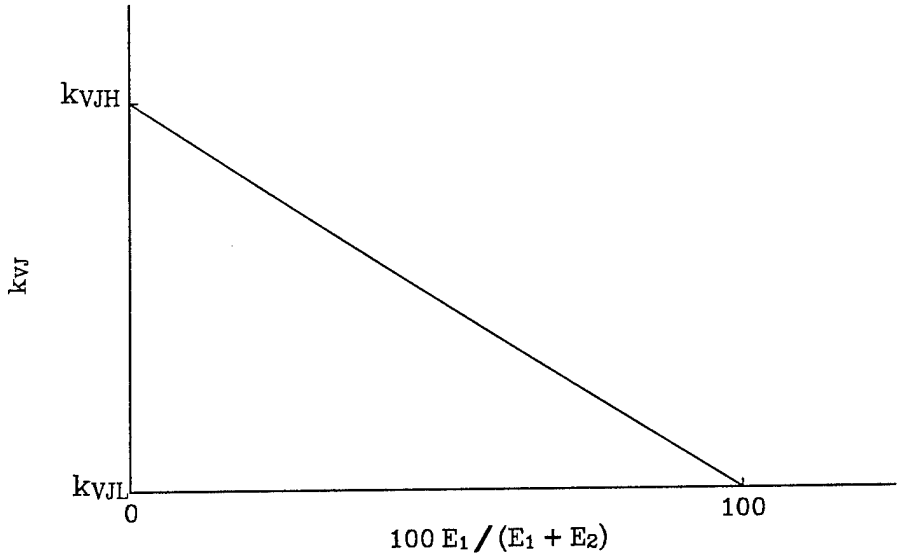

Figure 7.3 Adaptive k_{VJ}

this percentage is 0, all of the energy is in beam 2 and $k_{VJ}=k_{VJH}$. If all of the energy is in beam 1, then the percentage is 100 and $k_{VJ}=k_{VJL}$. Table 7.5 shows simulation results using various values of k_{VJL} and k_{VJH}. Note that the $k_{VJL}=40$ and $k_{VJH}=80$ design has approximately equal or slightly better performance than the corresponding best case constant k_{VJ} design for each disturbance input (see Table 7.4). Figures 7.4 - 7.6 show the energy time history plots for the three disturbance inputs and Figure 7.7 shows the time history of k_{VJ} for all three cases.

Since state feedback is necessary for the attitude/shape controller an observer will be present. The observer states can be used to estimate system energy. This adaptive design is simple to implement and results in performance superior to any of the constant

Table 7.5 Final Energy Data for Adaptive k_{VJ} Design

k_{VJL}	k_{VJH}	Disturbance on Beam(s)	$(T+V)\|_{t=.1}$
20	80	1	.006918
20	80	2	.02597
20	80	1 & 2	.04225
20	160	1	.005286
20	160	2	.02610
20	160	1 & 2	.04450
40	80	1	.005402
40	80	2	.02593
40	80	1 & 2	.04211
40	160	1	.006533
40	160	2	.02630
40	160	1 & 2	.04545

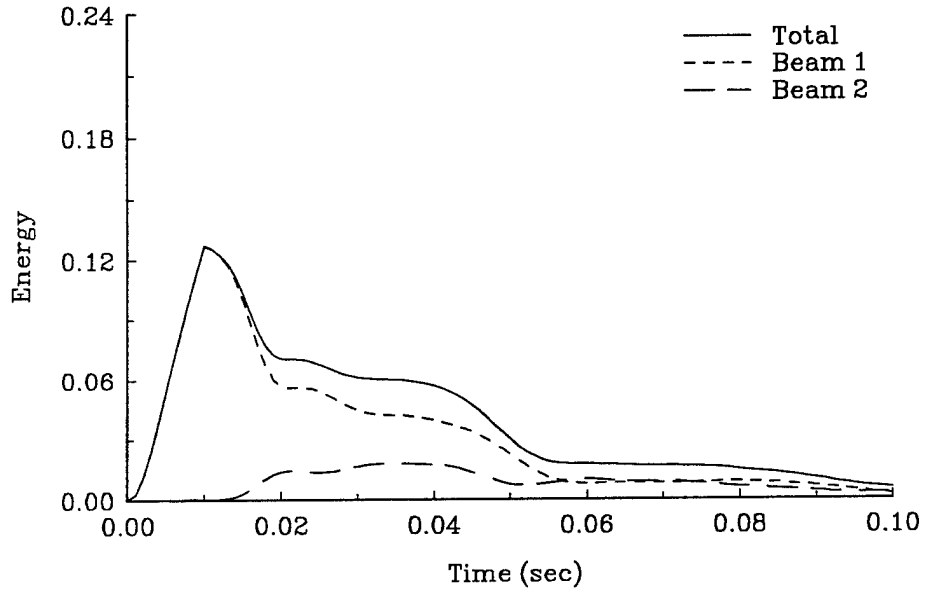

Figure 7.4 Energy vs t for Pulse Disturbance on Beam 1

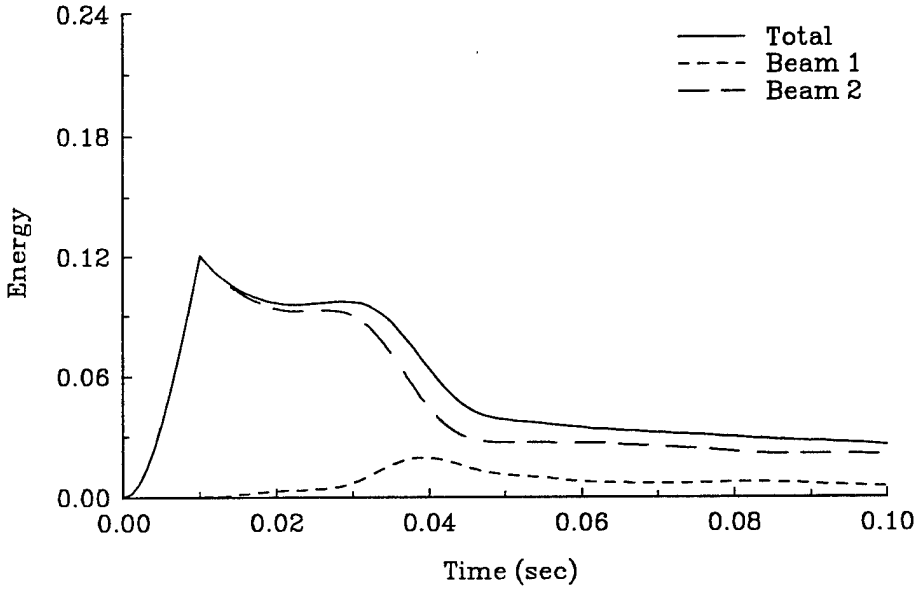

Figure 7.5 Energy vs t for Pulse Disturbance on Beam 2

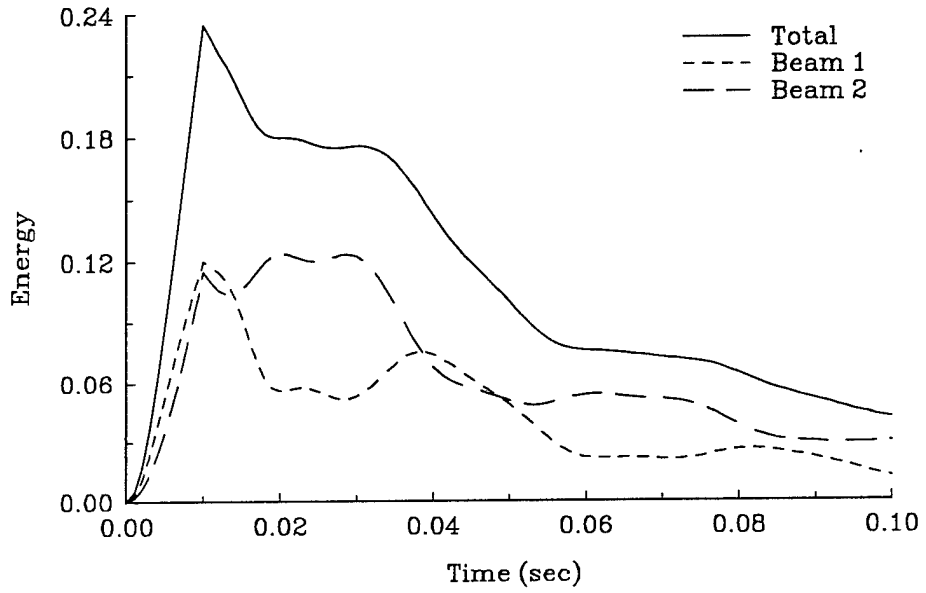

Figure 7.6 Energy vs t for Pulse Disturbance on Beams 1 & 2

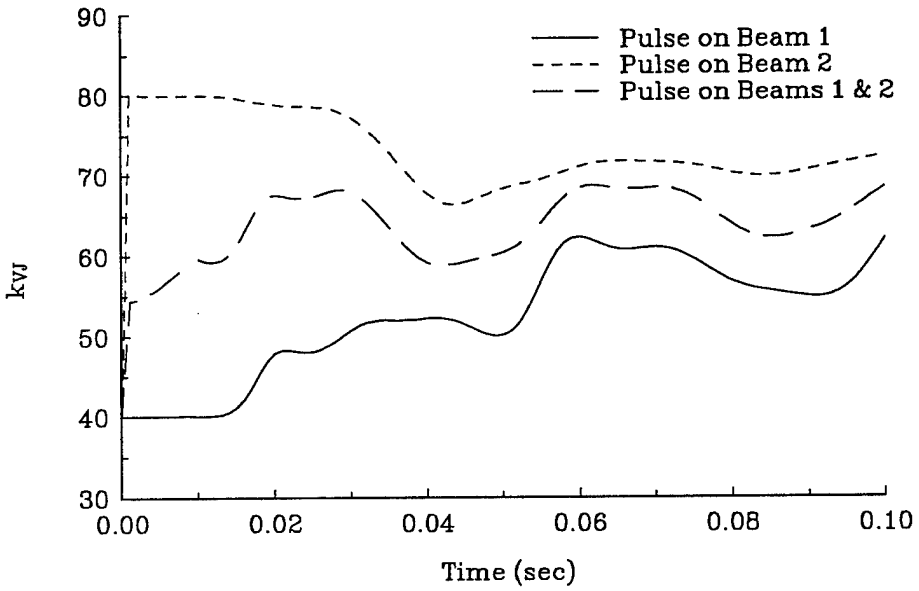

Figure 7.7 Adaptive k_{VJ} vs t

k_{VJ} designs. The superior performance is expected for all disturbances which transmit most of their energy into the fundamental mode of one or both beams.

7.4 Design Procedure

Control system design can rarely be described in terms of rigid procedures and design steps. The design process involves creativity and physical insight as well as the application of mathematical principles and tools and is highly iterative for large, realistic systems. The steps used in the VJEW control system design are summarized below.

1. Identify the Performance Goals

   The primary goal of the control system is to remove vibrational energy from the two beam system using the least amount of input energy. The performance measures were thus defined to be,

$$\text{Energy} = (T + V)|_{t=.1} \tag{7.1}$$

$$E_F = \int_0^{.1} (F_1 \dot{w}_1)^2 + (F_2 \dot{w}_2)^2 \, dt \, . \tag{7.2}$$

   These measures are to be minimized for thruster type inputs (i.e. pulse disturbances) to either beam.

2. Identify Control System Design Methodology

For the VJEW architecture the joint controller is defined by

$$F_N = k_{VJ} |\dot{\theta}| \ . \tag{7.3}$$

The shape controller forces are determined via LQR theory. LQR design techniques are particularly attractive since they allow system energy and a form of control power to be directly minimized. The cost functional is defined as

$$J = \int_0^\infty \rho_E (T + V) + (F_1^2 + F_2^2) \, dt \ . \tag{7.4}$$

3. Perform Parametric Study of k_{VJ}, ρ_E

Using the nonlinear simulation, performance data can be generated for various combinations of k_{VJ} and ρ_E. Assuming the beams are not identical will result in different values of k_{VJ} and ρ_E (which simultaneously minimize energy and power) for different input locations.

4. Investigate Adaptive Controller Design

To improve performance for a variety of inputs, look for the underlying physical reasons for optimum performance. For the

system studied here, this was identified as maximizing first mode damping in the beam with the most energy. Other simplifications which proved beneficial (in terms of implementation in a real time system) were to fix the feedback gains using averaged or mid-range values of k_{VJ} and ρ_E and to require that k_{VJ} vary as a function of parameters currently available.

5. Design State Observer

The loop transfer recovery (LTR) technique of Doyle and Stein was used to design the observer. This conveniently parameterizes the observer gain matrix in terms of a scalar, q. Lacking measurement error data allowed q to be chosen purely on the basis of minimizing the energy.

The above design steps are certainly not intended to be all-inclusive. Accurate knowledge of error sources, actuator dynamics, real time computer limitations, and the like will require other compromises in the design process. Despite their simplicity, the above steps are useful in identifying some performance indices and design procedures which may be applicable in many control systems designed to control flexural vibrations.

CHAPTER VIII

FREE-FREE BEAM SYSTEM

8.1 Introduction

The pinned-pinned beam system can be viewed as a sub-structure of a large built-up truss structure. Another type of system relevant to space structures is the free floating beam system shown in Figure 8.1. In the free floating (or free-free) system, the two beams are connected by a pin joint but are otherwise unconstrained. At the pin is a rotary spring and a semi-active joint. The rotary spring is necessary to keep the two beams from coming to rest in a nonaligned position. The semi-active joint is intended to be an energy dissipation / vibration control device. Also present are two actuators for attitude and position control.

In this chapter, the ability of the semi-active joint to remove vibrational energy from the free-free beam system is investigated. Since a spring is necessary at the joint, the effect of varying spring stiffness on the joint controller design is also included. Controllability issues are discussed since system motion which does not result in relative motion at the joint is not controllable from the joint moment.

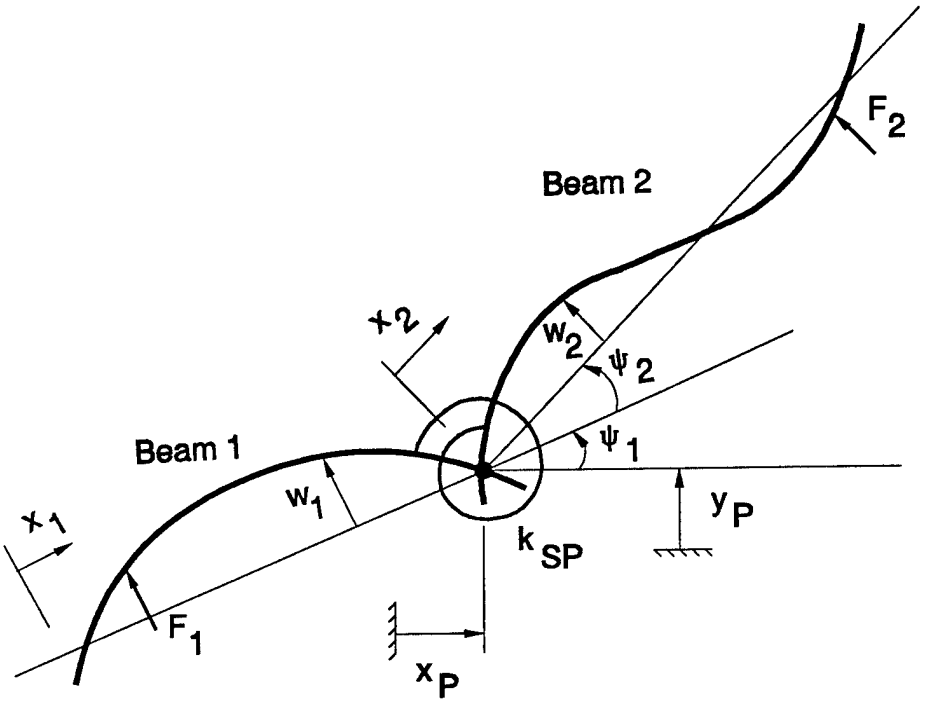

Figure 8.1 Free-Free Beam System

8.2 Free-Free Beam System Model

The free-free beam system is shown in Figure 8.1. Motion of the beams consists of rigid body translational and rotational modes and flexural vibration modes. The assumed modes method is used to derive the equations of motion. The generalized coordinates are

$$\underline{q} = \{ x_P \; y_P \; \psi_1 \; \psi_2 \; \eta_{11} \; \eta_{12} \cdots \eta_{1N_1} \; \eta_{21} \; \eta_{22} \cdots \eta_{2N_2} \}^T \tag{8.1}$$

where x_P and y_P are pin displacements, ψ_1 is the rigid body rotation angle of beam 1, ψ_2 is the rigid body rotation angle of beam 2 relative to ψ_1, and η_{ij} is the j^{th} modal amplitude of the i^{th} beam. The flexural displacement of each beam is given by

$$w_i(x_i,t) = \sum_{j=1}^{N_i} \phi_{ij}(x_i)\, \eta_{ij}(t) \;, \quad i = 1,2 \tag{8.2}$$

where ϕ_{ij} is the normalized mode shape function. The kinetic energy and potential energies are shown in equations (8.3) and (8.4) on the following page. (The ' notation is used to denote differentiation with respect to x_1 or x_2.)

Based on the kinetic and potential energy of the system as well as the system virtual work, $4+N_1+N_2$ equations of motion can be obtained and are given in equations (8.5) - (8.10).

$$
\begin{aligned}
T = \frac{\rho_1 A_1}{2} \int_0^{L_1} \Big(\Big[& \dot{x}_P - \dot{w}_1(x_1,t) \sin\psi_1 + \psi_1 (L_1 - x_1) \sin\psi_1 \Big]^2 \\
& + \Big[\dot{y}_P + \dot{w}_1(x_1,t) \cos\psi_1 - \psi_1 (L_1 - x_1) \cos\psi_1 \Big]^2 \Big) \, dx_1 \\
+ \frac{\rho_2 A_2}{2} \int_0^{L_2} \Big(\Big[& \dot{x}_P - \dot{w}_2(x_2,t) \sin(\psi_1 + \psi_2) \\
& - (\dot{\psi}_1 + \dot{\psi}_2) x_2 \sin(\psi_1 + \psi_2) \Big]^2 \\
& + \Big[\dot{y}_P + \dot{w}_2(x_2,t) \cos(\psi_1 + \psi_2) \\
& + (\dot{\psi}_1 + \dot{\psi}_2) x_2 \cos(\psi_1 + \psi_2) \Big]^2 \Big) \, dx_2 \, ,
\end{aligned}
\tag{8.3}
$$

$$
\begin{aligned}
V = & \frac{E_1 I_1}{2} \int_0^{L_1} \Big[w_1''(x_1,t) \Big]^2 \, dx_1 \\
& + \frac{E_2 I_2}{2} \int_0^{L_2} \Big[w_2''(x_2,t) \Big]^2 \, dx_2 \\
& + \frac{1}{2} k_{SP} \Big[\Psi_2 + w_2'(x_2,t)\Big|_{x_2 = 0} - w_1'(x_1,t)\Big|_{x_1 = L_1} \Big]^2 \, .
\end{aligned}
\tag{8.4}
$$

$$x_P: \quad \left[\rho_1 A_1 L_1 + \rho_2 A_2 L_2\right]\ddot{x}_P + \left[\frac{\rho_1 A_1 L_1^2}{2}\sin\psi_1 - \frac{\rho_2 A_2 L_2^2}{2}\sin(\psi_1+\psi_2)\right]\ddot{\psi}_1$$

$$+ \left[-\frac{\rho_2 A_2 L_2^2}{2}\sin(\psi_1+\psi_2)\right]\ddot{\psi}_2 + \sum_{j=1}^{N_1}\left[-\rho_1 A_1 \sin\psi_1 \int_0^{L_1}\phi_{1j}\,dx_1\right]\ddot{\eta}_{1j}$$

$$+ \sum_{j=1}^{N_2}\left[-\rho_2 A_2 \sin(\psi_1+\psi_2)\int_0^{L_2}\phi_{2j}\,dx_2\right]\ddot{\eta}_{2j}$$

$$+ \left[-\rho_1 A_1 \dot{\psi}_1 \cos\psi_1 \sum_{j=1}^{N_1}\dot{\eta}_{1j}\int_0^{L_1}\phi_{1j}\,dx_1 + \frac{\rho_1 A_1 L_1^2}{2}\dot{\psi}_1^2\cos\psi_1\right.$$

$$- \frac{\rho_2 A_2 L_2^2}{2}(\dot{\psi}_1+\dot{\psi}_2)^2\cos(\psi_1+\psi_2)$$

$$\left. - \rho_2 A_2 (\dot{\psi}_1+\dot{\psi}_2)\cos(\psi_1+\psi_2)\sum_{j=1}^{N_2}\dot{\eta}_{2j}\int_0^{L_2}\phi_{2j}\,dx_2\right]$$

$$= \left[-\sin\psi_1\right]F_1 + \left[-\sin(\psi_1+\psi_2)\right]F_2 \qquad (8.5)$$

$$
\begin{aligned}
y_P: \quad & \left[\rho_1 A_1 L_1 + \rho_2 A_2 L_2\right]\ddot{y}_P \\
& + \left[-\frac{\rho_1 A_1 L_1^2}{2}\cos\psi_1 + \frac{\rho_2 A_2 L_2^2}{2}\cos(\psi_1+\psi_2)\right]\ddot{\psi}_1 \\
& + \left[\frac{\rho_2 A_2 L_2^2}{2}\cos(\psi_1+\psi_2)\right]\ddot{\psi}_2 + \sum_{j=1}^{N_1}\left[\rho_1 A_1 \cos\psi_1 \int_0^{L_1}\phi_{1j}\,dx_1\right]\ddot{\eta}_{1j} \\
& + \sum_{j=1}^{N_2}\left[\rho_2 A_2 \cos(\psi_1+\psi_2)\int_0^{L_2}\phi_{2j}\,dx_2\right]\ddot{\eta}_{2j} \\
& + \left[-\rho_1 A_1 \dot{\psi}_1 \sin\psi_1 \sum_{j=1}^{N_1}\dot{\eta}_{1j}\int_0^{L_1}\phi_{1j}\,dx_1 + \frac{\rho_1 A_1 L_1^2}{2}\dot{\psi}_1^2 \sin\psi_1\right. \\
& - \frac{\rho_2 A_2 L_2^2}{2}(\dot{\psi}_1+\dot{\psi}_2)^2 \sin(\psi_1+\psi_2) \\
& \left. - \rho_2 A_2 (\dot{\psi}_1+\dot{\psi}_2)\sin(\psi_1+\psi_2)\sum_{j=1}^{N_2}\dot{\eta}_{2j}\int_0^{L_2}\phi_{2j}\,dx_2\right] \\
& = \left[\cos\psi_1\right]F_1 + \left[\cos(\psi_1+\psi_2)\right]F_2
\end{aligned}
\tag{8.6}
$$

$$\psi_1: \quad \left[\frac{\rho_1 A_1 L_1^2}{2}\sin\psi_1 - \frac{\rho_2 A_2 L_2^2}{2}\sin(\psi_1+\psi_2)\right]\ddot{x}_P$$

$$+\left[-\frac{\rho_1 A_1 L_1^2}{2}\cos\psi_1 + \frac{\rho_2 A_2 L_2^2}{2}\cos(\psi_1+\psi_2)\right]\ddot{y}_P$$

$$+\left[\frac{\rho_1 A_1 L_1^3}{3} + \frac{\rho_2 A_2 L_2^3}{3}\right]\ddot{\psi}_1 + \left[\frac{\rho_2 A_2 L_2^3}{3}\right]\ddot{\psi}_2$$

$$+\sum_{j=1}^{N_1}\left[-\rho_1 A_1 L_1\int_0^{L_1}\phi_{1j}\,dx_1 + \rho_1 A_1\int_0^{L_1}x_1\,\phi_{ij}\,dx_1\right]\ddot{\eta}_{1j}$$

$$+\sum_{j=1}^{N_2}\left[\rho_2 A_2\int_0^{L_2}x_2\,\phi_{2j}\,dx_2\right]\ddot{\eta}_{2j} + \left[\rho_1 A_1\dot{x}_P\cos\psi_1\sum_{j=1}^{N_1}\dot{\eta}_{1j}\int_0^{L_1}\phi_{1j}dx_1\right. \tag{8.7}$$

$$+\rho_1 A_1\dot{y}_P\sin\psi_1\sum_{j=1}^{N_1}\dot{\eta}_{1j}\int_0^{L_1}\phi_{1j}\,dx_1$$

$$+\rho_2 A_2\dot{x}_P\cos(\psi_1+\psi_2)\sum_{j=1}^{N_2}\dot{\eta}_{2j}\int_0^{L_2}\phi_{2j}\,dx_2$$

$$\left.+\rho_2 A_2\dot{y}_P\sin(\psi_1+\psi_2)\sum_{j=1}^{N_2}\dot{\eta}_{2j}\int_0^{L_2}\phi_{2j}\,dx_2\right]$$

$$=\left[-L_1+x_{F1}\right]F_1 + \left[x_{F2}\right]F_2$$

$$
\begin{aligned}
\psi_2: \quad & \left[-\frac{\rho_2 A_2 L_2^{\,2}}{2} \sin(\psi_1 + \psi_2) \right] \ddot{x}_P + \left[\frac{\rho_2 A_2 L_2^{\,2}}{2} \cos(\psi_1 + \psi_2) \right] \ddot{y}_P \\
& + \left[\frac{\rho_2 A_2 L_2^{\,3}}{3} \right] \ddot{\psi}_1 + \left[\frac{\rho_2 A_2 L_2^{\,3}}{3} \right] \ddot{\psi}_2 \\
& + \sum_{j=1}^{N_2} \left[\rho_2 A_2 \int_0^{L_2} x_2 \, \phi_{2j} \, dx_2 \right] \ddot{\eta}_{2j} \\
& + \left[\rho_2 A_2 \dot{x}_P \cos(\psi_1 + \psi_2) \sum_{j=1}^{N_2} \dot{\eta}_{2j} \int_0^{L_2} \phi_{2j} \, dx_2 \right. \\
& \left. + \rho_2 A_2 \dot{y}_P \sin(\psi_1 + \psi_2) \sum_{j=1}^{N_2} \dot{\eta}_{2j} \int_0^{L_2} \phi_{2j} \, dx_2 \right] \\
& + \left[k_{sp} \right] \psi_2 + \sum_{j=1}^{N_1} \left[-k_{sp} \phi'_{1j}(L_1) \right] \eta_{1j} + \sum_{j=1}^{N_2} \left[k_{sp} \phi'_{2j}(0) \right] \eta_{2j} \\
& = \left[x_{F2} \right] F_2 + \left[-1 \right] M_f
\end{aligned}
\tag{8.8}
$$

$$
\begin{aligned}
\eta_{1j}: \quad & \left[-\rho_1 A_1 \sin\psi_1 \int_0^{L_1} \phi_{1j}\, dx_1 \right] \ddot{x}_P + \left[\rho_1 A_1 \cos\psi_1 \int_0^{L_1} \phi_{1j}\, dx_1 \right] \ddot{y}_P \\
& + \left[-\rho_1 A_1 L_1 \int_0^{L_1} \phi_{1j}\, dx_1 + \rho_1 A_1 \int_0^{L_1} x_1\, \phi_{1j}\, dx_1 \right] \ddot{\psi}_1 \\
& + \sum_{k=1}^{N_1} \left[\rho_1 A_1 \int_0^{L_1} \phi_{1j}\, \phi_{1k}\, dx_1 \right] \ddot{\eta}_{1k} + \left[-\rho_1 A_1 \dot{x}_P \dot{\psi}_1 \cos\psi_1 \int_0^{L_1} \phi_{1j}\, dx_1 \right. \\
& \left. - \rho_1 A_1 \dot{y}_P \dot{\psi}_1 \sin\psi_1 \int_0^{L_1} \phi_{1j}\, dx_1 \right] + \left[-k_{sp}\, \phi'_{1j}(L_1) \right] \psi_2 \\
& + \sum_{k=1}^{N_1} \left[E_1 I_1 \int_0^{L_1} \phi''_{1j}\, \phi''_{1k}\, dx_1 + k_{sp}\, \phi'_{1j}(L_1)\, \phi'_{1k}(L_1) \right] \eta_{1k} \\
& + \sum_{k=1}^{N_2} \left[-k_{sp}\, \phi'_{1j}(L_1)\, \phi'_{2k}(0) \right] \eta_{2k} \\
& = \left[\phi_{1j}(x_{F1}) \right] F_1 + \left[\phi'_{1j}(L_1) \right] M_f
\end{aligned}
\tag{8.9}
$$

$$
\begin{aligned}
\eta_{2j}: \quad & \left[-\rho_2 A_2 \sin(\psi_1 + \psi_2) \int_0^{L_2} \phi_{2j}\, dx_2 \right] \ddot{x}_P \\
& + \left[\rho_2 A_2 \cos(\psi_1 + \psi_2) \int_0^{L_2} \phi_{2j}\, dx_2 \right] \ddot{y}_P \\
& + \left[\rho_2 A_2 \int_0^{L_2} x_2\, \phi_{2j}\, dx_2 \right] \ddot{\psi}_1 + \left[\rho_2 A_2 \int_0^{L_2} x_2\, \phi_{2j}\, dx_2 \right] \ddot{\psi}_2 \\
& + \sum_{k=1}^{N_2} \left[\rho_2 A_2 \int_0^{L_2} \phi_{2j}\, \phi_{2k}\, dx_2 \right] \ddot{\eta}_{2k} \\
& + \left[-\rho_2 A_2 \dot{x}_P (\dot{\psi}_1 + \dot{\psi}_2) \cos(\psi_1 + \psi_2) \int_0^{L_2} \phi_{2j}\, dx_2 \right. \\
& \left. - \rho_2 A_2 \dot{y}_P (\dot{\psi}_1 + \dot{\psi}_2) \sin(\psi_1 + \psi_2) \int_0^{L_2} \phi_{2j}\, dx_2 \right] \\
& + \left[k_{sp}\, \phi'_{2j}(0) \right] \psi_2 + \sum_{k=1}^{N_1} \left[-k_{sp}\, \phi'_{2j}(0)\, \phi'_{1k}(L_1) \right] \eta_{1k} \\
& + \sum_{k=1}^{N_2} \left[E_2 I_2 \int_0^{L_2} \phi''_{2j}\, \phi''_{2k}\, dx_2 + k_{sp}\, \phi'_{2j}(0)\, \phi'_{2k}(0) \right] \eta_{2k} \\
& = \left[\phi_{2j}(x_{F2}) \right] F_2 + \left[-\phi'_{2j}(0) \right] M_f \, .
\end{aligned}
\tag{8.10}
$$

The state equations can be written in matrix form as follows,

$$[M(\underline{q})]\ddot{\underline{q}} + [K]\underline{q} + \underline{G}(\dot{\underline{q}},\underline{q}) = [H(\underline{q})]\underline{u}, \tag{8.11}$$

where $[M(\underline{q})]$ is the mass matrix, $[K]$ is the stiffness matrix, $\underline{G}(\dot{\underline{q}},\underline{q})$ is a quadratic velocity term, $[H(\underline{q})]$ is the input coefficient matrix, and $\underline{u} = \{ F_1 \; F_2 \; M_f \}^T$ is the input vector. The $(\underline{q})$ notation signifies a dependence on the generalized coordinate vector. Defining $\underline{x}$ as,

$$\underline{x} = \begin{bmatrix} \dot{\underline{q}} \\ \underline{q} \end{bmatrix} \tag{8.12}$$

allows the state equations to be written in terms of first order differential equations,

$$\dot{\underline{x}} = [A_{SL}]\underline{x} + \underline{\Gamma} + [B_{SL}]\underline{u}\ , \tag{8.13}$$

where

$$[A_{SL}] = \left[\begin{array}{c|c} [0] & -[M(\underline{q})]^{-1}[K] \\ \hline [I] & [0] \end{array}\right] \tag{8.14}$$

$$\underline{\Gamma} = \begin{bmatrix} -[M(\underline{q})]^{-1}\,\underline{G}(\dot{\underline{q}},\underline{q}) \\ \underline{0} \end{bmatrix} \tag{8.15}$$

$$\left[B_{SL}\right] = \begin{bmatrix} \left[M(q)\right]^{-1}\left[H(q)\right] \\ \left[0\right] \end{bmatrix}. \tag{8.16}$$

Sticking dynamics at the joint are included in a manner identical to that for the pinned-pinned beam.

Mode shapes for the free-free system are based on the mode shapes of a pinned-free beam. Beam 1 mode shapes are for a free-pinned beam and beam 2 mode shapes are for a pinned-free beam. Since the free-pinned mode shapes are merely reflected pinned-free mode shapes, only the latter will be discussed below. For the pinned-free beam the boundary conditions are,

$$\begin{aligned}
&\text{i)}\ \ w(0,t) = 0 && \text{zero displacement at pin} \\
&\text{ii)}\ \ \left.\frac{\partial^2 w(x,t)}{\partial x^2}\right|_{x=0} = 0 && \text{zero moment at pin} \\
&\text{iii)}\ \ \left.\frac{\partial^2 w(x,t)}{\partial x^2}\right|_{x=L} = 0 && \text{zero moment at free end} \\
&\text{iv)}\ \ \left.\frac{\partial^3 w(x,t)}{\partial x^3}\right|_{x=L} = 0 && \text{zero shear at free end .}
\end{aligned} \tag{8.17}$$

Boundary conditions i), iii), and iv) are applicable to the beams in the free-free beam system. Boundary condition ii) requires a zero moment at the pin which is not the case when the spring and semi-active joint are present. Since this is a natural boundary

condition and not a geometric one, the pinned-free modes are nonetheless applicable. Using the above boundary conditions with the transverse vibration beam equation yields the following characteristic equation,

$$\tan a_j L = \tanh a_j L \ . \tag{8.18}$$

The roots of equation (8.18) have been tabulated in a variety of sources. An approximate relationship found to be fairly accurate for higher modes is

$$a_j L \approx \frac{\pi}{2} + j\pi \ . \tag{8.19}$$

Normalizing the mode shapes such that

$$\int_0^L \phi_j(x)\, \phi_k(x)\, dx = L\delta_{jk} \tag{8.20}$$

yields

$$\phi_j(x) = k_{1j} \sin(a_j x) + k_{2j} \sinh(a_j x) \tag{8.21}$$

where

$$k_{1j} = \left[\frac{2\sinh^2(a_j L)}{\sinh^2(a_j L) - \sin^2(a_j L)} \right]^{\frac{1}{2}} \tag{8.22}$$

$$k_{2j} = k_{1j} \frac{\sin(a_j L)}{\sinh(a_j L)} \ . \tag{8.23}$$

These mode shapes are for the pinned-free modes which correspond to beam 2. The free-pinned modes of beam 1 are given by

$$\phi_j(x) = k_{1j} \sin(a_j(L-x)) + k_{2j} \sinh(a_j(L-x)) \tag{8.24}$$

where k_{1j} and k_{2j} are given by (8.22) and (8.23), respectively. The first three pinned-free modes are shown in Figure 8.2. For the simulation and design studies, three modes per beam were used unless otherwise noted.

As seen from equations (8.5) - (8.10), the state equations are nonlinear. In order to use linear control system design techniques a linear approximation of the system is needed. This was generated numerically rather than analytically. Equation (8.13) can be written more generally as

$$\dot{\underline{x}} = \underline{f}(\underline{x}, \underline{u}) \ . \tag{8.25}$$

Letting

$$\begin{aligned} \underline{x} &= \underline{x}_o + \delta\underline{x} \\ \underline{u} &= \underline{u}_o + \delta\underline{u} \end{aligned} \tag{8.26}$$

where "o" represents the operating point about which the linearization is to occur, the linear perturbation equation is

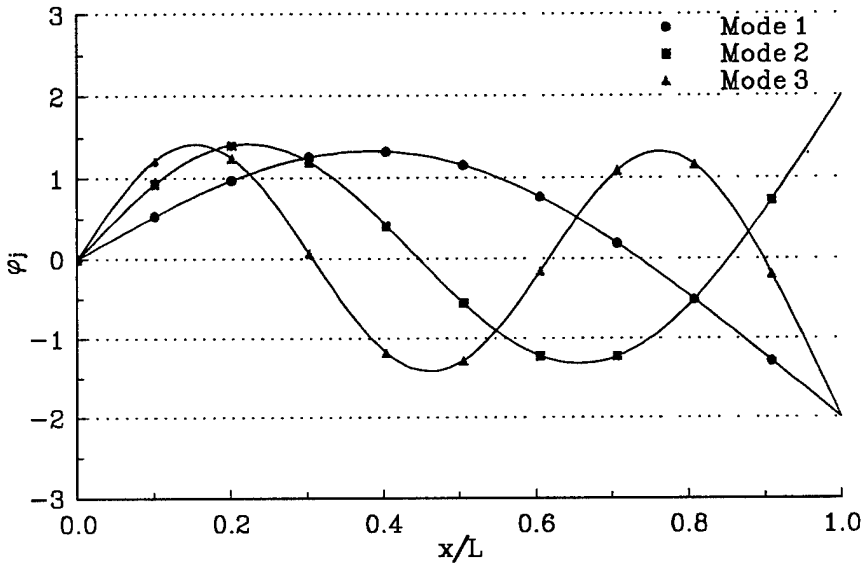

Figure 8.2 Pinned-Free Mode Shapes

$$\delta\dot{\underline{x}} = \nabla_{\underline{x}}\underline{f}\Big|_0 \delta\underline{x} + \nabla_{\underline{u}}\underline{f}\Big|_0 \delta\underline{u} \ . \tag{8.27}$$

The state and control jacobians ($\nabla_{\underline{x}}\underline{f}$ and $\nabla_{\underline{u}}\underline{f}$, respectively) were calculated using the IMSL routine DFDJAC [64].

8.3 Viscous Joint

The semi-active joint proved to be an effective means of dissipating energy in the pinned-pinned beam system. Although not the best in terms of performance, the viscous joint controller defined as

$$F_N = k_{VJ} |\dot{\theta}| \ , \tag{8.28}$$

yielded results comparable to more complex controller designs. In this section, the performance of the viscous joint controller is investigated for the free-free beam system. In addition to selecting k_{VJ}, the spring constant is also a design variable. The relationship between k_{VJ} and k_{SP} is discussed as well.

As in previous studies, pulse disturbances are used to determine the effectiveness of the joint. A simple attitude and position controller is used to keep the free-free system approximately horizontal and stationary. This design uses LQR techniques to define F_1 and F_2 via linear, constant gain, state feedback matrices. The LQR performance index is

$$J_{A/S} = \int_0^{\infty} \frac{1}{2}\left[20\dot{y}_P^2 + 40(\psi_1^2 + \psi_2^2) + 10(y_p{}^2 + \psi_1{}^2 + \psi_2{}^2) \right] + \frac{1}{2}\left[F_1{}^2 + F_2{}^2 \right] dt. \tag{8.29}$$

The resulting actuator inputs are then each passed through a first-order low pass filter with a corner frequency of 20 rad/sec. Restricting the actuator inputs to low frequency ranges ensures that vibration control is done primarily by the semi-active joint. The measure of performance for the semi-active joint is the kinetic and potential "flexural energy" in the beams plus the energy in the joint spring. The control of rigid body modes is not considered to be a requirement of the joint thus energy associated with rigid body motion is not included in the performance measure. The energy measure is thus given by

$$\begin{aligned} EM = & \sum_{i=1}^{2} \frac{\rho_i A_i}{2} \sum_{j=1}^{N_i} \sum_{k=1}^{N_i} \eta_{ij} \eta_{ik} \int_0^{L_i} \phi_{ij} \phi_{ik} \, dx_i \\ & + \sum_{i=1}^{2} \frac{E_i I_i}{2} \sum_{j=1}^{N_i} \sum_{k=1}^{N_i} \eta_{ij} \eta_{ik} \int_0^{L_i} \phi''_{ij} \phi''_{ik} \, dx_i \\ & + k_{SP} \left(\psi_2 + w_2'(x_2,t)\Big|_{x_2 = 0} - w_1'(x_1,t)\Big|_{x_1 = L_1} \right)^2 . \end{aligned} \tag{8.30}$$

Performance curves for a pulse disturbance on beam 1 and beam 2 are shown in Figures 8.3 and 8.4. The value of EM at t=0.4 sec is plotted for various values of k_{VJ} and k_{SP}. Both curve sets indicate that as k_{SP} increases, the ability to dissipate energy in the joint

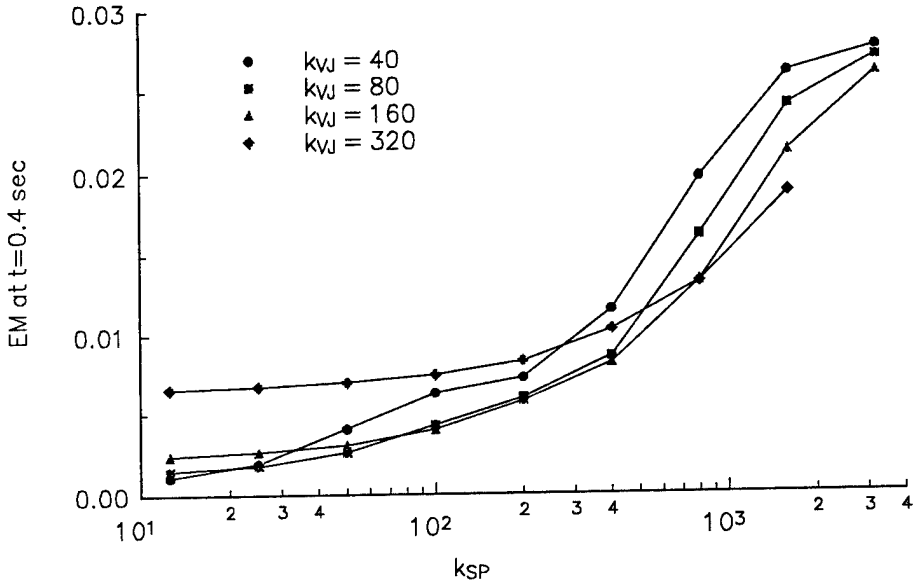

Figure 8.3 EM at t=0.4, Pulse Disturbance on Beam 1

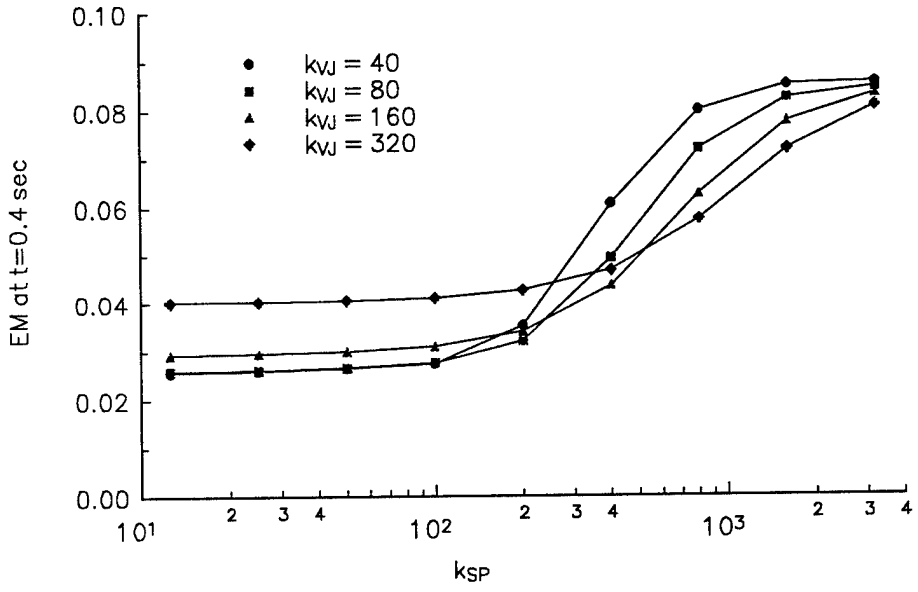

Figure 8.4 EM at t=0.4, Pulse Disturbance on Beam 2

decreases. A very high value of k_{SP} will not allow any joint motion and thus no energy can be dissipated. Note that as k_{SP} becomes very large, the curves converge. Low values of k_{SP} allow more energy dissipation by allowing more joint motion. However, a low value of k_{SP} may not be desirable due to the possibility of sticking away from the origin.

The ability of the semi-active joint to dissipate energy in the free-free architecture is less than that in the pinned-pinned system. Closed loop eigenvalues are shown in Table 8.1 for a pinned-pinned system and a free-free system each with a viscous joint. The modal damping is clearly higher for the pinned-pinned system modes. (The very low damping for the 109 rad/sec mode of the free-free system will be addressed in the next section.) The geometric constraints of the pinned-pinned system (all pin joints tied to ground) result in a higher effectiveness for the semi-active joint.

Table 8.1 Eigenvalues for Beam Systems with a Viscous Joint

Pinned-Pinned System $k_{VJ} = 75$		Free-Free System $k_{VJ} = 160$, $k_{SP} = 100$	
ζ_j	ω_j	ζ_j	ω_j
.159	23.4	.022	20.0
.022	79.4	.037	56.9
1	82.8	1	62.3
.364	127.	6.9×10^{-6}	109.
.066	221.	.017	192.
1.	344.	.014	293.
.199	501.	.020	614.
		1.	6413.

8.4 Controllability Assessment

The performance of the viscous joint in the free-free architecture is less than desired. The joint is not very effective in dissipating vibrational energy, particularly for high values of k_{SP}. This trend was explained in the previous section as stemming from the fact that a stiffer spring allows less joint motion and thus the semi-active joint can do less dissipative work. Stated another way, the modes become less controllable as k_{SP} increases. In this section, the loss of performance with increasing k_{SP} will be approached from a controllability viewpoint. Two measures of controllability are developed and then applied to the free-free beam system.

Controllability is often viewed as a binary quantity, either a system is controllable or it is uncontrollable. In practice, however, one has to be concerned with the degree of controllability. The fact that a system is controllable is of little practical significance if the feedback gains necessary to achieve good performance are unreasonably large. One measure of controllability is the controllability index [52], [65]. The controllability matrix for a linear time-invariant system is given by

$$[C] = \left[B \mid AB \mid A^2B \mid \ldots \mid A^{n-1}B \right] . \tag{8.31}$$

The partial controllability matrix is defined as

$$\left[C_q\right] = \left[B \mid AB \mid A^2B \mid \ldots \mid A^{q-1}B \right] , \quad 1 \le q \le n . \tag{8.32}$$

The controllability index is then the smallest value of q which gives n independent columns in $[C_q]$. According to Brogan [52], a smaller value of the controllability index represents "a stronger degree of controllability in some sense." For the case of single input systems (which are controllable), the controllability index is always n. Since the joint controller is a single input system, an alternate measure is needed to assess the effect of k_{SP} on controllability.

Since vibration theory develops equations of motion in terms of modes, the concept of modal controllability is particularly relevant. A system described by

$$\underline{\dot{x}} = [A]\underline{x} + [B]\underline{u} \tag{8.33}$$

can be transformed to the block diagonal (or Jordan) form,

$$\underline{\dot{x}}_D = [A_D]\underline{x}_D + [B_D]\underline{u} \tag{8.34}$$

using a similarity transformation in which

$$\underline{x} = [T]\underline{x}_D \tag{8.35}$$

where the columns of [T] are formed from the real and imaginary parts of the eigenvectors of [A]. Since the vibratory modes of the beam all have complex conjugate eigenvalues, the Jordan block of the j^{th} mode will have the form

$$\begin{bmatrix} \dot{x}_{D1j} \\ \dot{x}_{D2j} \end{bmatrix} = \begin{bmatrix} -\sigma_j & \omega_j \\ -\omega_j & -\sigma_j \end{bmatrix} \begin{bmatrix} x_{D1j} \\ x_{D2j} \end{bmatrix} + \begin{bmatrix} B_{Dj} \end{bmatrix} \underline{u} \ , \tag{8.36}$$

where the complex conjugate eigenvalue pair is

$$-\sigma_j \pm i\omega_j \ . \tag{8.37}$$

For the beam system which has zero natural damping and one input (M_f), (8.36) reduces to

$$\begin{bmatrix} \dot{x}_{D1j} \\ \dot{x}_{D2j} \end{bmatrix} = \begin{bmatrix} 0 & \omega_j \\ -\omega_j & 0 \end{bmatrix} \begin{bmatrix} x_{D1j} \\ x_{D2j} \end{bmatrix} + \begin{bmatrix} b_{D1j} \\ 0 \end{bmatrix} M_f \ . \tag{8.38}$$

The controllability matrix for the system in (8.38) is

$$[C] = \begin{bmatrix} b_{D1j} & 0 \\ 0 & -\omega_j b_{D1j} \end{bmatrix}, \tag{8.39}$$

thus the system is controllable if $b_{D1j} \neq 0$ and $\omega_j \neq 0$. Assume we wish to alter the modal dynamics using state feedback of the form

$$M_f = -\begin{bmatrix} k_1 & k_2 \end{bmatrix} \begin{bmatrix} x_{D1j} \\ x_{D2j} \end{bmatrix}. \tag{8.40}$$

The closed loop modal dynamics will have natural frequency and damping given by

$$\omega_{CLj} = -b_{D1j} k_2 \omega_j + \omega_j^2 \tag{8.42}$$

$$\zeta_{CLj} = \frac{b_{D1j} k_1}{2\sqrt{-b_{D1j} k_2 \omega_j + \omega_j^2}} . \qquad (8.41)$$

To achieve a desired level of damping while keeping the natural frequency constant requires,

$$k_1 = 2 \zeta_{CLj} \frac{\omega_j}{b_{D1j}}, \quad k_2 = 0 . \qquad (8.43)$$

Therefore, k_1 increases proportionally to ω_j/b_{D1j}, or

$$k_1 \propto \frac{\omega_j}{b_{D1j}} . \qquad (8.44)$$

The first measure of controllability (CM_1) will thus be

$$CM_1 = \text{abs}\left(\frac{\omega_j}{b_{D1j}}\right), \qquad (8.45)$$

which represents the amount of gain necessary to achieve a desired level of damping. Another approach to choosing feedback gains is to require the roots to lie on (or to the left of) the σ=-a line in the s plane. This requires that

$$k_1 \geq 2\,a \frac{1}{b_{D1j}} . \qquad (8.46)$$

In this case k_1 increases proportionally with $1/b_{D1j}$ and thus the second measure of

controllability is

$$CM_2 = \text{abs}\left(\frac{1}{b_{D1j}}\right). \tag{8.47}$$

The rationale in choosing these controllability measures is that the degree of modal controllability is directly related to the magnitude of the gain required to place the eigenvalues in desired locations. The lower the controllability measure, the easier it is to place the eigenvalues.

For the free-free beam system, the controllability measures for several modes are plotted versus a normalized spring stiffness in Figures 8.5 and 8.6. A model consisting of 4 modes for beam 1 and 7 modes for beam 2 was used to generate the controllability measures. As expected, all modes become less controllable as k_{SP} increases. Note the particular difficulty in controlling the 3rd mode (modes not plotted lie within the range shown by modes 1, 5, 7, and 9). This is the 109 rad/sec mode with practically zero damping in Table 8.1. Even at low values of k_{SP} this mode is still relatively difficult to control. By examining the eigenvectors of [A], it can be seen that the 3rd mode of the two beam system is predominantly composed of the 1st mode of beam 1 (η_{11}) and the second mode of beam 2 (η_{22}). These individual modes have natural frequencies close to each other and thus when excited produce very little joint motion, even in the absence of the joint spring.

When designing a structure to include joint damping, the beam geometries should

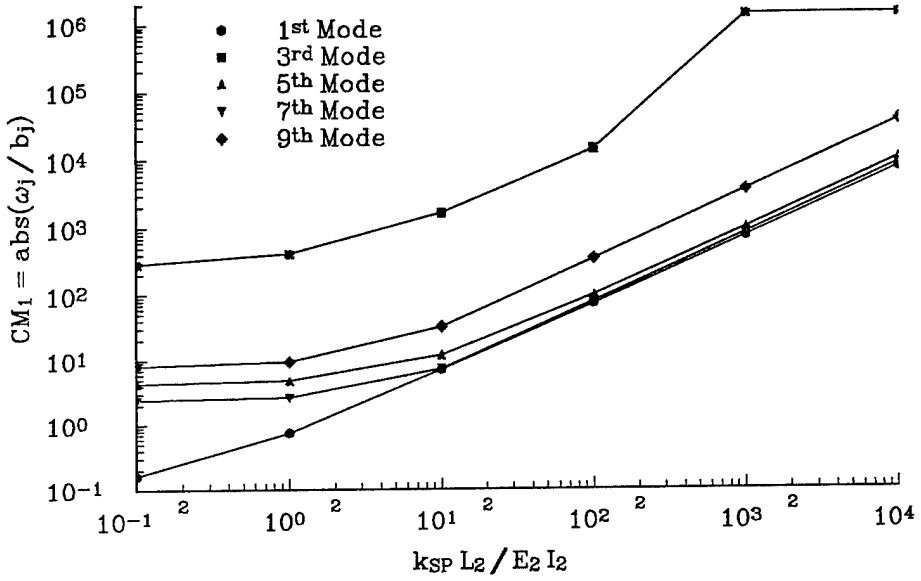

Figure 8.5 CM_1 for Nominal Free-Free Beam System

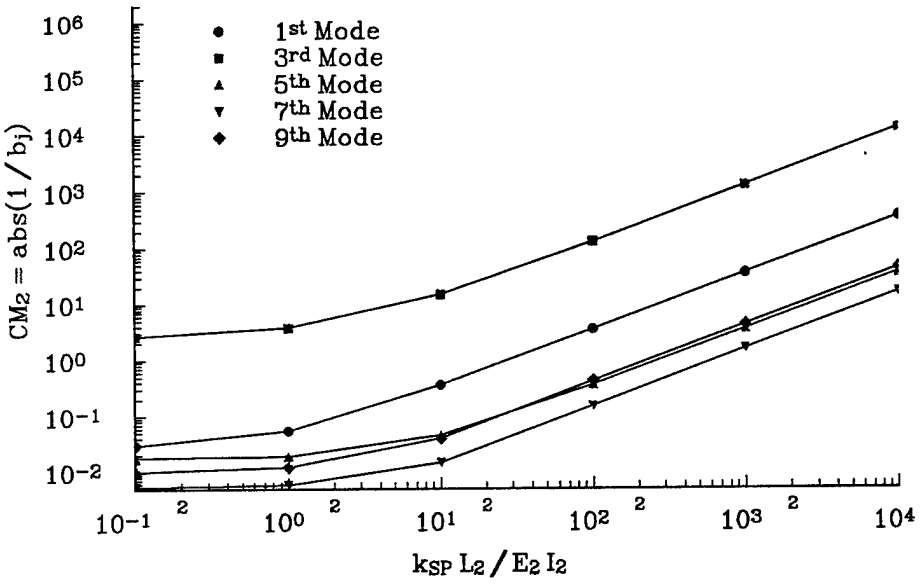

Figure 8.6 CM_2 for Nominal Free-Free Beam System

be chosen to avoid the frequency overlap described above. This is particularly important at the lower frequencies. By changing the length of beam 2 from 1.8 meters to 3.0 meters, the 3rd mode controllability indices were reduced to be in line with the other modes. Controllability measures for the L_2=3.0 meter case are shown in Figures 8.7 and 8.8. (Modes not plotted lie within the ranges shown.)

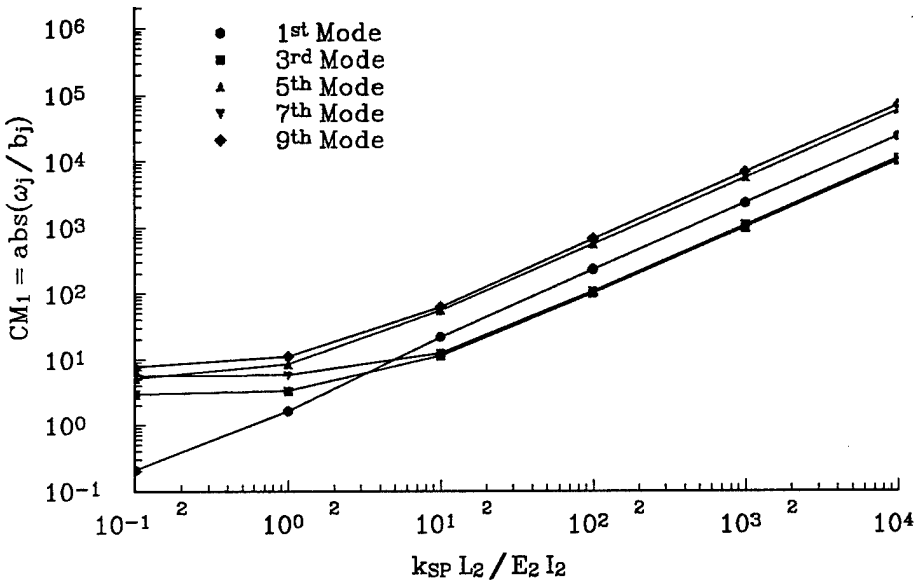

Figure 8.7 CM_1 for Free-Free Beam System with L_2 = 3 m

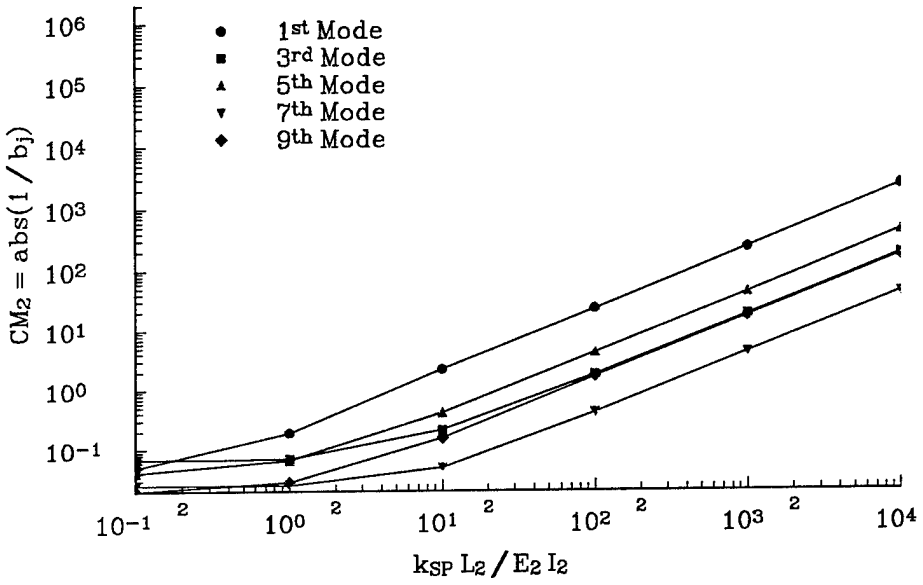

Figure 8.8 CM_2 for Free-Free Beam System with L_2 = 3 m

CHAPTER IX

SEMI-ACTIVE FRICTION DAMPING FOR SUSPENSION CONTROL PART 1: EXPERIMENTAL ASSEMBLY

9.1 Introduction

The previous chapters investigated the use of semi-active friction damping to control vibrations in flexible beams. The results thus far were obtained using computer simulations. In this and the following chapter, the semi-active friction damping concept is applied to an automotive suspension system. Performance data is generated using a scale model of a suspension system. Following a brief discussion of semi-active suspension system literature, the semi-active friction based suspension control system is introduced, followed by a description of the quarter car experimental setup. Experimental data is presented in Chapter 10.

In recent years, active and semi-active suspension systems have begun appearing on commercially available automobiles. Although only recently available to the public, the concept of active suspension systems has been a topic of research since the late 60's [66], [67]. References [68] - [71] are indicative of the current research trends in active suspension systems. The thrust of the research is to develop optimal and sub-optimal

techniques for defining the suspension force based on the available feedback quantities. Semi-active suspension systems in which the properties of a passive suspension element are actively controlled have also been the subject of research [45], [50], [72], [73]. These studies focus on defining a resistive force to produce desired ride quality and handling effects. The anticipated device for implementing the controllable resistive force is often a hydraulic damper with a variable orifice. In order to improve the performance of semi-active suspension systems, Hac' and Youn [74] have investigated using preview control. In this case, road irregularities are measured in front of the vehicle and this information is utilized by the controller to prepare the system for the oncoming input. The optimal semi-active preview controller was shown to be the clipped optimal active preview controller.

9.2 Suspension Control Using Semi-Active Friction Damping

Before proceeding, it is instructive to introduce the model and nomenclature most often used in suspension system design literature. Shown in Figure 9.1 is a two degree of freedom system representing a 1/4 car model, or one of the four suspension systems on an automobile. The upper mass, m_s, represents a portion of the car body weight and is referred to as the car body or sprung mass. The lower mass, m_u, represents the weight of the suspension elements (A-frame, wheel, rotor, brakes, etc.) and is referred to as the wheelset mass or unsprung mass. Between the car body and wheelset are the suspension

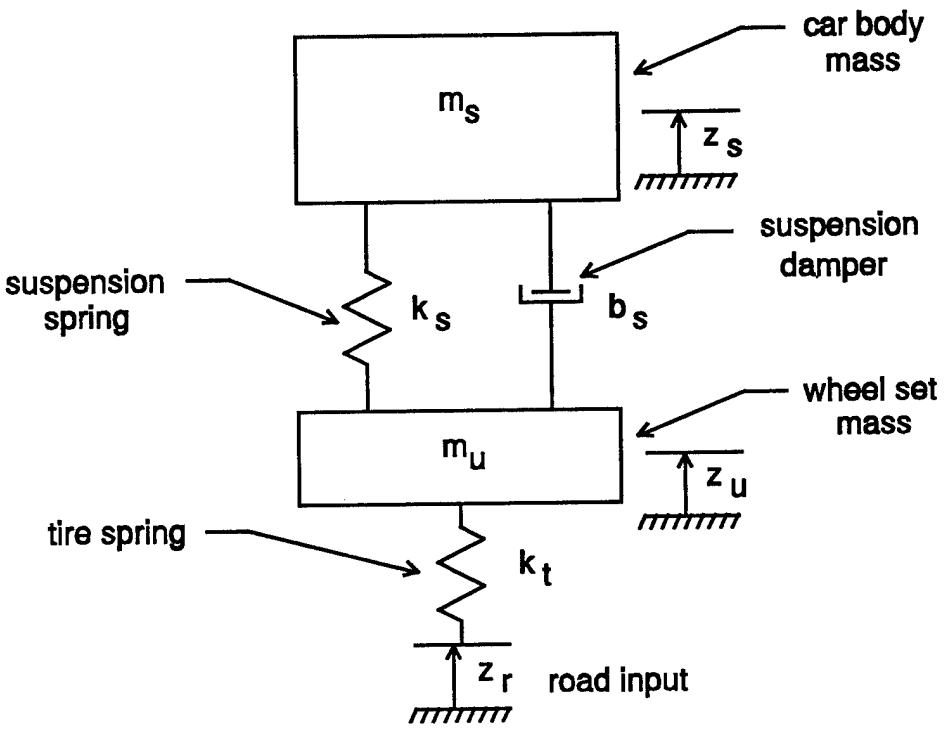

Figure 9.1 1/4 Car Model

spring (k_s) and a viscous damper (b_s). The tire is modeled as an additional spring of stiffness k_t between the wheelset and the road. Suspension displacement and velocity refers to the relative displacement and velocity between the car body and the wheelset (i.e. $z_s - z_u$ and $\dot{z}_s - \dot{z}_u$, respectively). Suspension force is the force applied to the two masses due to the damper. Values often cited in literature imply that the car body mass is approximately 7 times heavier that the wheelset mass and the tire spring is approximately 10 times stiffer than the suspension spring. The car body vibration mode has a resonant frequency around 1.25 hz and the wheelset mode natural frequency is approximately 11 hz.

When designing a suspension control system (or any control system) the requirements the control law place on the vibration control element should also be considered. For semi-active systems which rely on a variable orifice hydraulic damper, the bandwidth of the orifice controller needs to be quite high since the suspension force is linearly related to the relative velocity between the car body and the wheelset. The high bandwidth requirement of the orifice controller is notably evident when considering shock isolation. A vehicle encountering a pothole even at modest speeds will result in rapid changes in the suspension velocity. Since higher bandwidth control systems imply higher cost, it is desirable to keep the bandwidth requirement as low as possible. In [75], Redfield investigates using low bandwidth controllers in semi-active suspension systems. The suspension element is a variable orifice hydraulic element but the orifice control is based on car body velocity rather than suspension velocity. This assumes that the desired

suspension force is proportional to suspension velocity, with the proportionality constant varying at a low frequency. This work, however, fails to consider the shock isolation properties of the system, one of the key factors resulting in high bandwidth controllers.

An alternative approach to suspension control was introduced by Ferri and Heck in [76]. Their approach involved using a semi-active friction damper for vibration control. Figure 9.2 shows a 1/4 car model with the semi-active friction element. The normal force, N, is controllable. The three control laws shown in Figure 9.3 were investigated. Similar to the two beam viscous joint controller, control law 1 emulates a viscous damper. Using control law 3, effective damping and shock isolation were achieved. The normal force (and thus the suspension force) are low frequency variables since the control law includes the low pass filters. Shock isolation occurs due to the limiting of the normal force in the control law. To implement this force saturation feature in a hydraulic damper would require either the orifice bandwidth to be high enough to respond to the changing velocity (i.e. high bandwidth) or some type of bypass valve which will open when the cylinder pressure reaches a predetermined value. The decoupling of the suspension force from the suspension velocity is the clear impetus for pursuing the semi-active friction damper concept.

It is beyond the scope of this research to determine whether the semi-active friction damper, the high bandwidth hydraulic damper, of the low bandwidth hydraulic damper with a pressure relief valve is the best choice when considering all the performance, manufacturing, and cost issues. The goal of this research is to validate the

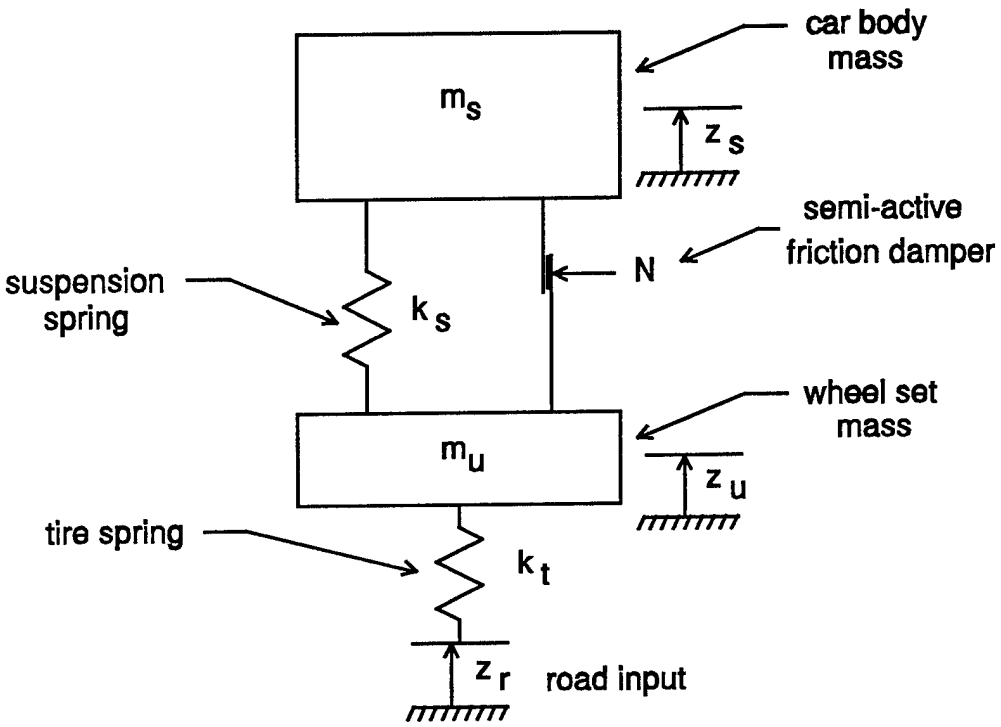

Figure 9.2 1/4 Car Suspension with Semi-Active Friction Damper

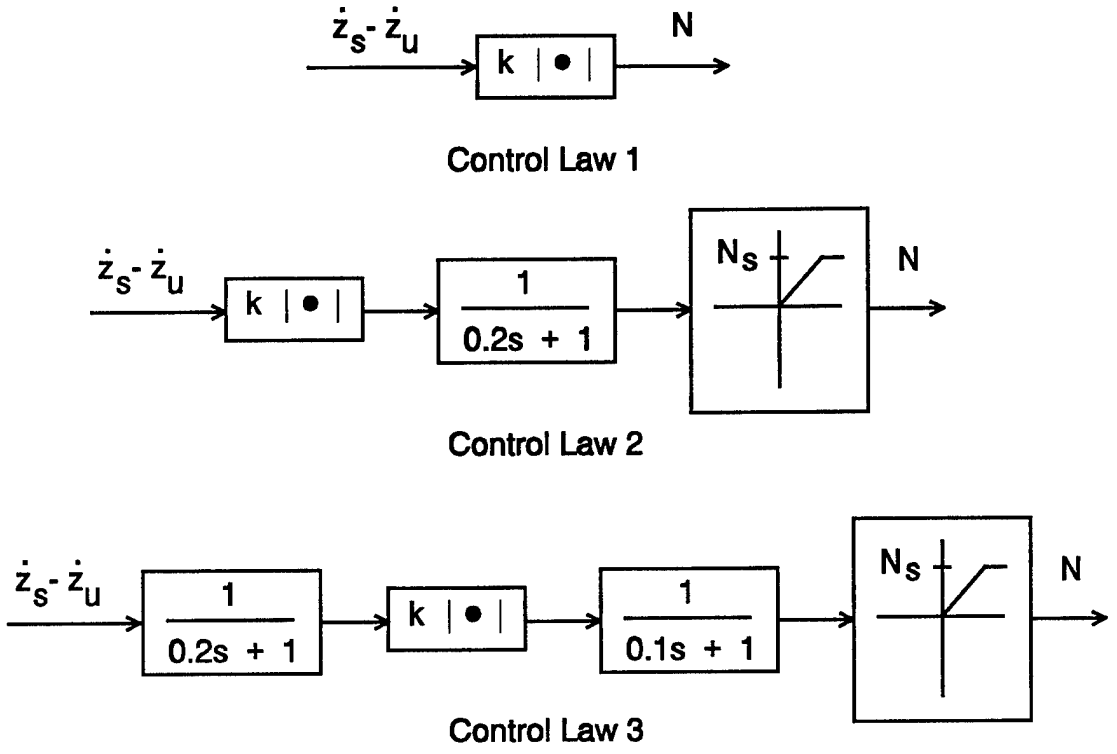

Figure 9.3 Quarter Car Control Laws

concept of using semi-active friction damping in vehicle suspension systems using a scale model, quarter car assembly. This research objective is achieved by accomplishing the following tasks:

1) Design a scale model, quarter car assembly which includes a semi-active friction damper.

2) Demonstrate the shock isolation properties of the semi-active friction damper.

3) Demonstrate effective suspension control using a low bandwidth controller.

9.3 Quarter Car Scale Model Assembly

9.3.1 Quarter Car Assembly

The purpose of the quarter car scale model hardware is to provide a platform on which to study the feasibility of the semi-active friction damping concept. Shown in Figure 9.4 is the quarter car assembly and all of the associated electronics. In this section the system level attributes of the experimental apparatus will be described. The subsystems which compromise the entire assembly will be discussed in the following sections.

Shown in Figure 9.5 is the quarter car assembly which includes the car body and wheelset masses, the suspension and tire springs, the semi-active friction damper (or clutch), sensors, guide rails, road displacement actuator, and the frame. The car body mass weighs 2.06 kg and the wheelset mass weighs 0.55 kg. Car body mode and

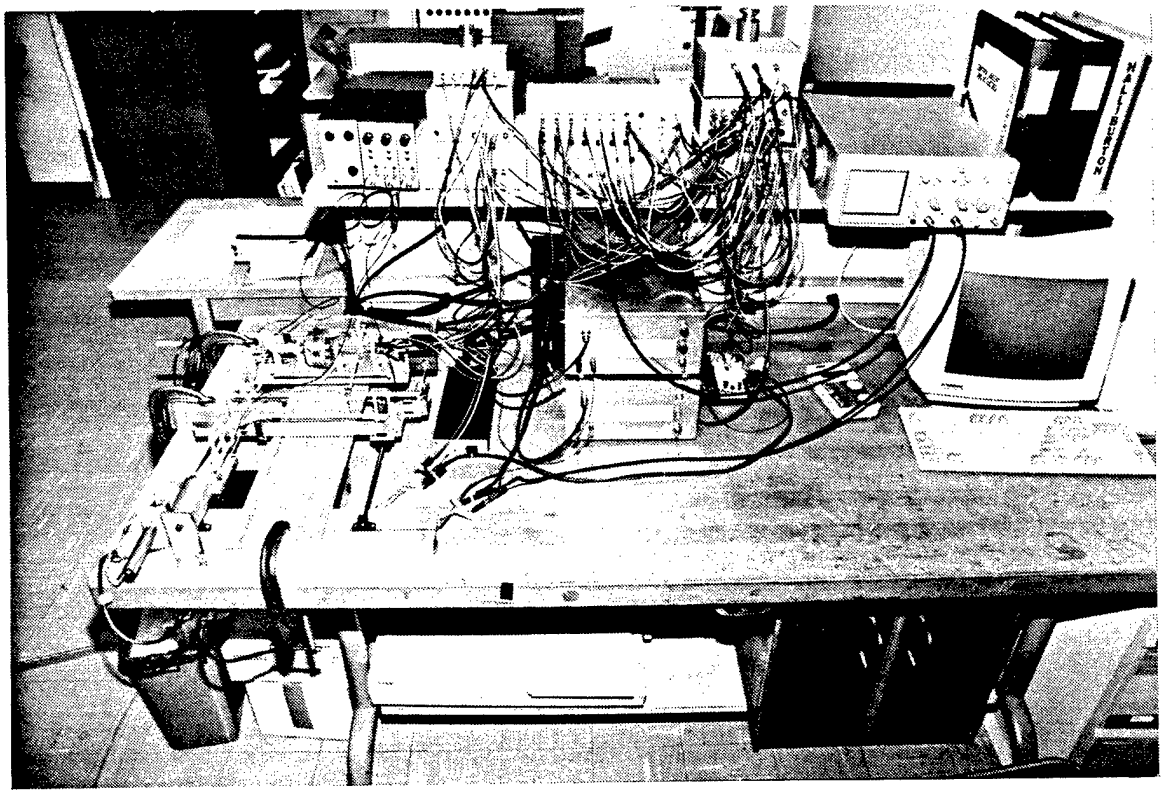

Figure 9.4 Quarter Car Experimental Setup

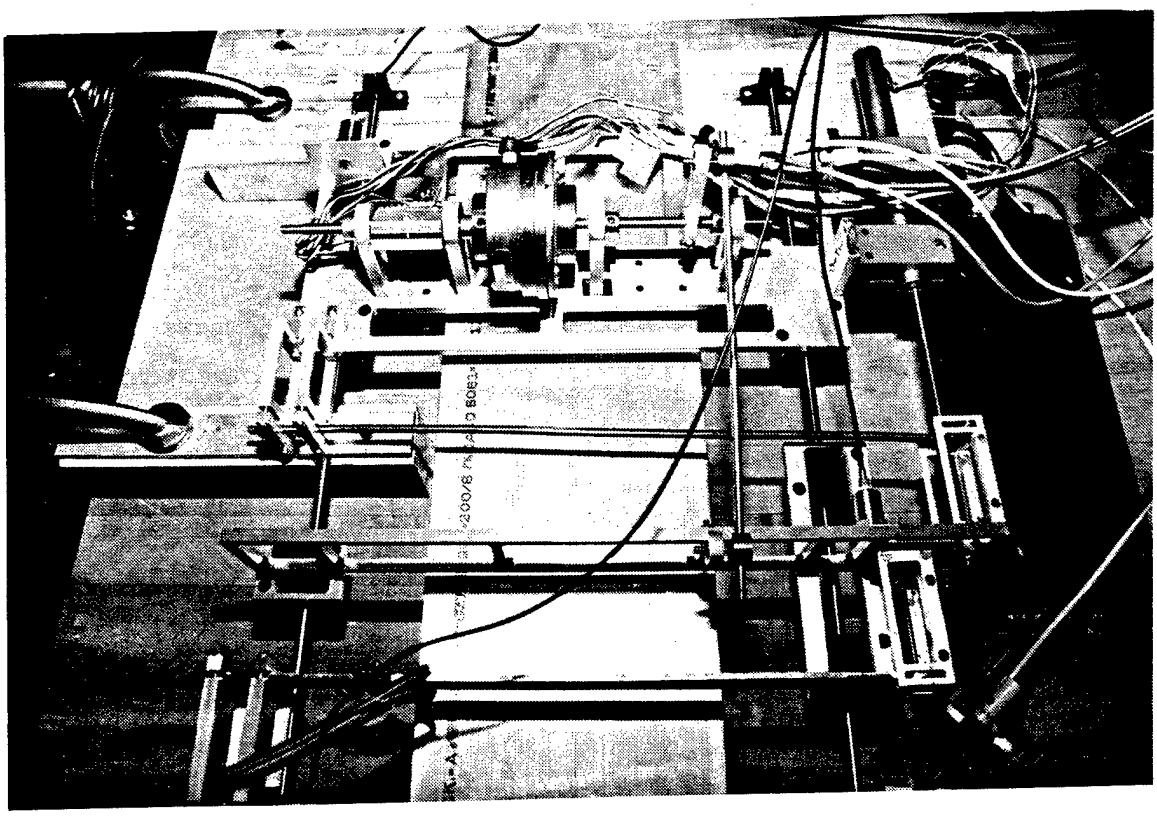

Figure 9.5 Car Body and Wheel Set Assembly

wheelset mode natural frequencies were measured at 1.25 hz and 8.5 hz respectively. Undamped frequency response data from the road displacement to the suspension deflection is shown if Figure 9.6. Using the mass and resonant frequency data, the suspension spring and tire spring stiffness were calculated to be 140 N/m and 1420 N/m, respectively. The ratio of the car body mass to wheelset mass is 3.8 rather than the desired value of 7. Adding an additional 1.75 kg to the car body mass and stiffening the springs (to maintain the resonant frequencies) would have resulted in the clutch being undersized. The undersizing of the clutch was viewed as more detrimental to the goal of validating the semi-active damper concept than was the low ratio between the masses, thus the current configuration was deemed acceptable.

One of the design goals was to minimize friction to the largest extent possible. To accomplish this, roller bearings are used in all shaft mountings and the masses travel on low friction linear bearings. The rail assembly (including the linear bearings) is a Thomson Industries 1BB-04-AHO double shaft end supported system. Overall length of the assembly is 0.61 m (24 in). A static coefficient of friction of 0.005 was achieved (in the linear bearings) after removing the bearing seals and replacing them with clearance retaining rings. The shafts are case hardened steel shafts 6.35 mm (0.25 in.) in diameter. To minimize flexing of the shafts, an additional shaft support was added between the car body and wheelset masses (see Figure 9.5).

To implement the quarter car control algorithms a Magitronic 33 Mhz, 80486 PC is used. The computer is equipped with a MetraByte DAS-16F data acquisition board.

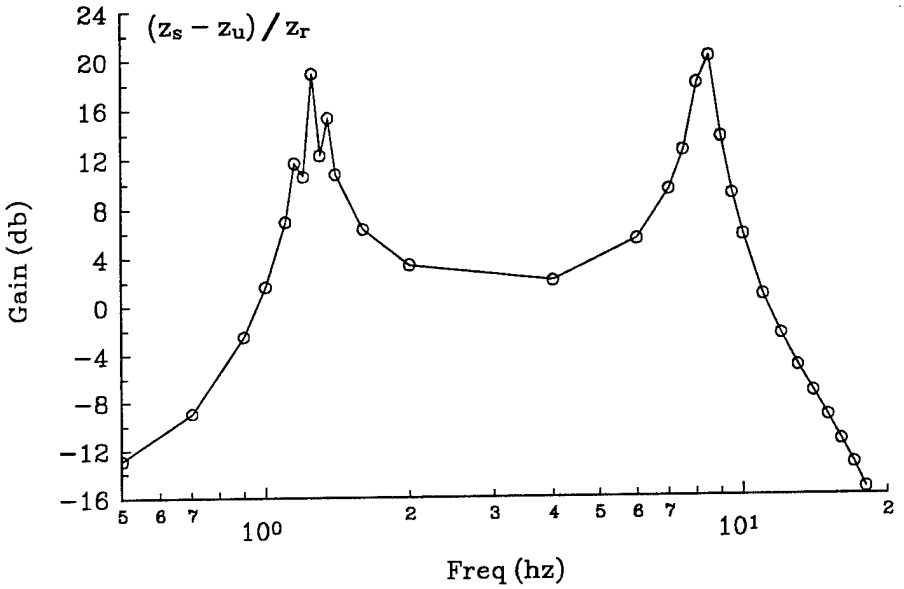

Figure 9.6 1/4 Car Open Loop Frequency Response

This board has 8 bipolar (or 16 single ended) analog input channels, 2 analog output channels, 4 digital input channels, and 4 digital output channels. The peak sample rate is 100,000 samples per second. A programmable clock on the data acquisition board is used for timer control when running the control software in real time. The quarter car software is written in the C programming language using the Borland C/C++ compiler.

9.3.2 Control Structure

A passive friction damper would give poor suspension control due to the stick-slip motion present in systems in which the normal force is a constant. The semi-active friction damper eliminates this by controlling the normal force at the frictional interface. In an ideal frictionally damped system, the suspension force is proportional to the normal force, thus controlling one controls the other. In reality, however, it is desirable to control suspension force directly since the friction parameters may vary. Suspension control is achieved by correctly controlling the suspension force, not the normal force at the frictional interface. In Figure 9.2 the suspension force is generated by a prismatic frictional interface. In the quarter car experiment an electromagnetic clutch is used to generate the frictional resistance force. Figure 9.7 shows a quarter car model with a clutch, crank, and connecting rod assembly. The equations of motion for the quarter car system shown in Figure 9.7 are as follows,

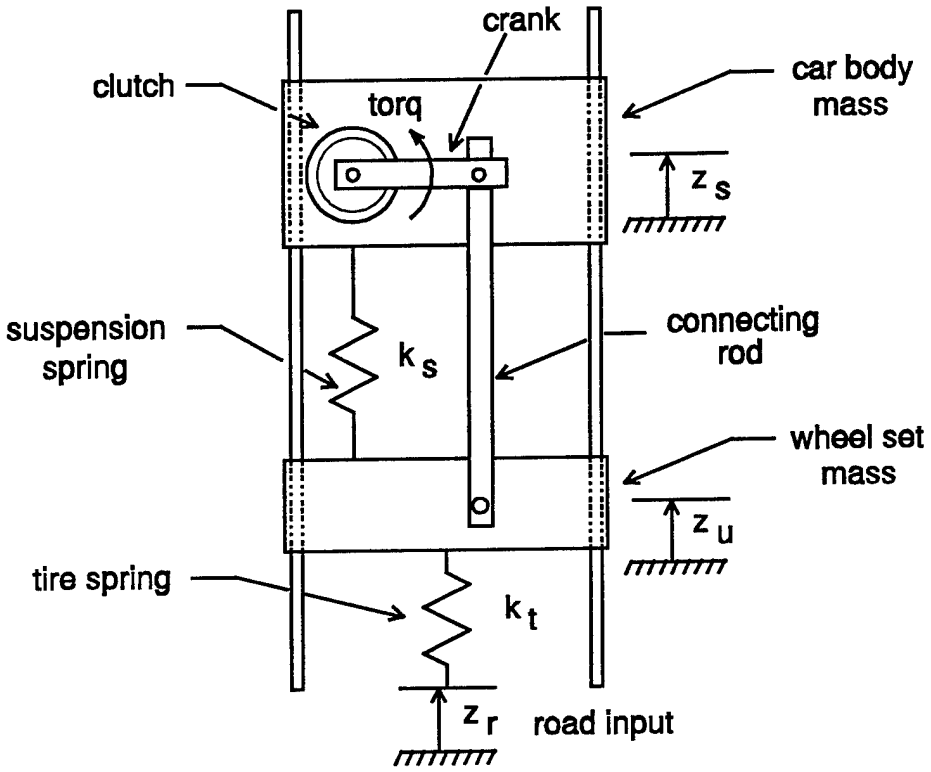

Figure 9.7 1/4 Car Model with Semi-Active Friction Clutch

$$\begin{bmatrix} \dot{z}_s - \dot{z}_u \\ \ddot{z}_s \\ \dot{z}_u - \dot{z}_r \\ \ddot{z}_u \end{bmatrix} = \begin{bmatrix} 0 & 1 & 0 & -1 \\ -\frac{k_s}{m_s} & 0 & 0 & 0 \\ 0 & 0 & 0 & 1 \\ \frac{k_s}{m_u} & 0 & -\frac{k_t}{m_u} & 0 \end{bmatrix} \begin{bmatrix} z_s - z_u \\ \dot{z}_s \\ z_u - z_r \\ \dot{z}_u \end{bmatrix} + \begin{bmatrix} 0 & 0 \\ \frac{1}{m_s}\frac{\partial \theta_c}{\partial z_s} & 0 \\ 0 & -1 \\ \frac{1}{m_u}\frac{\partial \theta_c}{\partial z_u} & 0 \end{bmatrix} \begin{bmatrix} \text{torq} \\ \dot{z}_r \end{bmatrix}, \quad (9.1)$$

where

$$\theta_c = \cos^{-1}\left[\frac{2L_1^2 - 2L_2(z_u - z_s) + (z_u - z_s)^2}{2L_1\sqrt{L_1^2 + (L_2 - (z_u - z_s))^2}}\right] - \cos^{-1}\left[\frac{L_1}{\sqrt{L_1^2 + (L_2 - (z_u - z_s))^2}}\right]. \quad (9.2)$$

In equations (9.1) and (9.2), m_s and m_u are car body and wheelset masses, z_s and z_u are car body and wheelset displacements, k_s and k_t are suspension and tire spring stiffnesses, torq is the resistive torque of the clutch, L_1 and L_2 are the crank and connecting rod lengths, z_r is the road displacement, and θ_c is the crank angle. Controlling the suspension force is now equivalent to controlling the resistive torque generated by the clutch. The suspension control task is thus segregated into two sub-tasks: 1) determine the desired clutch torque and 2) vary the voltage on the clutch coils to control clutch torque. This control structure is shown in Figure 9.8.

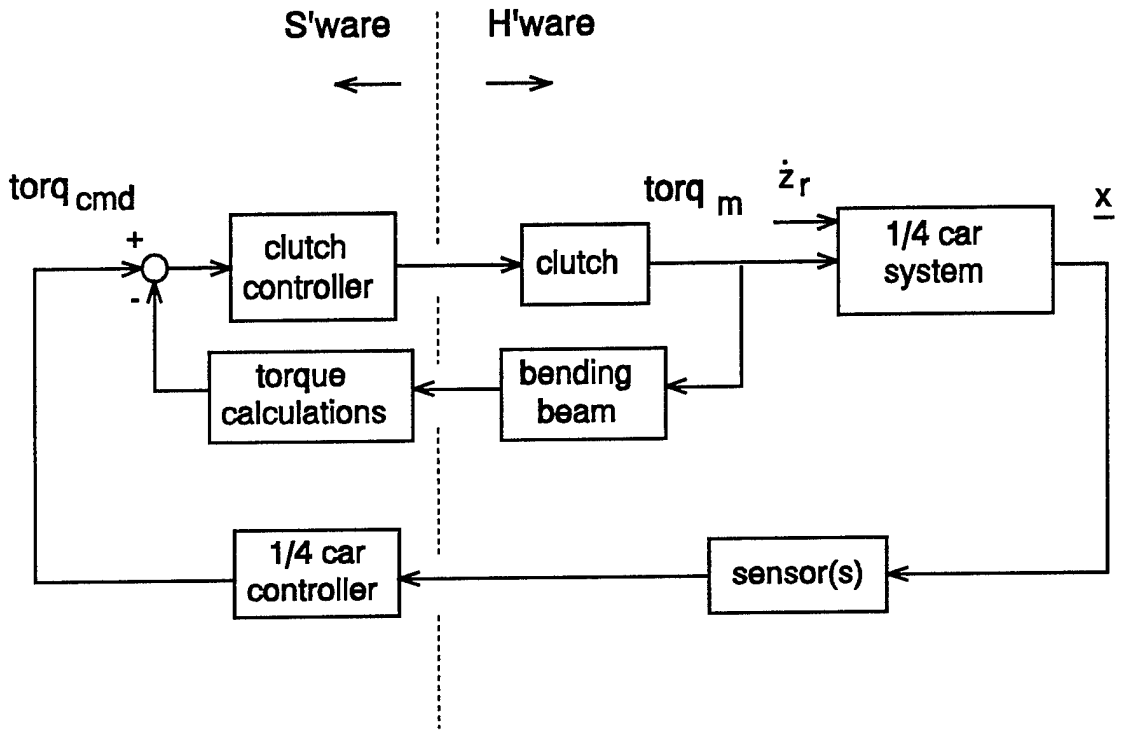

Figure 9.8 Control System Structure

The quarter car control algorithms in Figure 9.8 generate the desired resistive torque based on current system parameters. The control laws shown in Figure 9.3 are applicable here except that instead of calculating a normal force, the result is the resistive torque command. The clutch used to generate the resistive torque is an Electroid Company TS-BEC-30CC-8-8-24V-T electromagnetic clutch. This is a tensioning series clutch with a hard, carbon faced material at the frictional interface designed to operate in the continuous slip mode. The clutch is designed to give a linearly increasing torque with increasing coil voltage. The clutch has a mass of 0.97 kg (2.1 lbm) and generates a peak torque of 0.9 N-m (8 in-lbf). Response time (time from start of coil energizing to reaching 90% of rated torque) is approximately 35 milliseconds. To control clutch torque, a simple feedback loop is used. In order to implement the feedback loop, a measurement of the actual torque is needed. This is provided from four strain gages (in a bridge configuration) attached to a bending beam as shown in Figure 9.9. The output of the strain gage bridge is amplified before being filtered by an anti-aliasing filter and sampled by the data acquisition board. The amplifier boosts the strain gage bridge output to give approximately 3.8 V output per 1 N-m of torque. Figure 9.10 shows the torque control loop in detail. The power amplifier in Figure 9.10 amplifies the board output from a $0 \leftrightarrow 5$ V range to a $0 \leftrightarrow 28$ V range and also supplies the current required by the coil. Closed loop frequency response data is shown in Figures 9.11 and 9.12.

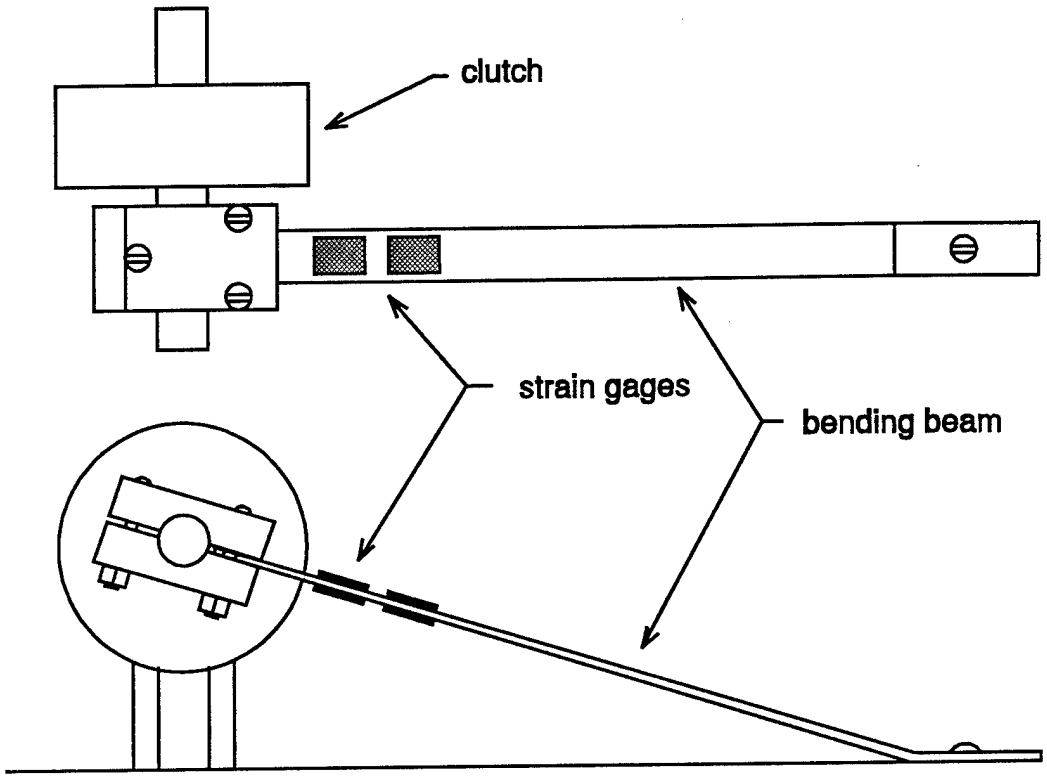

Figure 9.9 Torque Measurement Bending Beam

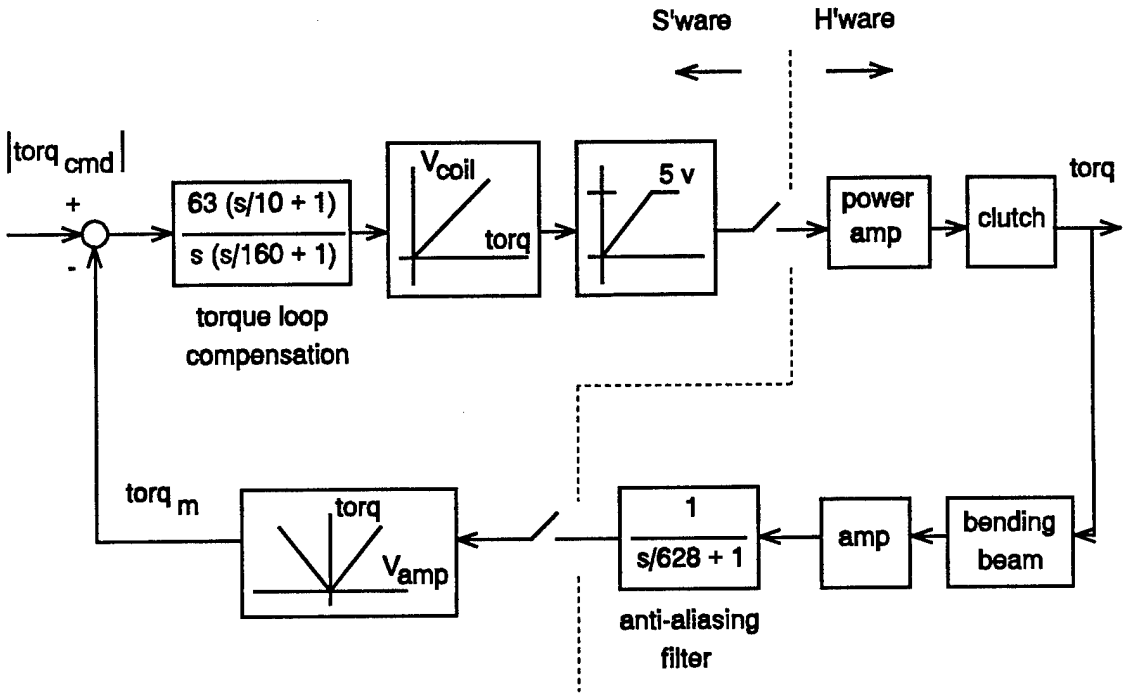

Figure 9.10 Torque Control Loop

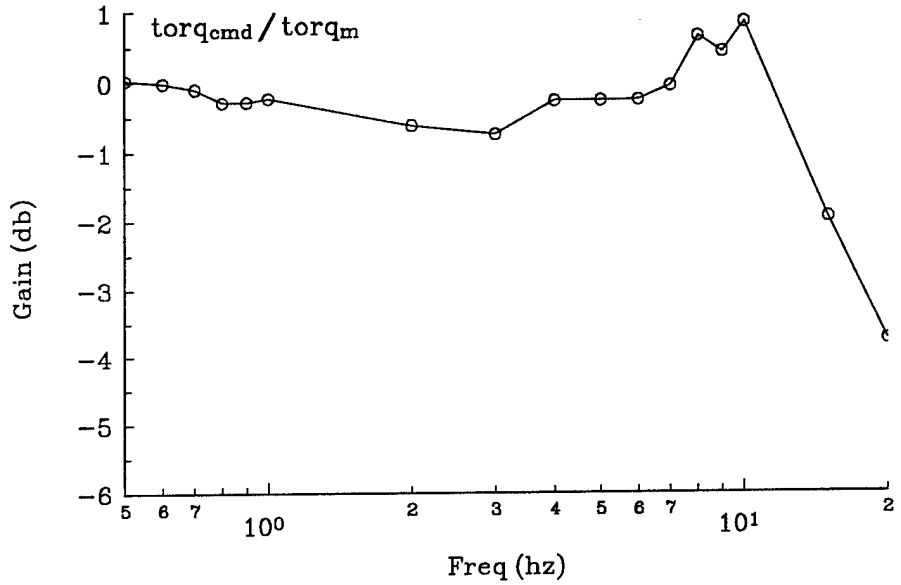

Figure 9.11 Torque Control Closed Loop Frequency Response Gain

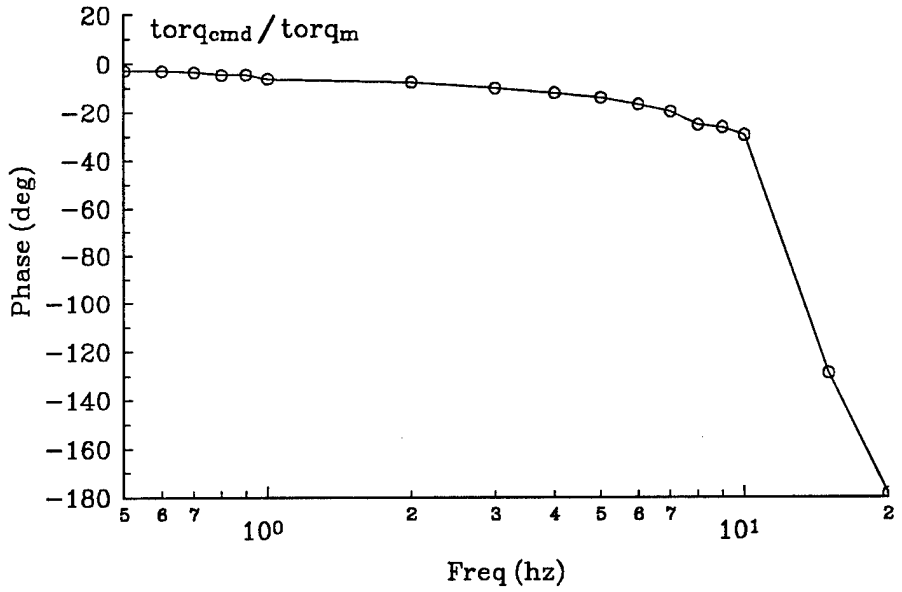

Figure 9.12 Torque Control Closed Loop Frequency Response Phase

9.3.3 Road Input Assembly

Disturbances are input to the quarter car system by the road actuator. The road actuator is a model 10-0.5-1 electromagnetic actuator manufactured by Aura Systems, Incorporated. Total linear travel of the actuator is 14.6 mm (0.57 in) and the maximum rated force is 44.5 N (10 lbf). To allow custom road profiles to be input to the quarter car system, a road control loop was designed. This control loop is shown in Figure 9.13. Measurement of the road displacement is from a Schaevitz Type E-1000 LVDT and an ATA-101 Analog Transducer Amplifier. Since the road actuator receives extension and retraction commands, processing is done on the $0 \leftrightarrow 5$ V output of the data acquisition board to convert it to a $-5 \leftrightarrow 5$ V range. This bipolar signal is then sent to a power amplifier with a gain of 5.26. It is important to note that when frequency response data is presented in later sections, the input is the measured road displacement, not the commanded road displacement. This ensures that gain and phase errors in the road control loop do not influence suspension performance data.

9.3.4 Sensors

In addition to the sensors required for torque and road control, several other sensors have been incorporated into the quarter car test setup. Accelerometers are mounted on the car body and wheelset masses as well as the road input. The accelerometers are Brüel & Kjær Type 4382. Each accelerometer has a Type 2651 charge

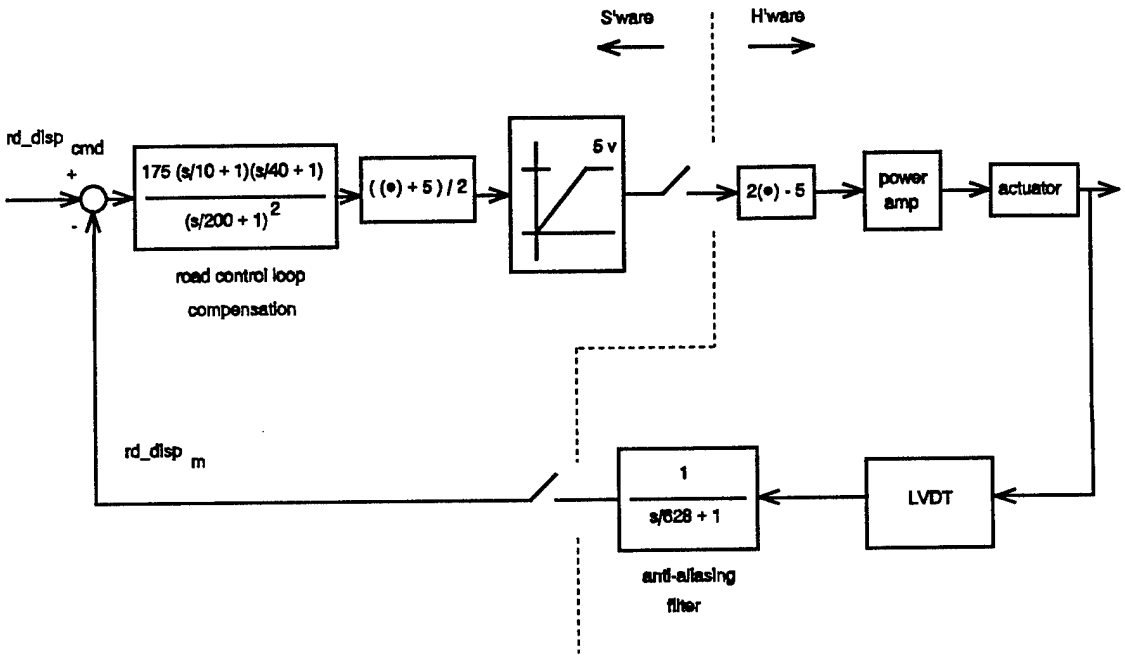

Figure 9.13 Road Control Loop

amplifier which are powered by a Type 2805 power supply. The car body accelerometer signal is amplified x15 and the wheelset and road input accelerometer signals are amplified x7. The amplified signals are then passed through anti-aliasing filters and sampled by the data acquisition board.

All three control laws shown in Figure 9.3 base the suspension force (or torque) on the suspension velocity. Suspension velocity is determined by numerically differentiating the suspension deflection. Suspension deflection is measured by an LVDT with the coil housing attached to the car body mass and the magnetic core attached to the wheelset mass. This LVDT is a Schaevitz Type E-1000 LVDT with an ATA-101 Analog Transducer Amplifier. Since the output of the LVDT amplifier is in the ±10 V range, no additional amplification is necessary before the signal is filtered by an anti-aliasing filter and sampled by the data acquisition board.

A key performance measure in suspension systems is the tire deflection. Large tire deflections are undesirable because they represent large changes in the traction force between the tire and the road. To measure tire deflection, four strain gages (in a bridge configuration) are attached to the fixed end of the tire spring. The output of the bridge is amplified to give an output of 2.7 V per 10 mm of tip deflection. This signal is then filtered by and anti-aliasing filter and sampled by the data acquisition board.

Performance measures for suspension systems typically involve many of the system states. Figure 9.14 shows all of the currently available system states. As shown in the figure, some are measured variables and others are derived from measurements.

Measured States

State	Measurement Device
Car Body Acceleration	Accelerometer
Wheel Set Acceleration	Accelerometer
Road Acceleration	Accelerometer
Road Displacement	LVDT
Tire Deflection	Strain Gage
Suspension Displacement	LVDT
Clutch Torque	Strain Gage

Derived States

State	Derived From
Car Body Displacement	Wheel Set Displacement, Suspension Displacement
Car Body Velocity	Car Body Displacement
Wheel Set Displacement	Road Displacement, Tire Deflection
Wheel Set Velocity	Wheel Set Displacement
Road Velocity	Road Displacement
Suspension Velocity	Suspension Displacement

Figure 9.14 Measured and Derived System States

In addition to the anti-aliasing filter, additional filtering is performed (in software) to remove the unwanted high frequency content from the signals. In particular, the accelerometer signals were found to contain 80 - 90 hz data resulting from structural vibrations of the various plates and structures in the setup. This high frequency data is removed by a 4^{th} order Chebyshev filter with a 25 hz passband and 0.1 db of passband ripple. The phase shift induced by the filtering does not affect the system performance since the data is not used in the real-time control algorithms but is used only for plotting and other post processing to evaluate system performance. Similarly, the other variables used only for output and post processing are filtered to allow only the relevant, low frequency (0 to 20 hz) content of the signal to influence the performance assessment.

CHAPTER X

SEMI-ACTIVE FRICTION DAMPING FOR SUSPENSION CONTROL PART 2: EXPERIMENTAL RESULTS

10.1 Introduction

The previous chapter introduced the concept of using a semi-active friction damper for automotive suspension control. A scale model quarter car assembly was also described. In this chapter experimental results which were generated using the scale model system will be presented. The goals of the experiments described in this chapter were to accomplish tasks 2 and 3 in section 9.2, i.e.:

2) Demonstrate the shock isolation properties of the semi-active friction damper.

3) Demonstrate effective suspension control using a low bandwidth controller.

In order to assess the performance of the suspension control system, several performance indices are needed. The suspension control literature contains examples of suitable indices. In [73], Miller used the following data as performance measures:

RMS Car Body Acceleration: $(\ddot{z}_s)_{RMS}$
RMS Tire Deflection: $(z_u - z_r)_{RMS}$
RMS Suspension Deflection: $(z_s - z_u)_{RMS}$.

The road input in Miller's studies is a white noise road velocity input. When designing

suspension control systems a scalar performance index is often defined by summing weighted mean squared values of the states (i.e., an index quadratic in the states). In [70], Karnopp defines two such performance indices. The first weights the tire deflection against the suspension force as follows,

$$J = \int_0^\infty \left(z_u - z_r\right)^2 + \rho F_s^2 \, dt, \tag{10.1}$$

where F_s is the suspension force and ρ is a weighting factor. The second index weights the suspension deflection against the suspension force,

$$J = \int_0^\infty \left(z_s - z_u\right)^2 + \rho F_s^2 \, dt. \tag{10.2}$$

Hrovat, et. al. in [45] define their performance index as

$$J = \int_0^\infty \left(z_s - z_u\right)^2 + \rho \ddot{z}_s^2 \, dt, \tag{10.3}$$

thus balancing suspension deflection and car body acceleration. The performance index used by Butsuen and Hedrick in [50] is

$$J = \int_0^\infty \ddot{z}_s^2 + \rho_1 \left(z_s - z_u\right)^2 + \rho_2 \dot{z}_s^2 + \rho_3 \left(z_u - z_r\right)^2 + \rho_4 \dot{z}_u^2 \, dt. \tag{10.4}$$

The performance indices reflect the tradeoff between ride quality, handling, and rattlespace or stroke length.

For the quarter car experiment, two composite performance measures were defined based on the work of Butsuen and Hedrick. The first index depends on RMS values,

$$J_{RMS} = \left(\ddot{z}_s\right)_{RMS} + \rho_1\left(z_s - z_u\right)_{RMS} + \rho_2\left(\dot{z}_s\right)_{RMS} + \rho_3\left(z_u - z_r\right)_{RMS} + \rho_4\left(\dot{z}_u\right)_{RMS}, \tag{10.5}$$

while the second depends on peak values,

$$J_{peak} = \left|\ddot{z}_s\right|_{peak} + \rho_1\left|z_s - z_u\right|_{peak} + \rho_2\left|\dot{z}_s\right|_{peak} + \rho_3\left|z_u - z_r\right|_{peak} + \rho_4\left|\dot{z}_u\right|_{peak}. \tag{10.6}$$

The RMS index is similar to that in (10.4). The peak value index is believed to have merit when assessing ride harshness. This relationship has not been correlated with test track performance; however, it is clear that peak values of the states are involved in overall system performance. The values of the weighting factors as defined in [50] are,

$$\left(\rho_1, \rho_2, \rho_3, \rho_4\right) = \left(400, 16, 400, 16\right). \tag{10.7}$$

These values are also used in (10.5) and (10.6), and should be assumed for all results given below unless otherwise stated.

Three separate road disturbance inputs were used in the experimental tests. The first two are shown in Figure 10.1. The short pulse input is generated by moving the road actuator from its retracted position to its extended position using the maximum coil voltage and then immediately reversing the coil voltage to retract to the original position. The long pulse is similar to the short pulse except that the retract command is delayed 0.4 seconds. These disturbances represent encountering a single road disturbance at

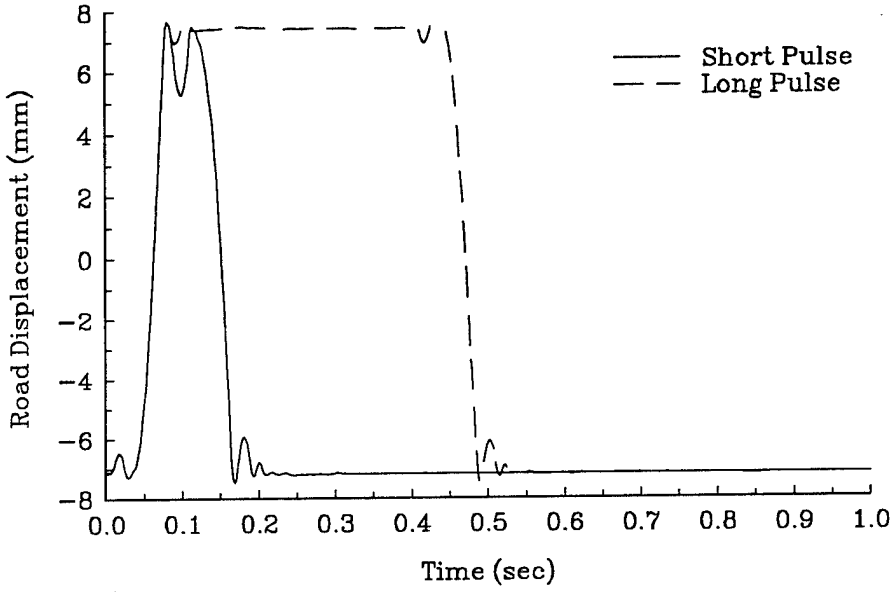

Figure 10.1 Pulse Disturbance Inputs

differing speeds. When using either of the pulse disturbances the duration of the test is 1.0 seconds. The third input is shown in Figure 10.2. This input superimposes two short pulse disturbances one second apart onto an 8.5 Hz sine disturbance of approximately 2 mm in amplitude. This input resembles a rumble strip with periodic large amplitude disturbances. When using this disturbance the duration of the test is 2.5 seconds. It should be noted that each road input will vary somewhat for differing suspension designs. The bandwidth and force capability of the road actuator are not high enough to prevent the road control loop from being influenced by the motion of the car body and wheelset masses. These differences are small and do not significantly affect the results. Figures 10.3 - 10.8 show free response data (quarter car controller inactive) for each of the three inputs described above. The figures show car body acceleration and suspension deflection, two parameters that illustrate the trade-off that must be made between ride comfort and handling. (The clipping of the suspension deflection in Figure 10.6 is due to the ±25.4 mm travel of the suspension deflection LVDT.)

The control laws investigated for suspension control were derived from those defined by Ferri and Heck in [76] (see Figure 9.3). Shown in Figure 10.9 are the control laws investigated herein. Control law 1 is a pure viscous control law. Control law 2 adds a torque command limit and control law 3 further adds a low pass filter. These control laws are intended to be a *first pass* and not a *final result* set of controllers. The objective is to validate the semi-active friction damper concept, more refined and higher performance controllers are to be the subject of future studies.

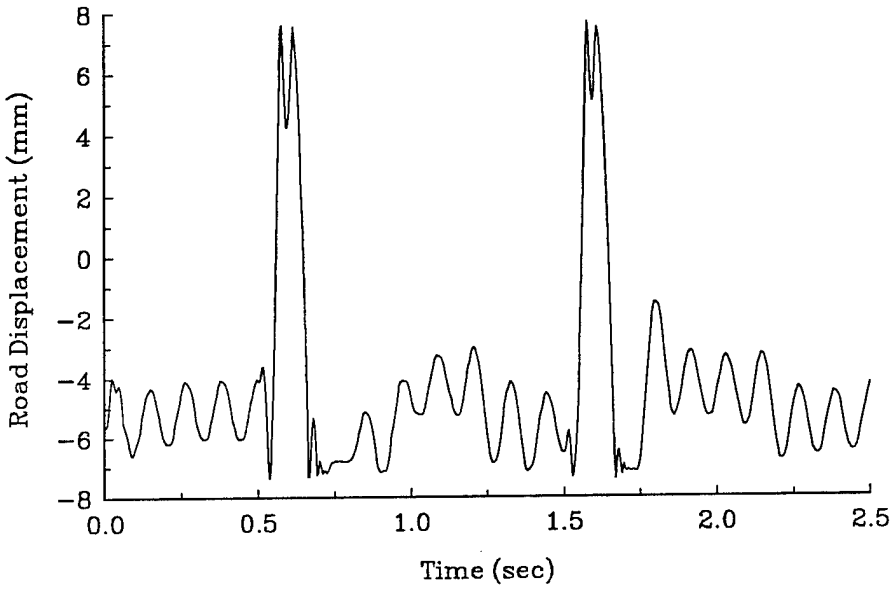

Figure 10.2 Sine + Pulse Disturbance Input

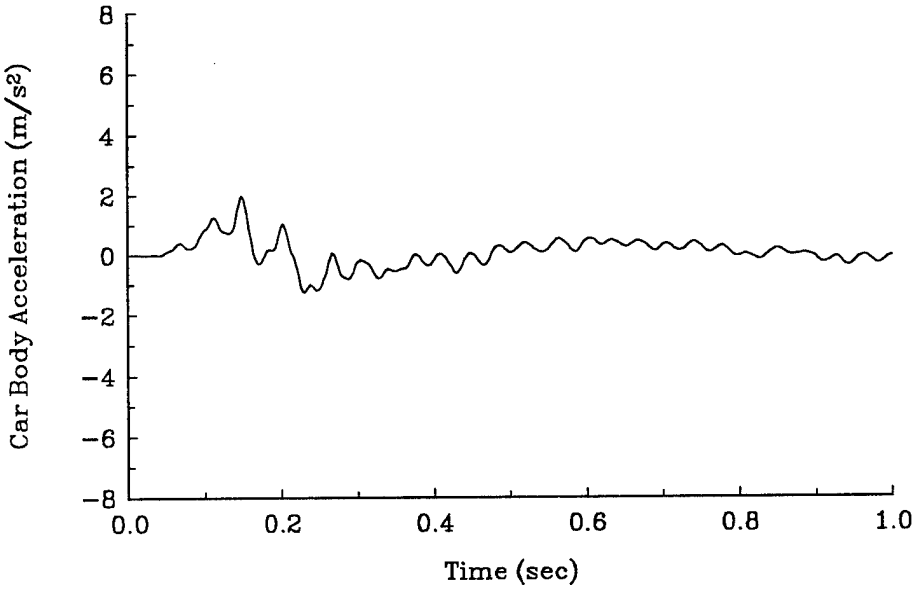

Figure 10.3 $\ddot{z}_s$ vs t, Short Pulse Free Response

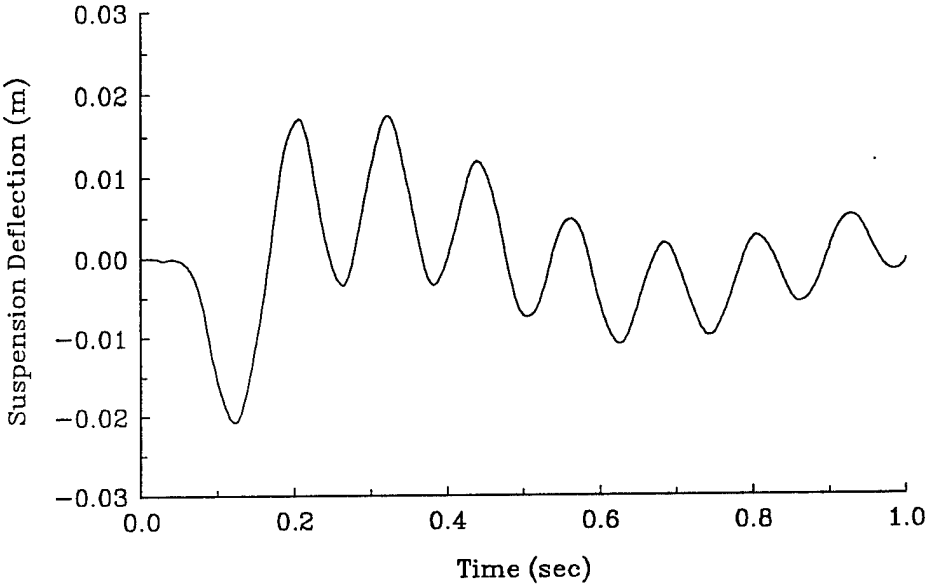

Figure 10.4 $(z_s - z_u)$ vs t, Short Pulse Free Response

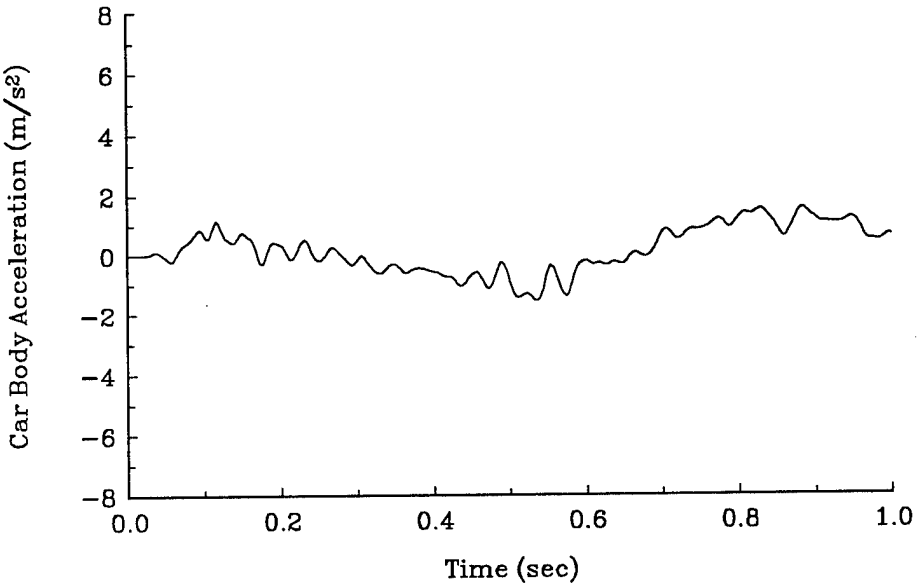

Figure 10.5 $\ddot{z}_s$ vs t, Long Pulse Free Response

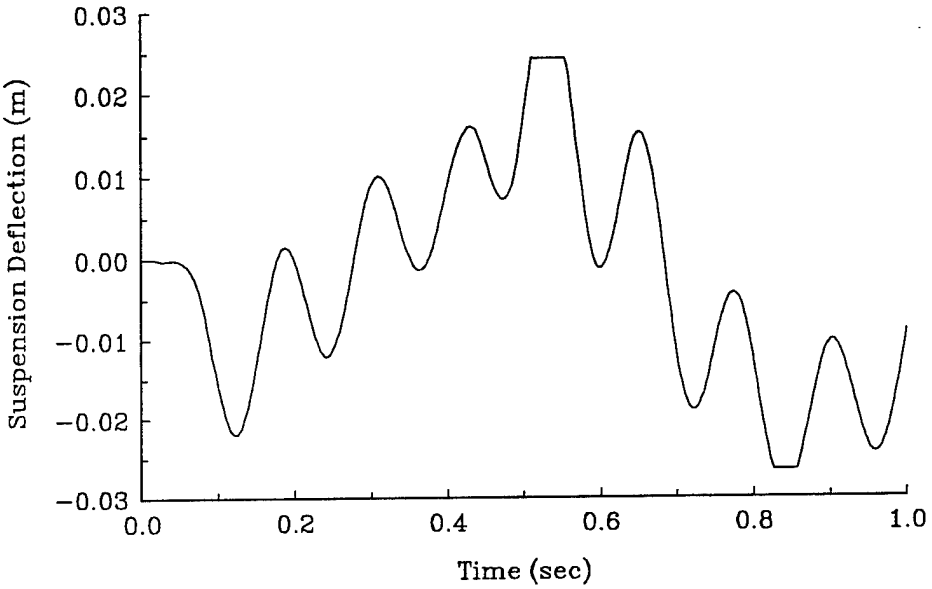

Figure 10.6 (z_s - z_u) vs t, Long Pulse Free Response

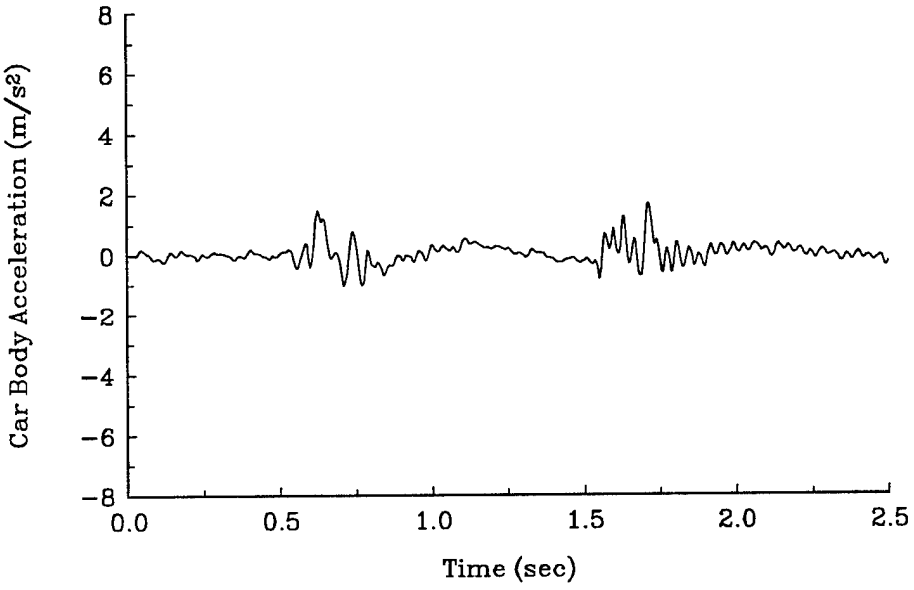

Figure 10.7 $\ddot{z}_s$ vs t, Sine + Pulse Free Response

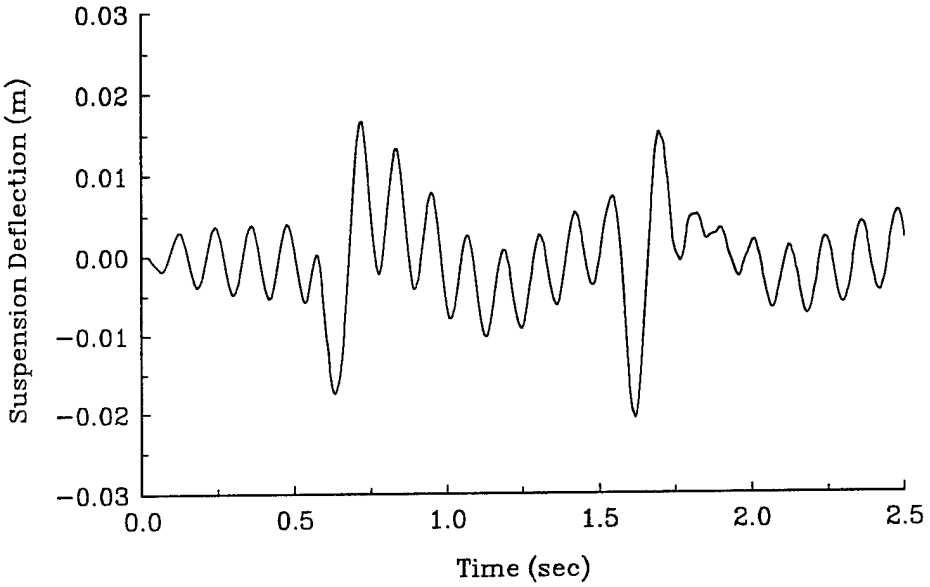

Figure 10.8 (z_s - z_u) vs t, Sine + Pulse Free Response

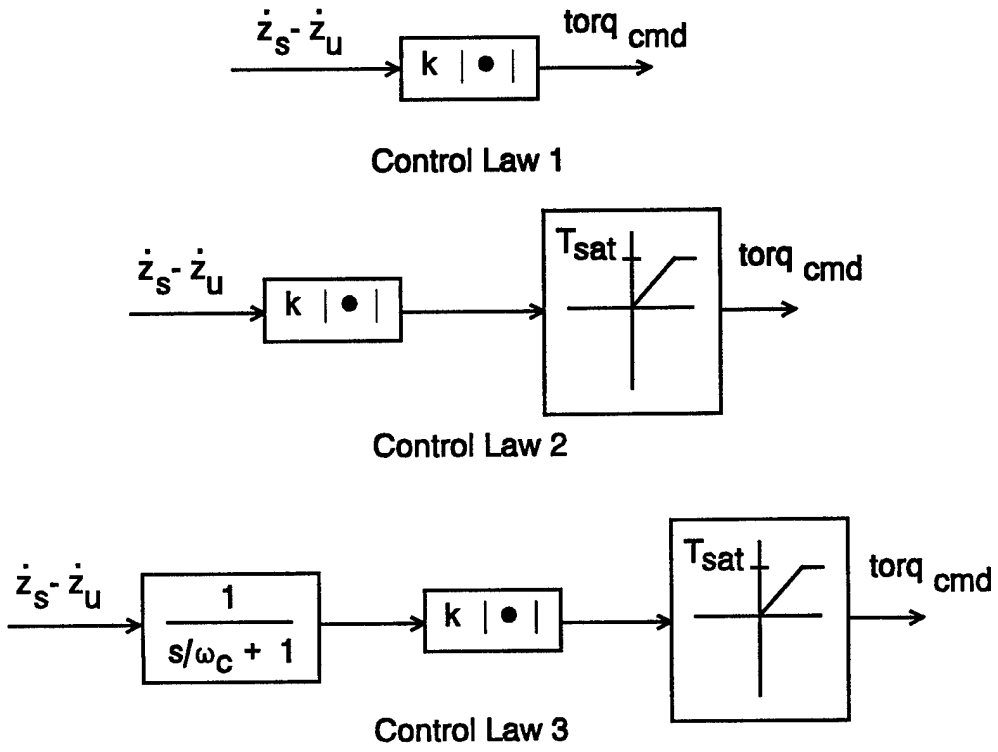

Figure 10.9 Quarter Car Control Laws

The next three sections will summarize the results of three parametric studies. In section 10.2 the gain is varied in control law 1. In section 10.3 the torque limit is varied in control law 2. In section 10.4 the cut-off or corner frequency of the low pass filter is varied in control law 3. For each of the three parametric studies, each value of the independent parameter was examined using each road input. For each road input, three runs were made and the data averaged to generate a single data point.

10.2 Parametric Study of Controller Gain

Control law 1 represents a pure viscous damper control law. In this section, performance of the suspension control system is shown as the controller gain, k, is varied. Figures 10.10 and 10.11 show J_{RMS} and J_{peak} as k is varied. Car body acceleration data is shown in Figures 10.12 and 10.13. Clearly the car body receives maximum isolation when the damper force is zero. Car body displacement RMS data is shown in Figure 10.14. The marked increase in the short pulse case for $k \geq 2.0$ is due to the clutch intermittently sticking away from the static equilibrium position. In a true viscous damper this would not occur, but with high controller gains the finite bandwidth and torque producing capability of the clutch result in intermittent sticking. Note that there is an expected tradeoff between RMS car body acceleration and displacement as k is varied; in other words car body isolation is accomplished at the expense of car body displacement. Wheelset acceleration is shown in Figure 10.15. Suspension deflection and

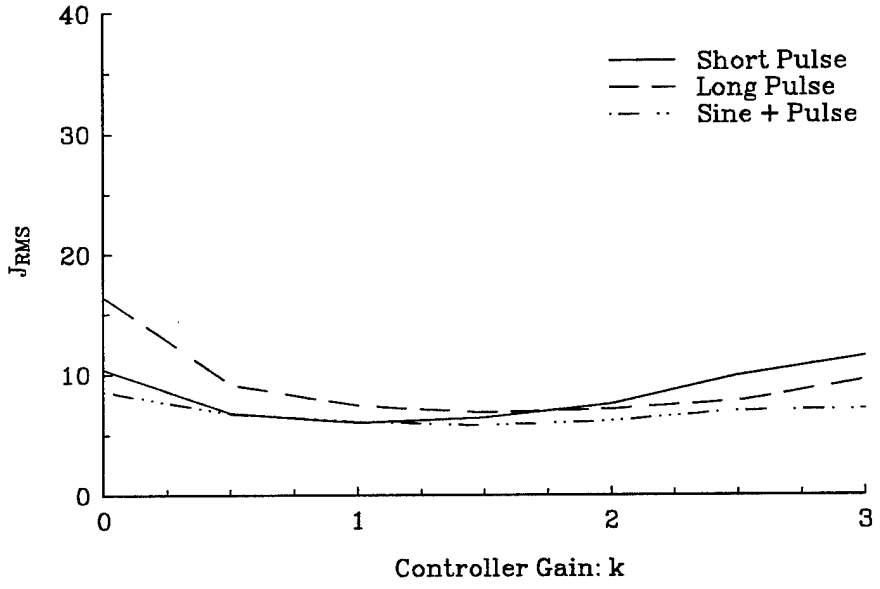

Figure 10.10 J_{RMS} vs k for Control Law 1

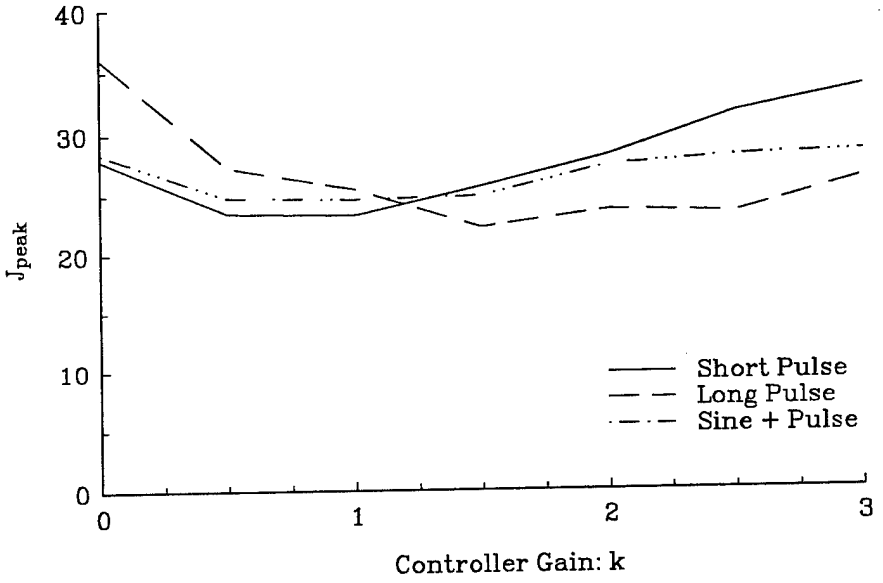

Figure 10.11 J_{peak} vs k for Control Law 1

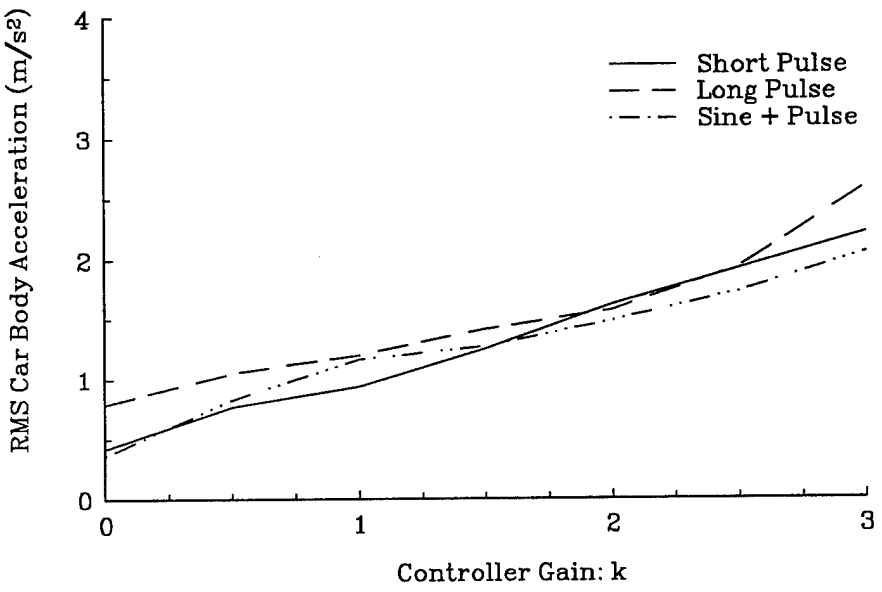

Figure 10.12 $(\ddot{z}_s)_{RMS}$ vs k for Control Law 1

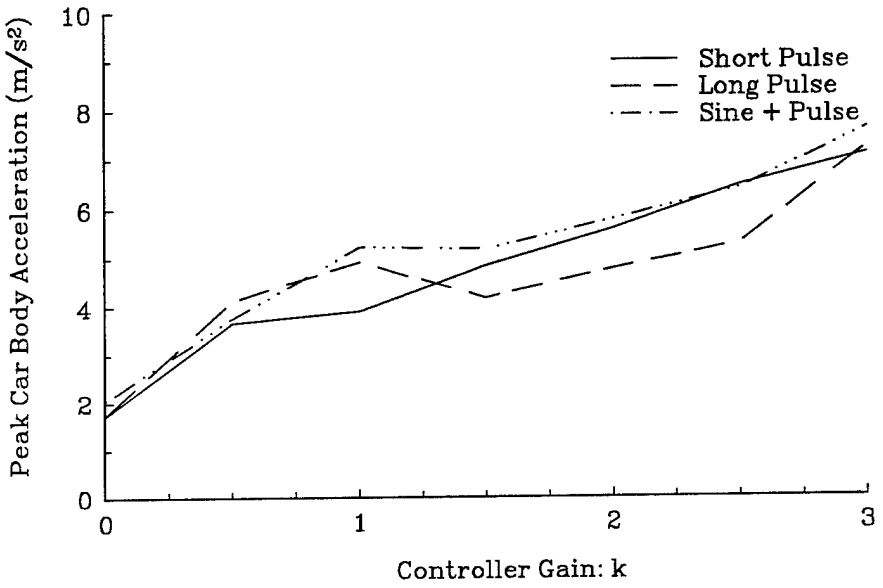

Figure 10.13 $(\ddot{z}_s)_{peak}$ vs k for Control Law 1

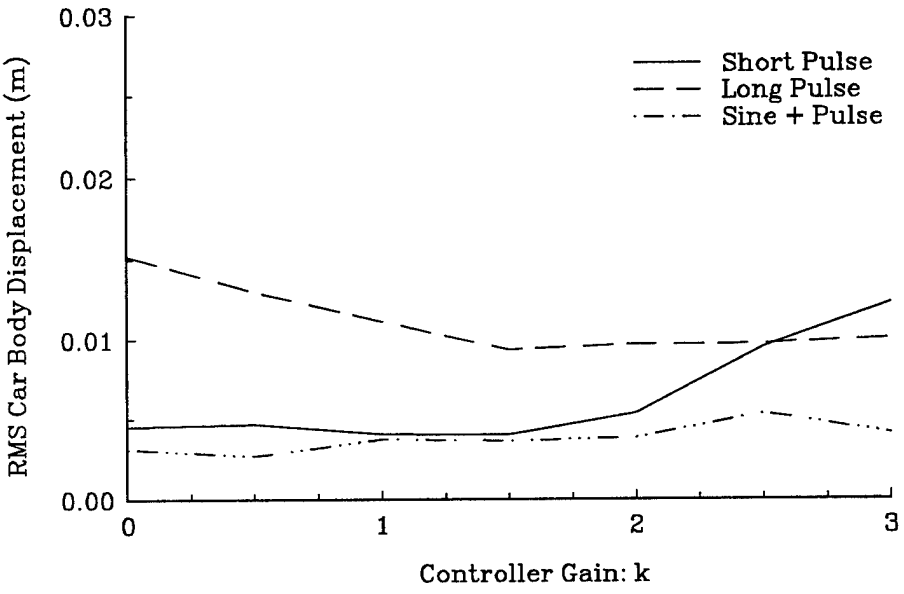

Figure 10.14 $(z_s)_{RMS}$ vs k for Control Law 1

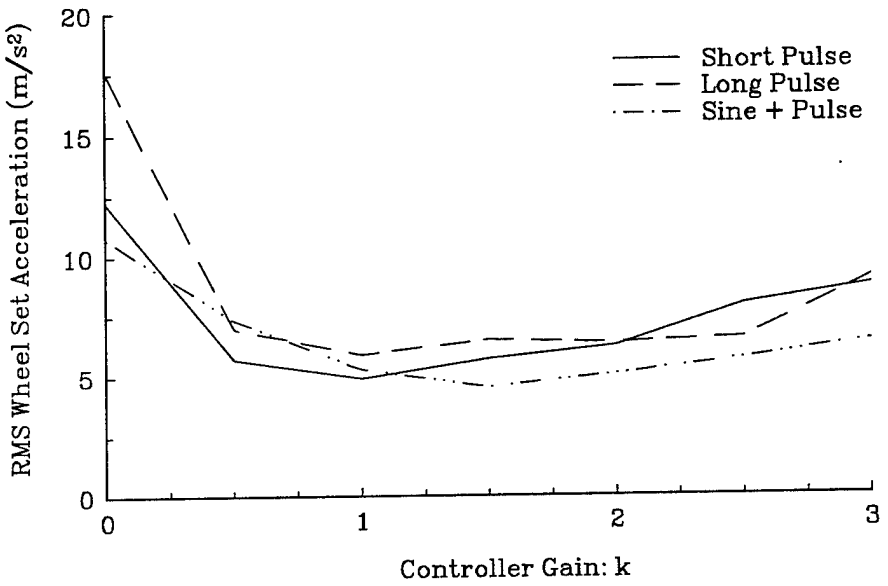

Figure 10.15 $(\ddot{z}_u)_{RMS}$ vs k for Control Law 1

tire deflection are shown in Figures 10.16 and 10.17. The previously mentioned sticking is also apparent in the suspension deflection curve. The composite performance measures in Figures 10.10 and 10.11 indicate that a value of 1.25 for k is a reasonable choice. Frequency response data from the road input to the car body and wheelset accelerations using k=1.25 is shown in Figure 10.18. Frequency response data from the road input to the suspension deflection, tire deflection, and car body displacement is shown in Figure 10.19. The frequency response curves represent the magnitude of the ratio of the indicated quantity to the amplitude of the road displacement in db. This data (as is the case for all the frequency response data herein) was generated using sine sweeps. For frequencies below 5 Hz, 10 cycles of the input were used at each frequency. For frequencies above 5 Hz, 2 seconds of the input were used at each frequency. This allows sufficient time to eliminate the effects of the transients induced by stepping the frequency. The amplitude of the sine wave is 7 mm for frequencies below 2 Hz and 2.5 mm for frequencies above 6 Hz. A linear transition occurs for frequencies between 2 Hz and 6 Hz. The higher amplitudes are desirable at the low frequencies to minimize the effects of stiction in the linear bearings. This amplitude is decreased for higher frequencies because of the very low damping of the second mode of free vibration. Time response curves of car body acceleration and suspension deflection for the three road inputs and k=1.25 are shown in Figures 10.20 - 10.25.

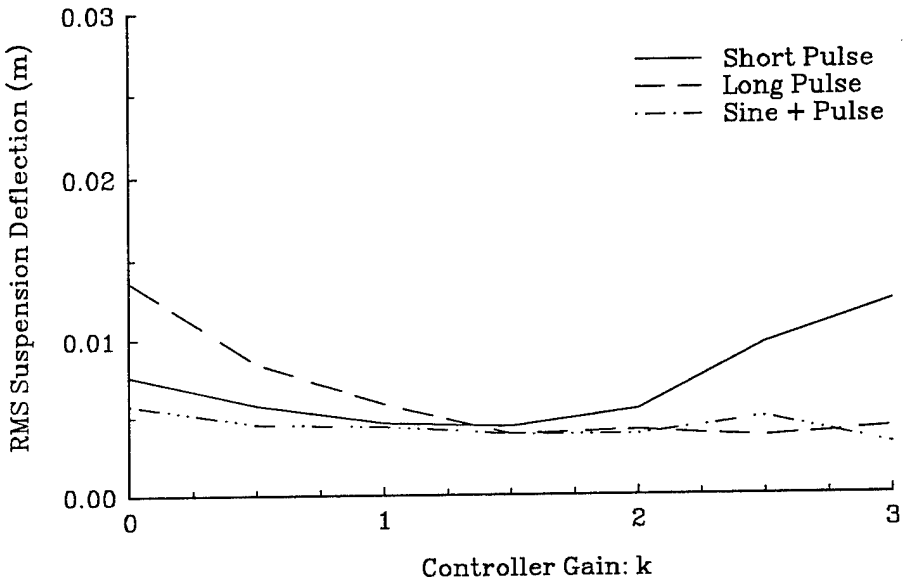

Figure 10.16 $(z_s - z_u)_{RMS}$ vs k for Control Law 1

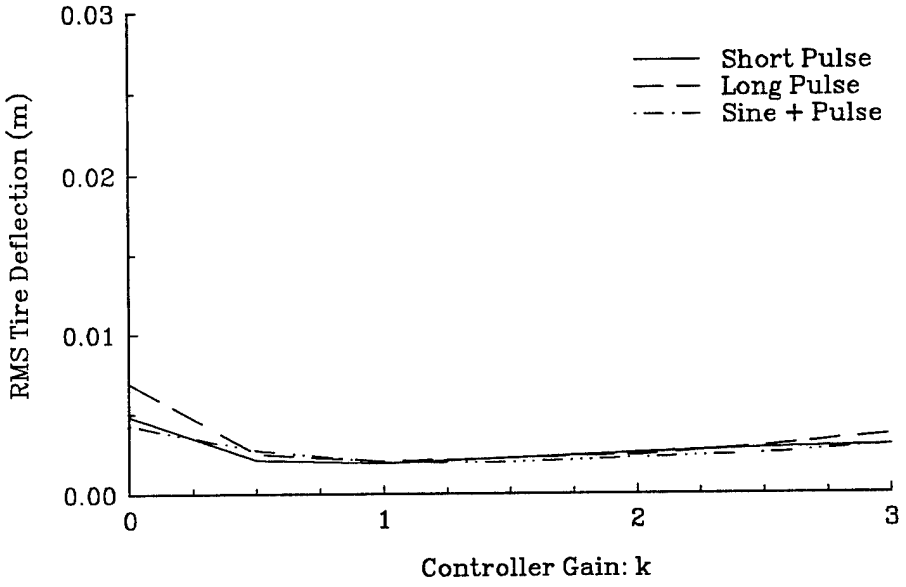

Figure 10.17 $(z_u - z_r)_{RMS}$ vs k for Control Law 1

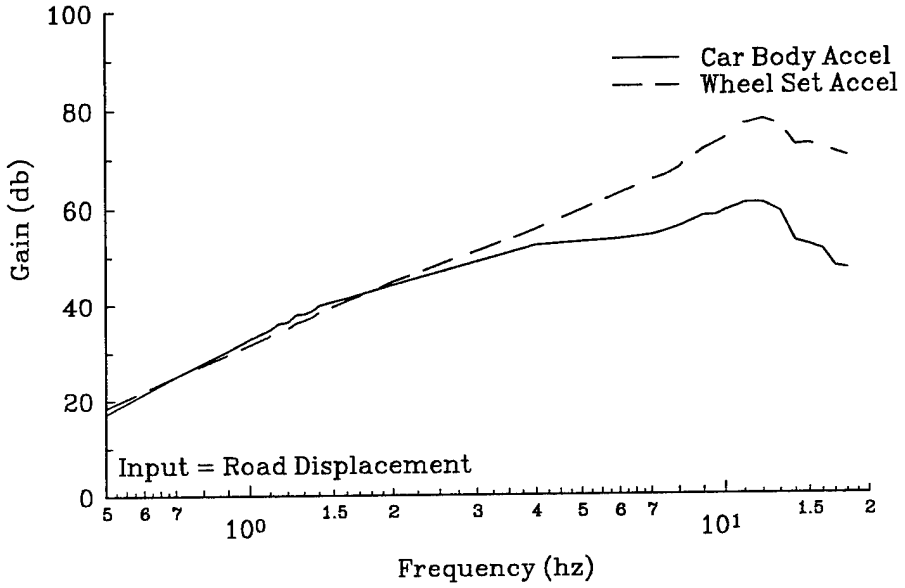

Figure 10.18 $\ddot{z}_s$, $\ddot{z}_u$ Frequency Response Data for Control Law 1

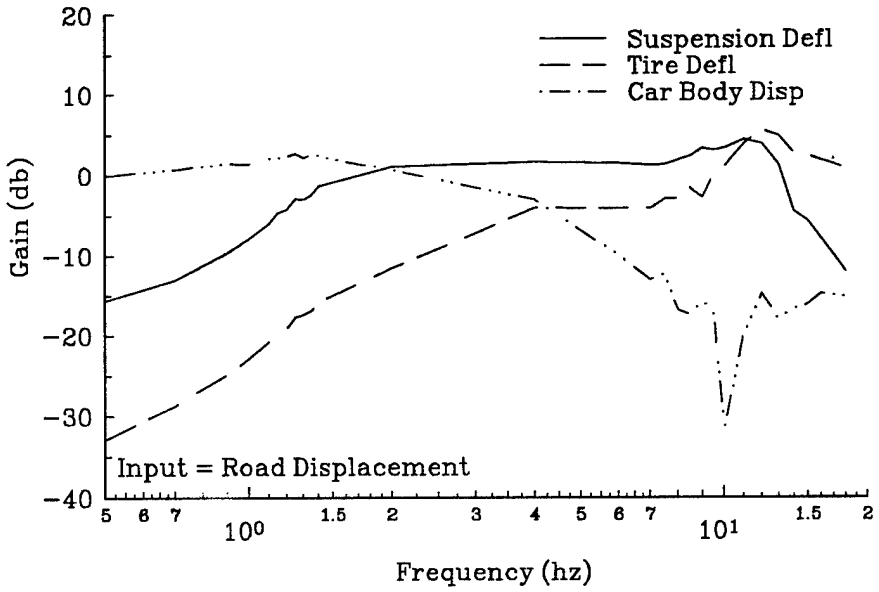

Figure 10.19 z_s-z_u, z_u-z_r, z_s Frequency Response Data for Control Law 1

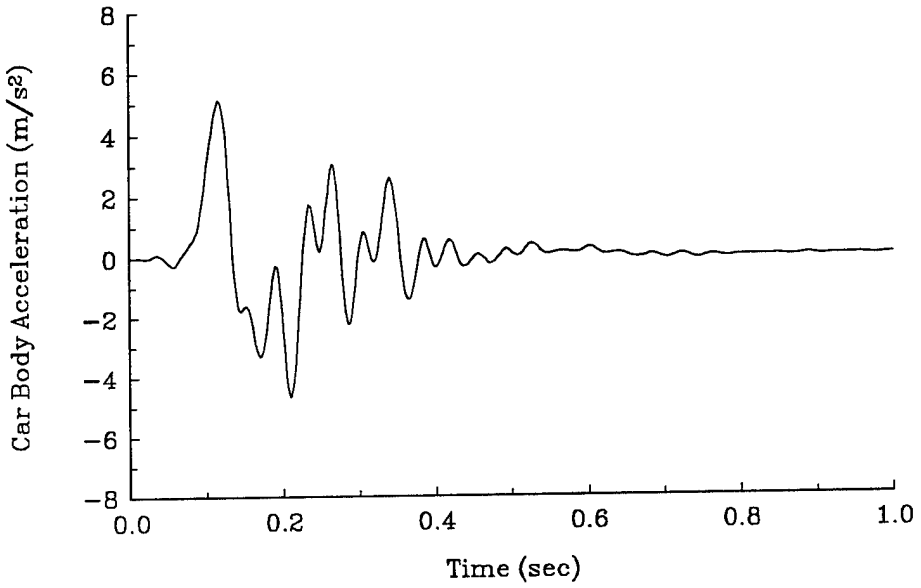

Figure 10.20 $\ddot{z}_s$ vs t, Short Pulse Response for Control Law 1

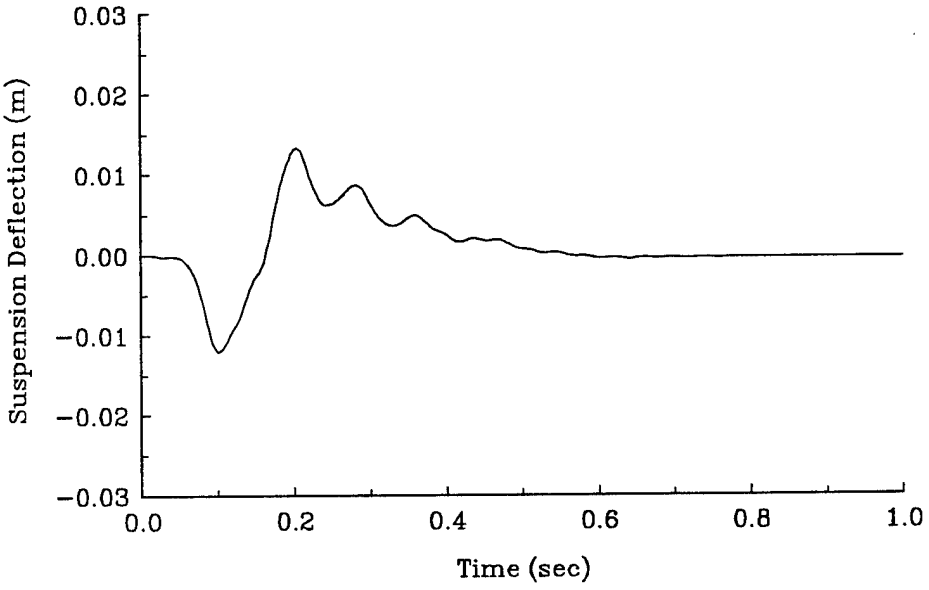

Figure 10.21 (z_s - z_u) vs t, Short Pulse Response for Control Law 1

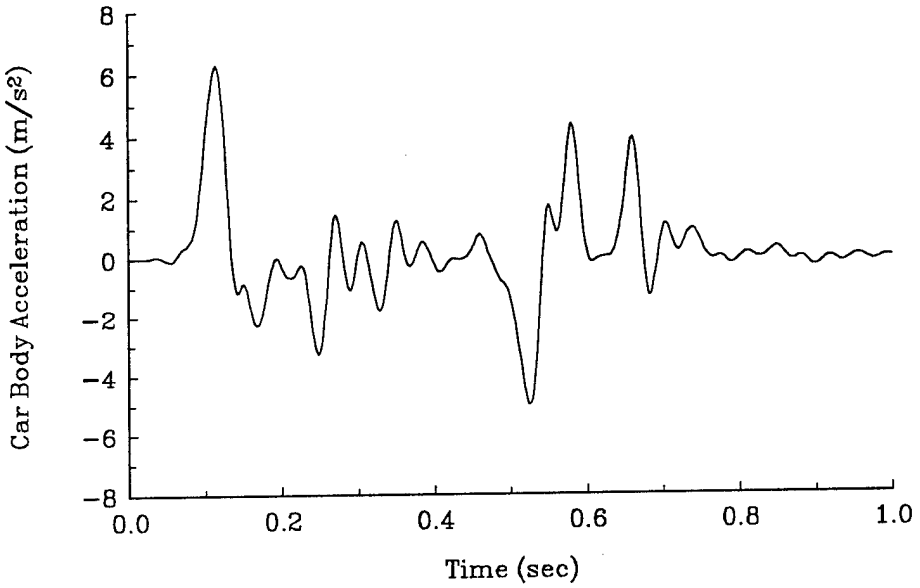

Figure 10.22 $\ddot{z}_s$ vs t, Long Pulse Response for Control Law 1

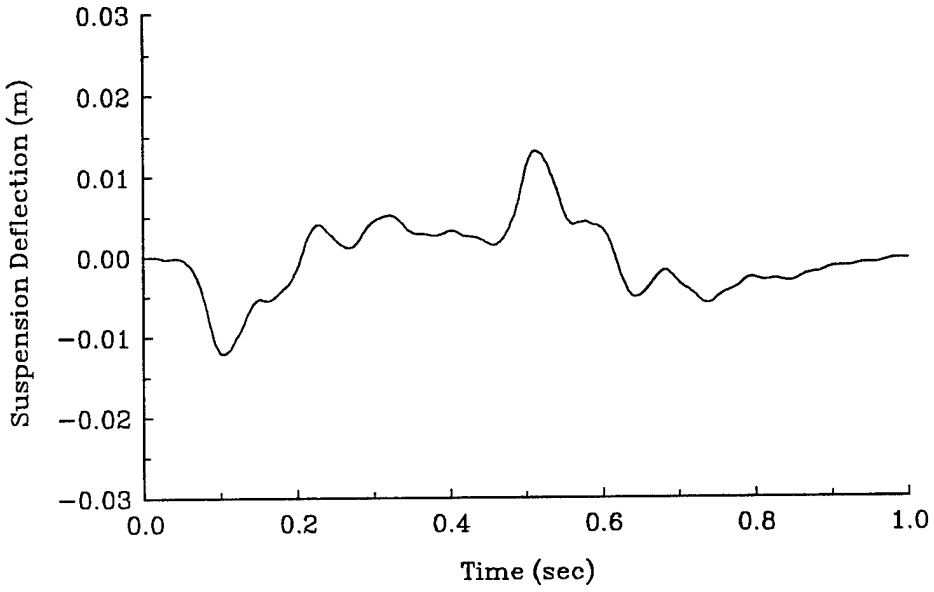

Figure 10.23 $(z_s - z_u)$ vs t, Long Pulse Response for Control Law 1

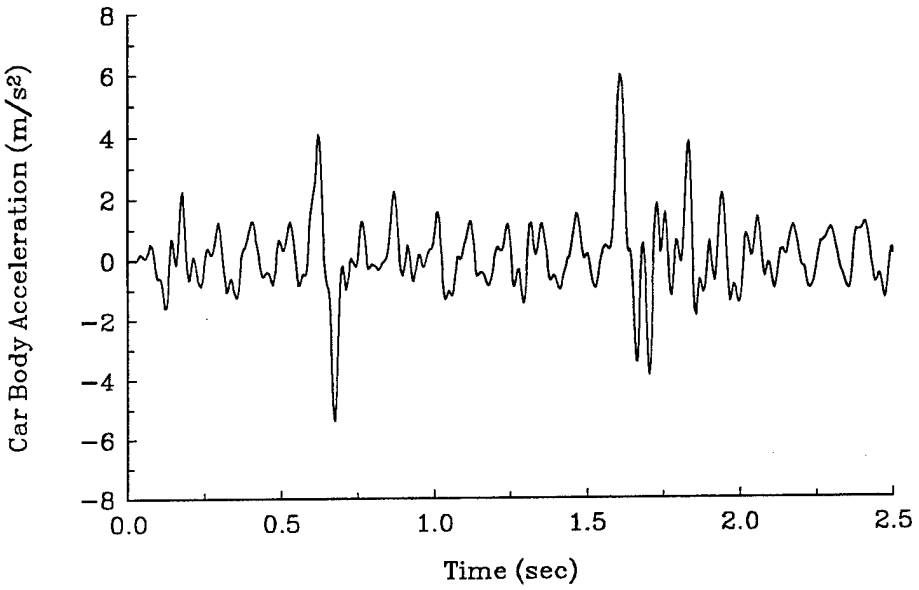

Figure 10.24 $\ddot{z}_s$ vs t, Sine + Pulse Response for Control Law 1

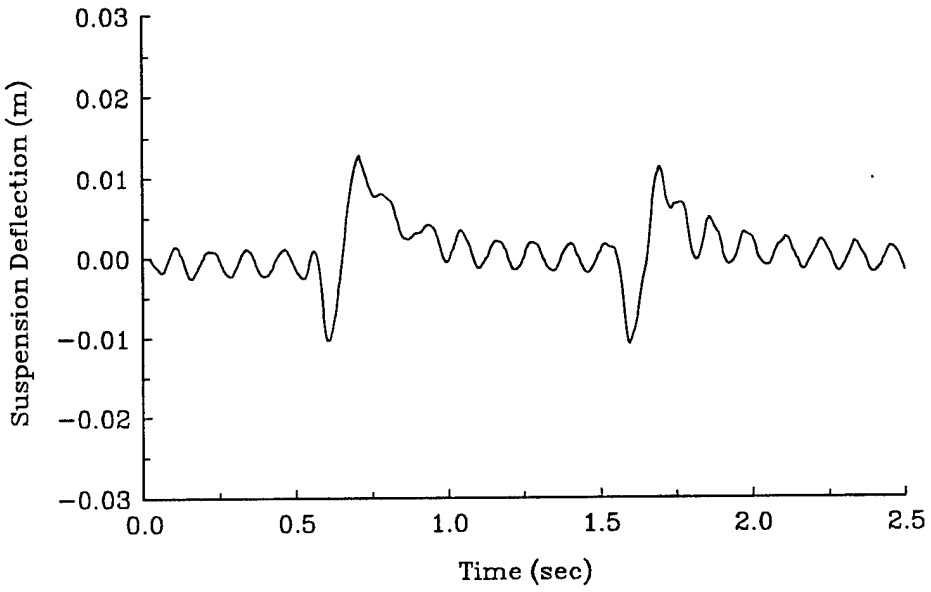

Figure 10.25 (z_s - z_u) vs t, Sine + Pulse Response for Control Law 1

10.3 Parametric Study of Torque Limit

One of the previously discussed advantages of a semi-active friction damper is the ability to limit the suspension force independent of the suspension velocity. In this section the benefit of a torque limit is studied. Control law 2 (Figure 10.9) is the viscous controller with a torque command limit. Limiting the torque command is advantageous because it reduces the acceleration experienced by the car body and also reduces the peak torque requirement of the clutch. Data for this parametric study was generated using a controller gain of 1.25. The composite performance indices are shown in Figures 10.26 and 10.27. Car body acceleration data is shown in Figures 10.28 and 10.29. Figure 10.30 shows the peak value of the measured clutch torque as a function of the commanded torque limit. Although not a one-to-one match, higher command limits result in higher measured torques. The effect of the torque limit is seen most clearly in the car body acceleration data. As expected, car body accelerations (RMS and peak values) decrease with a decreasing torque limit.

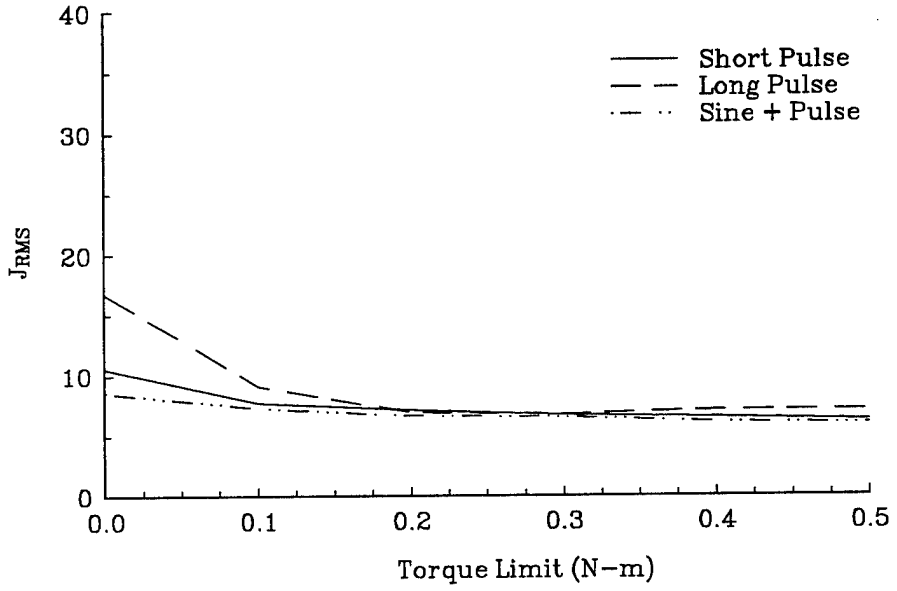

Figure 10.26 J_{RMS} vs T_{sat} for Control Law 2

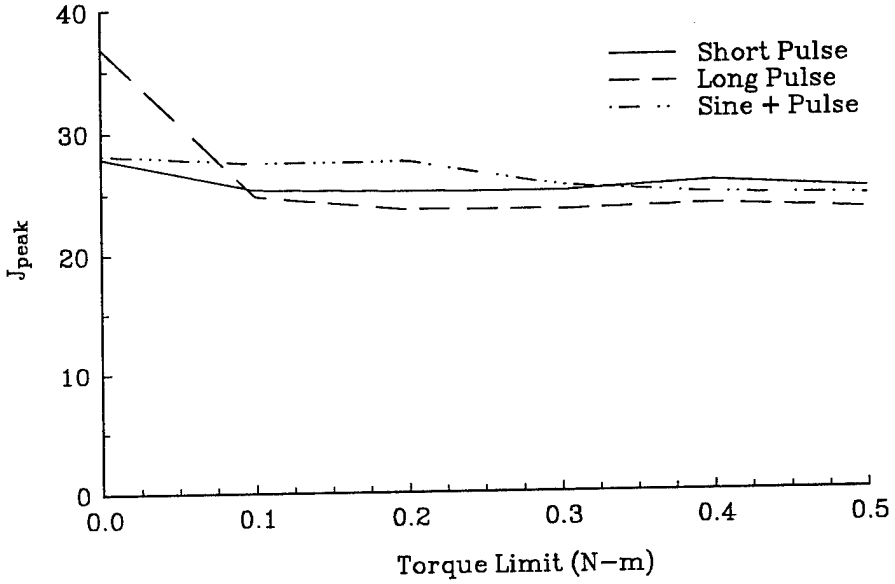

Figure 10.27 J_{peak} vs T_{sat} for Control Law 2

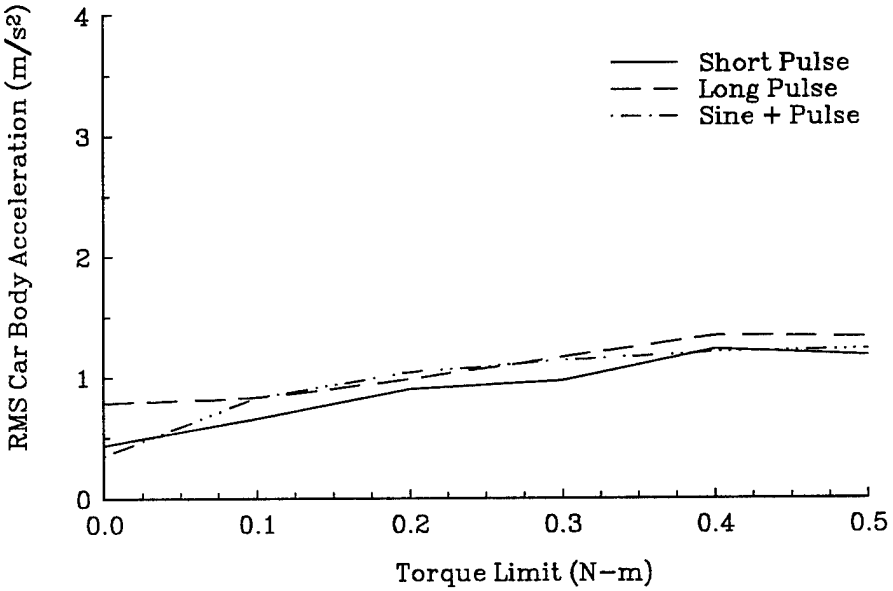

Figure 10.28 $(\ddot{z}_s)_{RMS}$ vs T_{sat} for Control Law 2

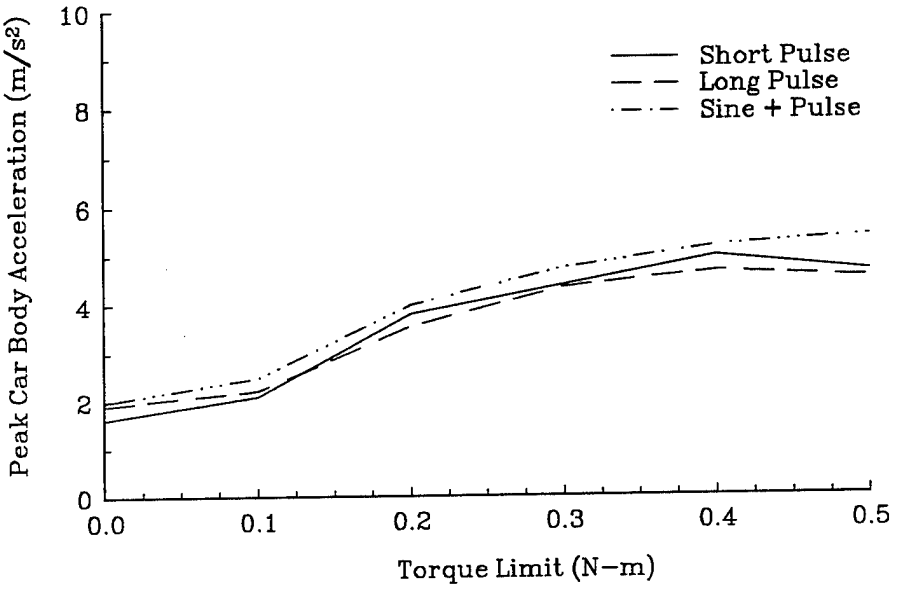

Figure 10.29 $(\ddot{z}_s)_{peak}$ vs T_{sat} for Control Law 2

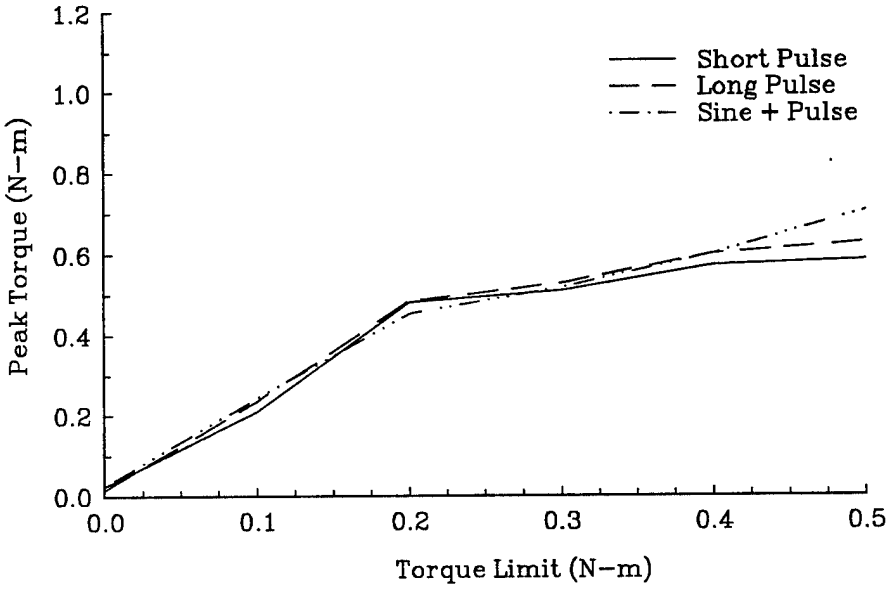

Figure 10.30 $(torq_{meas})_{peak}$ vs T_{sat} for Control Law 2

10.4 Parametric Study of Low Pass Filter Frequency

Control law 3 adds a low pass filter to control law 2 in order to demonstrate low frequency controller performance. For runs in this parametric study a controller gain of 1.25 and a torque limit of 0.2 N-m are used while the cut-off or corner frequency ω_c is varied. Composite performance index data is shown in Figures 10.31 and 10.32. Note that the case of ω_c = 10 rad/sec = 1.6 Hz (henceforth referred to as the low bandwidth controller) shows only modest decreases in performance as compared to the pure viscous controller with a gain of 1.25 (henceforth referred to as the viscous controller) shown in Figures 10.10 and 10.11. From this perspective, little penalty is incurred by having the 1.6 Hz low pass filter in the control law. Car body acceleration and displacement data is shown in Figures 10.33 - 10.35. Comparing this data to the viscous controller data in Figures 10.12 - 10.14 shows that car body accelerations are lower (RMS and peak values) for the low bandwidth case while RMS car body displacement is lower for the viscous case. Wheelset acceleration (Figure 10.36) is higher for the low bandwidth controller. Suspension deflection and tire deflection data is shown in Figures 10.37 and 10.38, respectively. The viscous controller has a 2 mm lower RMS suspension deflection than the low frequency controller (compare Figure 10.37 to 10.16) while the RMS tire deflection data is approximately equal (compare Figure 10.38 to 10.17). Frequency response data from the road input to the car body and wheelset accelerations is shown in Figure 10.39. Frequency response data from the road input to the suspension deflection,

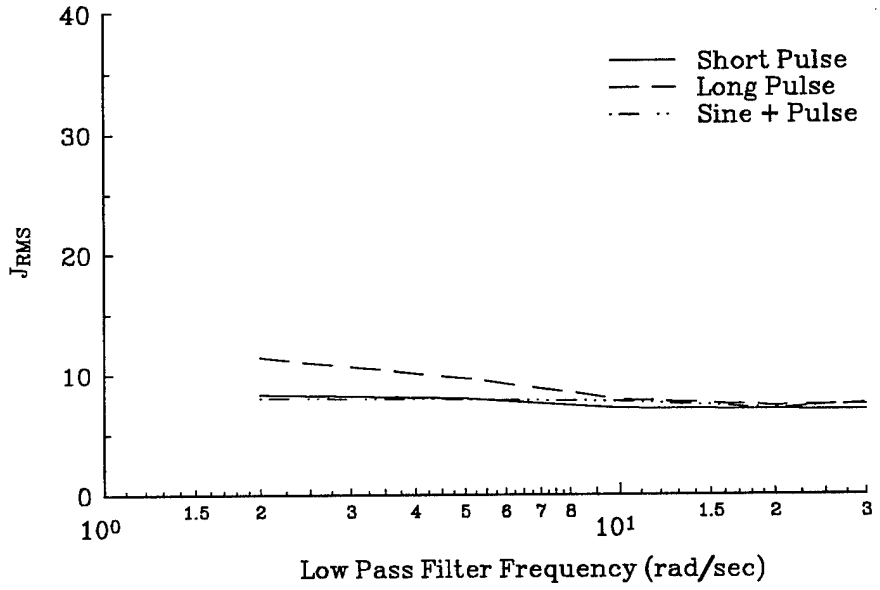

Figure 10.31 J_{RMS} vs ω_c for Control Law 3

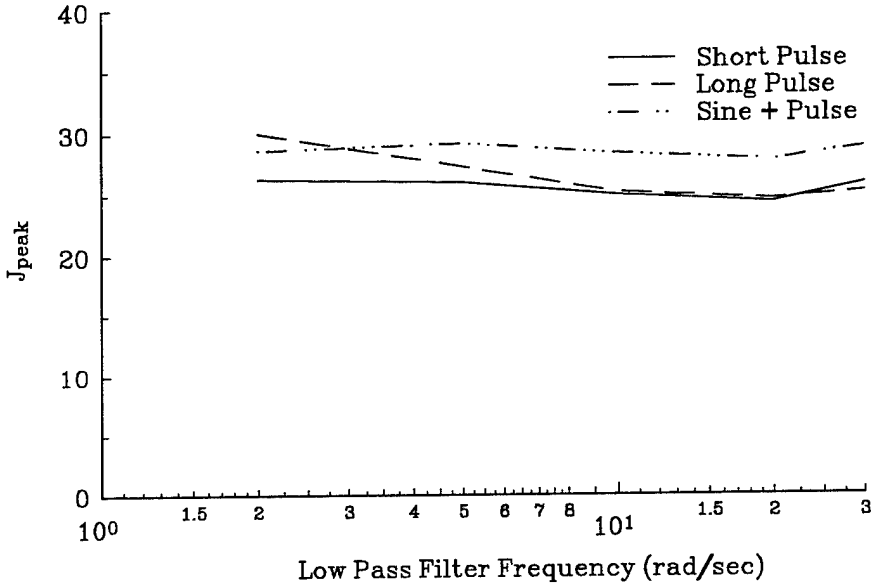

Figure 10.32 J_{peak} vs ω_c for Control Law 3

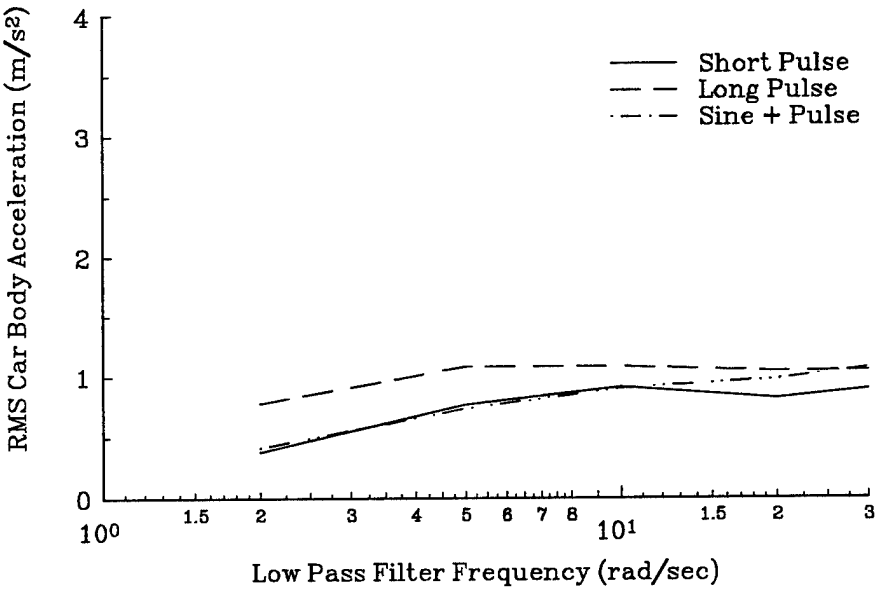

Figure 10.33 $(\ddot{z}_s)_{RMS}$ vs ω_c for Control Law 3

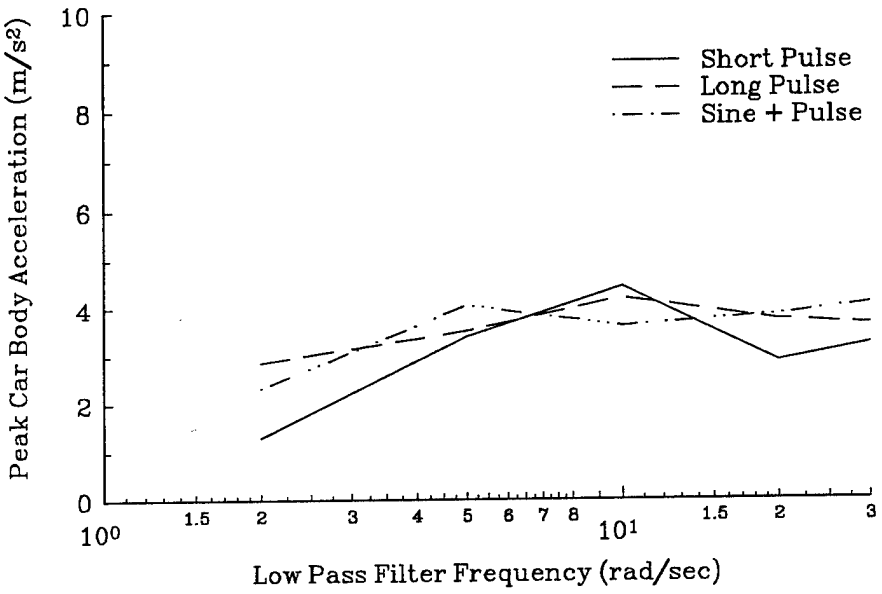

Figure 10.34 $(\ddot{z}_s)_{peak}$ vs ω_c for Control Law 3

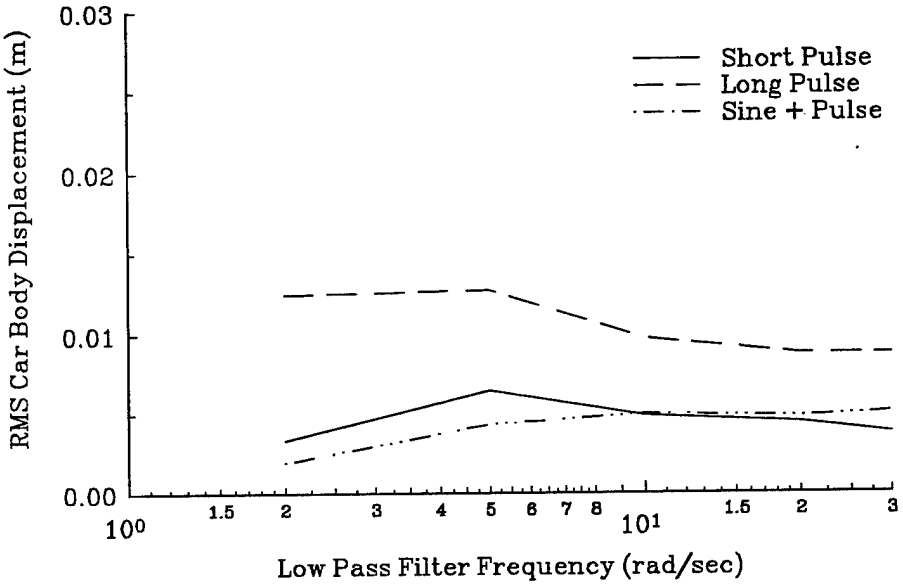

Figure 10.35 $(z_s)_{RMS}$ vs ω_c for Control Law 3

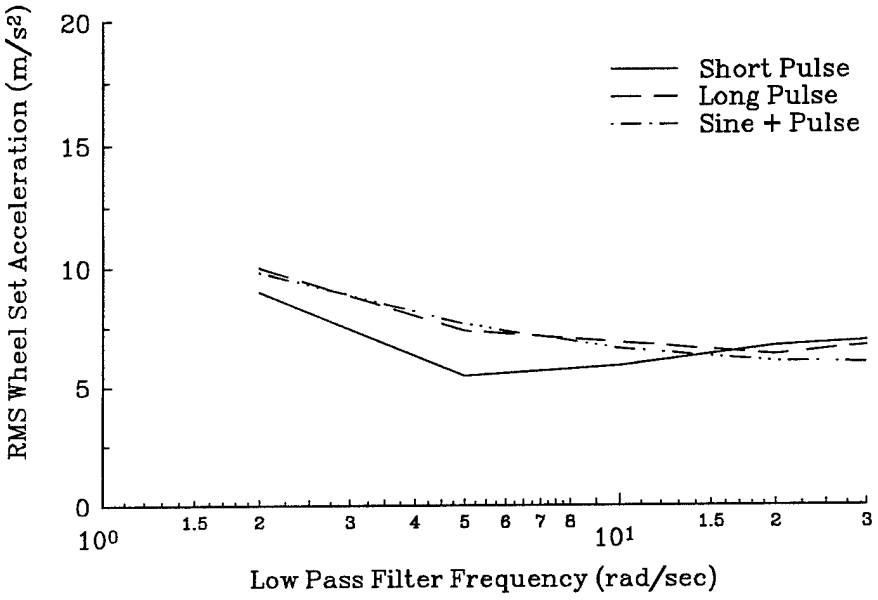

Figure 10.36 $(\ddot{z}_u)_{RMS}$ vs ω_c for Control Law 3

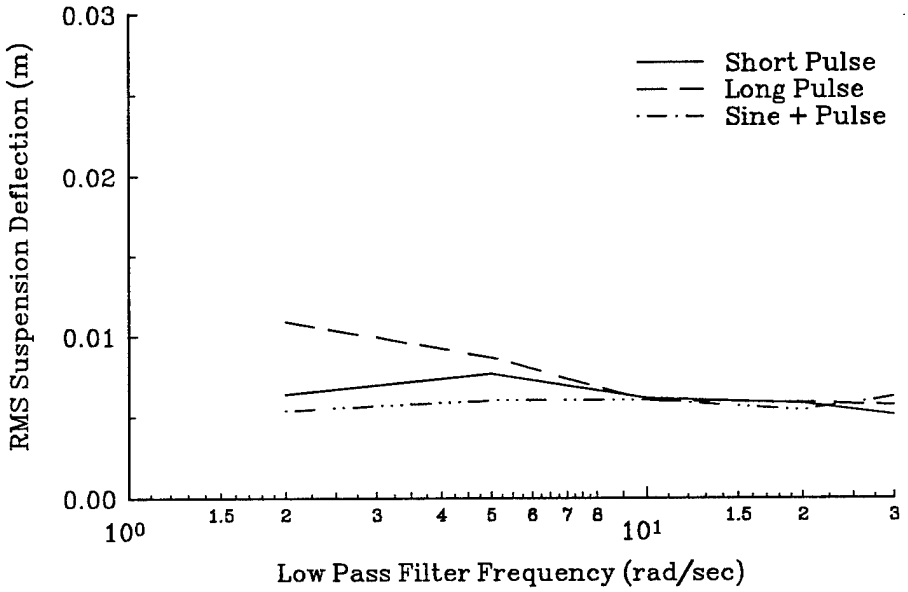

Figure 10.37 $(z_s - z_u)_{RMS}$ vs ω_c for Control Law 3

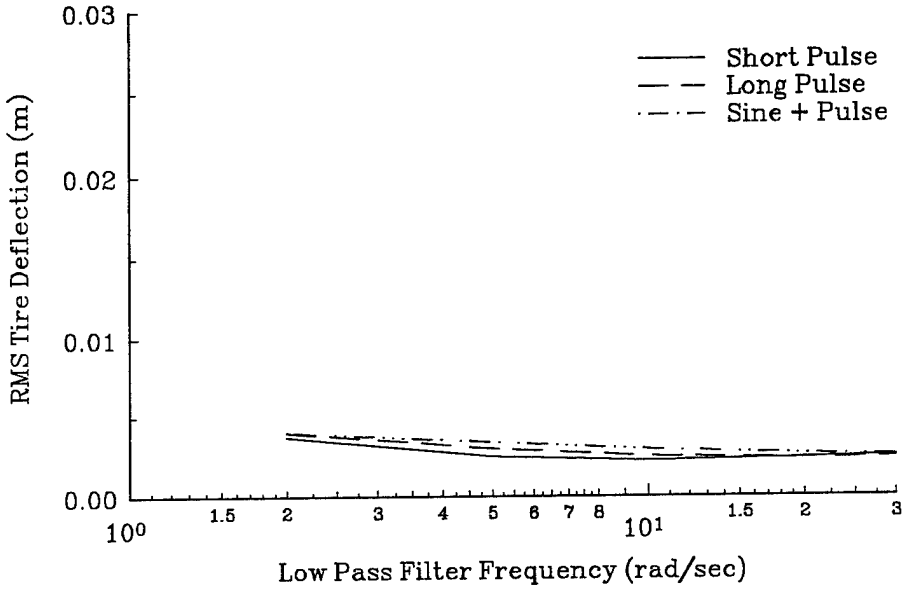

Figure 10.38 $(z_u - z_r)_{RMS}$ vs ω_c for Control Law 3

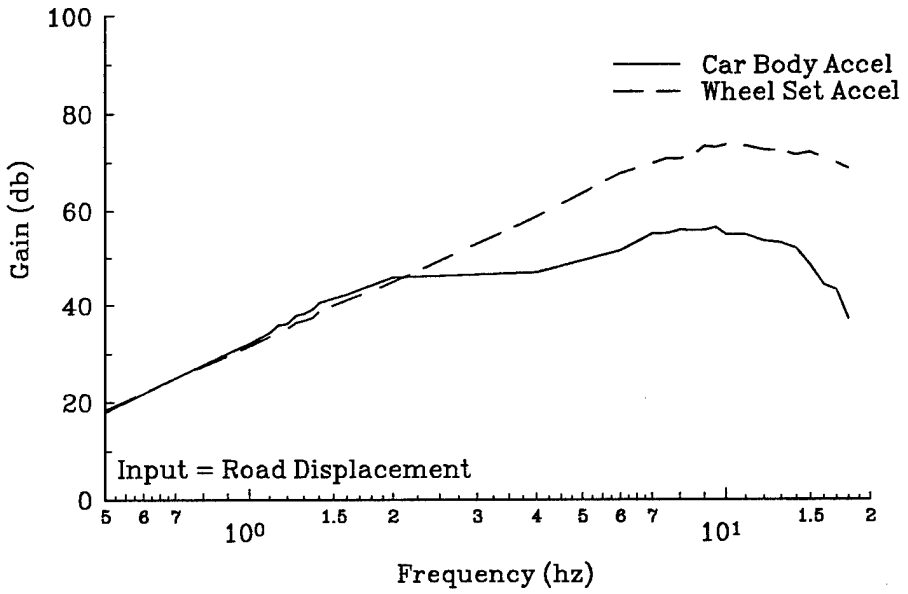

Figure 10.39 $\ddot{z}_s$, $\ddot{z}_u$ Frequency Response Data for Control Law 3

tire deflection, and car body displacement is shown in Figure 10.40. The frequency response data for the low frequency controller does not show significant differences from the frequency response data for the viscous controller in Figures 10.18 and 10.19. Time response curves of car body acceleration and suspension deflection for the three road inputs with k=1.25, T_{sat}=0.2 N-m, and ω_c=10 rad/sec are shown in Figures 10.41 - 10.46.

While the frequency response data appears similar for the viscous controller and the low bandwidth controller, one difference was noted during the tests which does not appear in any of the data presented thus far. While performing the frequency response tests, a peculiar oscillation was observed on the car body displacement. Figure 10.47 shows car body displacement versus time for the low bandwidth controller case when the road input is a 10 Hz sinusoid disturbance. The origin of the 1 Hz oscillation is not known and is not present in the viscous controller case. Clearly, it is a result of nonlinearities in the system since a purely linear system cannot generate subharmonics or superharmonics. Further tests revealed the nature of the oscillation can be altered by changing the torque limit or low pass filter frequency. Although not a desirable phenomenon, this oscillation does not negate the significant amount of encouraging data for the low bandwidth controller.

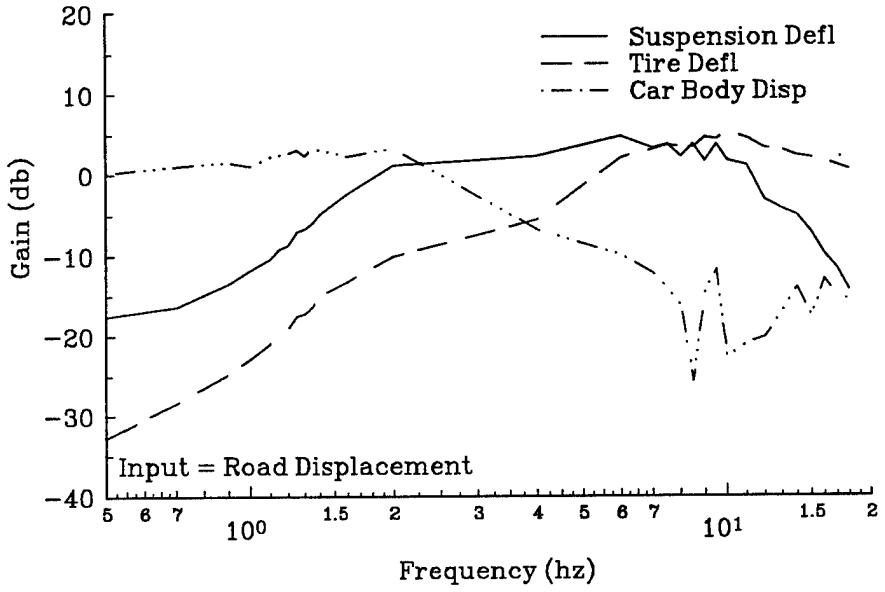

Figure 10.40 z_s-z_u, z_u-z_r, z_s Frequency Response Data for Control Law 3

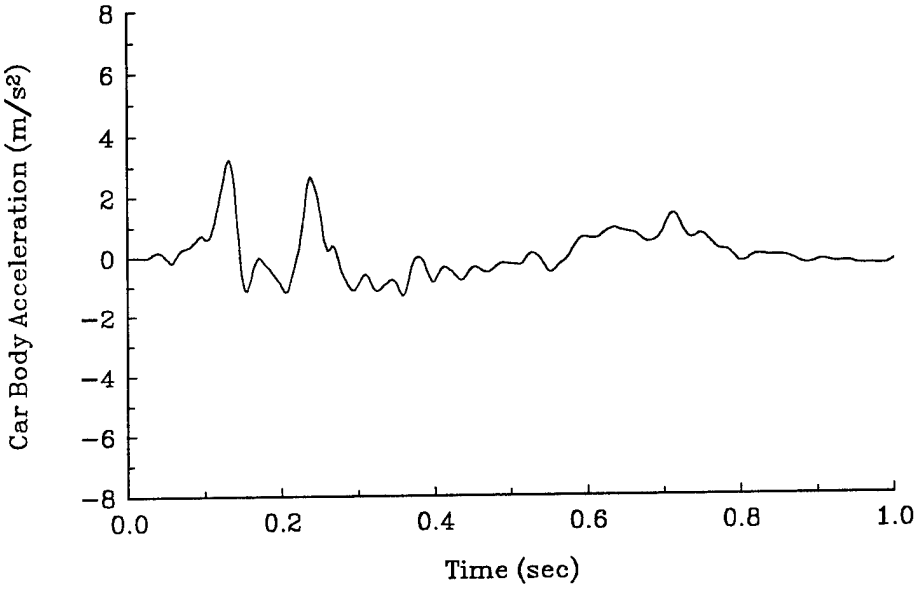

Figure 10.41 $\ddot{z}_s$ vs t, Short Pulse Response for Control Law 3

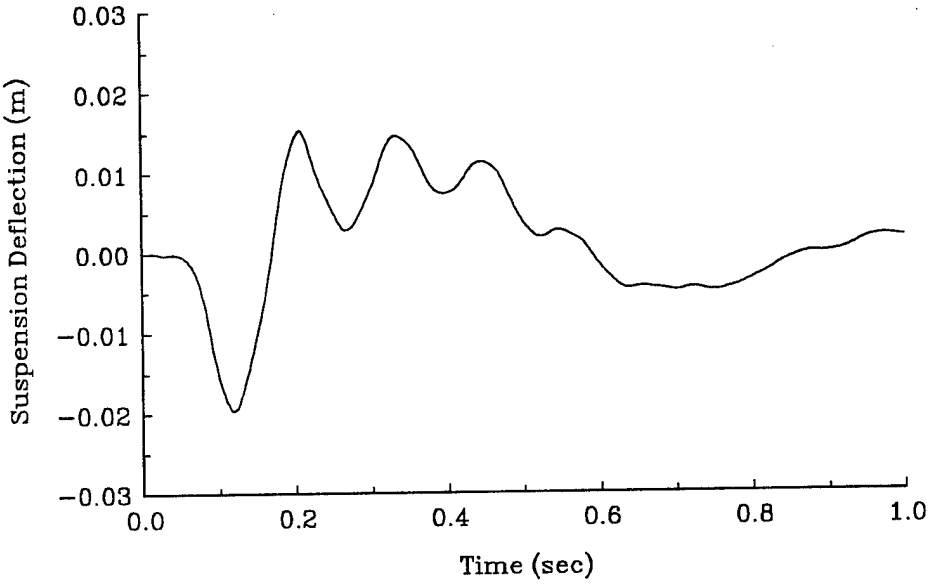

Figure 10.42 $(z_s - z_u)$ vs t, Short Pulse Response for Control Law 3

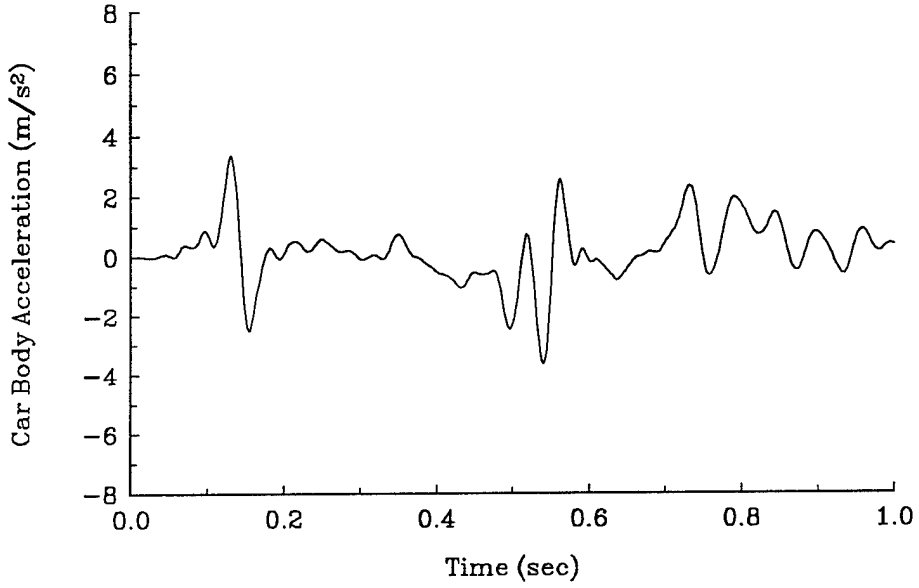

Figure 10.43 $\ddot{z}_s$ vs t, Long Pulse Response for Control Law 3

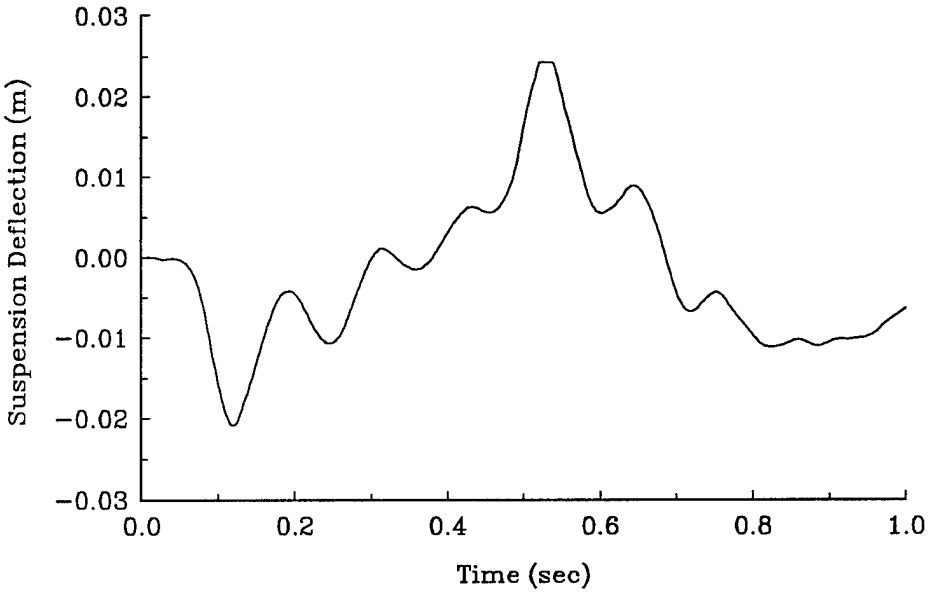

Figure 10.44 $(z_s - z_u)$ vs t, Long Pulse Response for Control Law 3

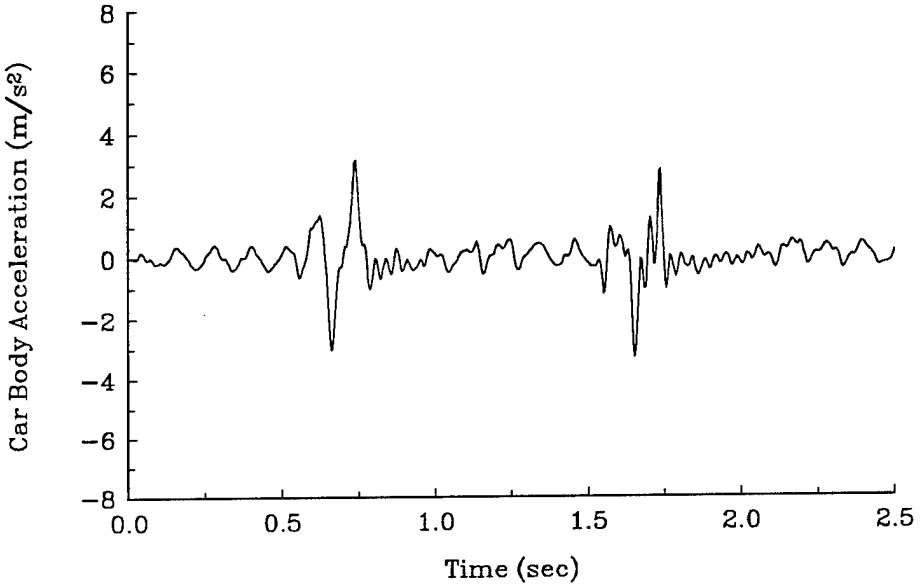

Figure 10.45 $\ddot{z}_s$ vs t, Sine + Pulse Response for Control Law 3

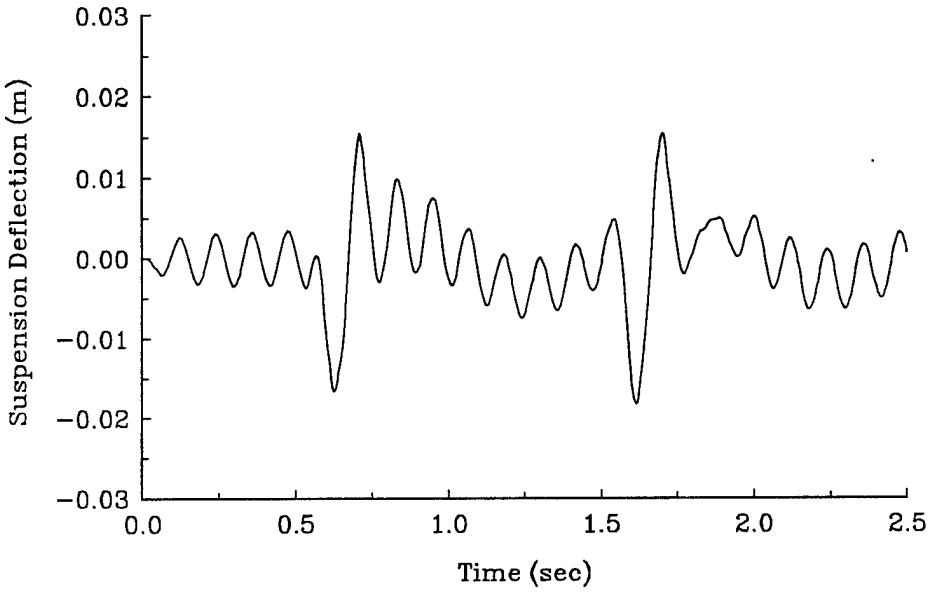

Figure 10.46 $(z_s - z_u)$ vs t, Sine + Pulse Response for Control Law 3

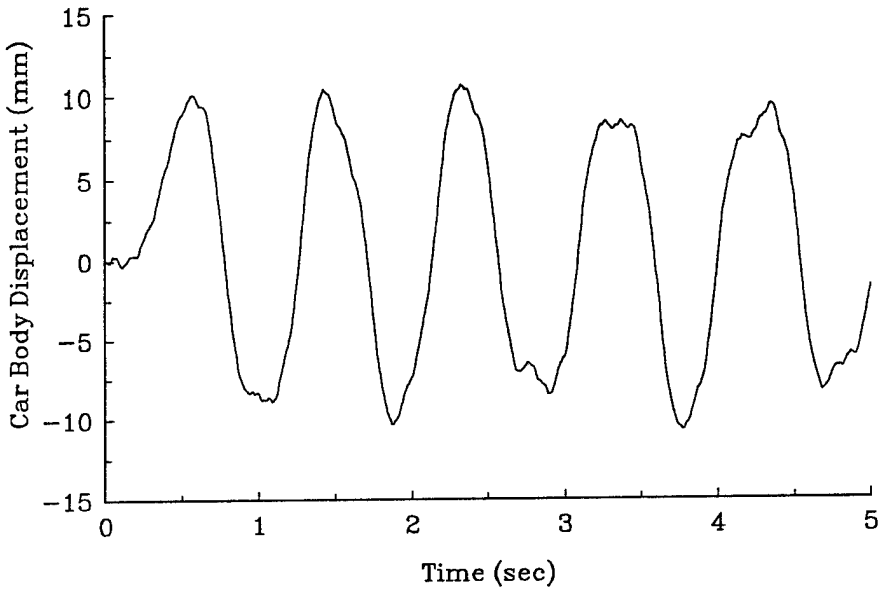

Figure 10.47 z_s vs t for Control Law 3 with 10 hz Disturbance Input

10.5 Summary

There were three objectives for the quarter car experiment. The first objective was to build a scale model quarter car suspension system. This was accomplished as discussed in Chapter 9. The second objective was to experimentally demonstrate the shock isolation properties of the semi-active friction damper. This was shown in section 10.3. Shock isolation was achieved by imposing a torque limit in the control law. The car body acceleration data clearly shows a decrease in both RMS and peak levels as the torque limit is decreased. It was also encouraging that the composite performance measures were not significantly affected by imposing a torque limit equal to or above 0.2 N-m. Since the implementation of the torque limit is not related to the system states, it can be implemented in controllers without regard to bandwidth.

The third objective was to demonstrate effective suspension control using a low bandwidth controller. This was demonstrated in section 10.4. The control law with a 1.6 Hz low pass filter had comparable performance to the pure viscous controller. These are encouraging results, particularly in light of the fact that this is the first generation quarter car assembly, first generation semi-active friction damper, and first generation low bandwidth controller. Future research will inevitably result in a better understanding of the current problems (such as the 1 Hz oscillation) as well as an improved experimental setup. Further efforts in the torque control loop design as well as quarter car control

algorithm design with the *explicit* goal of achieving suspension control with a low bandwidth controller should yield performance to rival the higher bandwidth systems currently in use.

CHAPTER XI

SUMMARY, CONCLUSIONS, AND RECOMMENDATIONS FOR FUTURE WORK

11.1 Semi-Active Friction Damping for LSS Vibration Control

Chapters 2-8 describe the concept of dissipating vibrational energy in a structure by incorporating semi-active friction damping at the joints. The envisioned applications are large built-up truss structures which would be deployed in space. A small, flexible, two beam structure with a single semi-active joint is used as a representative scale model system.

The design of control systems begins by formulating a mathematical model of the mechanical system to be controlled. For the two beam system, the assumed modes method was used to model the flexible beams. This approach requires modeling studies to define the type and number of modes necessary for an accurate model. In Chapter 3, three modal series were investigated. Sine modes which satisfy the geometric boundary conditions and polynomial modes which also satisfy the geometric boundary conditions and can carry a moment at the center pin (as required by the natural boundary conditions) proved to be roughly equivalent in terms of system eigenvalues, frequency response

characteristics, and time response characteristics. The sine modes were chosen due to their computational advantages over the polynomial modes. Mixing the sine and polynomial modes in a single modal series expansion did not prove beneficial. The approach used to evaluate the different models is an appropriate blueprint for most modeling studies.

There are many possible approaches for designing the semi-active joint controller. In Chapter 4, M_f (the frictional moment) is defined as a linear function of the system states. A joint controller designed using LQR theory with a cost functional based on the flexural energy in the beams proved to be very effective in dissipating the vibrational energy in the two beam system. This controller resulted in a minimal amount of control clipping (to enforce the semi-active constraint) and no joint lock-up. The viscous joint controller, which defines M_f as proportional to $\dot{\theta}$ (the joint angular rate) is attractive because it relies on feedback of a readily measured quantity rather than requiring full state feedback. However, this implementation advantage is offset by poorer performance.

The semi-active joint controller designed using LQR methods requires the control to be clipped in an ad-hoc manner in order not to violate the semi-active constraint (i.e., $F_N \geq 0$). The question arises as to the performance penalty incurred by not considering the $F_N \geq 0$ constraint during the design process. In Chapter 5, this is addressed by studying the controller design problem in which the semi-active requirement is an explicit control constraint. Numerical procedures were used to solve the piecewise linear two point boundary value problem which arises when the variational approach is used to solve the

optimal control problem. The results showed that little (if any) performance penalty is incurred by ignoring the control constraint during the controller design process.

The control of large space structures will include correct positioning and alignment of the structure (attitude control) as well as structural vibration control. These tasks can be performed by segregated control systems or by an integrated control system. In Chapter 6, additional actuators are included in the two beam system to represent attitude controller inputs. Two control structures are considered. In the VJEW design, the joint controller is designed using $\dot{\theta}$ feedback. In a separate step the attitude controller is designed (assuming the joint controller is already in place) using LQR techniques with an energy based cost functional. The second design combines the joint and attitude controllers into one design. This is the EW design and also uses LQR techniques and an energy based cost functional. The analysis of these two designs yielded some very interesting results. One expected advantage of the VJEW design was that the joint controller could be designed prior to the design of the attitude controller. The simulation and analysis data indicated that while it is possible to design the joint controller without considering the design of the attitude controller, a penalty in performance would likely be incurred. The best values for k_{VJ}, the viscous gain, could not be determined except by parametric studies which included the attitude controller. Furthermore, the location of the disturbance input affected the choice of k_{VJ}. Conversely, the EW controller which integrated the joint controller and attitude controller into one did not show any sensitivity to the location of the input disturbance. Since each controller design relied on full state

feedback, observer design issues were also addressed. Using the loop transfer recovery (LTR) technique parameterizes the observer gain matrix in terms of a scalar q. Loop transfer recovery occurs as q is increased. The value of q is usually limited by the amount of sensor noise present. However, the analysis shows that there are performance and stability issues which cannot be addressed until the low order controller / observer pair is implemented in the high order plant. In particular, performance decreased for values of q greater than 1000. This is contrary to the result obtained when the controller, observer, and plant are the same dimension (and the plant is minimum phase). Similar to the trends in control system performance, the gain and phase margins do not always increase for increasing values of q. Another unexpected result was that for the value of q which maximized performance in both the VJEW and EW controllers (q=1000), the EW controller had higher gain and phase margins.

In most control systems where the designer is trying to maximize performance over a broad range of operating conditions, some type of adaptive control system is used. This is particularly the case when the desired value of a controller parameter is known to vary with respect to a function of the system states. In Chapter 7, an adaptive controller was designed to reduce the sensitivity of the VJEW controller to the location of the disturbance input. By varying k_{VJ} as a function of the energy in beam 1, improved performance was achieved.

Another type of system relevant to space structures is the free-free system in which the two beams are connected by a semi-active pin joint but are otherwise

unconstrained. This system was investigated in Chapter 8. Joint damping was not found to be as effective in controlling vibrations in the free-free system as in the pinned-pinned system. This was due to the existence of vibratory modes which result in little or no motion at the joint, thus eliminating the ability of the semi-active joint to control that mode.

This thesis has shown that using semi-active joints to control structural vibrations is a feasible concept if the undesirable vibratory motion results in relative motion at the joint. It represents the first in-depth treatment of using semi-active joint damping for vibration control. The medium for generating the resistive force was a frictional joint. However, except for situations which joint lock-up occur, the results are applicable for any passive device which can be actively controlled. The motivation for assuming a frictionally damped joint stems in part from the suitability of this type of joint for a space environment. Another motivation is the concept of a passive friction joint in which the joint normal force is a function of the joint angle (for example, the elliptical pin joint).

The two beam system was chosen as a suitable, scale model system with which to investigate the semi-active joint concept. The analytical results obtained using this system are fairly thorough, although small refinements may be possible. For example, the optimal output feedback technique could be explored as a means of choosing the viscous gain k_{VJ} in a more systematic way. Rather than continuing the analytical studies described above, two alternative directions are recommended. The first is to experimentally verify the semi-active joint concept using a two beam system. To some

extent, the experimental investigation into semi-active suspension using dry friction is relevant to vibration control of flexible systems. Still, there are significant differences that need to be addressed in a flexible system experiment. Preliminary designs for this experiment have been generated with the final design and fabrication expected in the next year. Using a frictionally damped joint will be advantageous because it allows the use of commercially available electromagnetic clutches which are well suited for active control. Since the joint controller will not have infinite bandwidth, some analytical work using an actuation system which is band limited (when compared to the two beam system dynamics) will be necessary. This work should precede the clutch selection. A second research effort which would yield beneficial results would be to incorporate the semi-active joint in a more complex structure. Ideally the system would represent a small but realistic space structure or a portion of one. Depending on the structure, more than one semi-active joint may be appropriate.

11.2 Semi-Active Friction Damping for Suspension Control

Chapters 9 and 10 describe how semi-active friction damping was used in an automotive suspension system. Whereas the work on the two beam system was analytical in nature, the suspension system research was almost entirely experimental. A quarter car scale model suspension system was designed, fabricated, and utilized to generate the performance data.

The experimental assembly was described in detail in Chapter 9. All of the goals for the design of the scale model system were not met but nevertheless the system did provide a suitable representation of a suspension system. In particular the ratio of the car body mass to the wheelset mass was 3.8 rather than the desired value of 7. In order to get the mass ratio closer to the desired value of 7, two options are available. The first option is to add weight to the car body mass. As stated earlier this will require the springs to be stiffened and will result in the clutch being undersized. Stiffening the springs is an easy task since the springs are simple cantilever springs and are easily designed and fabricated. To keep the clutch from being undersized, the crank can be shortened. If the desired crank length becomes very small, a rack and pinion system can replace the crank and connecting rod assembly. This would increase the effectiveness of the clutch but possibly at the expense of higher friction. As the crank length decreases and the rotational velocity of the clutch rotor increases, inertial properties of the clutch rotor and shaft assembly may also become influential. Additionally, the larger crank angles would introduce nonlinearities into the system. The second option is to decrease the mass of the wheel set mass. This will require a design change to the wheel set assembly since removing mass will result in an undesirable reduction in structural stiffness. One promising design change is to add another linear bearing rail assembly between the two existing rails. The free end (end opposite the spring mounts) of the wheel set crossbar would mount to a bearing on this intermediate rail thus allowing the length of the crossbar to be shortened and the weight to be reduced.

Due to the emphasis on low weight, the wheel set structure in the current design is noticeably flexible. A 30 hz natural frequency is easily seen on the crossbar during testing. This vibration does not affect the performance measures significantly, however, the design modifications necessary to eliminate it are simple enough to warrant implementation. As mentioned above, adding a third rail assembly and shortening the crossbar length is one option. Also a stiffening brace could be added. A preliminary design of this brace indicates that only 33 g would be added to the mass of the wheel set assembly.

For test and evaluation purposes it would be desirable to have better performance from the torque control loop. Several options are available to do this. The simplest option would be to redesign the torque loop compensation filter. Care was taken in the design of this loop compensation but improvements may still be achievable. A spiking power supply could also be used to improve performance. Response time for the clutch decreases from 35 milliseconds to 17 milliseconds when a 90 V spike is initially applied to the coil. Tests indicate that the bulk of the response time results from the inductance of the clutch coil. The coil inductance problem is exacerbated by the fact that only uni-directional voltages are applied to the clutch. Allowing bi-polar voltages to the coil may also improve performance by reducing the coil de-energizing time.

One final design change would be to modify the setup for vertical operation. This is not believed to be as critical an issue as the above modifications since its main goal is to allow tire hop studies (times when the tire leaves the road surface) to be conducted.

The changes required for this are numerous. The cantilever springs would need to be replaced with coil springs since it would be very difficult to design cantilever springs which could withstand the required static deflection. The rail assembly would need to be lengthened to accommodate the new springs. An additional LVDT would be needed since strain gages could no longer be used to measure tire deflection. A new road actuator would be needed since the current one would be undersized. A third rail assembly would be needed to locate the road actuator in the center of the assembly. Other issues would certainly arise as the design modifications were implemented.

The concept of a semi-active suspension system is not a new idea. However, the idea of using a semi-active friction device to provide the damping is a new concept. As opposed to the two beam semi-active damper, the fact that the damping mechanism is friction based is crucial due to the inherent (and desirable) shock isolation properties. Additionally, having a friction based damper decouples the damping force from the suspension velocity which is important when considering low bandwidth controller performance. The data presented in Chapter 10 validates the shock isolation and low bandwidth controller techniques for the frictionally damped semi-active suspension system. This work represents the first experimental verification of these ideas.

The ability to provide shock isolation using a torque limit set in software is believed to have advantages over hydraulic dampers which must use a pressure relief valve. Also, decoupling the damping force from the suspension velocity should give additional flexibility when designing the control system. These ideas need further

investigation. The benefits of using a frictionally damped system need to be quantified in order to justify pursuing the semi-active friction damper for a full size application. This would include studying the benefits in a quarter car system as well as a full car system (with 4 semi-active systems). The ability to generate large suspension forces with little or no suspension velocity may prove beneficial in cornering or braking. Aside from the suspension system control system, other mechanical systems should be explored for possible applications. Systems which require shock isolation, such as machine tools, may benefit from the advantages of semi-active friction damping. Another feature which may prove beneficial is the ability of the damper to lock-up. This has previously been viewed as detrimental but there may be applications where it is desirable to periodically prohibit motion. Having proved the *validity* of the semi-active friction damping herein, these and other applications will indicate the *utility* of the concept.

APPENDIX A

STATE WEIGHTING MATRIX FOR Ė COST FUNCTIONAL

The performance index for this case is

$$J = \int_0^{\infty} \dot{E} + \rho M_f^2 \, dt \, . \tag{A.1}$$

The energy of the two beam system, E, is given by

$$\begin{aligned} E &= T + V \\ &= \frac{1}{2} \underline{x}^T [W] \underline{x} \end{aligned} \tag{A.2}$$

where

$$[W] = \begin{bmatrix} [M] & [0] \\ --- & --- \\ [0] & [K] \end{bmatrix} . \tag{A.3}$$

Differentiating (A.2) gives

$$\dot{E} = \frac{1}{2} \left[\dot{\underline{x}}^T [W] \underline{x} + \underline{x}^T [W] \dot{\underline{x}} \right] . \tag{A.4}$$

The derivative of the state vector is given by the state equation,

$$\dot{\underline{x}} = \left[A_{SL}\right]\underline{x} + \underline{B}_M M_f \,. \tag{A.5}$$

Substituting (A.5) into (A.4) and simplifying yields the following expression for $\dot{E}$,

$$\dot{E} = \frac{1}{2}\left[\underline{x}^T \; M_f\right]\begin{bmatrix} \left[A_{SL}\right]^T[W] + [W]\left[A_{SL}\right] & \vert & [W]\underline{B}_M \\ \hline \underline{B}_M{}^T[W] & \vert & 0 \end{bmatrix}\begin{bmatrix} \underline{x} \\ M_f \end{bmatrix}. \tag{A.6}$$

Using (A.6), (A.1) can be written as

$$J = \int_0^\infty \frac{1}{2}\left[\underline{x}^T \; M_f\right][\Gamma]\begin{bmatrix} \underline{x} \\ M_f \end{bmatrix} dt \tag{A.7}$$

where

$$[\Gamma] = \begin{bmatrix} \left[A_{SL}\right]^T[W] + [W]\left[A_{SL}\right] & \vert & [W]\underline{B}_M \\ \hline \underline{B}_M{}^T[W] & \vert & 2\rho \end{bmatrix}. \tag{A.8}$$

The plant dynamics matrix, $[A_{SL}]$, is given by

$$\left[A_{SL}\right] = \begin{bmatrix} [0] & \vert & -[M]^{-1}[K] \\ \hline [I] & \vert & [0] \end{bmatrix} \tag{A.9}$$

Using (A.3) and (A.9), the following result can be easily derived,

$$\left[A_{SL}\right]^T\left[W\right] + \left[W\right]\left[A_{SL}\right] = \left[0\right], \tag{A.10}$$

which simplifies the expression for $[\Gamma]$ as follows,

$$\left[\Gamma\right] = \begin{bmatrix} [0] & | & [W]\underline{B}_M \\ \text{-------} & | & \text{-------} \\ \underline{B}_M{}^T[W] & | & 2\rho \end{bmatrix}. \tag{A.11}$$

The optimal control problem specified by the state equations in (A.5) and the performance index in (A.7) and (A.11) is equivalent to the following problem [46],

$$\dot{\underline{x}} = \left[\left[A_{SL}\right] - \underline{B}_M\underline{B}_M{}^T[W]/\rho\right]\underline{x} + \underline{B}_M M_f \tag{A.12}$$

$$J = \int_0^\infty \frac{1}{2}\underline{x}^T\left[-[W]\underline{B}_M\underline{B}_M{}^T[W]/\rho\right]\underline{x} + \rho M_f^2\, dt\,. \tag{A.13}$$

The state weighting matrix for the equivalent system is

$$\left[Q^*\right] = -[W]\underline{B}_M\underline{B}_M{}^T[W]/\rho\,, \tag{A.14}$$

which is not positive semi-definite [77] since there exist no matrix $[\gamma]$ such that

$$\left[Q^*\right] = [\gamma]^T[\gamma]\,. \tag{A.15}$$

In fact, by inspection, $[Q^*]$ is negative semi-definite.

APPENDIX B

DERIVATION OF THE VALUE OF COSTATE LAGRANGE MULTIPLIER

Before considering the costate Lagrange multiplier in the bilinear formulation, it is instructive to return briefly to the linear model formulation. The equations of motion are

$$\dot{\underline{x}} = \left[A_{SL}\right]\underline{x} + \underline{B}_M M_f \,. \tag{B.1}$$

The performance index of interest is

$$J = \frac{1}{2}\underline{x}^T\left[S_f\right]\underline{x}\,|_{t=t_f} + \frac{1}{2}\int_0^{t_f}\underline{x}^T\left[Q\right]\underline{x} + r F_N^2\, dt \,, \tag{B.2}$$

or equivalently,

$$J = \frac{1}{2}\underline{x}^T\left[S_f\right]\underline{x}\,|_{t=t_f} + \frac{1}{2}\int_0^{t_f}\underline{x}^T\left[Q\right]\underline{x} + r_M M_f^2\, dt \,, \tag{B.3}$$

where

$$r_M = \frac{r}{\left(k_G \mu_D\right)^2} \,. \tag{B.4}$$

In (B.4) k_G and μ_D are the joint geometric factor and kinetic coefficient of friction,

respectively. The feedback control that optimizes (B.3) is

$$M_f = \frac{-\underline{B}_M{}^T [S(t)] \underline{x}}{r_M} \tag{B.5}$$

where [S(t)] is the solution to the following Riccati equation,

$$\begin{aligned} -[\dot{S}(t)] = [A_{SL}]^T [S(t)] + [S(t)][A_{SL}] \\ - [S(t)] \underline{B}_M \underline{B}_M{}^T [S(t)] / r_M + [Q] . \end{aligned} \tag{B.6}$$

The control given by (B.5) is for an active joint, no restriction has been placed on M_f up to this point. Substituting (B.5) into (B.1) yields

$$\dot{\underline{x}} = \left[[A_{SL}] - \underline{B}_M \underline{B}_M{}^T [S(t)] / r_M \right] \underline{x} . \tag{B.7}$$

Since [S(t)] is a continuous function, so is the state $\underline{x}$, the control M_f, and the costate $\underline{\lambda}$. A smooth and continuous M_f, however, results in a discontinuous F_N since

$$F_N = \frac{M_f}{k_G \mu_D} \operatorname{sgn}(\dot{\theta}) . \tag{B.8}$$

Thus if t_i represents a zero crossing of $\dot{\theta}$, then

$$F_N(t_i^+) = -F_N(t_i^-) . \tag{B.9}$$

The optimal value of F_N must be the same for the linear or bilinear formulation. Both formulations are appropriate to this point since the semi-active constraint has yet to be introduced. Returning to the bilinear formulation, the normal force at the zero crossing

is given by

$$F_N(t_i^+) = -F_N(t_i^-) - \frac{\sigma\left[C_\theta\right]\underline{B}_F^1}{\lambda_Z r} \quad . \tag{B.10}$$

Since (B.9) and (B.10) must yield the same result, σ=0.

One of the advantages of using the bilinear formulation is that if the unconstrained case can be solved, the inequality control constraint is then simply appended as a control requirement. The optimal F_N is thus calculated using the optimal feedback gains and then forced to be greater than or equal to zero when necessary. This creates regions of constrained and unconstrained trajectories. The problem then becomes to extremize J using these segmented trajectories, a task best left to numerical routines.

BIBLIOGRAPHY

[1] Venneri, S. L. and Mullville, D. R., "Control of Flexible Structures," *Aerospace America*, Vol. 27, Jan. 1989, pp. 36-37

[2] "Vibration Damping Studied for Weapons in Space," *Aviation Week and Space Technology*, Vol. 121, 2 Jul. 1984, pp. 54

[3] Nurre, G. S., Ryan, R. S., Scofield, H. N., and Sims, J. L., "Dynamics and Control of Large Space Structures," *AIAA Journal of Guidance, Control, and Dynamics*, Vol. 7, No. 5, 1984, pp. 514-526

[4] Bicos, A. S., Pak, Y. H., Trent, C. L., and Uitto, R. J., "Passive and Active Vibration Suppression of Large Space Structures," *SPIE Fiber Optic Smart Structures and Skins II*, Vol. 1170, 1989, pp. 359-371

[5] Balas, M. J., "Active Control of Flexible Systems," *Journal of Optimization Theory and Applications*, Vol. 25, No. 3, 1978, pp. 415-436

[6] Meirovitch, L., Baruh, H., and Oz, H., "A Comparison of Control Techniques for Large Flexible Systems," *AIAA Journal of Guidance, Control, and Dynamics*, Vol. 6, No. 4, Jul.-Aug. 1984, pp. 302-310

[7] Schaechter, D. B. and Eldred, D. B., "Experimental Demonstration of the Control of Flexible Structures," *AIAA Journal of Guidance, Control, and Dynamics*, Vol. 7, No. 5, Sept.-Oct. 1984, pp. 527-534

[8] Buchanan, H. J., Schock, R. W., and Waites, H. B., "An On-Orbit Experiment for Dynamics and Control of Large Structures," *AIAA Journal of Guidance, Control, and Dynamics*, Vol. 7, No. 5, Sept.-Oct. 1984, pp. 554-562

[9] Horta, L. G., Juang, J. N., and Junkins, J. L., "A Sequential Linear Optimization Approach for Controller Design," *AIAA Journal of Guidance, Control, and Dynamics*, Vol. 9, No. 6, Nov.-Dec. 1986, pp. 699-703

[10] Chiang, H. D., Thorp, J. S., Wang, J. C., and Lu, J., "Optimal Controller Placements in Large Scale Linear Systems," *IEE Proceedings D (Control Theory and Applications)*, Vol. 139, No. 1, Jan. 1992, pp. 79-87

[11] Chen, G. S., Garba, J. A., and Wada, B. K., "Vibration Suppression for Precision Segmented Reflector Backup Structure," *SPIE Active Telescope Systems*, Vol. 1114, 1989, pp. 508-520

[12] Joshi, S. M., Control of Large Flexible Space Structures, Springer-Verlag, New York, 1989

[13] Creamer, N. G., and Junkins, J. L., "Low-Authority Eigenvalue Placement for Second-Order Structural Systems," *AIAA Journal of Guidance, Control, and Dynamics*, Vol. 14, No. 3, May-June 1991, pp. 698-701

[14] Cannon, R. H. and Rosenthal, D. E., "Experiments in Control of Flexible Structures with Noncolocated Sensors and Actuators," *AIAA Journal of Guidance, Control, and Dynamics*, Vol. 7, No. 5, Sept.-Oct. 1984, pp 546-553

[15] Balas, M. J., "Direct Velocity Feedback Control of Large Space Structures," *AIAA Journal of Guidance, Control, and Dynamics*, Vol. 2, No. 3, May-Jun. 1979, pp. 252-253

[16] Joshi, S. M., "Robustness Properties of Collocated Controllers for Flexible Spacecraft," *AIAA Journal of Guidance, Control, and Dynamics*, Vol. 9, No. 1, Jan.-Feb. 1986, pp. 85-91

[17] Bailey, T. and Hubbard, J. E., "Distributed Piezoelectric-polymer Active Vibration Control of a Cantilever Beam," *AIAA Journal of Guidance, Control, and Dynamics*, Vol. 8, No. 5, Sept.-Oct. 1985, pp. 605-611

[18] Burke, S. E. and Hubbard, J. E., "Active Vibration Control of a Simply Supported Beam using a Spatially Distributed Actuator," *IEEE Control Systems Magazine*, Vol. 7, No. 4, Aug. 1987, pp. 25-30

[19] Connally, J. A. and Hubbard, J. E., "Low Authority Control of a Composite Cantilever Beam in Two Dimensions," *Proceedings of the 1988 American Control Conference*, Vol. 3, 1988, pp. 1903-1908

[20] Tzou, H. S., "Integrated Distributed Sensing and Active Vibration Suppression of Flexible Manipulators using Distributed Piezoelectrics," *Journal of Robotic Systems*, Vol. 6, No. 6, Dec. 1989, pp. 745-767

[21] Turner, J. D., and Chun, H. M., "Optimal Distributed Control of a Flexible Spacecraft During a Large-Angle Maneuver," *AIAA Journal of Guidance, Control, and Dynamics*, Vol. 7, No. 3, May-June 1984, pp. 257-264

[22] Lane, J. S. and Dickerson, S. L., "Contribution of Passive Damping to the Control of Flexible Manipulators," *ASME Computers in Engineering 1984*, Las Vegas, NV

[23] Alberts, T. E., "Augmenting the Control of a Flexible Manipulator with Passive Mechanical Damping," Ph.D. Thesis, School of Mechanical Engineering, Georgia Institute of Technology, Atlanta, GA, Sept. 1986

[24] Nashiff, A. D., Jones, D., and Henderson, J. P., Vibration Damping, John Wiley and Sons, New York, 1985

[25] Semercigil, S. E., Popplewell, N., and Tyc, R., "Impact Damping of Random Vibrations," *Journal of Sound and Vibration*, Vol. 122, No. 1, 8 Apr. 1988, pp. 178-184

[26] Panossian, H. V., "Nonobstructive Impact Damping Applications for Cryogenic Environments," *Proceedings of Damping 1989*, 8-10 Feb. 1989, West Palm Beach, FL, pp. KBC1-KBC9

[27] Crawley, E. F., and O'Donnel, "A Procedure for Calculating the Damping in Multi-Element Space Structures," *Acta Astronautica*, Vol. 15, Dec. 1987, pp. 987-996

[28] Hertz, T. J. and Crawley, E. F., "Displacement Dependent Friction in Space Structural Joints," *AIAA Journal*, Vol. 23, Dec. 1985, pp. 1996-2000

[29] Ferri, A. A., "Modeling and Analysis of Nonlinear Sleeve Joints of Large Space Structures," *AIAA Journal of Spacecraft and Rockets*, Vol. 25, No. 5, 1988, pp. 354-360

[30] Bowden, M. and Dugundji, J., "Joint Damping and Nonlinearity in Dynamics of Space Structures", *AIAA Journal*, Vol. 28, No. 4, Apr. 1990, pp. 740-740

[31] Alberts, T. E., Hastings, G. G., Book, W. J., and Dickerson, S. L., "Experiments in Optimal Control of a Flexible Arm with Passive Damping," *Proceedings of the 5th VPI&SU/AIAA Symposium on Dynamics and Control of Large Structures*, 12-14 Jun. 1985, Blacksburg, VA

[32] Sinha, A. and Griffin, J. H., "Effects of Static Friction on the Forced Response of Frictionally Damped Turbine Blades," *Journal of Engineering for Gas Turbines and Power*, Vol. 106, Jan. 1984, pp. 65-69

[33] Singh, M. P. and Malushte, S. R., "Seismic Response of Simple Structures using Spring-Assisted Sliding Slabs with Coulomb Damping," *Earthquake Engineering and Structural Dynamics*, Vol. 19, Feb. 1990, pp. 189-203

[34] Stefanides, E. J., "Frictional Damping Smooths Automatic Washer Spin Cycles," *Design News*, Vol. 44, 15 Feb. 1988, pp. 226-227

[35] Foelsche, G. A., Griffin, J. H., and Bielak, J., "Transient Response of Joint Dominated Space Structures: A New Linearization Technique," AIAA Paper 88-2393, Apr. 1988

[36] Hertz, T. J., and Crawley, E. F., "Damping in Space Structure Joints," AIAA Paper 84-1039-CP, 17-18 May 1984, Palm Springs, CA

[37] Prucz, J., Reddy, A. D., Rehfield, L.W., and Trudell, R. W., "Experimental Characterization of Passively Damped Joints for Space Structures," *AIAA Journal of Spacecraft and Rockets*, Vol. 23, Nov.-Dec. 1986, pp. 568-575

[38] Prucz, J., "Analysis of Design Tradeoffs for Passively Damped Structural Joints," *AIAA Journal of Spacecraft and Rockets*, Vol. 23, Nov.-Dec. 1986, pp. 576-584

[39] Ferri, A. A. and Heck, B.S., "Analytical Investigation of Damping Enhancement using Active and Passive Structural Joints," *AIAA Journal of Guidance, Control, and Dynamics*, Vol. 15, No. 5, Sept.-Oct. 1992, pp. 1258-1264

[40] Book, W. J., "Modeling, Design, and Control of Flexible Manipulator Arms: A Tutorial Review," *Proceedings of the 29th IEEE Conference on Decision and Control*, Vol. 2, Dec. 1990, pp. 500-506

[41] Cudney, H. H., Horner, G. C., and Inman, D. J., "Vibration Control of Flexible Beams Using an Active Hinge," *Proceedings of the 5th VPI&SU/AIAA Symposium on Dynamics and Control of Large Structures*, 12-14 Jun. 1985, Blacksburg, VA, pp. 455-470

[42] Ferri, A. A., "Analysis of Flexible Structures with Nonlinear Joints", Invited Paper, *Proceedings of the Seventh International Modal analysis Conference*, Las Vegas, NV, Jan. 30 - Feb. 2, 1989

[43] Meirovitch, L. and Kwak, M., "Convergence of the Classical Rayleigh-Ritz Method and the Finite Element Method", *AIAA Journal*, Vol. 28, NO. 8, August 1990, pp. 1509-1516

[44] Kreindler, E. and Rothschild, D., "Model-Following in Linear-Quadratic Optimization," *AIAA Journal*, Vol. 14, No. 7, July 1976, pp. 835-842

[45] Hrovat, D., Margolis, D. L., and Hubbard, M., "An Approach Toward the Optimal Semi-Active Suspension," *ASME Journal of Dynamic Systems, Measurement, and Control*, Vol. 110, Sept. 1988, pp. 288-296

[46] Bryson, A. E. and Ho, Y. C., Applied Optimal Control, Hemisphere, New York, 1975

[47] Bryson, A. E., Denham, W. F., and Dreyfus, S. E., "Optimal Programming Problems with Inequality Constraints I: Necessary Conditions for Extremal Solutions," *AIAA Journal*, Nov. 1963, pp. 2544-2550

[48] Oberle, H. J. and Grimm, W., "BNDSCO - A Program for the Numerical Solution of Optimal Control Problems," English Translation of DFVLR-Mitt. 85-05

[49] Stoer, J. and Bulirsch, R., Introduction to Numerical Analysis, Springer, New York, 1983

[50] Butsuen, T. and Hedrick, J. K., "Optimal Semi-Active Suspensions for Automotive Vehicles: The 1/4 Car Model," Advanced Automotive Technologies - 1980, A. M. Karmel, E. H. Law, and S. R. Velinsky, eds., pp. 305-319, ASME Winter Annual Meeting, San Francisco, CA

[51] Bernstein, D. S. and Hyland, D. C., "Optimal Projection Approach to Robust Fixed-Structure Control Design", Mechanics and Control of Large Flexible Structures, Vol. 129, AIAA Progress in Astronautics and Aeronautics, J. L. Junkins (ed.), 1990, pp. 237-293

[52] Brogan, W. L., Modern Control Theory, Prentice-Hall, New Jersey, 1985

[53] Doyle, J. C. and Stein, G., "Robustness with Observers," *IEEE Transactions on Automatic Control,* Vol. AC-24, No. 4, Aug. 1979, pp. 607-611

[54] Doyle, J. C., "Guaranteed Margins for LQG Regulators," *IEEE Transactions on Automatic Control,* Vol. AC-23, No. 4, Aug. 1978

[55] Stein, G. and Athans, M., "The LQG/LTR Procedure for Multivariable Feedback Control Design," *IEEE Transactions on Automatic Control,* Vol. AC-32, No. 2, Feb. 1987, pp. 105-114

[56] Fu, M., "Exact, Optimal, and Partial Loop Transfer Recovery," *Proceedings of the IEEE 29th Conference on Decision and Control,* Honolulu, HI., Dec. 1990, pp. 1841-1846

[57] Turan, L., Mingori, D. L., and Goodwin, G. C., "Loop Transfer Recovery Design Using Biased and Unbiased Controllers," *Proceedings of the IEEE 29th Conference on Decision and Control,* Honolulu, HI., Dec. 1990, pp. 1835-1840

[58] Cetinkunt, S. and Yu, W-L., "Modified LQG/LTR-Based Controller Design for Distributed Parameter Motion Control Systems," *Computers and Structures,* Vol. 40, No. 4, 1990, pp. 1017-1025

[59] Doyle, J. C. and Stein, G., "Multivariable Feedback Design: Concepts for a Classical/Modern Synthesis," *IEEE Transactions on Automatic Control,* Vol. AC-26, No. 1, Feb. 1981, pp. 4-16

[60] Safonov, M. G., Laub, A. J., and Hartmann, G. L., "Feedback Properties of Multivariable Systems: The Role and Use of the Return Difference Matrix," *IEEE Transactions on Automatic Control,* Vol. AC-26, No. 1, Feb. 1981, pp. 47-65

[61] Postlethwaite, I. and Foo, Y. K., "Representations of Uncertainty and Robustness Tests for Multivariable Feedback Systems," Multivariable Control, S. G. Tzafestas (ed.), pp. 151-160

[62] Lehtomaki, N. A., Sandell, N. R., and Athans, M., "Robustness Results in Linear-Quadratic Gaussian Based Multivariable Control Designs," *IEEE Transactions on Automatic Control,* Vol. AC-26, No. 1, Feb. 1981, pp. 75-92

[63] Newsome, J. R., and Mukhopadhyay, V., "A Multiloop Robust Controller Design Study Using Singular Value Gradients," *AIAA Journal of Guidance, Control, and Dynamics,* Vol. 8, No. 4, Aug. 1985, pp. 514-519

[64] IMSL Math Library, Version 1.0, April 1987

[65] Kailath, T., Linear Systems, Prentice-Hall, New Jersey, 1980

[66] Bender, D. K., "Optimum Linear Preview Control with Application to Vehicle Suspension," *ASME Journal of Basic Engineering*, 1968, pp. 213-221

[67] Crosby, M. J. and Karnopp, D. C., "The Active Damper - A New Concept in Shock and Vibration Control," *43rd Shock and Vibration Bulletin Part 4*, June 1973, pp. 119-133

[68] Hrovat, D., "A Class of LQG Optimal Actuators," *Automatica*, Vol. 18, No. 1, 1982, pp. 117-119

[69] Cheok, K. C., Loh, N. K., and McGee, H. D., "Optimal Suspension Design with Microcomputerized Parameter Optimizing Damping," *IEEE Proceedings of 23rd Conference on Decision and Control*, Dec. 1984, pp. 400-406

[70] Karnopp, D. C., "Two Contrasting Versions of the Optimal Active Vehicle Suspension," *ASME Journal of Dynamic Systems, Measurement, and Control*, Vol. 108, Sept. 1986, pp. 264-268

[71] Yue, C., Butsuen, T., and Hedrick, J. K., "Alternative Control Laws for Automotive Active Suspensions," *ASME Journal of Dynamic Systems, Measurement, and Control*, Vol. 111, No. 2, pp. 286-291

[72] Hrovat, D., Margolis, D. L., and Hubbard, M., "Suboptimal Semi-Active Vehicle Suspensions," *Proceedings of the 1980 Joint Automatic Control Conference*, Aug. 1980

[73] Miller, L. R., "Tuning Passive, Semi-Active, and Fully Active Suspension Systems," *IEEE Proceedings of the 27th Conference on Decision and Control*, Dec. 1988, pp. 2047-2053

[74] Hac', A., and Youn, I., "Optimal Semi-Active Suspension with Preview Based on a Quarter Car Model," *ASME Journal of Vibrations and Acoustics*, Vol. 114, Jan. 1992, pp. 84-92

[75] Redfield, R. C., "Low-Bandwidth Semi-Active Damping for Suspension Control," *Proceedings of the 1990 American Control Conference*, May 1990, pp. 1357-1362

[76] Ferri, A. A., and Heck, B. S., "Semi-Active Suspension Using Dry Friction Energy Dissipation," *Proceedings of the 1992 American Control Conference*, Chicago, IL, June 24-26, 1992, pp. 31-35

[77] Strang, G., Linear Algebra and Its Applications, Harcourt Brace Jovanovich, San Diego, CA, 1988, pp. 339

VITA

Jeffrey Scott Lane was born on July 1, 1960 in Jacksonville, Florida. After attending nine separate schools and living in ten states and two foreign countries, he received his high school diploma from the Singapore American School in 1978. Upon graduating from high school, he attended Middle Georgia College in Cochran, Georgia where he earned an Associate of Science Degree in June 1980. In the fall of 1980, Jeff began his studies at the Georgia Institute of Technology where he earned a Bachelors Degree in Mechanical Engineering in December of 1982 and a Masters Degree in March of 1984. After receiving the Masters Degree, he began working at the Missile Systems Division of Rockwell International where he designed guidance and control systems for tactical missiles. After winning a National Defense Science and Engineering Graduate Fellowship from the Department of Defense and a Presidential Fellowship from Georgia Tech in 1990, Jeff returned to Georgia Tech as a full-time student to complete his Ph.D. degree. Upon graduating, Jeff will begin employment with the Milliken Research Corporation in Spartanburg, South Carolina.